University of Southampton

Partial Discharge Detection In Cable Systems

by

Yuan Tian

A thesis submitted for the Degree of

Doctor of Philosophy

in

The Department of Electronics and Computer Science

April 2001

UNIVERSITY OF SOUTHAMPTON

ABSTRACT

FACULTY OF ENGINEERING AND APPLIED SCIENCE

DEPARTMENT OF ELECTRONICS AND COMPUTER SCEINCE

Doctor of Philosophy

PARTIAL DISCHARGE DETECTION IN CABLE SYSTEMS

by Yuan Tian

This thesis is concerned with the development of suitable methods for partial discharge (PD) detection, quantification and location within high voltage cable systems. Acoustic emission (AE) techniques are suitable for PD on-line monitoring. This approach is free from electrical interference. Application of acoustic emission techniques to PD detection in polymeric cable insulation has been investigated using a planar experimental model. The obtained AE signals were processed in the time and frequency domains, as well as using statistical patterns and operators. Factors influencing AE signal measurement and attenuation have been investigated. The relationship between the discharge acoustic emission and electric signals has been evaluated. AE measurements have been used to investigate PD behaviour during electrical tree growth within cable insulation. Artificial neural networks (ANN) were used to characterise AE signals. The frequency spectrum obtained by short duration Fourier transform of AE signal and the wavelet decomposition coefficients were used as ANN input parameters. Both the feed forward neural network using the back propagation algorithm and the Kohonen self organising map neural network using the learning vector quantization algorithm were applied. Results indicate that ANN can identify different PD sources effectively.

The development of capacitive coupler techniques for PD on-line detection has been investigated. High detection sensitivity can be obtained and PD site location can be realised by evaluating the time of flight from more than one coupler. A cross-correlation algorithm was implemented to automatically estimate the time of flight. An alternative PD test method for long cable/joint system has been established. This method reduces the power supply requirement of the test system.

The capacitive coupler, acoustic emission sensor and radio frequency current transducer (RFCT) were used to detect partial discharges within a 132 kV cable joint. PD detection, location, calibration and distinguishing between internal discharges and external noise, using the capacitive coupler technique, were investigated. The AE signal attenuation within the cable joint was investigated. Acoustic location of the PD site was studied through analysis of time of flight between the discharge electric pulse and different AE sensor outputs. The RFCT measured signal to noise ratio was improved by wavelet de-noising. PD measurements for a cable section with water terminations indicated that the detection sensitivity for the capacitive coupler approach was higher than a simple screen interruption method.

Contents

List of Figures

List of Tables

List of Symbols and Abbreviations

Symbols

α	angle between the magnetic field by current on the sheath and loop
ρ	density
μ	mean value of the distribution
φ	phase
ε_0	dielectric constant in the vacuum
μ_0	permeability in vacuum
$\psi_{a,b}(x)$	mother wavelet
φ_i	phase position
$\omega_{ij}^{[k]}$	weight connections
φ_{in}^{-}	inception phase in the negative half of the voltage cycle
φ_{in}^{+}	inception phase in the positive half of the voltage cycle
ε_r	dielectric constant in the insulation material
μ_r	relative permeability of the insulation material
$-\Delta U$	internal voltage by space charge
ΔU_a	voltage change over C_a
ΔU_b	voltage change over C_b
ΔU_c	voltage change in the void
ΔU_q	instant voltage change across the cable
ρv	acoustic characteristic impedance
$\psi_{xy}(m)$	cross spectrum estimate

$\psi_{yx}(m)$	cross spectrum estimate
A	area of the sensor loop
$B_i^{[k]}$	threshold vector
C_0	capacitance per meter of cable
C_1	distributed coupler capacitance
C_2	coupler stray capacitance
C_3	capacitance of the cable section with insulation gap
C_4	stray capacitance of the insulation gap
C_a	equivalent capacitance of the rest of the dielectric
C_b	equivalent capacitance of the dielectric in contact with the void
C_{ca}	capacitance of the cable
CC	cross correlation factor
C_c	equivalent capacitance of the void
C_k	coupling capacitor
C_m	relevant capacitance of the model
C_s	stray capacitance between the coupler sensor and the cable sheath
C_x	sample under test
d	distance between electrodes
D	length of the whole sheath break
D1	distance between the coupler sensor and the cable sheath
D2	length of coupler sensor
D_c	diameter of the conductor
D_i	diameter of the insulation
d_j	Euclidean distance
E_A	acoustic energy
E_E	electric energy
E_{max}	maximum electric field stress
f	frequency
$H_n^-(\varphi)$	$H_n(\varphi)$ for the negative half of the voltage cycle
$H_n(\varphi)$	the pulse count distribution
$H_n^+(\varphi)$	$H_n(\varphi)$ for the positive half of the voltage cycle
$H_{qmax}(\varphi)$	the maximal discharge amplitude distribution
$H_{qn}^-(\varphi)$	$H_{qn}(\varphi)$ for the negative half of the voltage cycle

$H_{qn}(\varphi)$	the mean pulse height distribution
$H_{qn}^{+}(\varphi)$	$H_{qn}(\varphi)$ for the positive half of the voltage cycle
K	constant
K_1	constant
K_2	constant
K_3	constant
Ku	kurtosis
Ku(-)	kurtosis for $H_n^{-}(\varphi)$
Ku(+)	kurtosis for $H_n^{+}(\varphi)$
L_0	inductance per meter of cable
L_1	distributed coupler inductance
L_2	inductance of the cable section with insulation gap
MCC	modified cross correlation factor
N	effective number of loops
n	frequency per unit time
N^{-}	number of discharges in the negative half of the voltage cycle
N^{+}	number of discharges in the positive half of the voltage cycle
n_{ij}	number of AE signals
P_A	acoustic wave pressure
Φ	phase asymmetry
Q	discharge asymmetry
q	relative magnitude
Q^{-}	sum of signal amplitudes in the negative half of the voltage cycle
Q^{+}	sum of signal amplitudes in the positive half of the voltage cycle
q_a	apparent charge
q_c	practical charge in the void
q_j	AE signal amplitude
r	needle tip radius
R	reflection coefficient
R_1	matching impedance
R_2	the detection impedance
R_3	impedance between the coupler and the cable sheath
R_a	matching impedance

R_b	matching impedance
R_c	matching impedance
R_s	impedance between the coupler sensor and the cable sheath
R_{xy}	FFT-based cross correlation indicating signal x leads signal y
rxy	time-based cross correlation indicating signal x leads signal y
R_{yx}	FFT-based cross correlation indicating signal y leads signal x
ryx	time-based cross correlation indicating signal y leads signal x
S_A	output of acoustic sensor
Sk	skewness
Sk(-)	skewness for $H_{qn}^{-}(\varphi)$
Sk(+)	skewness for $H_{qn}^{+}(\varphi)$
σ	standard deviation of the distribution
T1	simulation of a 1 m long cable section
T2	simulation of a 1.6 m long cable section
U_c	voltage over the void
U_{cb}	breakdown voltage for gas
U_p	discharge pulse
U_s	inverse voltage due to discharge
v	acoustic velocity
V	amplitude of the test voltage
V1	simulation of a pulse generator
V_1	voltage produced by the inductive sensor
V_c	voltage over the cable
V_i	inception voltage
V_{im}	applied voltage magnitude
W	discharge energy
ψ	wavelet function
$W_f(a,b)$	wavelet transform
x	mean signal amplitude in a phase window in the positive half cycle
x_i	random variable
$X_i^{[k]}$	neural network inputs
y	mean signal amplitude in a phase window in the negative half cycle
Z_0	cable characteristic impedance
Z_d	input unit

Abbreviations

AC	alternating current
AE	acoustic emission
AES	acoustic emission sensor
ANN	artificial neural network
ART	adaptive resonance theory
BP	back propagation
CT	current transducer
DC	direct current
DCS	directional coupling sensor
DGA	dissolved gas analysis
EPR	ethylene propylene rubber
ERA	electrical research association
FFT	fast fourier transform
GIS	gas insulated substation
HDPE	high density polyethylene
HF	high frequency
HFCP	high frequency current probe
HV	high voltage
HVP	high voltage probe
IEC	international electrical commission
LDPE	low density polyethylene
LVQ	learning vector quantization
PD	partial discharge
PE	polyethylene
pe	processing element
PF	power frequency
PVC	polyvinyl chloride
RFCT	radio frequency current transducer
SDFT	short duration fourier transform
SGP	surge protector
SNR	signal to noise ratio

SOM	self organising map
TDR	time domain reflectometry
UHF	ultra high frequency
VHF	very high frequency
XLPE	cross linked polyethylene

Acknowledgements

My acknowledgement must go to Dr Paul Lewin for his guidance, support and encouragement in every part of this work, without which the completion of this thesis would not be possible. My gratitude must also go to Professor Tony Davies, for providing me this precious opportunity to do research in the High Voltage Laboratory and for his guidance and support throughout the duration of this project.

I would also like to express my appreciation to all my colleagues in the high voltage group for their assistance and patience. In particular, to Mr Roland Caldecutt, Mr Neil Palmer and Mr Richard Howell for the assistance in the technical work, and to Mr Mingli Fu, Mr Matthew Brown for the valuable discussions. The help from Dr George Chen for both my work and life is something I will always appreciate.

My gratitude is also extended to The National Grid Company plc, the funding company for this project, and in particular to Professor Steve Swingler, Dr Graham Hathaway, Dr Zac Richardson and Dr Simon Sutton for their advice and support.

Last but not least, I would like to thank my parents, my wife and the whole family for their love, support and encouragement throughout the duration of my study in England.

To my dearest parents.

Chapter 1

Introduction

The term "partial discharge" (PD) is defined by IEC 270 as a localised electrical discharge that only partially bridges the insulation between conductors and which may or may not occur adjacent to a conductor [1]. A PD is confined in some way that does not permit complete failure of the system, i.e. collapse of the voltage between the energised electrodes such as the cable conductor and neutral.

Partial discharge is often caused by the existence of a void inside or on the surface of the insulation. The dielectric constant of gas is lower than that of a liquid or solid. Under an alternating electric field, the electric stress is inversely proportional to the dielectric constant. If a void exists in a liquid or solid medium, the electric stress for the void will therefore be higher than the surrounding dielectric. On the other hand, the breakdown strength of a gas is lower than the breakdown strength of the liquid or solid. Consequently partial discharges occur within the void.

Apart from voids, there are other sources that can generate partial discharges. If a conductive particle exists within the insulation, electric field concentration will be formed and may lead to partial discharge. Likewise, a needle-shape conductor or a protrusion on the surface of the conductor will also generate highly concentrated electric fields and can produce partial discharge. In addition, a floating potential can be formed if a conducting part of any electrical apparatus is not correctly grounded, or

high potential differences can be caused due to the bad contact between conductors. Partial discharges can be generated in both cases.

Apart from within the electrical apparatus, discharges can also occur at the high voltage terminal of electrical apparatus. Surface discharges may occur along the interface between the dielectric and air. Corona can be formed around a conductor that is surrounded by gas, if the electric field around the conductor reaches the breakdown strength of the gas.

Partial discharge activity may lead to the eventual breakdown of insulation. Therefore, PD detection is very important. In fact, partial discharge tests have been used for over 50 years to measure the quality of electrical insulation. Such tests generally are performed off-line within a well-screened laboratory, using voltages higher than the normal operational voltage. The test circuit should be able to detect the permissible discharge quantity regulated for the test object. However, sometimes the goal of PD measurement is to detect deterioration while the apparatus is in normal use, i.e. PD on-line monitoring. Interference may be severe under on-line conditions, and the PD test has to be carried out at the normal operating voltage. Therefore, PD on-line monitoring is very different from conventional electrical detection. On-line monitoring may not be able to detect small discharges during the initiation of insulation deterioration, but it should be able to detect discharges that will endanger operational safety. It should be able to warn the user when the deterioration has reached a certain defined level, in order to prevent the occurrence of breakdown.

The principle objective of this thesis is to investigate the application of acoustic emission and capacitive coupler techniques to partial discharge detection within cable systems. Chapter 2 introduces the fundamental theory and general PD detection methods for power apparatus. Chapter 3 presents a review of partial discharge detection and location within cable systems. Disturbances and methods of rejection are also detailed. Chapter 4 investigates the acoustic emission measurement of partial discharges using an experimental planar model. Acoustic emission measurement is also applied to study the partial discharge behaviour during electrical tree growth in XLPE cable insulation, and to detect partial discharges from an epoxy sample. The application of artificial neural networks to acoustic emission signal characterisation is investigated in Chapter 5. Chapter 6 details the application of capacitive couplers to partial discharge detection for cables and the influence of an insulation gap on the capacitive coupler performance. Chapter 7 investigates the application of potential on-

line monitoring methods, including the capacitive coupler, the acoustic emission sensor and the radio frequency current transducer, to partial discharge detection for cable joint. A comparison between the capacitive coupler and the screen interruption sensor is performed using a cable section. Finally the conclusions of the work and recommendations for further study are presented in Chapter 8.

Chapter 2

Partial Discharge Fundamentals

2.1 The Mechanisms of Gaseous Discharge

Partial discharge activity often occurs within a void. To interpret the partial discharge phenomenon, it is necessary to understand gaseous discharge mechanisms. The theoretical gas discharge mechanisms include the Townsend theory and the Streamer theory [2-7].

- The Townsend Theory

Free electrons are accelerated under the electric field and collide with the neutral gaseous molecule. If the kinetic energy of the electron is high enough, a new electron and a positive ion will be formed. New electrons and original free electrons will continue to be accelerated and collide into other molecules, producing new electrons, which will lead to electron avalanche. On the other hand, the formed positive ions move toward the cathode and enhance the electric field around the cathode. The positive ion will then be accelerated and bombard the cathode, causing the cathode to emit electrons that are called the secondary electrons. Eventually the electron avalanche will be maintained without depending on free electrons, and the gaseous discharge will become self-sustaining.

- The streamer theory

The initiating electron starts an avalanche by the simple Townsend mechanism. As the electrons move faster, they are concentrated at the head of the electron avalanche, followed by positive ions. The space charges significantly strengthen the electric field at the head of the electron avalanche, while the middle part of the avalanche can be considered as a plasma column with weak electric field, making the recombination of ions and electrons easier. The recombination process produces a lot of photons. The photons ionise the neutral molecules near the avalanche head with high electric field and emit electrons. The electrons move toward the anode and a second electron avalanche is formed. The second avalanche will then connect the original avalanche and enlarge the plasma column. When the plasma has bridged the anode and the cathode, gaseous discharge with a narrow discharge channel occurs. This is the so-called streamer discharge. The speed of photon-induced ionising is faster than that of electron-induced ionising, thus the streamer discharge is more rapid than the Townsend discharge. The time to breakdown is 1 to 10 ns for streamer discharge and 80 to 800 ns for Townsend discharge, for cavities with a thickness of 0.1 to 1 mm [8].

2.2 Types of Gaseous Discharge

Gaseous discharge generally can be divided into pulse discharge (e.g. spark discharge) and pulseless discharge (e.g. glow discharge) [3,6,9,10]. Partial discharge generally belongs to the category of pulse discharge, for which separate pulses can be observed at certain phase positions of the applied voltage cycle. For pulseless discharge, separate pulses cannot be observed, but the excited light can be detected, and the low frequency discharge current and the acoustic wave associated with discharges measured.

2.3 The Partial Discharge Process

Partial discharge occurs within a partial area between electrodes. The space charge produced by discharges will accumulate in this area, and affect the electric field. The discharge process is an intermittent process generating a series of discharge pulses.

2.3.1 The internal discharge process

For an internal discharge due to a void within the insulation, the exchange and accumulation of charges in the void cannot be directly measured, however, they can be reflected by the change of charge on the two electrodes on either side of the insulation [7,10]. The relationship can be analysed using the equivalent circuit shown in Figure 2.1.

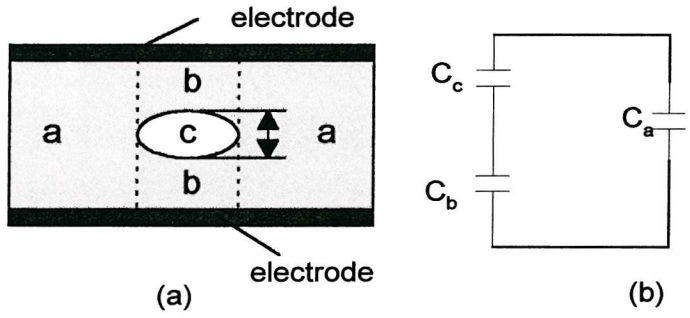

(a) void in solid dielectric (b) equivalent circuit

Figure 2.1 Partial discharge equivalent circuit

Where C_c is the equivalent capacitance of the void, C_b is the equivalent capacitance of the dielectric in contact with the void and C_a is the equivalent capacitance of the rest of the dielectric.

When an alternating voltage is applied to the electrodes, the voltage across the void U_c will change with the applied voltage before it reaches the breakdown voltage for the gas (U_{cb}). Discharge occurs when the void voltage reaches U_{cb}. Due to the discharge, a large amount of neutral gas molecules are ionised into positive ions, electrons and negative ions, thus producing a large amount of space charges. Under the applied electric stress, these space charges move to the wall of the void and cause an internal voltage $-\Delta U$ which is inverse to the applied voltage, as shown in Figure 2.2. Thus the accumulated void voltage is the addition of the two:

$$U_r = U_{cb} - \Delta U < U_{cb} \qquad (2.1)$$

The discharges are then extinguished as the accumulated void voltage is less than the breakdown voltage. The void voltage is then increased due to the increase of the applied voltage, and a second discharge will occur when the voltage again reaches U_{cb}. An inverse voltage ΔU is created due to the space charge. If the accumulated charge due to the first discharge has not been lost, the inverse voltage will then be $-2\Delta U$. Consequently the void voltage is dropped again to U_r, and the discharge is

extinguished. If the discharge process occurs n times before the applied voltage reaches the peak, the internal voltage will be -nΔU due to the space charge effect. U_c drops after the applied voltage is over the peak, and discharge will restart when the void voltage reaches - U_{cb}, i.e.

$$-n\Delta U + U_c = - U_{cb} \tag{2.2}$$

In this case, the direction of the movement of the space charge is determined by the direction of the electric field established by the internal space charge. Therefore, part of the accumulated charge is neutralised, and the internal voltage is dropped with a ΔU. The voltage over the void drops to - U_r and discharge is extinguished. Afterwards, the absolute value of the void voltage increases as the applied voltage decreases and reaches - U_{cb} again, consequently discharge restarts. If ΔU is the same for each discharge and U_{cb} is equal to the absolute value of - U_{cb}, the charge produced by discharges will disappear when the applied voltage passes through zero, and a new discharge cycle will start at the second half of the power cycle. The discharge pattern for the internal void case is generally symmetric for the positive and negative half of the power cycle.

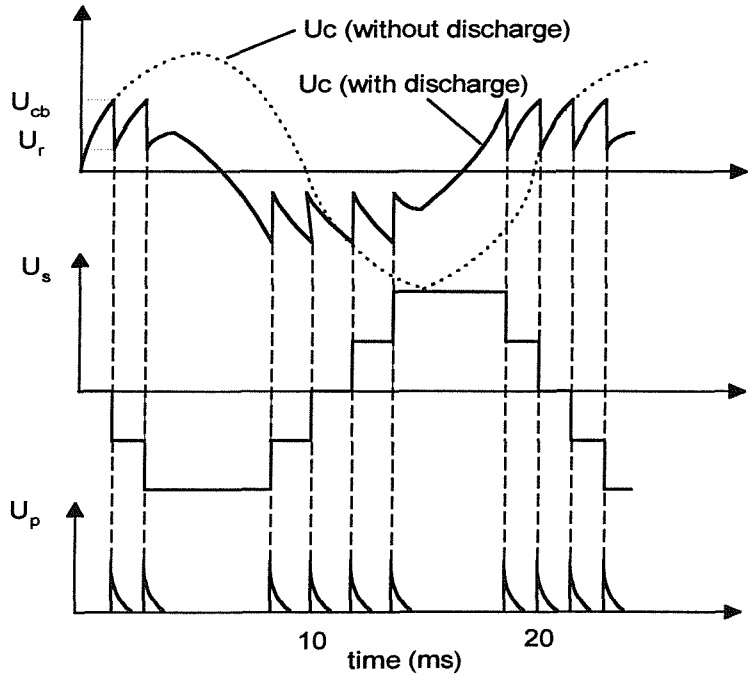

U_c:applied voltage; U_s:inverse voltage due to discharge; U_p: discharge pulse

Figure 2.2 The discharge process

Figure 2.3 shows a practical internal discharge pattern. The discharge magnitude is not the same for every discharge and discharges generally occur at the rising part of the applied voltage magnitude (the first and the third quadrants). Only when the discharge is very intense can the discharge pattern be extended to the falling part of the applied voltage (the second and the fourth quadrants). There may co-exist several discharge voids. Even in the case of a single void, discharges may only occur in part of the area rather than the whole area of the void. Consequently discharges can differ in size. Still, if part of the space charge is lost during the discharge process and the absolute value of the accumulated inverse voltage $-n\Delta U$ is smaller than the absolute value of $-U_{cb}$, discharges will not occur at the second and the fourth quadrants of the power cycle. Due to the above reasons, the practical discharge pattern is often different from the theoretical analysis.

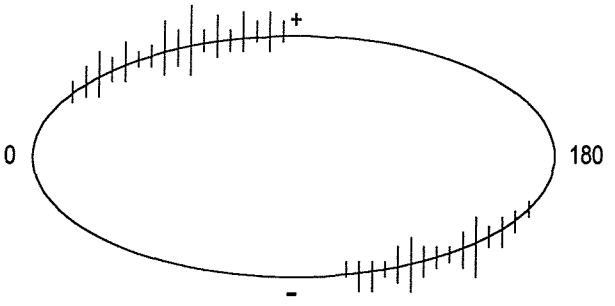

Figure 2.3 Practical internal discharge

2.3.2 The corona discharge process

Corona discharge occurs around sharp points or the edges of a high voltage electrode surrounded by gas. The gas molecules move freely and space charges generated from the discharge do not stay within the space. Therefore, the corona discharge process is distinct from the discharge processes related to voids [5,7,10]. Figure 2.4a shows a point-plane electrode system. When the applied voltage is increased and the electric stress around the point reaches the gas breakdown strength, discharges occur around the point. Discharge generally occurs when the point electrode is negative, for the reason that electrons are easily emitted from the negative electrode and the ions bombard the cathode to cause secondary electron emission. The positive ions move towards the point, and electrons travel away from the point and towards the plane electrode. At a greater distance from the cathode the electrons slow down and attach themselves to neutral molecules. Two regions with space charge are formed. A

positive space charge has been built up in the nearest vicinity of the point by the slow positive ions which are left after the ionisation of the gas molecules. At a greater distance the negative ions which are formed by adhesion of the electrons to the gas molecules cause negative space charge. The negative space charge shields the electric field at the point, the positive ions move into the point without producing further ionisation as the field strength is too low, and the discharge extinguishes. After the extinction the negative space charge moves away to the anode, the electric stress rises and the next discharge starts. Figure 2.4b shows practical corona discharges for one ac voltage cycle. They occur around the negative peak of the applied voltage. They are equal in size and have same phase spacing.

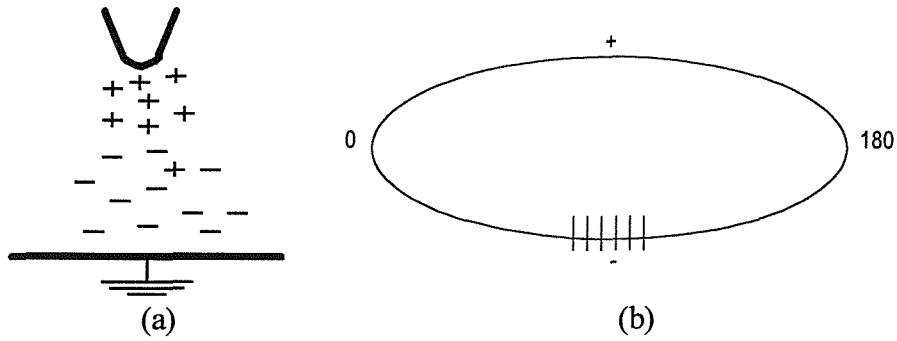

Figure 2.4 The corona discharge

2.4 Partial Discharge Parameters

Several descriptive discharge quantities have been introduced to describe the characteristics of a discharge. IEC-270 [1] defines the following partial discharge quantities: apparent charge, maximal charge, average charge, repetition rate, average discharge current, the quadratic rate, the discharge power, the discharge energy, inception voltage and extinction voltage. Among these quantities, the apparent charge, the discharge repetition rate, the inception voltage and the discharge energy are most widely applied.

Apparent charge is the charge transfer in the sample when the voltage is applied. The relationship between the apparent charge and the practical charge (the charge transfer in the void) can be deduced using the equivalent circuit in Figure 2.1. If the voltage change in the void is ΔU_c when partial discharge occurs, the practical charge in the void will be:

$$q_c = \Delta U_c (C_c + \frac{C_a C_b}{C_a + C_b}) \tag{2.3}$$

Generally, the void size is small and the following relationship exists:

$$C_a >> C_b, \quad C_a > C_c, \quad C_c > C_b \tag{2.4}$$

Therefore,

$$q_c = \Delta U_c (C_c + C_b) \tag{2.5}$$

$$\Delta U_a = \Delta U_c \frac{C_b}{C_a + C_b} \approx \Delta U_c \frac{C_b}{C_a} \tag{2.6}$$

Thus the apparent charge in the whole sample is:

$$q_a = \Delta U_a (C_a + \frac{C_c C_b}{C_c + C_b}) \approx \Delta U_a C_a \approx \Delta U_c C_b \tag{2.7}$$

According to Equation 2.5,

$$q_a = \frac{C_b}{C_b + C_c} q_c \tag{2.8}$$

Equation 2.8 indicates that, the apparent charge is smaller than the practical charge. However, the practical charge cannot be measured while the apparent charge can be measured easily by a discharge detector. Consequently the apparent charge has been used for partial discharge evaluation.

The largest repetitive apparent charge is defined as the discharge magnitude for a sample, and the discharge magnitude is used to evaluate the partial discharge level. It is believed that discharges below a certain magnitude are harmless to the dielectric material. This magnitude is called the permissible discharge magnitude. It is stipulated for electrical apparatus, and the detection circuit used must be able to detect discharges of at least that magnitude and ideally smaller.

The discharge repetition rate is the equivalent number of discharges in one second for the time period of measurement.

The inception voltage is the applied voltage (r.m.s.) at which the initial discharge can be observed. In practice, the inception voltage is usually determined when the discharge reaches the permissible discharge magnitude that has been stipulated for the electrical apparatus.

The discharge energy is the energy dissipated by a discharge. When the voltage across the void drops from U_{cb} to U_r (Figure 2.2), the energy is

$$W = \frac{1}{2}\left(C_c + \frac{C_a C_b}{C_a + C_b}\right)\left(U_{cb}{}^2 - U_r{}^2\right) \approx \frac{1}{2}(C_c + C_b)U_{cb}\Delta U_c \tag{2.9}$$

If a discharge occurs when the applied voltage magnitude is V_{im}, U_{cb} can be calculated as:

$$U_{cb} = \frac{C_b}{C_b + C_c} V_{im} \tag{2.10}$$

Thus,

$$\begin{aligned} W &= \frac{1}{2}(C_c + C_b)\frac{V_{im}}{C_b + C_c} C_b \Delta U_c \\ &\approx \frac{1}{2} V_{im} q_a = \frac{\sqrt{2}V_i}{2} q_a \approx 0.7 V_i q_a \end{aligned} \tag{2.11}$$

Where V_i is the inception voltage. Thus the discharge energy W is in a simple way related to the apparent charge. The discharge energy may cause deterioration of the dielectric.

2.5 Partial Discharges under DC Stress

When dc voltage is applied, discharges occur during the rise of the voltage, as in the case of ac voltage. After the voltage has become constant, discharges occur infrequently [7,10]. If the discharge repetition rate is very low, discharges even with high magnitude will not have a detrimental effect on the insulation. Therefore, the discharge repetition rate is the most important parameter when evaluating partial discharge at dc voltages. The discharge repetition rate increases with the applied voltage, the conductivity of the dielectric and the temperature. Usually the conductivity of dielectrics is very low and consequently the discharge repetition rate is also low.

Partial discharges at dc voltage are less harmful to the insulation than under ac stress. However, due to the increase in voltage rating of dc power apparatus and the correspondingly increase of operating temperature, it is important that partial discharge measurements under dc stress are undertaken as part of the development process of dc power equipment.

2.6 Effect of Partial Discharge on Insulation Performance

2.6.1 Mechanism of electrical ageing

Partial discharge is the main reason for the electrical ageing and insulation breakdown of high voltage electrical apparatus. Electrical ageing is a complicated process, and may be caused by several phenomena [5,7,10,11] such as:

- Ion and electron bombardment, which can break the chemical bond and cause cracking of the insulation material.
- Thermal degradation. Very high temperatures can be generated at the discharge site. Burning or melting of the insulation material can often be seen on a dissected sample that has been under long-term ageing but without breakdown. High temperatures will cause thermal cracking, increase the dielectric conductivity and dielectric loss, which will in turn accelerate the electrical ageing process, leading eventually to the final breakdown of the insulation.
- Formation of chemical products in the ionised gas, such as ozone and nitric acid, which can corrode the insulation material and wreck the dielectric performance.
- Radiation products such as ultraviolet rays, χ rays and γ rays, which may break the main bond and decompose the high molecule into a monomer. For some materials, the rays can impel the cross-link among molecules and make them brittle.
- Effect of mechanical force. The high-pressure gas and the acoustic oscillation wave due to intermittent and blasting discharges may crack the insulation and form new discharge sites.

The above effects often occur simultaneously. However, one mechanism may dominate for different dielectric materials operating under different working conditions. For example, charged particle bombardment is significant if the applied electric stress is high and the void dimension is large; Thermal degradation will dominate at high temperatures, under high dielectric loss, or if the heat endurance performance of the material is poor; Chemical by-products can be a key factor if humidity is high or if the pollution level is significant.

2.6.2 Electrical ageing process

Deterioration due to internal and surface discharges starts as surface erosion. This erosion may be caused by thermal degradation, soft χ rays or ultraviolet radiation. As this occurs the discharges become concentrated near the periphery of the void and a number of deep pits are formed. As the depth of the pits grows, the energy of the discharge increases and carbonisation of the pit can also occur. Finally the stress at the top of pit approaches the intrinsic electric strength of the dielectric over a distance of some microns owing to the field concentration around its sharp tip. The dielectric breaks down over this distance, and the field concentration moves to the new tip. Consequently electrical trees are formed and grow [10].

For internal discharges in impregnated paper, various gases are decomposed from the oil. Wax that is formed from the oil by ionisation remains on the papers, strengthening the discharge and consequently weakening the insulation. Discharges in voids adjacent to the conductor attack the insulation and penetrate the first paper layer after some time. Surface discharges occur along the layers and trees or carbonised tracks are formed. The tracks follow the weakest points in the insulation such as the butt-gaps between paper tapes [7,10,12].

Water trees are channel-shaped structures which develop in the form of minute trees in the insulation material as a result of moisture ingress and a reduction in breakdown strength. The development of water-trees takes place over some years. Water-trees can occur continuously in a cable without reducing its functional capacity. The critical phase begins when the discharge inception stress at the tips of a water-tree is exceeded. This is referred to the transformation of a water-tree into an electrical tree [13]. Since water-trees in the insulating material are likely to pave the way for future electrical trees, they can also be used to measure the ageing condition of the plastic or impregnated paper cables [11,14].

As corona discharges usually occur around bare conductors, they cannot attack insulation in the same way as internal and surface discharges. Only indirect action by ozone formed by corona may deteriorate neighbouring dielectrics. However, corona is of interest because it produces radio disturbances and causes dielectric losses for high voltage lines.

Figure 2.5 shows the tree development process. The electrodes are embedded inside polyethylene. Tree discharges occur when the electric field around the needle tip

is enough high. Figure 2.5(a) indicates the initial tree with a few branches; 2.5(b) indicates that tree is growing with more branches; 2.5(c) indicates that some thin branches have bridged the other electrode but no breakdown occurs; 2.5(d) indicates that the final breakdown occurs when a large and destructive current flows through the conducting path between the electrodes.

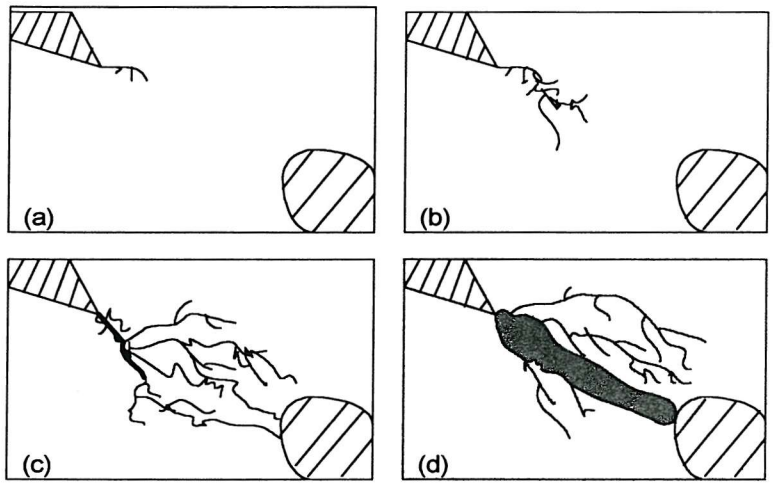

Figure 2.5 The development of electrical tree

Apart from tree growth leading to breakdown, there are other reasons for failure. For example, the insulation material may be softened or melted due to extreme high temperatures at the discharge site, which can lead to thermal breakdown. Breakdown may also be caused by a large amount of gas in the oil due to its poor gas absorption. Different electric apparatus under different operational conditions may have different ageing processes.

2.7 Partial Discharge Detection Methods

Partial discharges generate both physical phenomena (including electrical, acoustic and optical phenomena) and chemical changes. Partial discharge is associated with the charge transfer and the loss of discharge energy. The pulse transient change also produces an electromagnetic wave. There are also non-electric information from partial discharges, such as acoustic waves, light, and chemical by-products. Consequently partial discharge detection can be generally categorised into electrical, acoustic, optical and chemical methods.

- Electrical detection

The frequency spectrum of the partial discharge electrical signal can reach above 1 GHz, but PD signals are attenuated more at higher frequencies. The conventional electrical method according to IEC 270 [1] generally works in the frequency range from tens to hundreds of KHz, and is the one used most in the manufacturing industry. For over 50 years it has been applied to different power apparatus, such as power capacitors, transformers, electrical machines, circuit breakers, gas insulated substation (GIS), cables and cable accessories. This method offers good detection sensitivity and can give an indication of the magnitudes of partial discharges. However, the nature of the test limits its application to off-line testing only.

Electrical detection can also be realised through capacitive couplers or inductive sensors such as current transducers. Some sensors work within the frequency range of the conventional electrical detection, but many work in higher frequency ranges, such as in the very high frequency (VHF) range from 30 MHz to 300 MHz, or in the ultra high frequency (UHF) range from 300 MHz to above 1 GHz [15]. These sensors are easy to apply, and may be used to locate partial discharges. They are suitable for partial discharge on-line monitoring. Through careful selection of the measuring frequency range, the signal/noise ratio (SNR) can be improved. The major disadvantages with these approaches are the difficulty of quantifying the detection sensor output with the discharge apparent quantity (in pC), and the difficulty of inferring the nature and form of the discharge activity [16].

For partial discharge detection in motors and generators, much research work has been undertaken into the application of capacitive couplers and high frequency current transducers (HFCT) [17-21]. HFCT can be placed around a grounding lead, and capacitive couplers can be installed in stator slots of generator as internal sensors. Current transducers have also been applied to the PD detection in power transformers [22-26], the current transducers are usually clamped around the transformer terminals to detect the current. For gas insulated substations (GIS), recent research work has concentrated on detecting partial discharges in the UHF range. PD signals inside GIS can generate UHF radiation, and the UHF signals propagate effectively along the GIS chambers. On the other hand, the UHF noises in power networks usually attenuate rapidly during propagation. Therefore, high detection sensitivity and high anti-interference ability can be achieved by using the UHF sensing technique [27-31].

- Acoustic detection

When a partial discharge occurs, there is a rapid release of energy, some of which is emitted as acoustic energy. The use of acoustic transducers to detect partial discharges is attractive on a number of counts: the test equipment is small; no additional high voltage capacitors are required; it is not necessary for the power supply to be disconnected, thus it is suitable for on-line monitoring; acoustic detection is free from electrical interference and external discharges will not be detected. The main disadvantage with the acoustic method is of the attenuation of acoustic wave during its propagation, and the difficulty of quantifying the acoustic sensor output with the discharge apparent quantity (in pC).

Acoustic sensors include the accelerometers operating in the audio range (below 20 KHz) and acoustic emission (AE) sensors operating in the ultrasonic range (above 20 KHz). Accelerometers have mainly been involved in detecting discharges in circuit breakers [32-34]. AE sensors have been widely applied to a range of power apparatus, including power transformers [35-38], GISs [39-41], generators [42], capacitors [43], cables and cable accessories (Section 3.3.3).

- Optical detection

Optical methods are seldom applied to partial discharge detection in power apparatus, due to the low detection sensitivity and difficulty in application. There have been some attempts to use this approach. For example, discharge optical signals in GIS have been measured with a photo-multiplier tube using a photon-counting technique [44,45].

- Chemical detection

Partial discharge activity invariably results in changes in the chemical composition of the dielectric, these changes have been exploited in the detection of PD activity.

In GIS, under PD activity, the SF_6 decomposes to characteristic chemical species. Among them SOF_2 and SO_2F_2 are two important ones. Consequently the detection of those gases confirms the presence of PD [41,46,47].

In power transformers, PD activity can be inferred by the chemical detection of changes in the transformer oil [48,49]. Dissolved gas analysis (DGA) has been developed extensively. It has been argued that DGA is perhaps the simplest and

cheapest technique available for on-line testing of transformers, requiring minimum disruption to normal procedures. In addition, sample collection and analysis can be carried out readily and at very short notice. Fault gases typically generated include acetylene, methane, hydrogen, carbon dioxide and ethylene plus (to a lesser extent) ethane, oxygen, nitrogen and carbon monoxide [50].

Unfortunately, despite progress to date, chemical detection provides only an integrated measure of prevalent PD activity and provides little or no indication of its nature, intensity, extent or location [16]. Consequently chemical methods have not been widely applied to the PD detection.

Chapter 3

Review of Partial Discharge Detection within Cable Systems

3.1 Overview

Partial discharge testing has been used for over 50 years to measure the quality of electrical insulation, and sometimes, to detect if insulation deterioration has occurred in high voltage apparatus. It has been the main non-destructive electrical test for cable insulation, especially extruded plastic cable insulation such as Polyethylene (PE), cross-linked Polyethylene (XLPE), Polyvinyl Chloride (PVC) and Ethylene Propylene Rubber (EPR).

Since the late 1950s, research into the development of detectors for the pd measurement has been carried out worldwide. Typical instruments include the Robinson (UK), Hipotronics and Biddle (USA), Haefely and Tettex (Switzerland) and Tur Mut (Germany) [7]. The book "Discharge Detection in High Voltage Equipment" [10] in 1964 by Dr. F. H. Kreuger of the NKF cable factory of Netherlands, established the fundamentals of partial discharge measurement techniques. Later, the CIGRE no.21 technical commission (high voltage cables) organised the partial discharge working group, to establish the partial discharge test standard for cables. Since the 1970s, plastic cables have been widely utilised in industrialised countries, especially

PE, XLPE and EPR insulated cables. Collaborative research in 1979 among five key cable factories in Germany and the University of Hanover proposed new ideas to distinguish testing long lengths of cable and short lengths of cable, which was accepted by International Electrical Commission (IEC) as the standard partial discharge test for cables in 1985.

Partial discharge testing is important for both oil-impregnated paper cables and extruded plastic cables. For oil-impregnated paper cables, partial discharges along the paper layer and the paper gap cause damage to the insulation and may eventually lead to breakdown. However, partial discharge testing is crucial to extruded plastic cables for a variety of reasons:

- Voids and particles may exist within the insulation due to the impurity of the material. Due to improper manufacture, a gap may exist at the interface between the insulation and the semiconducting screen layer, and the semiconducting layer may protrude towards the insulation. Partial discharges occur due to the existence of voids, particles, gaps or protrusions.
- The discharge endurance performance of extruded plastic insulation can be weak. For example, the H atom within the polyethylene molecule may cause an oxidation reaction and consequently degrade insulation performance.
- Since 1960s, long-term tests and practical experience have indicated that the ageing and breakdown of the extruded plastic cable insulation is due to treeing (electrical tree, water tree or electrochemical tree) [7]. Although the mechanisms and regularity differ for different trees, the origin and development of trees are related to partial discharge activity.

Cables and their accessories are generally tested and inspected at the factory prior to being transported to the customer. Manufacturing defects are typically detected during factory testing procedures. Yet, failure can occur during initial integrity testing of the installed cable system or within a relatively short time after installation. Such failures can be the result of transportation damage as well as installation problems. The least controlled part of the process is the field installation. Defects can also be introduced while the electrical apparatus is in use. For example, cavities can gradually form due to the different expansion or contraction coefficients for different materials such as the conductor and dielectric over the operating temperature range, or due to the decomposition of insulation due to ageing.

Cable accessories (terminations and joints) are usually installed in the field. Consequently defects leading to partial discharge are more likely to exist. Based on this consideration, partial discharge on-line monitoring should concentrate on cable accessories.

3.2 Characteristics of Partial Discharge Detection in Cables

Compared with other power apparatus, the capacitance of cables is very large. The capacitance per length unit of a circular single-core cable can be calculated using the following equation:

$$C = \frac{2\pi\varepsilon_0\varepsilon_r}{\ln\frac{D_i}{D_c}}(F/m) \qquad (3.1)$$

Where ε_0 is the dielectric constant in the vacuum, which is 8.85×10^{-12} (F/m); ε_r is the dielectric constant in the insulation material, which is 2.3 for PE and XLPE; D_i is the diameter of the insulation (not including the thickness of the outer semiconducting screen); D_c is the diameter of the conductor (including the thickness of the inner semiconducting screen);

Due to the large cable capacitance, partial discharge testing requires a high capacity power transformer. For example, for cables with a voltage rating of 275 kV, IEC recommends the power transformer with a voltage rating of 480 kV and capacity of 10,000 KVA [7]. To lower the requirement for power capacity, power compensation at the primary or secondary winding of the power transformer is usually required. Alternatively, a series resonant tuned HV source can be used for cable testing.

Cable terminations are required when a PD test for a cable is carried out. Obviously the cable termination itself should be discharge free. There are various kinds of cable terminations, such as oil-impregnated, SF_6-filled, and de-ionised water terminations. For de-ionised water terminations, the cable outer semiconducting layer is stripped off for a certain length at both cable ends, and both cable ends are immersed into the de-ionised water. The electric field distribution along these sections of cable insulation is determined by the resistance distribution of the de-ionised water, therefore, the electric field distribution at the cable ends is improved. Consequently the discharge endurance strength at the cable ends is improved. As water will ionise and generate heat under the high electric field, to control the conductivity of the water, the

water needs to be de-ionised, cooled and circulated. Water terminations have been used during the experimental work of this thesis.

3.3 PD Detection Methods for Cable Systems

As discussed earlier (section 2.7), PD detection can be realised using electrical, acoustic, optical and chemical methods. For PD detection in cables or cable accessories, acoustic emission and electrical methods are most widely applied, though chemical detection has also been attempted. Unlike GIS, electrical detection in the UHF range is not suitable for cables and cable accessories as the discharge UHF signals are attenuated significantly by the semiconducting screen. However, conventional PD electrical detection and non-conventional coupling methods operating in the high frequency or in the very high frequency range, can be applied effectively.

When a partial discharge occurs within cable insulation, a very small portion of the total energy is emitted as acoustic energy. Acoustic measurements of partial discharge rely on the detection of a pressure wave formed from a sudden deformation within the electrically stressed material. Compared to the conventional electrical method, the detection of acoustic emission is attractive on a number of counts: the test equipment is small; it is not necessary to disconnect the power supply; and it is free from electrical interference. The main disadvantage of an acoustic approach is the attenuation of the acoustic wave during propagation through the cable materials/interfaces. Attenuation causes problems with detection sensitivity and acoustic signal quantification in terms of an apparent discharge quantity.

3.3.1 Conventional electrical detection

This is the method proposed by the Electric Research Association (ERA). For short cables (less than 300 m in length), the test circuit is shown in Fig. 3.1 [51]. When a partial discharge occurs, there is an instant voltage change of ΔU_q across the cable. A pulse current is produced if ΔU_q is coupled to the detection impedance (input unit) through the coupling capacitor C_k. The partial discharge pulse can then be displayed on the PD detector oscilloscope.

It is usually necessary to fit stress relief cones, or to use semi-conducting putty or tape, in order to avoid discharges due to unnatural stresses at the cable ends. Discharge free cable terminations can also be applied.

The function of the input unit is to collect the high frequency pulse signals produced by partial discharge, and at the same time suppress the power frequency and low frequency harmonic signals. The input unit must be matched to the capacitance of the cable. The coupling capacitor C_k is used to couple the partial discharge pulse to the detection impedance, at the same time, it removes almost all of the power frequency voltage, thus enabling the detection impedance and the PD detector to work safely and sensitively. The coupling capacitor itself should be partial discharge free.

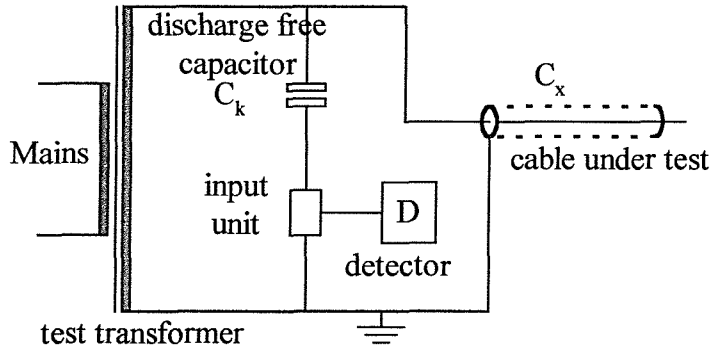

Figure 3.1 PD testing method for short lengths of cable

Longer cables should be tested using the circuit shown in Figure 3.2 [51]. In this method, the cable which is treated as a transmission line, is terminated at its far end by its characteristic impedance R in series with a high voltage discharge free capacitor. The capacitor serves both to reduce the power rating of the resistor and the consumption at power frequencies while maintaining the correct impedance within the passband of the discharge detector. The near end of the cable is coupled to the input unit via a discharge free capacitor.

In recent years, some multifunctional partial discharge measuring systems that utilise both the conventional detection principle and the computer digital technology, have been developed [52,53]. They can measure and evaluate partial discharges in high voltage insulation in compliance with the IEC 270 recommendation [1]. In addition, discharge statistical distribution histograms, such as n (repetition rate) – φ (phase), n – q (discharge magnitude), q – φ, can be plotted and analysed; Statistical operators, such as Skewness, Kurtosis, Cross-correlation factor, can also be calculated. Histograms

and statistical operators may be used for partial discharge pattern identification [54-60].

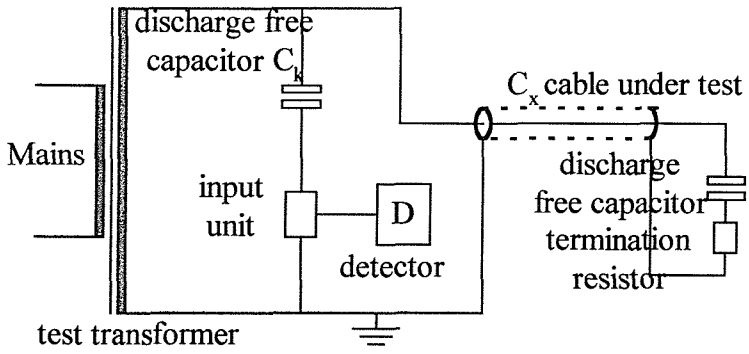

Figure 3.2 PD testing method for long lengths of cable

Conventional PD electrical detection is the preferred method of testing within manufacturing industry. For over 50 years it has been applied to different power apparatus. This method offers good detection sensitivity and can give an indication of the level of partial discharge. In general, permissible discharge magnitude is stipulated for a cable or cable accessory. For example, the IEC 840 standard (1988) stipulates that, for cables with a voltage rating from 30 to 150 kV, the permissible discharge magnitude is 10 pC, at a PD test voltage of one and a half times the rated voltage. The Japanese power regulation stipulates that, for cable accessories with a voltage rating of 66 kV, the permissible discharge magnitude is 50 pC, at a PD test voltage of one and a quarter times the rated voltage [7].

The main disadvantage of the ERA method is that it is not suitable for the on-line PD detection, because of its demands on the power supply and the need for a coupling capacitor.

3.3.2 Non-conventional electrical detection methods

These approaches are based on the high frequency characteristics of a discharge pulse. Partial discharges can be considered as electromagnetic pulses while travelling along the cable and the coaxial structure of the cable acts as a wave guide for the electromagnetic wave. The travelling speed of a discharge pulse in PE material is about 60% that of light [61]. The semi-conductive screens of the cable result in severe attenuation of the high frequency components of the discharge pulses. There are various non-conventional coupling methods.

3.3.2.1 Screen interruption technique

It is possible to measure a discharge pulse by connecting a measuring impedance over an interruption in the metal earth screen of the cable. This impedance can be a coaxial measuring cable, as shown in Figure 3.3. Thus the impedance of the coaxial measuring cable is connected in parallel with the resistance of the insulation screen. A discharge pulse will give a small voltage drop over the impedance. The coaxial measuring cable can then be connected to an oscilloscope for measurement [61,62,63]. An interruption can be made anywhere in the metallic sheath of a cable. When discharges from specific accessories have to be measured, the interruption should be made close to the accessory. An interruption is incorporated deliberately with some joint designs.

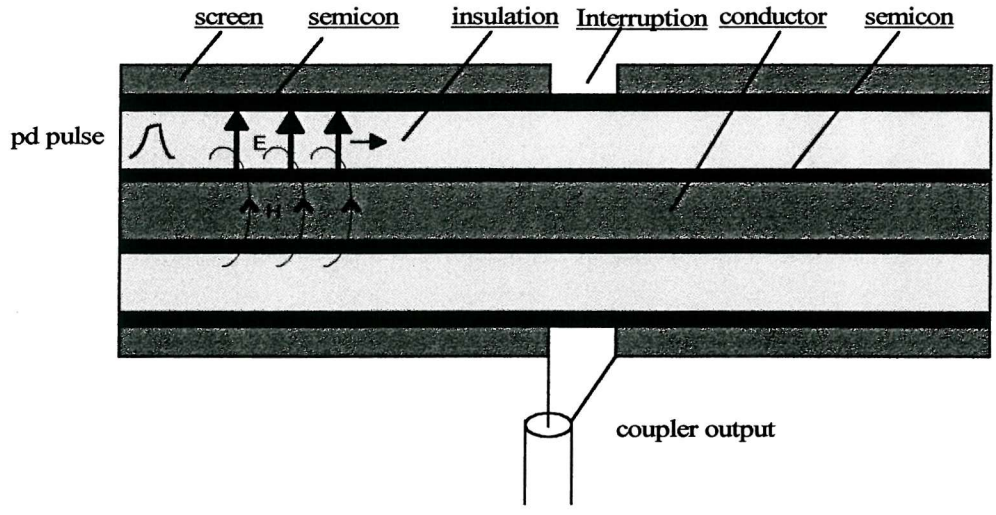

Figure 3.3 Interruption in the metallic earth screen of a cable section

In order to obtain the best response, the measuring cable should be connected to the sheath near the edge of the interruption. At the same time, the sheath on both sides of the interruption should be short-circuited for power frequency currents. If the short-circuit current lead is connected to the sheath on both sides, 100 mm from the interruption, this short-circuit will not disturb the partial discharge measurement [61].

The main disadvantage of this method is that a cut on the metal earth screen is necessary for discharge measurements. The sheath interruption limits the short circuit current handling ability. For on-line measurements, one has either to short the measurement impedance by an inductor that can handle the short circuit current or over voltage protection needs to be placed in parallel with the impedance. Additionally, not

only discharge signals travelling within the cable, but also noise causes a voltage drop in the measurement impedance, thus reducing overall sensitivity.

3.3.2.2 Inductive coupler detection of magnetic fields due to discharge activity

In the insulation of a power cable, a PD generates high frequency electromagnetic pulses that travel along the sheath and conductor of the cable in opposite directions. In the vicinity of the PD source, the discharge pulses are carried by a small portion of the sheath. However, these pulses will distribute uniformly along the circumference of the sheath at some distance away from the source, depending on the wavelength of the discharge pulses. PD pulses in the VHF range can travel few hundred meters before they are distributed around the entire circumference of the cable sheath. However, this distance is reduced to only few metres in the UHF range [64]. The unbalanced current distribution in the sheath will result in a magnetic field outside the cable, as shown in Figure 3.4. The magnetic field can be detected by an inductive coupler wrapped around the cable.

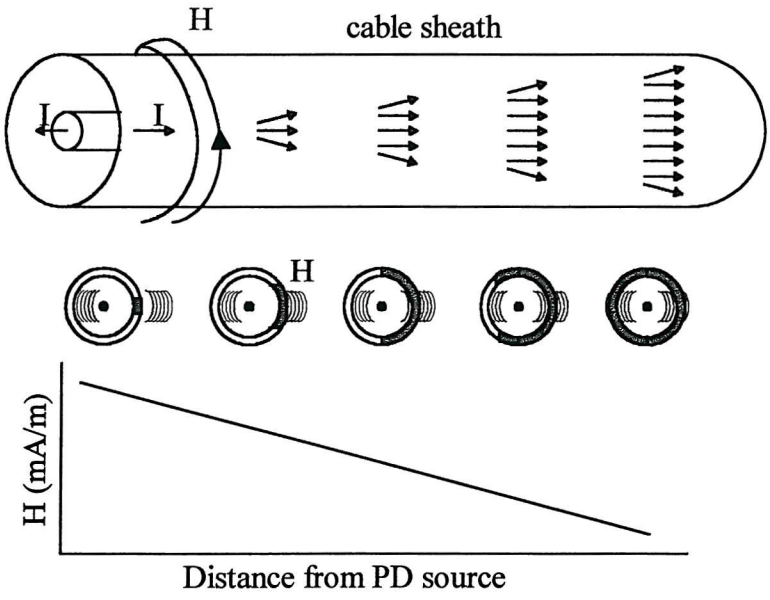

Figure 3.4 Typical magnetic field distribution due to a PD in solid shielded cable

For cables that have a helical shaped metal screen of individual wires, the discharge pulses are forced to follow the helical wire or screen resulting in a relatively high magnetic field outside the cable. This will increase the detection sensitivity in the VHF range. Consequently the magnetic field can be detected using a single-turn open loop inductive coupler without a magnetic core [61,62]. Figure 3.5 shows such an inductive

sensor. It consists of a copper band with one end attached to the ground of a coaxial measuring cable (U) and the other end attached to its centre conductor. The existence of the cable plastic jacket does not interfere with the magnetic field, so the coil can be applied around the cable plastic jacket.

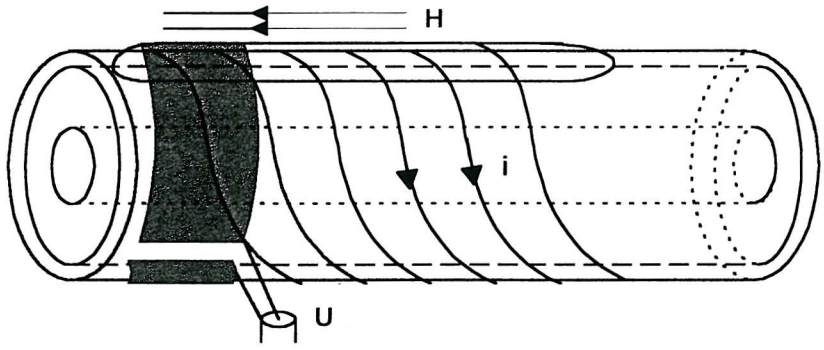

Figure 3.5 Coil around the plastic sheath of a cable with helically wound wires as the earth screen

The inductive coil is very easy to use, and no modification of the cable is necessary. With a coil the measurement can be carried out anywhere along the cable simply by moving the coil, consequently the discharge site may be accurately located. The coil output signal amplitude is proportional to the rate of change of the magnetic flux through the sensor loop. Thus a pulse which has had its highest frequencies attenuated is hard to detect. This can be helpful in reducing noise containing lower frequencies. On the other hand, it also strongly limits the examinable length of the cable sample.

Pultrum and Van Riet [61] have made on site measurements and found that with this coil technique the noise level is generally equivalent to 10 pC. This is low compared with that obtained using traditional electrical detection (100s to 1000s pC), and also to the noise level of 40 pC obtained using screen interruption technique (section 3.3.2.1). However, a great limitation for the coil technique is that it cannot be used on cables containing a metallic inner sheath, as this removes the axial magnetic field.

In order to have high sensitivity in detecting magnetic fields, it is necessary to have a sensor with a large open loop. The magnetic field produced by the currents will induce a voltage across this loop. Since the size of the sensor has to be small to be less susceptible to background noise and to be installed easily along the cable, coils have been constructed of a number of loops arranged in series [65]. Therefore the voltage produced by this sensor is the total sum of the voltages produced in each loop. Such

developed sensor can detect small discharges without using amplifiers. This avoids any impedance mismatching at the terminals of the sensors when using an amplifier. The sensor output signals can be directly measured with an oscilloscope [65].

In solid shielded cables, the magnetic fields generated by PD activity outside the cable are much lower. Consequently a High Frequency Current Probe (HFCP) can be applied around the cable [64,66]. The HFCP works on the principle of sampling the magnetic field around the cable (the primary) by secondary turns on a toroid transformer. The induced voltage on the output of the current probe is proportional to the permeability of the toroid, its cross sectional area, number of secondary turns, magnetic field outside the cable and the signal frequency. The detected signals are coupled to a spectrum analyser via a preamplifier [64].

3.3.2.3 Current transducer (CT) detection of discharge current

In order to detect the discharge current flowing through the conductor that connects the metallic ground screen of the cable to the main earth [67-71], a current transducer can be clamped around the conductor (Figure 3.6). The output signal from the sensor can then be filtered and amplified before further processing. This method is non-intrusive and convenient to use. It does not require any connection to live apparatus and can be applied in most field tests without taking equipment out of service.

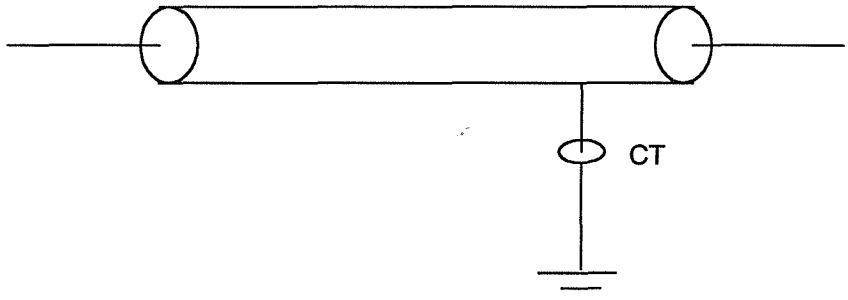

Figure 3.6 Using HFCT to detect partial discharges in cable

An alternative approach is to detect the current within the outer sheath of the cable joint. Heizmann, Aschwanden, Hahn, Laurent and Ritter [72] have investigated the on-site PD measurement of pre-moulded cross-bonding joints of 170 kV XLPE and EPR cables. In this case, the outer shield of the joint body is connected to the cable shield by means of copper braids. One of these braids was passed through a current transducer containing ferrite core. The output of the sensor is connected to either a network analyser or a fast digital oscilloscope. The use of a CT provides a separation between the shield of the HV cable and the measuring circuit, which is important for noise suppression. This sensor design requires no modification of the active part of the joint, and it easily can be installed without additional risk for the safety of the joint (Figure 3.7).

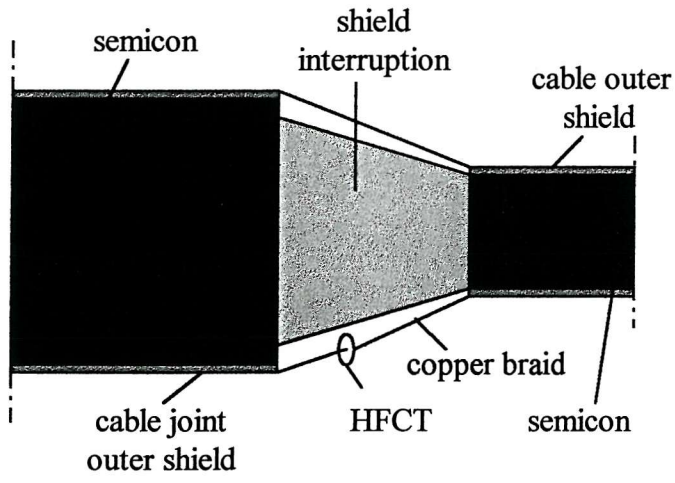

Figure 3.7 HFCT to detect current in the outer shield

3.3.2.4. Directional coupler technique

The directional electromagnetic coupling technique [73] is well known in other applications (e.g. microwaves). For cable applications, the directional coupler couples energy into one of two output ports. This is done such that energy travelling in one direction in the cable causes a larger signal at one of the two output ports of the coupler. Energy that travels in the other direction will mainly couple to the other output port. Such a coupler is characterised by its coupling factor and its directivity. The coupling factor describes how much energy is coupled from the cable into the output ports. Directivity quantifies the ability to distinguish between forward and backward propagating signals. Directional couplers should not be considered as either

purely capacitive or inductive [74]. Rather, it can be understood in terms of distributed parameters. Strong coupling leads to a good coupling factor and a balance between both couplings is needed to achieve high directivity. To avoid any degradation of the HV performance of the cables, the directional coupler is installed between the outer semicon layer and the metallic cable sheath. A short strip of metal is placed on the outer semicon layer and attached to two output connectors.

To apply this methodology, sensors are placed to the left and to the right of a cable joint as shown in Figure 3.8. Signals propagating 'forward' (as indicated in Figure 3. 8) are coupled to ports A and C, signals propagating 'backward' are coupled to ports B and D. PD in the joint will be coupled to ports C and B. The sensors can be within the joint housing or can be mounted after joint installation on the cable close to the joint [75-78].

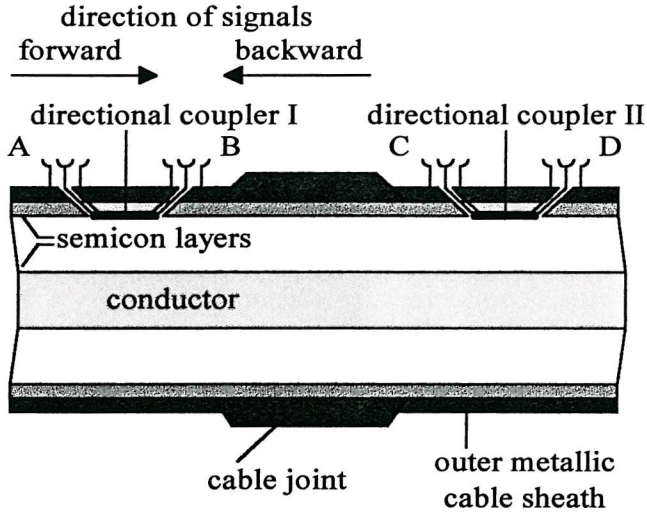

Figure 3.8 Principal arrangement of two DCS at a cable joint

3.3.3 Acoustic emission detection

The acoustic wave is a mechanical oscillation wave. Strong collisions occur between molecules in the partial discharge area and macroscopically form stress. Studies of the acoustic emission associated with tree growth and void formation in polyethylene have revealed two distinct modes, burst-type and impulse-type. It is believed that the burst-type of emission is associated with the initiation and growth of a tree, and the impulse-type is caused by PD in voids [79].

The percentage of transformation from the total discharge energy into acoustic energy is very difficult to calculate, and also differs with different materials. It is generally estimated to be very small and is quoted as less than 1% [7].

In solids, different types of internal and surface waves can occur. The most common internal waves are longitudinal waves and transverse waves. Longitudinal waves excite particle motion in the direction of propagation and transverse waves excite particle motion perpendicular to the direction of propagation. Surface waves travel along a material surface and are often referred to as Raleigh waves. The characteristics of AE signals within materials are complicated by wave type. The speed of waves as they propagate varies from material to material. By definition the most rapidly propagating wave in a solid is the longitudinal wave. For polyethylene the speed of propagation for the longitudinal wave is about 2000 m/s. The velocity of propagation of transverse waves is usually of the order of 50% that of the longitudinal waves, and the velocity of the surface wave is usually of the order of 90% that of the transverse waves [80,81].

The acoustic wave attenuates during propagation within the material. Attenuation is generally related to wave dispersion, wave reflection and heat transfer. In solid materials, the main reason for attenuation is molecule bounce, which transfers the acoustic energy into heat. The level of attenuation is frequency dependent. The higher the frequency of the wave, the more it is attenuated. The attenuation of ultrasound in air at constant temperature and humidity increases with frequency f, by a power greater than f^1 but less than f^2. In fluids, attenuation is usually proportional to f^2, while for solids attenuation is roughly proportional to f [7,80].

Significant interface attenuation of an acoustic wave is caused by the mismatch of the acoustic characteristic impedance when the acoustic wave propagates from one medium into another medium. The acoustic characteristic impedance of a material depends on the product of the density ρ (in kg/m^3) of the material and velocity v (in m/s) of sound in that material, and is expressed as ρv in kg/m^2s. The loss of ultrasound from one medium to another can be represented by the reflection coefficient:

$$R = \frac{\rho_1 \upsilon_1 - \rho_2 \upsilon_2}{\rho_1 \upsilon_1 + \rho_2 \upsilon_2} \tag{3.2}$$

Where $\rho_1 v_1$ and $\rho_2 v_2$ are the acoustic characteristic impedance of the two media respectively. Obviously, the more the two media are acoustically mismatched, the

greater the reflection of ultrasonic waves at the media interface. The loss of the acoustic wave propagating from air to a solid material is much more than that from the air to liquid or from liquid to solid materials. Based on the above consideration, the use of some type of liquid couplant, such as grease or silicone oil, between the sensor and the surface of the material containing the acoustic wave, is essential.

Acoustic waves from electrical discharges are usually monitored by transducers that measure sound pressure levels. These transducers fall into two general classes – resonant e.g. piezoelectric materials and non-resonant e.g. electromagnetic, strain or capacitance gauges. Non-resonant transducers can be used to detect stress-waves having frequencies up to 20 MHz. Piezo-electric devices are usually used to detect waves with frequencies centred on a particular resonant frequency [82]. Most applications of acoustic emission have used piezo-electric detectors principally because of their high sensitivity at the frequency of interest combined with a low sensitivity to mechanical noise and robustness.

The acoustic wave produced by partial discharge has a wide frequency range from 10 Hz to 10 MHz [7]. The choice of acoustic sensor frequency for PD diagnostic testing must be based on the acoustic emission signatures of different PD and the sound attenuation factors in different media and interfaces. In general, acoustic waves produced from partial discharges have a rich component in the lower frequency part of the acoustic emission spectrum. It has been recommended that 80 to 300 KHz is a useful frequency measuring range for solid materials where PD occur within internal voids [80].

Basically, acoustic detection and location of PD is appealing because it is simple and sensitive, often easy to apply and usually unaffected by electrical interference. The travel time of the acoustic wave from the PD source to the acoustic sensor can be determined by simultaneously recording the PD electrical and acoustic signals. With multiple sensors at different locations, and travel time converted to distance, triangulation procedures will yield the PD location. In practice, there are a considerable number of problems encountered. Acoustic waves will reach the sensors via devious routes via different media with different acoustic wave velocities. Attenuation and reflection of ultrasound also cause problems to the detection sensitivity. A considerable amount of research into the use of acoustic emission for PD detection in cables and cable accessories has been under taken [83-89].

3.3.4 Dielectric fluid analysis

The technique of Dissolved Gas Analysis (DGA) has been gaining acceptance for the condition assessment of dielectric fluid-filled cables and accessories. DGA is performed to determine the by-product gases of partial discharge induced deterioration. The technique requires removal of a small amount of dielectric fluid from the cable or cable accessory. Consequently, the technique requires removal of the circuit from service for safety reasons and to allow access to fluid filled areas within the system components. For the method to provide maximum information, the circuit under evaluation should have been energised for an extended period of time. In this way, any source of partial discharge would have time to produce dissolved gases.

Results of dissolved gas analysis are obtained in the laboratory by analysing the field obtained samples using a gas chromatograph. Consequently there is some time delay between sampling of the fluids and receipt of results. Interpretation of dissolved gases is based on the type of gases present and their concentration. The primary indicator gases for partial discharge activity are hydrogen, acetylene and methane. Other gases of importance were considered to be ethane, ethylene, propane, propylene, isobutane, carbon monoxide, carbon dioxide, oxygen and nitrogen. Interpretation of the results depends on the types of gases present, the ratios of the various gases, the operating conditions, and the types of materials present in the cable accessory. Based on the different levels of evolved gases, different actions, such as immediate repair, scheduled repair, monitor or retest, clean and no action needed at all, have been recommended [90].

The main disadvantage of this method is that it provides only an integrated measure of prevalent PD activity and that it can only roughly indicate the severity of the PD activity, but provides little or no indication of its nature, intensity and location. The nature of this method limits itself to off-line applications. Consequently, this method has not been applied widely to the PD detection in cables and cable accessories.

3.4 PD Location in Cable Systems

The location of discharges within cable systems is important for two reasons. Firstly, economic losses can be minimised by replacing the short length of faulty cable section

only, and keeping the rest of the cable. To find a defect, some manufacturers simply cut the rejected cable in half and retest each section until the defect was isolated. This is a time-consuming and expensive process, as the cable ends need to be terminated for each test. Often sections of good cables are scrapped unnecessarily using this technique. Secondly, it is of interest for the development of cable. If a discharge is located, the cause can often be determined and the fault may either be repaired or prevented in subsequent production.

The most common technique for PD location is Time Domain Reflectometry (TDR) [91-93]. Figure 3.9 illustrates the principle of the method. The test cable has an open remote end B and is connected to an excitation voltage source at point A. The excitation voltage is gradually increased until PD pulses are generated (this voltage is referred to as the PD inception voltage). One such signal, in the form of a short duration pulse, travels towards A while, simultaneously, a similar signal travels to B where it gets reflected and starts travelling back towards A. A signal detection system, located at A, records the direct and reflected signals which are separated by a distance 2x, proportional to twice the travel time from C to B. These signals experience reflections at A, then at B and return back to A to be recorded again by the instrument. The PD instrument is coupled to end A by means of a shielded HV capacitor. The instrument usually contains a high pass filter and amplifier. The location x of the defect site is calculated as a ratio to the total cable length L by the expression:

$$\frac{x}{L} = \frac{t_x}{t_L} \tag{3.3}$$

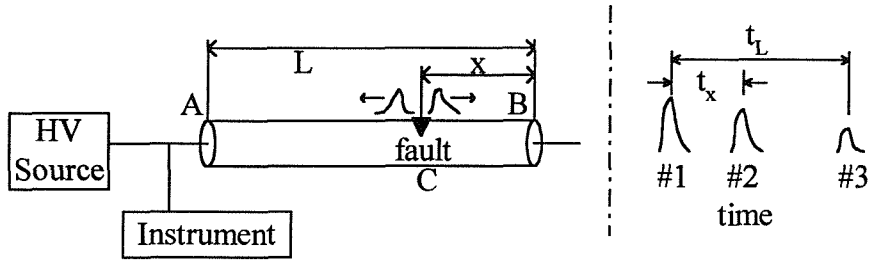

Figure 3.9 Schematic representation of the TDR principle

TDR is a common technique for locating partial discharges in cable. However, there are some problems that exist with this method:

- When discharges are close to one terminal causing the incident pulse to overlap the reflected one, the existing method based on TDR may fail to determine the delay time between pulses or to interpret the recorded signal. Lack of sensitivity in this case may result in an incorrect interpretation as these discharges may be mistaken for corona from the terminals or signals from other sources injected or induced into the terminals. In this case, it is advisable to exchange the cable measuring end and the far end. If it still doesn't work, a small section of cable might be removed from the overlapping end and the cable retested.
- For PD location with the TDR method, the measuring system must have high detection sensitivity, as the permissible discharge magnitude for cables is usually low and the discharge pulse attenuates significantly during propagation along the cable. It is often very difficult to register the reflected pulses. The distortion of the pulse which worsens with time, causes a shift of the pulse maximum. External disturbances also occur during the measurement. All of these lead to difficulty and reduction in the location accuracy [94]. To increase the signal / noise ratio (SNR) and the sensitivity of this method, different signal processing techniques have been investigated, such as correlation [95] and linear prediction [96].
- In TDR based techniques, it is necessary to disconnect the specimen from the system and all high voltage equipment in the measuring circuit has to be discharge free to avoid any erroneous readings.

Any PD location method which can be carried out on cables in service is of great interest. This may be realised by applying two or more acoustic emission sensors, inductive or capacitive electric sensors, and studying the time of flight for different sensors, considering the travelling speed of discharge pulse (electric or acoustic).

3.5 Disturbance

3.5.1. Sources of disturbance

Generally electrical disturbance falls into two categories [97]:

- Disturbances that occur even if the test circuit is not energised. They may be caused for example by switching operations in other circuits, commutating machines, high-voltage tests in the vicinity, radio transmissions, inherent noise of

the measuring instrument and so on. They may also occur when the power supply is connected but at zero voltage.

- Disturbances that only occur when the circuit is energised but do not occur in the test object. They may include for example partial discharges in the testing transformer, on the high-voltage conductors, disturbances caused by imperfectly earthed objects in the vicinity and disturbances caused by imperfect connections in the area of the high voltage. Disturbances may also be caused by higher harmonics of the test voltage within the bandwidth of the measuring instrument.

Acoustic noises are those not from the PD source, such as test machine noise (in laboratory testing), plant operating noise (in field testing), flow noise from pumps and valves, all manner of frictional processes and mechanical impact [98].

3.5.2 Detecting, distinguishing and rejecting disturbance

Voltage-independent sources of disturbance can be detected by a reading on the measuring instrument when the test circuit is not energised. The voltage-dependent sources of disturbance can be detected in the following manner: the test object is either removed or replaced by an equivalent capacitor having no significant partial discharges. Several methods may be helpful in distinguishing between PD and noise:

- The use of an oscilloscope as an indicating instrument helps the observer to distinguish between discharges in the test object and external disturbances. It sometimes makes it possible to determine the type of discharges.
- Interpretation of phase-resolved PD patterns. Based on physical knowledge and experience on PD behaviour, phase-resolved PD patterns may be interpreted to distinguish between disturbance and PD by either human experts or computer-based expert systems [75,99,100,101]. In an expert system, the human knowledge is implemented into a computer program either by training the program or by establishing decision rules.
- As stated in section 3.4, time-domain reflectometry can determine whether there is PD source within the cable and if so the location. Non-conventional electrical detection methods can also give independent confirmation of partial discharges in the test object.

Generally, reduction of disturbance can be achieved by proper one-point grounding of the HV test area, suitably grounding all conducting structures in the vicinity of the test and by filtering the power supplies for the test and measuring circuits. The best reduction is achieved by testing in a shielded room where all electrical connections into the room are made through effective filters.

Under industrial conditions, the sensitivity is limited by the presence of noise. Various methods exist, which may be used individually or in combination in order to separate the true partial discharge signals from noises [97,102,103,104]. Some of these methods are described below.

- Disturbance rejection in time domain. This is the so-called noise gating. The acquisition of a signal is inhibited for a short period of time when a noise is detected by a separate detection channel, e.g. an antenna. The effectiveness of the method depends on the ability to establish a reliable gating signal and the total length of disturbed time periods.
- Disturbance rejection in frequency domain. For example, to reduce the broadcast radio interference, band-stop filters can be applied and tuned to the frequencies where the interference occurs. Alternatively, narrow-band instruments can be used which are tuned to a frequency at which the interference level is negligible.
- Pulse averaging. Many disturbances in an industrial environment are random whereas true discharges recur at approximately the same time in each cycle of applied voltage. It is therefore possible to reduce the level of randomly occurring disturbances by using signal-averaging techniques.

Chapter 4

Acoustic Emission Detection of Partial Discharges

4.1 Introduction

The investigation of partial discharge detection in cable insulation using acoustic emission measurements is described in this chapter. Acoustic emission detection has been applied to detect partial discharges from a planar experimental model. The obtained AE signals were processed in the time and frequency domain, as well as using both two-dimensional and three-dimensional statistical patterns. Resultant statistical operators have been calculated. The factors influencing AE signal measurement and attenuation through different materials and interfaces have been investigated. The relationship between the discharge acoustic emission and electric signals has been studied. AE measurement of partial discharge behaviour during electrical tree growth in XLPE cable insulation has been studied. Finally AE measurement has been applied to detect partial discharges from an epoxy composite sample.

4.2 Acoustic Emission Measurement of Partial Discharges Generated using a Planar Model

A planar model has been developed (Figure 4.1) to investigate the characteristics of AE signals as a result of a partial discharge produced from a void within the polymeric insulation.

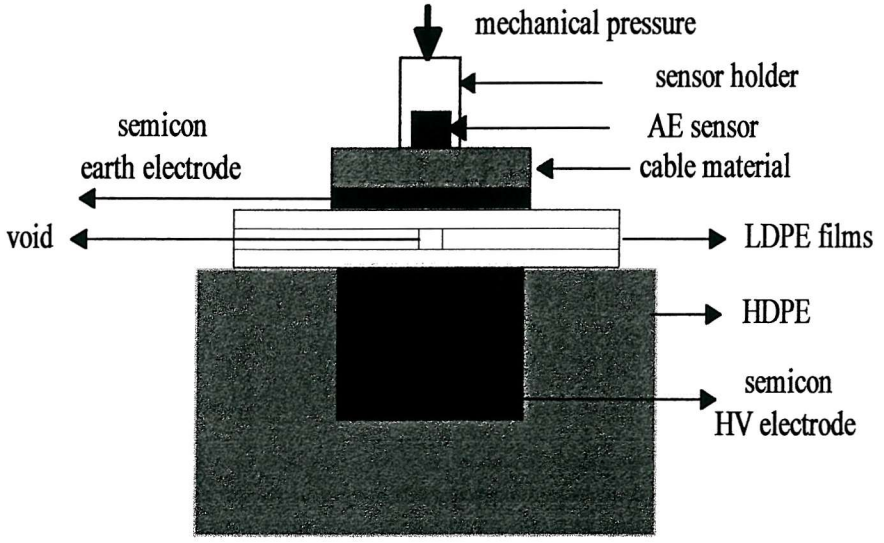

Figure 4.1 A planar experimental model

The model consists of a cylinder of high-density polyethylene (HDPE) and a three-layer sandwich of low-density polyethylene (LDPE) films. In the centre of the HDPE cylinder, there is semiconducting PE with thickness of 50 mm used as the high voltage (HV) electrode. Above the LDPE films, there is semiconducting PE with thickness of 2 mm used as the low voltage electrode. Semiconducting mastics were put around both electrodes to reduce the stress concentration at the edges and ensure that microscopic discharges do not occur. Thus the only discharge site is the void in the middle layer. For the experiments a gold HV electrode was coated onto the bottom film, and a gold earth electrode onto the top film. The middle layer was used to simulate a discharge void by creating a small hole using a needle. To study the AE signal attenuation, different cable materials of varying thickness, such as polyethylene (PE) and Ethylene Propylene Rubber (EPR), were applied between the semicon earth electrode and the AE sensor.

During the experiments consistent pressure between the AE sensor and the test cell was obtained using a torque wrench to tighten the clamping mechanism. This ensured that the possible effect on the acoustic measurement due to variation in applied external mechanical pressure was minimised. To prevent the acoustic emission signal attenuation due to the existent interface between the AE sensor and the cable material, silicon grease was applied as the acoustic couplant.

This planar experimental model is modular in construction allowing void size, void position, void number, void shape, void depth, material type, acoustic interface, working electric stress and mechanical pressure to be easily altered. Table 4.1 indicates the ways in which the model can be reconfigured.

Table 4.1 Planar model variables

Variables	**How Achieved**
Void size	Vary diameter of the hole in the middle of the film
Void position	Make void in upper, middle or lower LDPE film
Void number	Make one or more voids
Void shape	Vary the thickness of the middle film and the diameter of the hole, to form shapes as flat, cylindrical and hole
Void depth	Use different thickness of insulation cylinder on top of semicon earth electrode
Material type	Use PE, EPR or mixed PE and EPR
Acoustic interface	With or without couplant between the AE sensor and the cable material
Working stress	Vary applied voltage
Mechanical pressure	Reset the torque wrench

4.2.1. Measuring system

Figure 4.2 shows the measuring system to detect AE signals due to partial discharges from the experimental planar model. In order to study the relationship between the discharge acoustic and electric signals, conventional electrical detection according to IEC-270 was applied.

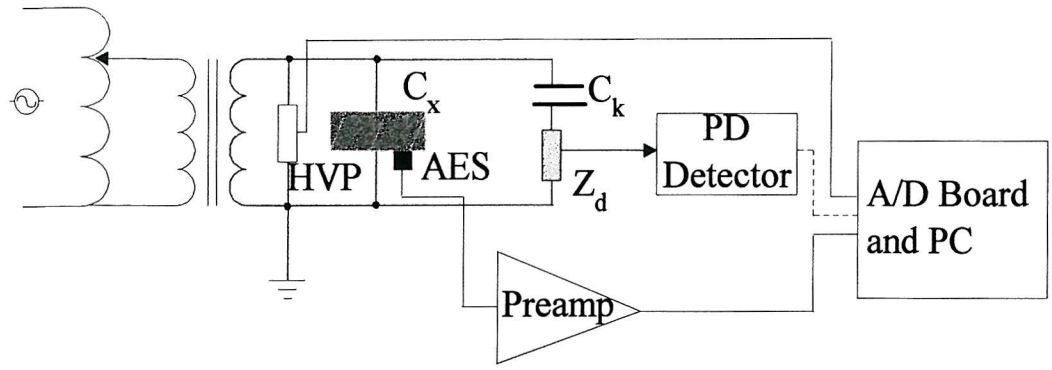

C_x – Planar model; C_k – Coupling capacitor; Z_d – Input unit; AES – Acoustic emission sensor; HVP – High voltage probe

Figure 4.2 Measuring system to detect PD from the planar model

The AE sensor used is a R15D sensor manufactured by Physical Acoustics Limited. The sensor is of the piezoelectric type and has a ceramic piezoelectric element. The resonant frequency of the sensor is 150 KHz with a peak sensitivity of –64 dB (Ref. 1 v/μbar). The sensor is compact with a diameter of 18 mm and a height of 17 mm. It is important to note that the R15D sensor has a differential connection. The sensor contains two crystal elements of opposite polarity. The outputs of these elements are fed to the two inputs of a differential preamplifier. AE signals of opposite polarity on the two leads are amplified, whereas electromagnetic interference produces signals of the same polarity that are common-mode rejected by the preamplifier. This is useful in an electromagnetically noisy environment.

The AE signal produced by the piezoelectric element in the sensor needs to be amplified before transmission to the measurement circuitry. The preamplifier should be placed nearby the AE sensor and provide optimum sensor coupling, suitable gain and excellent cable drive capability. The used preamplifier is a 1220A type manufactured by Physical Acoustics Limited. It has 40/60 dB switchable gain and 20 – 1200 KHz bandwidth (-3 dB). The input can be either single-ended or differential. The P-APSU power supply unit is used to provide the 28 V dc for the preamplifier. The P-APSU unit can either be supplied by mains or by battery.

The coupling capacitor has capacitance of 1.0 nF and is the model PSF-50/1/700 manufactured by Hipotronics Company. The partial discharge detector is of model 5 type 700 manufactured by Robinson Instruments. The No. 2 input unit

(Robinson Instruments) has a capacitance tuning range between 25 and 400 pF. The Tektronix® high voltage probe is a voltage divider with ratio of 1/1000.

The Analogue to Digital Converter T3012 board is manufactured by IMTEC GmbH (Germany). It is a very fast dual-channel data acquisition board with 4 MB internal memory. Each channel module has a 12-bit low noise A/D converter with a maximum sampling rate of 30 MHz. The trigger source for the board can be either one of the two channels or the external trigger input. If the high voltage probe output is input into one channel and the board is triggered by this channel, the discharge acoustic or electric signals can be presented with respect to the ac phase information. Alternatively, if 50 Hz ac reference signal is used as the external trigger for the board, both discharge acoustic and electric signals can be simultaneously presented and compared in a phase-related way. The board is installed in the PCI-slot of the Gateway® Pentium II 233 MHz computer.

IMTEC GmbH provided software with the T3012 board. It can display the acquired data from both channels in time and frequency domain, as well as saving the data into data formats available to other commercial computer software. In this study, all obtained data has been further processed and analysed using MatLab®.

4.2.2. Main acoustic emission parameters

In PD conventional electrical detection according to IEC-270, the discharge apparent quantity and the discharge repetition rate are two important parameters. Similarly, for acoustic emission measurement, signal *amplitude* and *hit* are two primary parameters to describe the acoustic emission signals [98,105]. The maximal peak value of an AE oscillatory waveform is defined as the amplitude and one waveform corresponds to one hit. The signal amplitude can be related to the intensity of the source producing an acoustic emission. It governs the detectability of the acoustic emission event, and it is the appropriate variable to use for attenuation measurement. In addition, signal amplitude can be used for statistical presentation and analysis, which might be helpful to AE signal characterisation. A computer program has been developed to determine the AE signal amplitude. The method is to set two thresholds: The first threshold is a value with which the amplified AE signal is compared, when the AE signal exceeds this threshold, the software timer begins, and when for a pre-defined continuous amount of time, all values of the AE signal are below the first threshold, the timer

ends, thus gives a definition of one acoustic pulse with a maximum amplitude. Here the pre-defined time is the second threshold. Suitable selection of it is very important, as if the time is set too small, the timer may expire in the middle of the signal and software system will treat the next part of the signal as a separate signal, producing invalid data; on the other hand, if the time is set too long, a separate signal may be included along with the first signal, producing invalid data again. The developed program has two default thresholds with good matching, but if the calibration result is not good enough, they should be reset. Figure 4.3 illustrates the amplitude of an AE signal.

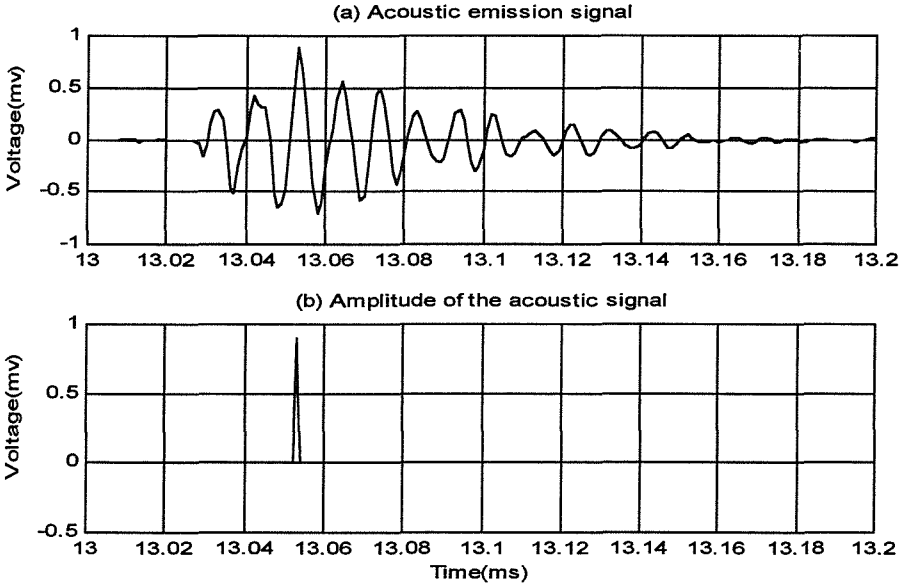

Figure 4.3 Amplitude of an acoustic emission signal

4.2.3. Presentation of discharge acoustic emission signals

4.2.3.1. Time and frequency domain presentation

Figure 4.4 shows the synchronously measured discharge acoustic emission (via AE sensor) and electric signals (via the PD detector) and spectrum for one 50 Hz power cycle. In this case, the middle LDPE film of the three-layer sandwich films in the planar model (Figure 4.1) has a void with diameter of 2 mm and thickness of 0.2 mm. The PD inception voltage is about 1.1 kV and the measurement was carried out at 30% above the PD inception voltage. The sampling rate of the A/D board is 1 MHz, thus at 50 Hz there are 20,000 data points in each cycle. The frequency spectrum was obtained by Fast-Fourier Transform (FFT) and the frequency of interest consequently lies in the first 500 KHz. The frequency component for the acoustic emission signal has a

dominant peak at 150 KHz, which is the resonant frequency of the AE sensor. The spectrum of the discharge electric signal, which is determined by the input unit and the amplifier of the discharge detector, is mainly below 200 KHz. Compared with the clean acoustic spectrum, there are some discrete disturbance frequencies. Figure 4.5 shows a pair of related acoustic and electric signal pulses.

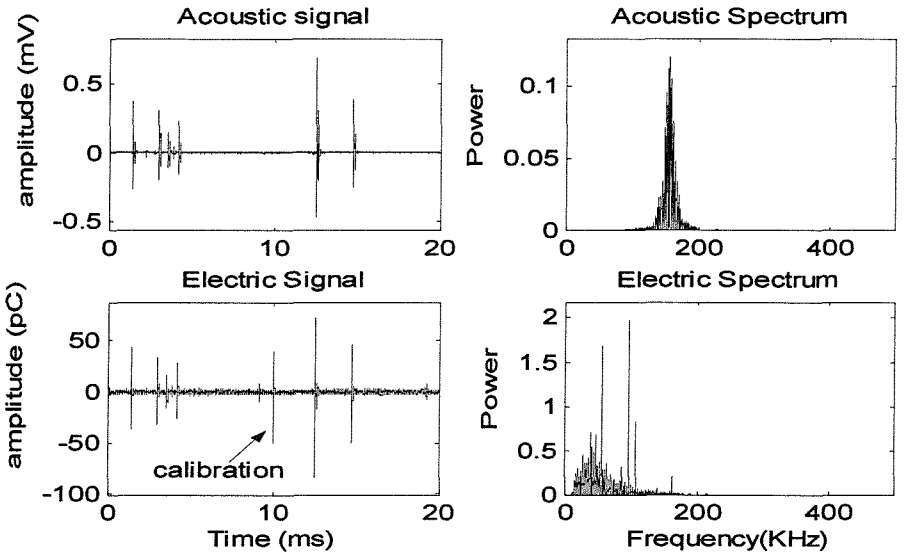

Figure 4.4 PD acoustic and electric signals and spectra

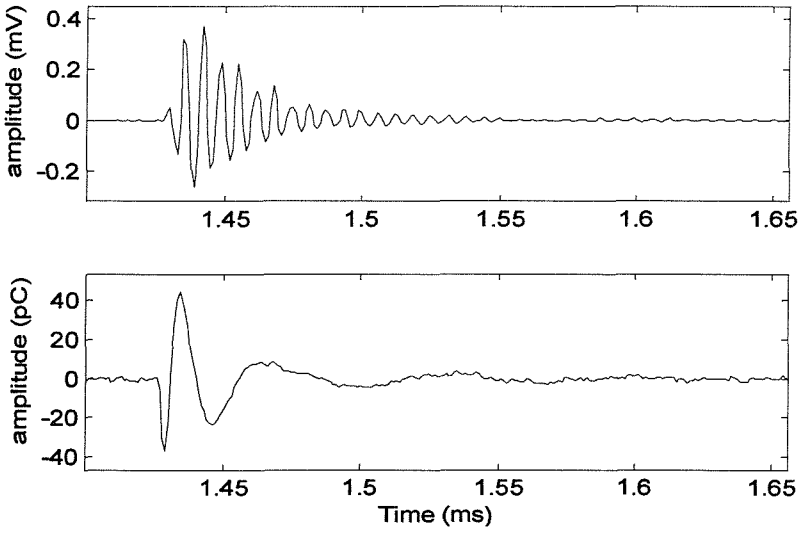

Figure 4.5 PD acoustic emission and electric waveforms

4.2.3.2. Two-dimensional statistical pattern

PD phenomena that occur in a dielectric medium are inherently complex stochastic processes, it is therefore necessary to take statistical characteristics into account when performing any analysis. By measuring pulse distribution as a function of the phase

angle, it is possible to obtain information about the phenomena that cause the pulse distributions. The following phase-position quantities have been defined: the pulse count distribution $H_n(\varphi)$, which represents the number of observed discharges in each phase window as a function of the phase angle; $H_{qmax}(\varphi)$, which represents the maximal discharge amplitude in each phase window; the mean pulse height distribution $H_{qn}(\varphi)$, which represents the average discharge amplitude in each phase window as a function of the phase angle. $H_{qn}(\varphi)$ is derived from the total discharge quantity in each phase window divided by the total number of discharges in the same phase window.

According to several authors, the time dependence of the pulse count phase distribution $H_n(\varphi)$ and the mean pulse height distribution $H_{qn}(\varphi)$ provide a good description of changes in discharge patterns [106-115]. The $H_n(\varphi)$ quantity contains information of the intensity of discharges as a function of their phase angle. The $H_{qn}(\varphi)$ quantity allows noise reduction due to the difference between the statistical characteristics of the discharge pulses and that of noise pulses as a function of phase angle.

The resolution on the phase angle axis is determined by the number of phase windows. This number should be as large as possible to give higher precision, but this is at the expense of decreased data processing speed and increased memory requirements. It has been found that 200 phase windows can give reasonable and sufficient resolution which has also been indicated by Tanaka [109]. The number of magnitude windows was selected in the same way and 50 was found to be a reasonable quantity to give sufficient resolution.

To generate enough data for statistical analysis, each experiment was conducted over 500 continuous power cycles. Figure 4.6 shows the two-dimensional statistical pattern $H_{qmax}(\varphi)$, $H_n(\varphi)$ and $H_{qn}(\varphi)$, for the discharge acoustic emission signals. In this experiment, the void was in the middle film, had a diameter of 2 mm and a thickness of 0.2mm. The applied electric stress was 5 kV/mm.

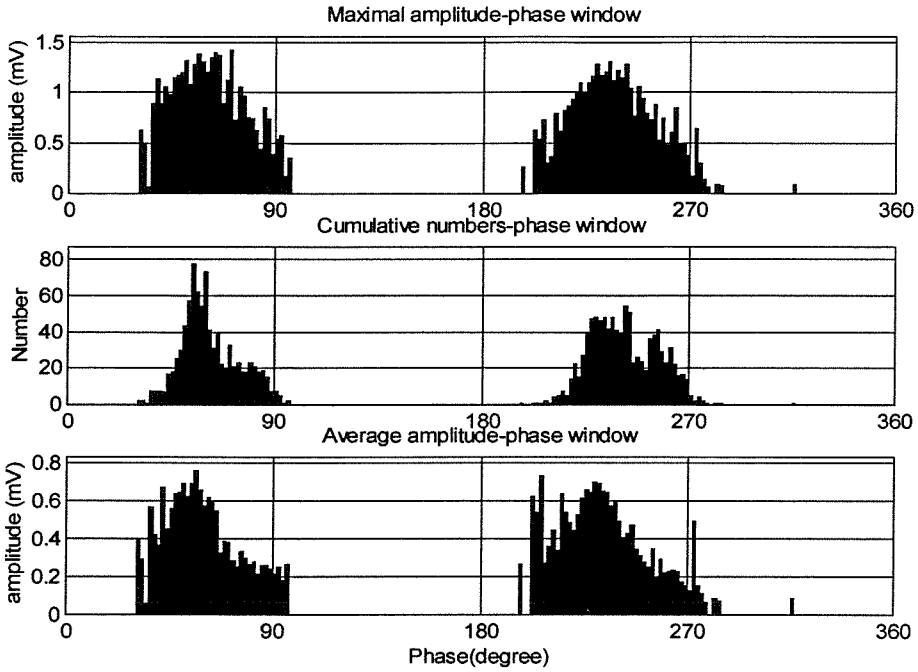

Figure 4.6 Discharge acoustic emission two-dimensional pattern

4.2.3.3. Three-dimensional φ-q-n pattern

In addition to the two-dimensional phase-related patterns, three-dimensional Phase-Charge-Number (φ-q-n) patterns have been used to analyse discharge signals [113-120]. This is the characterisation of the partial discharges by their angular position on the AC cycle (φ), their relative magnitude (q) and their frequency per unit time (n). These three parameters may be used to construct a three-dimensional surface from which important features may be extracted. Rather than the accumulative signal numbers and average signal amplitudes in each phase window, for AE measurement, φ-q-n represents the number of AE signals n_{ij} having both phase position φ_i and amplitude q_j. φ-q-n is considered to be the most complete form of graphical PD presentation. Figure 4.7 shows the relevant three-dimensional φ-q-n patterns for the discharge acoustic emission signals relating to Figure 4.6.

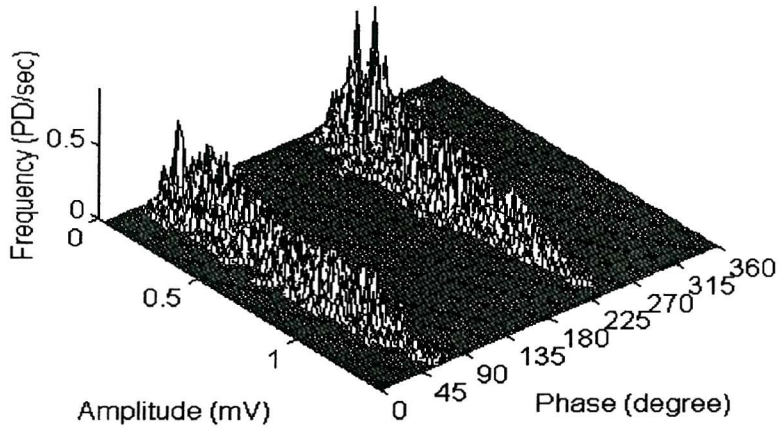

Figure 4.7 Discharge acoustic emission φ-q-n pattern

4.2.3.4. Statistical operators

Practical discharges occur during a voltage cycle in two sequences, for each half of the voltage cycle separate discharge patterns can be measured. Therefore the $H_n(\varphi)$ and $H_{qn}(\varphi)$ quantities are characterised by two distributions: for the positive half of the voltage cycle $H_{qn}^+(\varphi)$, $H_n^+(\varphi)$ and for the negative half of the voltage cycle $H_{qn}^-(\varphi)$, $H_n^-(\varphi)$. To study the difference between the distributions in both halves of the voltage cycle the following statistical operators have been used:

- Discharge asymmetry

The discharge asymmetry Q is the quotient of the mean discharge level of the $H_{qn}(\varphi)$ distribution in the positive and in the negative half of voltage cycle:

$$Q = \frac{Q^- / N^-}{Q^+ / N^+} \tag{4.1}$$

Where Q^+ and Q^- are the sum of signal amplitudes of the $H_{qn}(\varphi)$ distribution in the positive and negative half of the voltage cycle; N^+ and N^- are the number of discharges of the $H_{qn}(\varphi)$ distribution in the positive and negative half of the voltage cycle.

- Phase asymmetry

The phase asymmetry Φ is used to study the difference in inception voltage of the $H_{qn}(\varphi)$ distribution in the positive and negative half of the voltage cycle:

$$\Phi = \frac{\varphi_{in}^-}{\varphi_{in}^+} \tag{4.2}$$

Where φ_{in}^{+} and φ_{in}^{-} are the inception phases of the $H_{qn}(\varphi)$ distribution in the positive and the negative half of the voltage cycle.

- The cross-correlation factor

The factor CC is used to evaluate the difference in shape of distribution $H_{qn}^{+}(\varphi)$ and $H_{qn}^{-}(\varphi)$. The following formula is used to calculate the cross-correlation factor:

$$CC = \frac{\sum xy - \sum x \sum y / n}{\sqrt{\left[\sum x^2 - \left(\sum x\right)^2 / n\right]\left[\sum y^2 - \left(\sum y\right)^2 / n\right]}} \tag{4.3}$$

Where x is the mean signal amplitude in a phase window in the positive half of the voltage cycle; y the mean signal amplitude in the corresponding phase window in the negative half of the voltage cycle; and n the number of phase windows per half cycle.

Thus, the differences between the distributions $H_{qn}^{+}(\varphi)$ and $H_{qn}^{-}(\varphi)$ are described by three independent parameters: phase asymmetry Φ, discharge asymmetry Q and cross-correlation factor CC. A cross correlation CC=1 means 100% shape symmetry and a value of 0 indicates total asymmetry. However, CC tells nothing about the height of the distribution. For that purpose the discharge asymmetry Q or phase asymmetry Φ are used. Both these variables are defined in such a way that they are equal to 1 in the case of fully symmetric distributions and smaller than one in the case of asymmetric ones. The asymmetry factors can be easily combined by multiplication. This is defined as the modified cross-correlation factor (MCC).

- The modified cross-correlation factor

MCC is used to evaluate the differences between discharge patterns in the positive and the negative voltage cycle. It is defined as the product of phase asymmetry Φ, discharge asymmetry Q and cross-correlation factor CC:

$$MCC = \Phi \cdot Q \cdot CC \tag{4.4}$$

It is known that in the case of a single defect, discharge parameters can be fairly well described by a normal distribution process. Therefore to get a better evaluation of $H_n(\varphi)$ and $H_{qn}(\varphi)$ quantities, statistical parameters for a normal distribution can be used:

- Skewness Sk. An indicator of the asymmetry of a distribution with respect to a normal distribution:

$$Sk = \frac{\sum_{i=1}^{n} (x_i - \mu)^3 f(x_i)}{\sigma^3 \sum_{i=1}^{n} f(x_i)} \tag{4.5}$$

- Kurtosis Ku. The indicator for the deviation from the normal distribution:

$$Ku = \frac{\sum (x_i - \mu)^4 \cdot f(x_i)}{\sigma^4 \sum f(x_i)} - 3 \tag{4.6}$$

Where x_i is random variable, $f(x_i)$ is its probability distribution function; μ is the mean value of the distribution; and σ is the standard deviation of the distribution:

$$\sigma^2 = \frac{\sum_{i=1}^{n} (x_i - \mu)^2 f(x_i)}{\sum_{i=1}^{n} f(x_i)} \tag{4.7}$$

$$\mu = \frac{\sum_{i=1}^{n} x_i f(x_i)}{\sum_{i=1}^{n} f(x_i)} \tag{4.8}$$

These statistical operators describe the shape of the distribution. They may therefore be used to characterise the distribution functions $H_n(\varphi)$ and $H_{qn}(\varphi)$ more precisely. Skewness (Sk) indicates the asymmetry of the distribution and Sk is zero for a symmetric distribution, positive when the distribution is asymmetric to the left, and negative when the distribution is asymmetric to the right. Kurtosis (Ku) indicates the sharpness of the distribution and Ku is zero for a normal distribution. For a sharper than normal distribution Ku is positive, and if the distribution is flatter than the normal distribution the Ku is negative. Figure 4.8 shows an example for the above relationship.

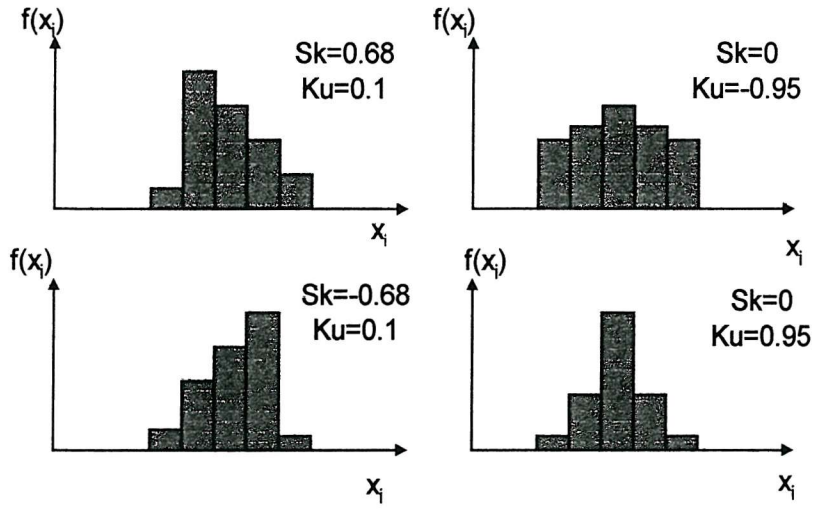

Figure 4.8 Distribution with different Sk and Ku

Investigation has revealed that no discrimination could be obtained by the use of Skewness of $H_n(\varphi)$ and Kurtosis of $H_{qn}(\varphi)$ [108]. Consequently they will not be utilised. Table 4.2 shows the statistical operators for the two-dimensional patterns of the discharge acoustic signals. Sk(+) is the Skewness for $H_{qn}^{+}(\varphi)$; Sk(-) is the Skewness for $H_{qn}^{-}(\varphi)$; Ku(+) is the Kurtosis for $H_n^{+}(\varphi)$; Ku(-) is the Kurtosis for $H_n^{-}(\varphi)$; CC, Q, Φ and MCC are as defined before. From the experimental data obtained from the 2 mm diameter void of thickness of 0.2 mm under a stess of 5 kV/mm, the statistical operators have been calculated (Table 4.2). The calculated results reflect the discharge acoustic statistical patterns (Figure 4.6).

Table 4.2 Statistical operators

	Sk(+)	Sk(-)	Ku(+)	Ku(-)	CC	Q	Φ	MCC
Acoustic	0.417	0.593	0.343	-0.064	0.804	1.048	0.556	0.468

4.2.4. Factors influencing the AE measurement

4.2.4.1. Effect of electric stress

Figure 4.9 shows the influence of applied electric stress on the maximal discharge amplitude (in pC), maximal acoustic signal amplitude (in mV), and the total number of acoustic signals measured over a ten power cycle period. In this experiment, the void exists in the middle film and has a diameter of 2 mm and thickness of 0.2mm. When

the applied electric stress is increased, both the signal amplitude and number of measured signals increase. The trend for the peak amplitude to increase with applied stress is similar for the discharge electric and acoustic signals. The applied electric stress appears to have greater influence on the number of discharges rather than on the peak amplitude.

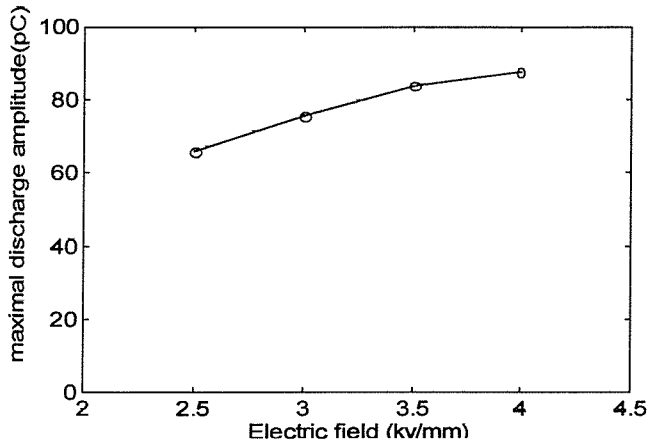

(a) discharge apparent quantity (pC)

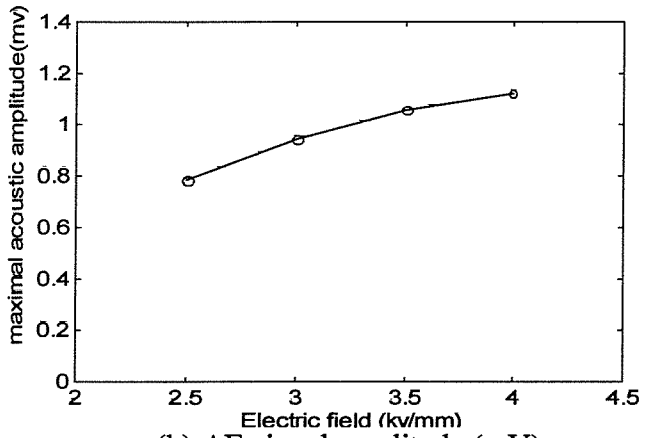

(b) AE signal amplitude (mV)

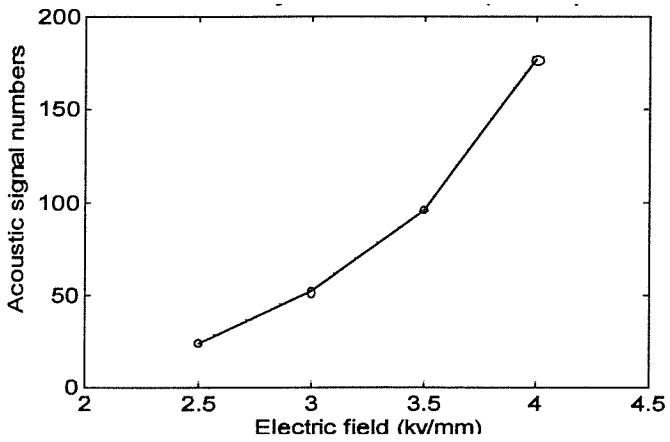

(c) number of AE signals occurring over 10 power cycles

Figure 4.9 Effect of applied electric stress on discharge signals

Figure 4.10 and Figure 4.11 show the three-dimensional φ-q-n patterns and two-dimensional statistical patterns for AE signals for two different applied electric stresses. In this case the internal film has a void 3mm in diameter and 0.2 mm in thickness. Discharges occur predominantly in the first and third quadrants of the power cycle, and are basically symmetric. When the electric stress is increased, both amplitudes and numbers of AE signals increase, and the patterns seem to occur earlier as they also occur around the zero-crossing phase positions of the power cycle.

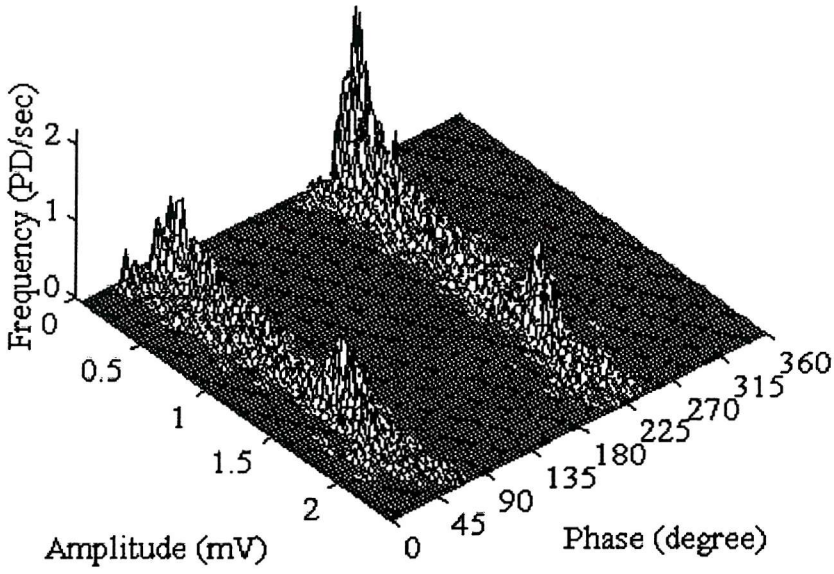

(a) Internal void –3 mm, electric stress – 4 kV/mm

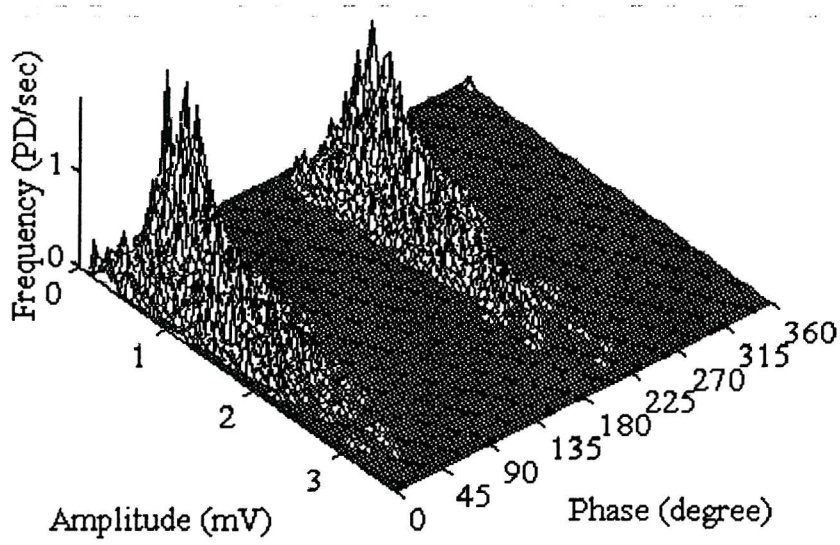

(b) Internal void –3 mm, electric stress – 5 kV/mm

Figure 4.10 Effect of applied electric stress on AE φ-q-n patterns

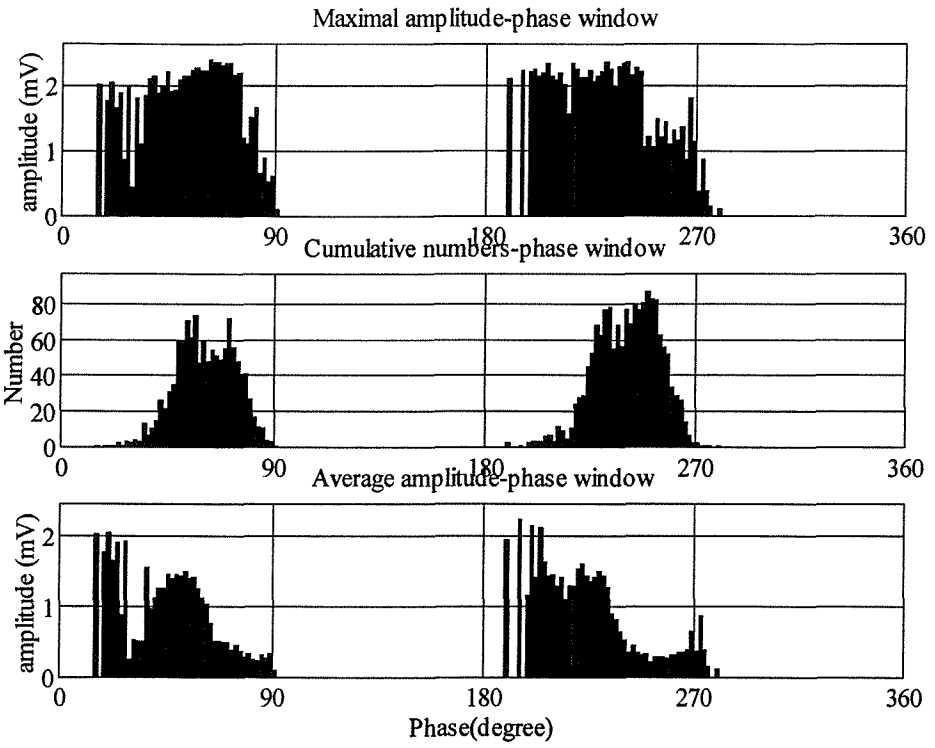

(a) Internal void –3 mm, electric stress – 4 kV/mm

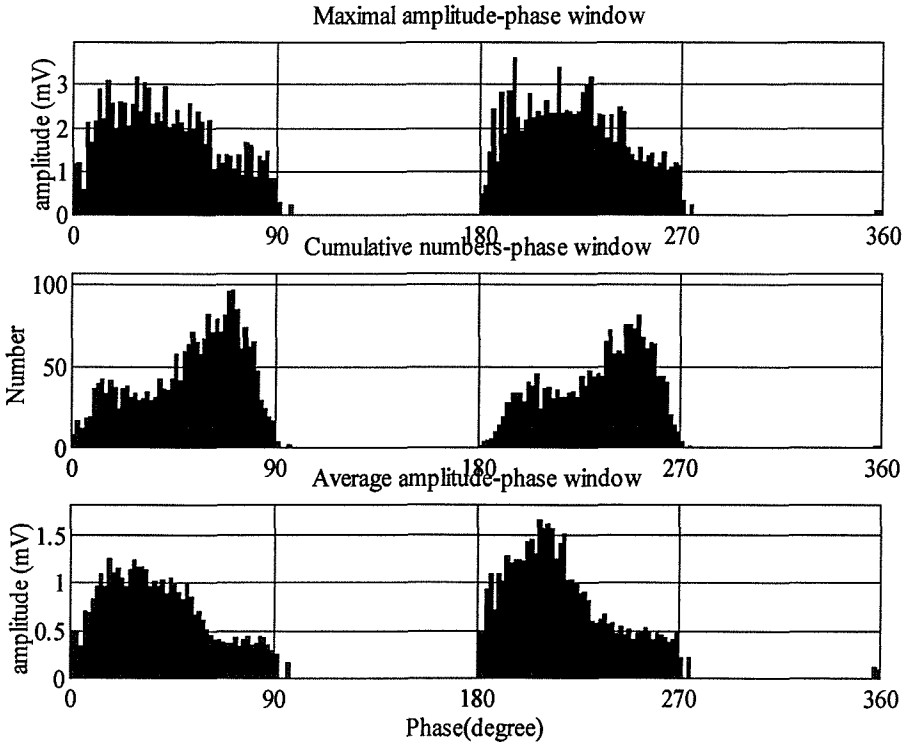

(b) Internal void –3 mm, electric stress –5 kV/mm

Figure 4.11 Effect of applied electric stress on AE two-dimensional patterns

The statistical operators for the above two cases have been calculated, as shown in Table 4.3. Six of the eight statistical operators changed significantly, except Sk(+) and CC. This indicates that increasing the applied electric stress may significantly influence the distribution of PD activity.

Table 4.3 Statistical operators for AE patterns at different applied electric stresses

	Sk(+)	Sk(-)	Ku(+)	Ku(-)	CC	Q	Φ	MCC
Void- 3 mm, 4 kV/mm	0.303	0.750	-0.262	-0.086	0.842	0.811	0.667	0.456
Void – 3 mm, 5 kV/mm	0.483	1.213	0.081	0.060	0.962	1.383	1	1.329

4.2.4.2. Effect of test time

The influence of test time on both the discharge apparent quantity (pC) and the acoustic signal amplitude (mV) has been investigated (Figure 4.12). For this experiment, an internal void with diameter of 2 mm and thickness of 0.2 mm was used. The applied electric stress was 5 $kVmm^{-1}$.

During the first 20 minutes, the discharge activity increases due to an increase in the discharge area. The discharge signal is then attenuated. Figure 4.13 shows the AE signal φ-q-n plots obtained from 500 cycles of data at different times during the test. The discharge AE signals occur predominantly within the first and third quadrant over the test time period, and AE signals become attenuated with increasing time. This may be due to an increase of pressure within the void from gas released through pd activity. An increase in void internal pressure would raise the discharge inception voltage. Consequently, PD activity cannot be sustained under the same applied stress. Another possibility is that the space charges generated by partial discharges accumulate at the wall of the void and decrease the internal electric field within the void, which would have a corresponding effect on the amount of PD activity.

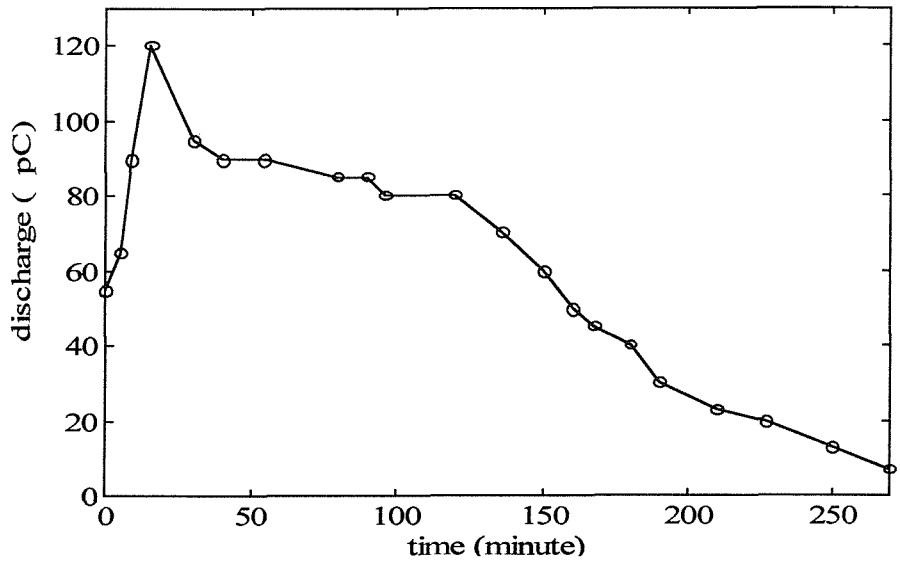

(a) discharge apparent quantity

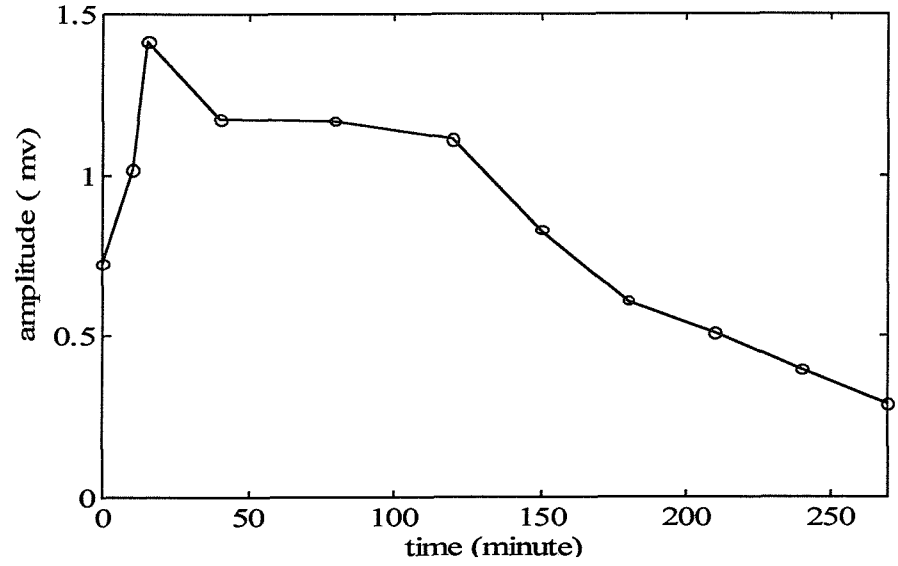

(b) AE signal amplitude

Figure 4.12 Discharge signal magnitude against test time

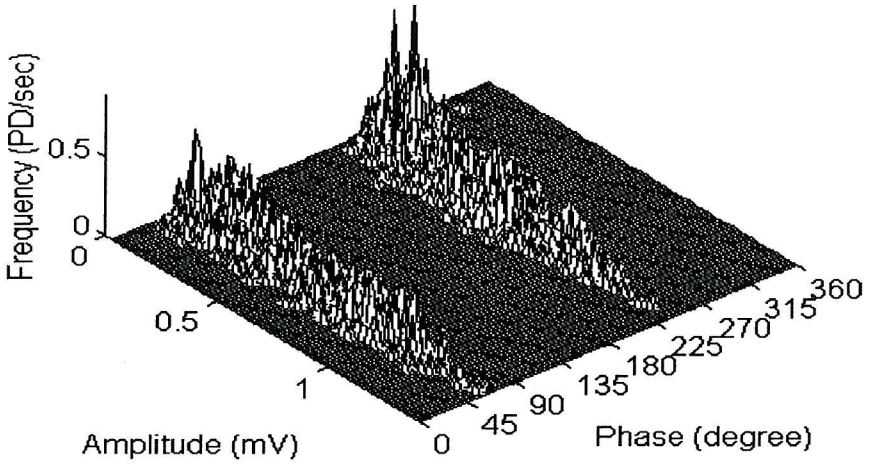

(a) 0 –15 min.

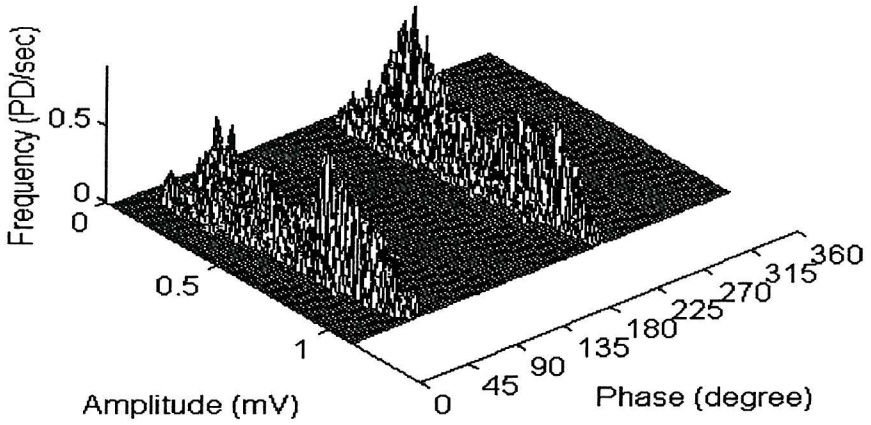

(b) 80 – 95 min.

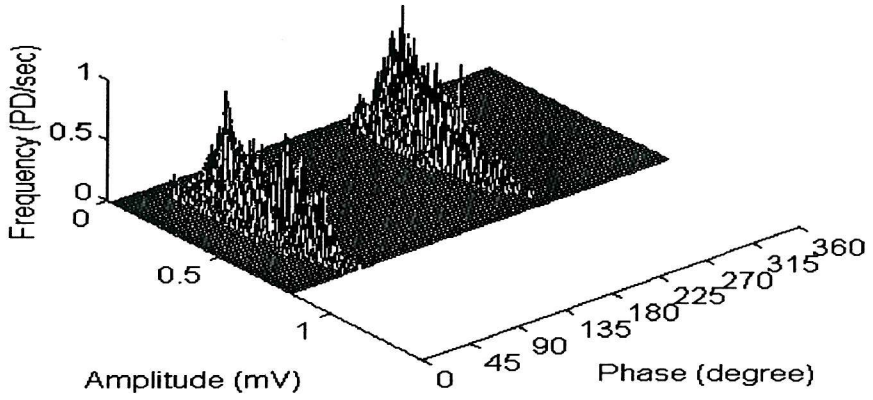

(c) 150 –165 min.

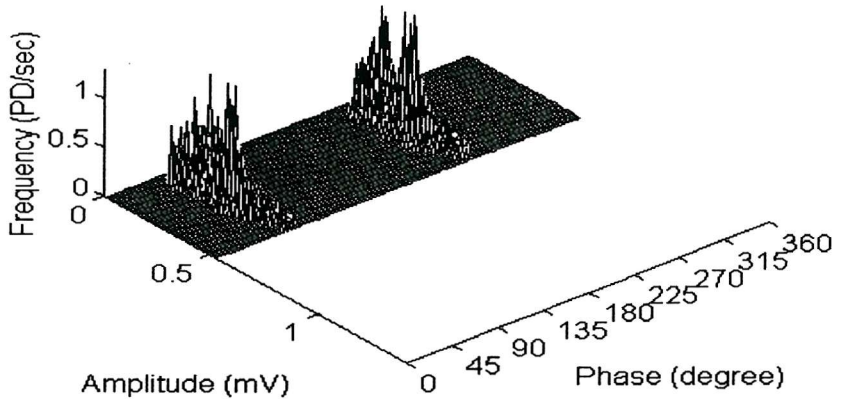

(d) 210 –225 min.

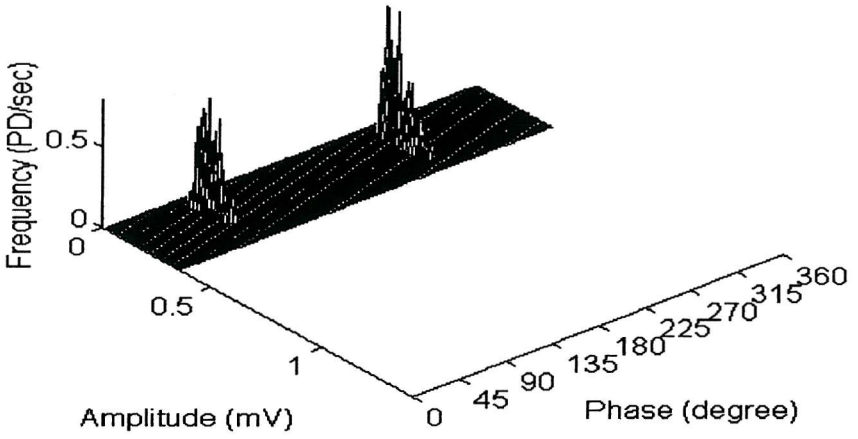

(e) 255 –270 min.

Figure 4.13 AE signal φ-q-n patterns against test time

The statistical operators for the above AE signal patterns have been calculated (Table 4.4). Kurtosis for both the positive and negative half cycle varies more significantly with time compared to the other operators.

Table 4.4 Statistical operators for AE signals with different test time

	Sk(+)	Sk(-)	Ku(+)	Ku(-)	CC	Q	Φ	MCC
0 –15 min.	0.417	0.593	0.343	-0.064	0.804	1.048	0.556	0.468
80–95	0.495	0.517	-0.284	-0.675	0.925	0.696	0.813	0.524
150–165	0.556	0.525	-1.12	1.152	0.819	0.728	0.818	0.488
210 –225	0.384	0.460	-0.927	-0.787	0.928	0.973	0.923	0.834
255 –270	-0.243	0.089	-0.143	-0.173	0.892	0.929	1.026	0.849

4.2.4.3 Effect of void size

Figure 4.14 shows the three-dimensional φ-q-n patterns and two-dimensional statistical patterns for AE signals obtained from three samples consisting of a 0.2mm thick centre film containing a 1,2 or 3mm diameter hole. For comparison, all the experiments were carried out at the same electric stress of 5 kv/mm. To avoid any possible effect of test time on the measurements, measured data were obtained immediately after the test voltage was applied.

Discharges also predominantly occur in the first and third quadrant of the power cycle, and are generally symmetric for the two quadrants. The results indicate that the greater the diameter of the void, the larger the AE signal maximal amplitude and the greater the number of discharges. This can be explained as in theory a larger void contains a larger discharging area.

The statistical operators for the three cases have been calculated (Table 4.5). The statistical operators vary significantly, except CC and Q.

Table 4.5 Statistical operators for AE patterns with different void sizes

	Sk(+)	Sk(-)	Ku(+)	Ku(-)	CC	Q	Φ	MCC
Void- 3 mm	-0.083	-0.013	0.692	0.482	0.917	0.856	1.283	0.999
Void – 2 mm	0.417	0.593	0.343	-0.064	0.804	1.048	0.556	0.468
Void – 1 mm	-0.059	-0.162	-0.855	0.636	0.901	0.846	1.118	0.852

4.2.4.4. Effect of void position

Voids at different positions such as an internal void, a hv-bounded void or an earth-bounded void, may have different discharge characteristics. Moreover, in practice more than one void may exist within the cable insulation. To investigate the influence of void position and void number, an experiment was undertaken using six different arrangements of the planar model (Figure 4.15). Figure 4.16 shows the relevant three-dimensional patterns for each arrangement. The diameter of the void was 2 mm and thickness 0.2 mm. Experiments were carried out using a stress of 2.5 kV/mm. To avoid any possible time influence on the AE measurements, data was obtained immediately after electric stress was applied to one of the samples.

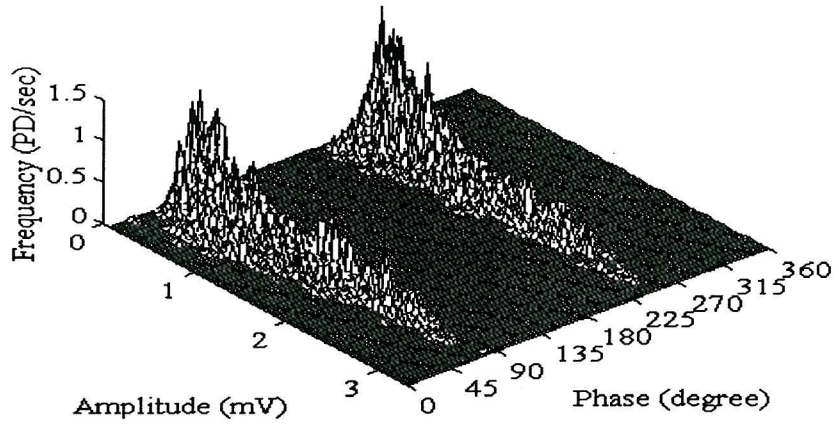

(a) void diameter of 3 mm

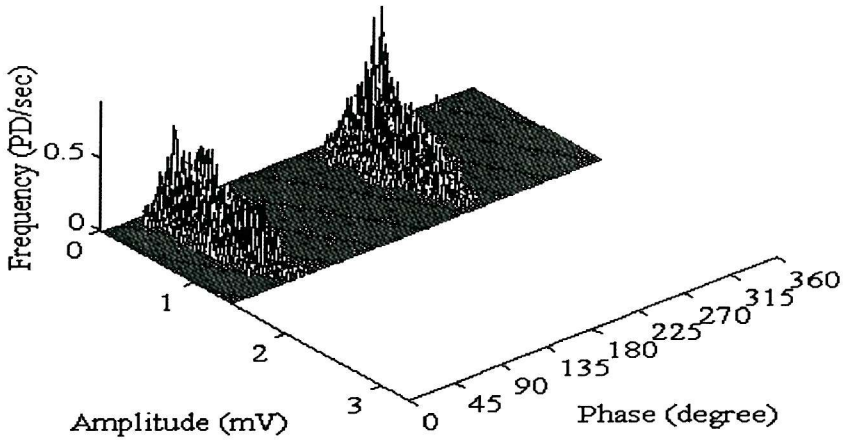

(b) void diameter of 2 mm

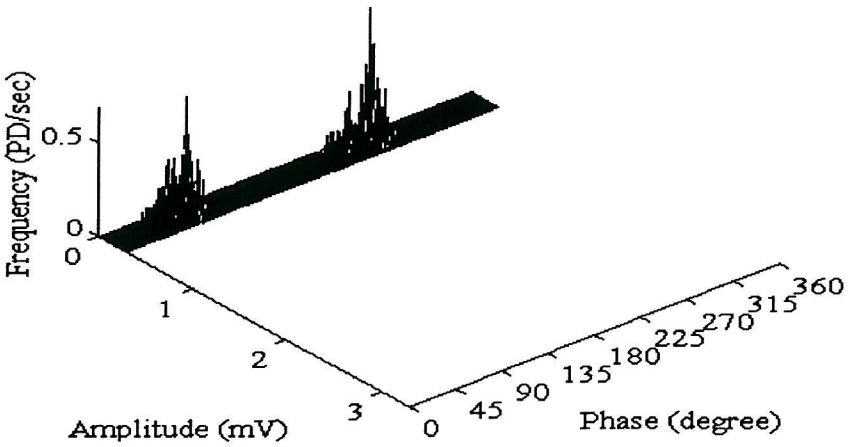

(c) void diameter of 1mm

Figure 4.14 Influence of void size on AE three-dimensional patterns

In all six cases, discharges occur predominantly in the first and third quadrants of the power cycle. The discharge pattern in the first and third quadrant is generally

symmetric for the internal void(s), but less symmetric for the earth-bounded and hv-bounded void(s). More acoustic emission signals with lower amplitude occur in the third quadrant for the hv-bounded void or voids and in the first quadrant for the earth-bounded void or voids. It can be explained as electrons are easier to emit from the negative electrode, and the positive ions bombard the electrode surface to produce a second electron emission, thus lowering the discharge inception voltage for the negative electrode bounded void, and this in turn acts to reduce discharge magnitude. However, it should be noted that partial discharge itself is a complicated stochastic process, the gas pressure within the void and the space charge effect will also influence the discharge process. Consequently variation of the statistical pattern may occur.

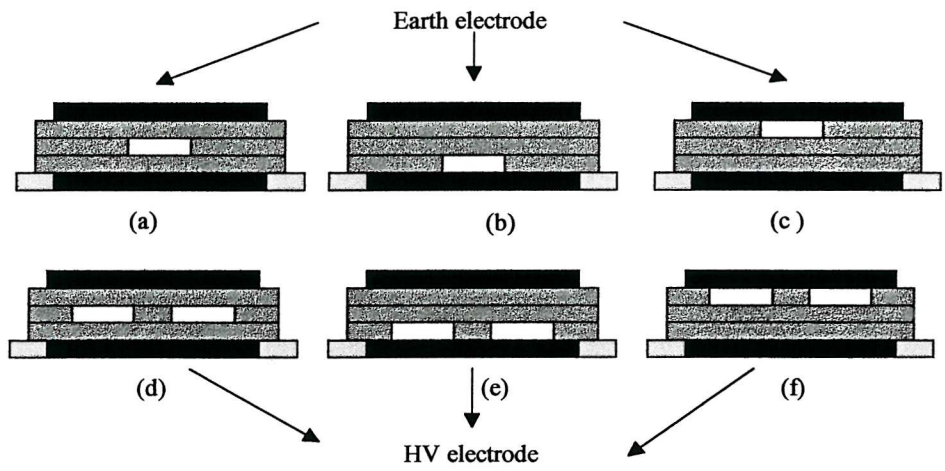

Figure 4.15 Experimental arrangement for different void (s) positions

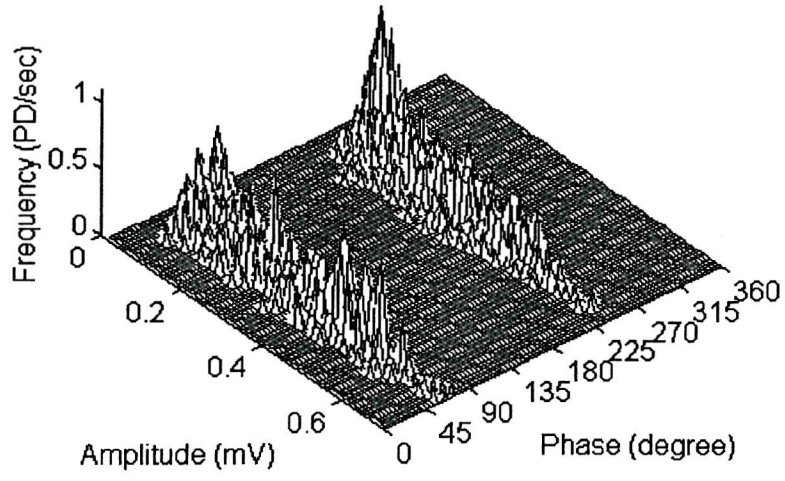

(a) one internal void

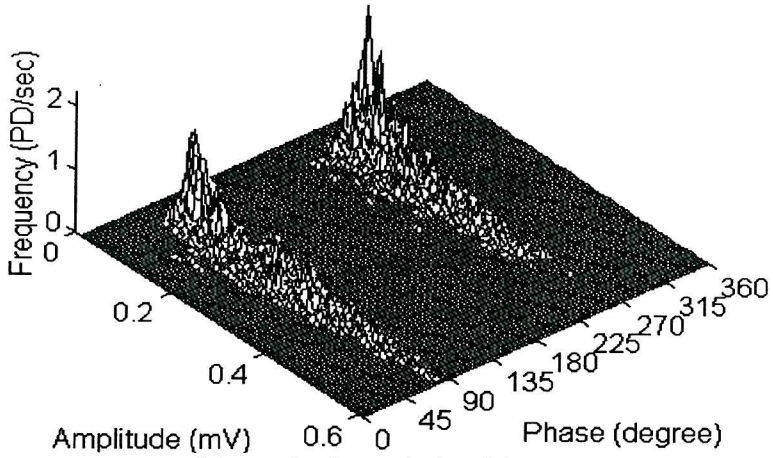

(b) one hv-bounded void

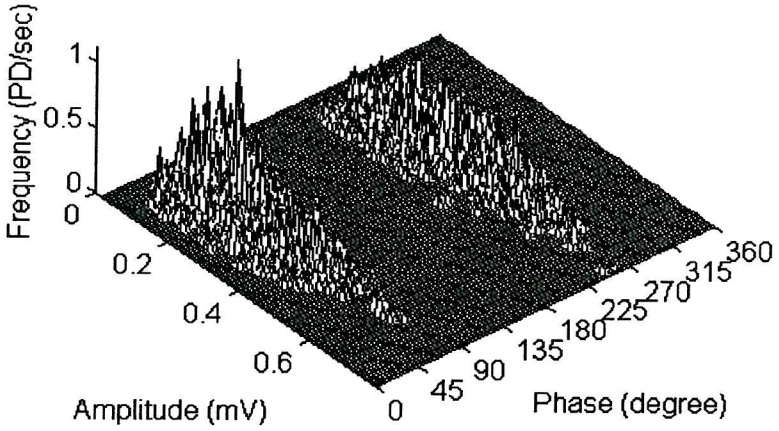

(c) one earth-bounded void

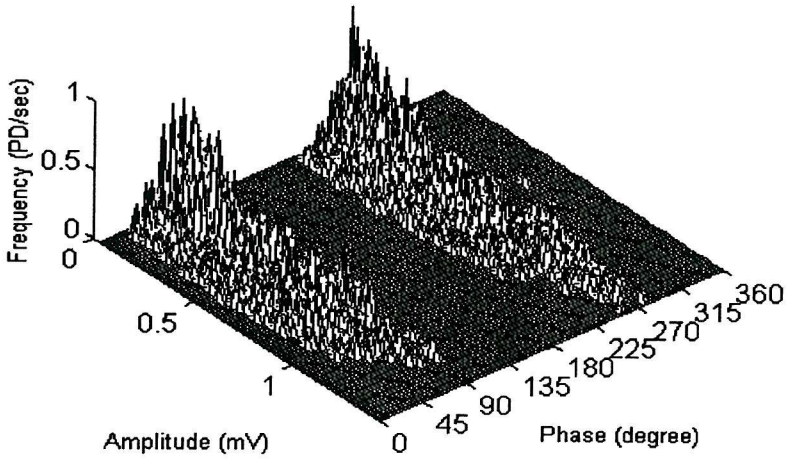

(d) Two internal voids

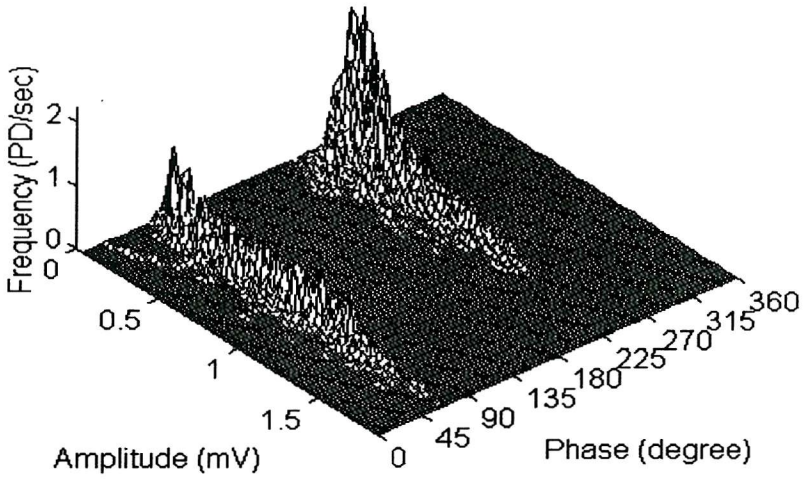

(e) Two hv-bounded voids

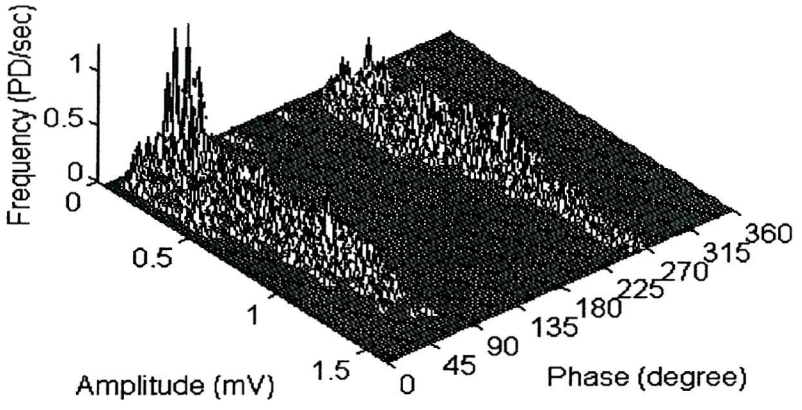

(f) Two earth-bounded voids

Figure 4.16 Three-dimensional AE patterns for void (s) at different positions

4.2.4.5. Attenuation by various materials and interfaces

The AE signal attenuation characteristics of Polyethylene (PE), Ethylene Propylene Rubber (EPR) and a mixture of PE and EPR have been investigated. Figure 4.17 shows the AE signal attenuation characteristics for a discharge level of 50 pC, with and without silicon grease between the AE sensor and different cable materials (Figure 4.1). If no couplant is applied, the detected AE signal is smaller when the applied cable material is PE than EPR. It would be expected that the solid PE would attenuate the AE signal less than the softer EPR [7]. However, the interface attenuation due to the existence of air gap between the AE sensor and the cable material is more significant than the internal attenuation effects. Under mechanical pressure, the EPR is

compressed, thus reducing the interface attenuation. When a couplant is applied, the interface attenuation is reduced and AE signals are more attenuated by EPR than by PE.

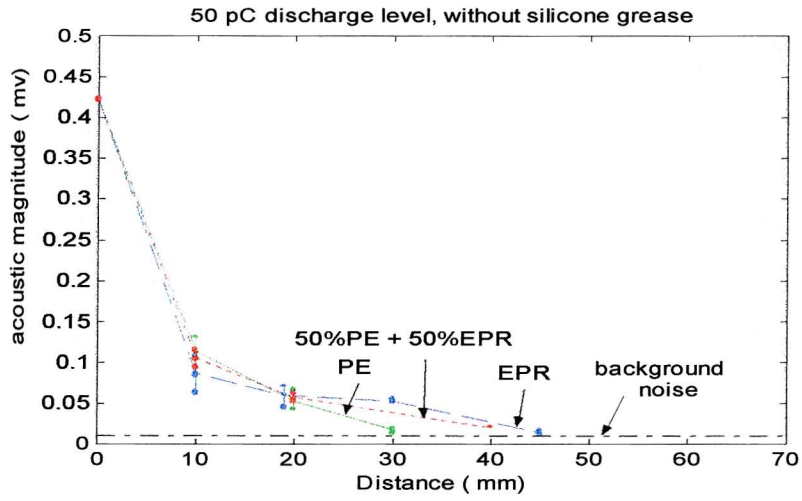

(a) without couplant

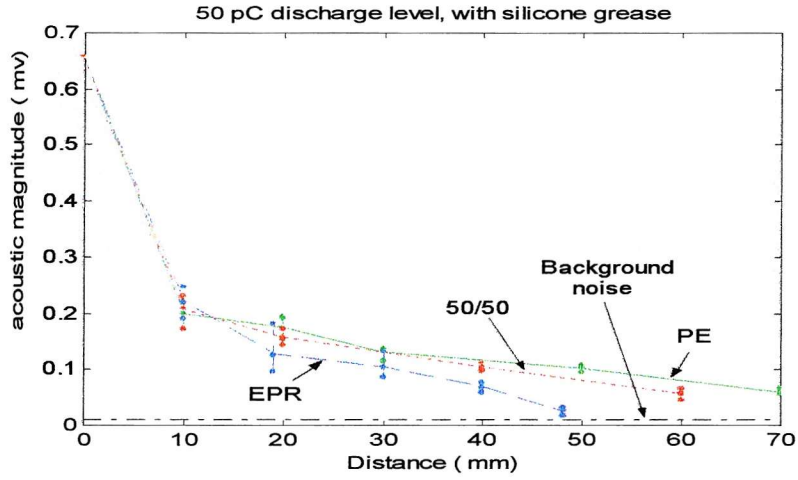

(b) with couplant

Figure 4.17 AE Signal attenuation with different materials and interfaces

4.2.5. Relationship between discharge acoustic and electric signals

The relationship between discharge acoustic and electric signals has been investigated. Figure 4.18 shows the two-dimensional statistical pattern for the discharge acoustic and electric signals. The obtained results indicate that discharge acoustic and electric signals may be related to each other as similar statistical patterns can be obtained under experimental condition.

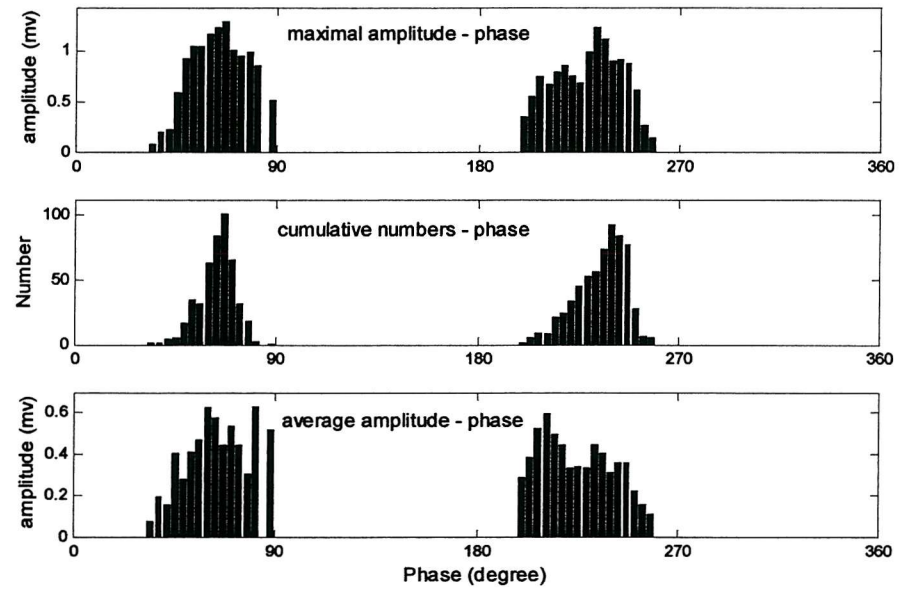

(a) Acoustic statistical pattern

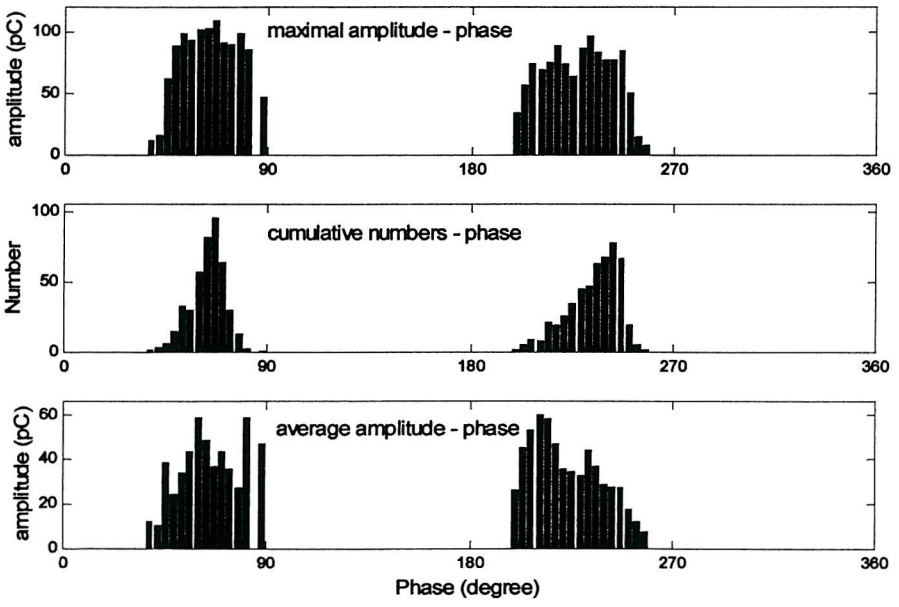

(b) Electric statistical pattern

Figure 4.18 Discharge acoustic and electric two-dimensional patterns

For PD electrical detection, according to the equivalent circuit, the PD pulse voltage amplitude can be quantified as the apparent charge in pC. For the acoustic method, there is no standard approach to quantification of the apparent charge. The reasons for this are that the principles of acoustic emission due to partial discharge activity have not been fully understood and that the attenuation of the acoustic wave during propagation is complex. Consequently, it is very difficult, if not impossible, to calibrate the acoustic emission signal amplitude with an apparent PD charge in pC.

4.2.5.1 Theoretical analysis

The acoustic energy is part of the total partial discharge energy, from the energy transformation, it is possible to deduce the relationship between acoustic wave pressure and PD apparent charge.

The acoustic energy and the acoustic wave pressure have the following relationship [121]:

$$E_A = \frac{4\pi r^2 P_A{}^2 t}{2\rho v} \tag{4.9}$$

Where r is the distance from the acoustic source to the sensor, P_A is the acoustic pressure, ρ is the density of the medium, v is the velocity of the acoustic wave, t is the time period to sample the acoustic signals, and E_A is the acoustic energy during time period of t. If during a stipulated time period t (t is constant), within a medium (ρv is constant), at a distance (r is constant), the relationship in (4.9) can be presented as

$$E_A = K_1 P_A{}^2 \tag{4.10}$$

Where K_1 is constant. The principle of piezoelectric AE sensor is to measure the acoustic wave pressure, thus the output of sensor S_A is proportional to P_A , therefore,

$$E_A = K_2 S_A{}^2 \tag{4.11}$$

Where K_2 is constant, and is determined by K_1 and the sensor scale coefficient.
On the other hand, for the electrical detection, the energy of each partial discharge is:

$$E_E = \frac{1}{2} VQ \tag{4.12}$$

Where V is the amplitude of the test voltage during partial discharge and Q is the PD apparent quantity.

When a partial discharge occurs, the acoustic energy is $1/K_3$ of the electric energy, such that

$$E_E = K_3 E_A \tag{4.13}$$

Therefore, the PD apparent quantity is

$$Q = \frac{2K_2K_3S_A^{\ 2}}{V} = KS_A^{\ 2} \tag{4.14}$$

Where V is constant and $K=2K_2K_3/V$. In practice, K_3 may decrease with the increase of discharge, therefore, the following empirical equation may be applied [7],

$$Q = KS_A^{\ n} \tag{4.15}$$

Where K is constant and n is somewhere between 1 and 2.

4.2.5.2. Experimental investigation

In order to verify Equation 4.15, experimental work has been undertaken to investigate the relationship between the discharge electric signals obtained using a standard PD detector and the acoustic emission signal. In this case, three different internal voids with diameter of 1 mm, 2 mm and 3 mm and with thickness of 0.2 mm were studied. The applied electric stress was 5 kV/mm. The maximal amplitude of each acoustic emission was automatically determined and plotted against the apparent PD quantity for different internal voids (Figure 4.19). The apparent PD quantity was obtained using a X-Y recorder connected to the conventional PD detector.

Figure 4.19 reflects the relationship as in Equation (4.15). It should be noted that the aim of the experiment was to study the relative relationship between discharge acoustic and electric signals rather than to find an absolute mV/pC calibration.

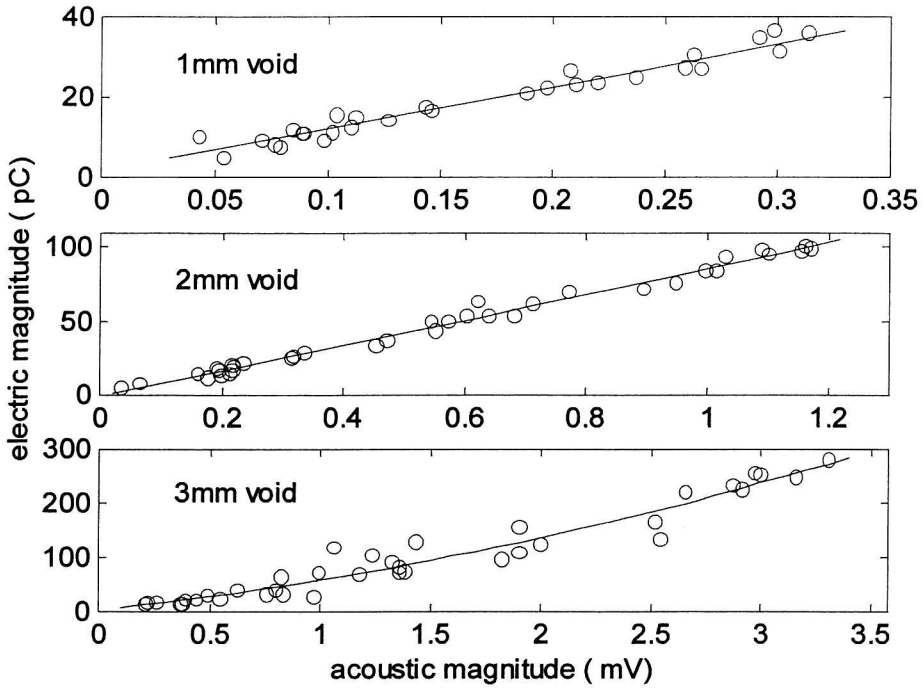

Figure 4.19 Correlation between the discharge acoustic and electric magnitudes

4.3 Acoustic Emission Measurement of PD Behaviour during Electrical Tree Growth in XLPE Insulation

When polymeric insulation systems are subjected to high electrical stresses, they are susceptible to localised degradation at stress enhancements caused by voids or contaminants within the insulation or protrusions at electrode/insulation interfaces. The electrical tree structure growth in solid dielectric is a result of partial discharge within the tree channels. When treeing occurs, the material around the stressed area decomposes, building hollow carbonised channels. These channels have a hair-like structure with a diameter of a few micrometers [122]. Electrical tree formation is one of the main causes of the polymeric insulation degradation.

Research work has been carried out to investigate the partial discharge behaviour of electrical trees [123-131]. In particular, combined partial discharge detection and video monitoring of tree growth have shown a strong correlation between the partial discharge activity and the spatial and temporal development of the electrical tree [131].

Acoustic emission measurements have been applied to investigate acoustic emission characteristics due to partial discharges during electrical tree growth within the cross-linked polyethylene (XLPE) cable insulation. The test arrangement is shown in Figure 4.20 and 4.21.

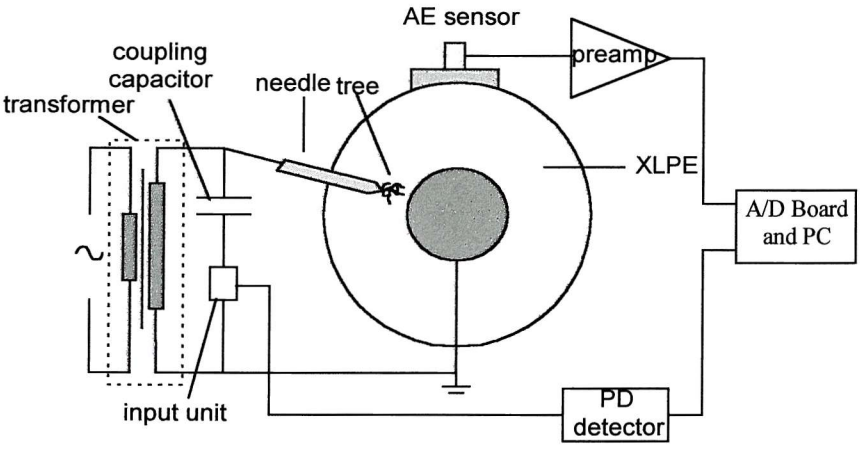

Figure 4.20 Schematic arrangement for AE measurement of treeing discharges

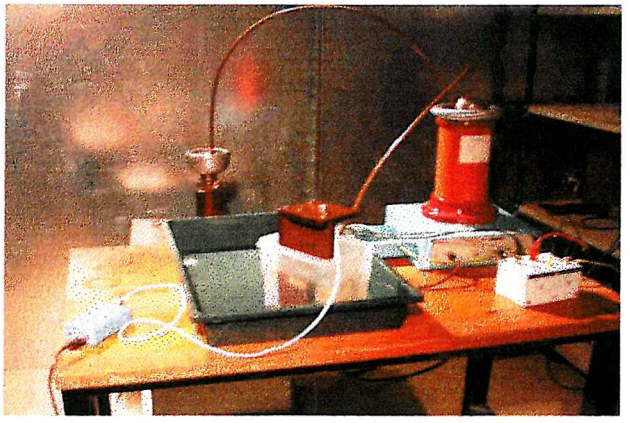

Figure 4.21 The experiment to measure treeing discharge

The samples under test are 20mm slices of XLPE from 66 kV rated conductor cable insulation. The conductor has been removed. The preparation of the sample involves the insertion of a needle electrode, in the well-known needle-to-plane electrode arrangement. The needles used were 1 mm in diameter either made of steel leading to a 5 μm pin-tip radius or made of tungsten leading to a 3 μm pin-tip radius. Testing was performed with the sample placed in a silicone oil bath to prevent external discharges.

Conventional PD electrical detection according to IEC-270 was applied. Before the test sample was connected, the discharge detector voltage meter was calibrated using a standard high voltage meter. The partial discharge detector, input unit,

coupling capacitor, AE sensor, preamplifier, ADC board and PC were the same as used for earlier experiments (section 4.2.1).

Partial discharge occurs around the needle tip and electrical tree starts to grow if the electric field is high enough. The tree growth rate is related to many factors, such as the applied voltage, the needle tip radius, the medium in which the tree grows, with or without a void gap around the needle tip, the distance between electrodes, and the space charge effect.

The hyperbolic radius formulae used in determining the electric field stress is shown in Equation 4.16. The formula is applicable for the traditional pin-to-plane electrode arrangement:

$$E_{max} = \frac{2\,V}{r \ln (4\,d / r)} \tag{4.16}$$

Where E_{max} is the maximum electric field stress; V is the applied Voltage; r is the needle tip radius; d is the needle-to-plane spacing.

This formula has been adopted by Champion, Dodd and Alison for predicting the tree types, such as branch, branch-bush and bush [131]. Different types of trees can be observed using a CCD microscope system [132]. Figure 4.22 shows the CCD images of different types of trees. The branch type of tree advances towards the earth plane and the branching frequency increases as the tree grows. The bush type of tree grows widely and densely, and the bulk of the discharge activity takes place within the bush. The bush-branch type of tree is a structure during the transition from branch type to bush type.

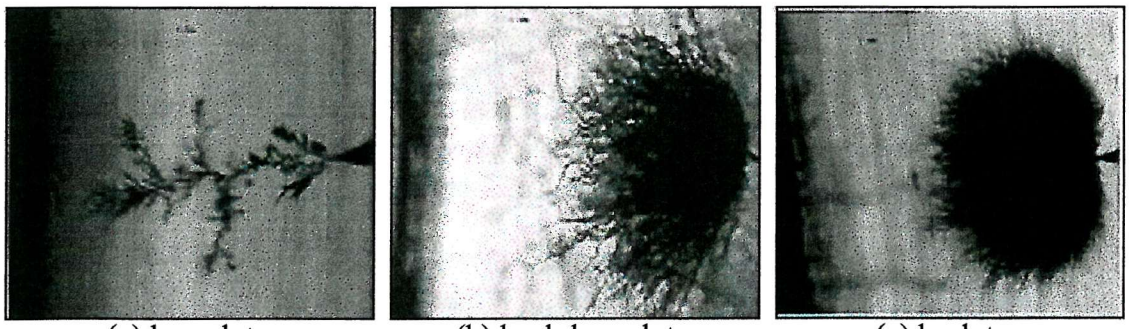

(a) branch tree (b) bush-branch tree (c) bush tree

Figure 4.22 Different types of electrical tree [132]

When an electrical tree is formed in a solid dielectric due to partial discharge activity, blasts occur and the related stress also generates acoustic waves. Acoustic emission

characteristics with test time (until sample breakdown) have been investigated. The power supply is current limited and will turn off if sample breakdown occurs. Figure 4.23 shows the acoustic emission magnitude development with the test time (sample breakdown occurs after 42 minutes). In this case, the tungsten needle tip radius was 3 μm, the distance between electrodes 3mm, and the applied voltage 11 kV. Initially the discharge was 40 pC and this increased to 100 pC before breakdown occurred. Acoustic emission magnitude generally increases as the tree grows, though there are fluctuations.

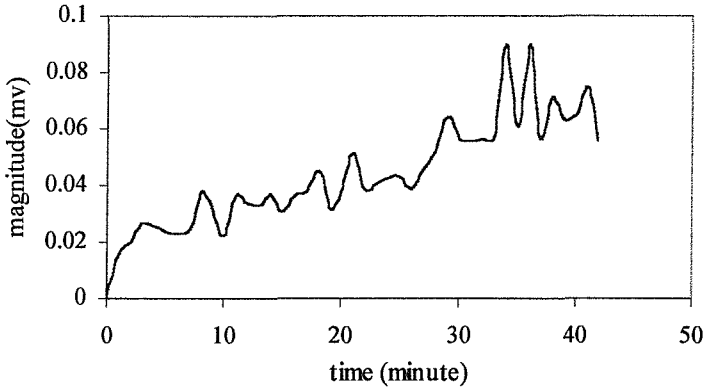

Figure 4.23 AE magnitude against test time (breakdown occurs after 42 min.)

Figures 4.24 shows the discharge acoustic emission φ-q-n patterns for the same sample at different test time (related with Figure 4.23). AE signals were obtained continuously for 250 cycles, the number of the phase windows is 200 and the number of the magnitude windows is 50. The threshold for the AE signal is 0.0125 mV, which means that signals below this level were assumed to be noise.

During the first time period (a), discharges occur predominantly in the first and third quadrant and the discharge repetition rate is low. During the second time period (b), the discharge magnitude range does not vary but more discharges have occurred. During the third and fourth time period, more discharges occur and signal amplitudes are also gradually increased. It can be noted that some discharge pulses also occur within the second and fourth quadrant. Some larger signals occur during the last time period before the breakdown occurs.

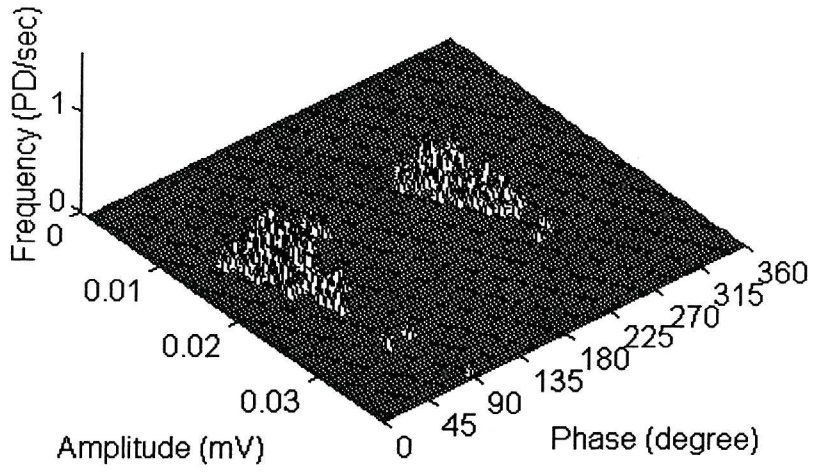

(a) 0 – 7 min.

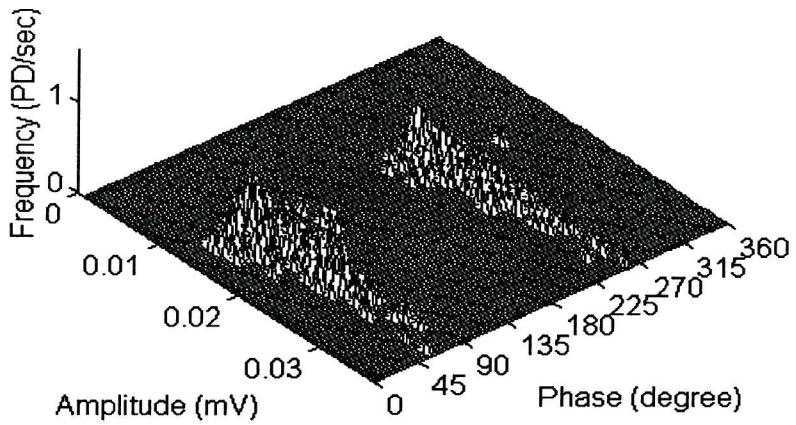

(b) 8 – 16 min.

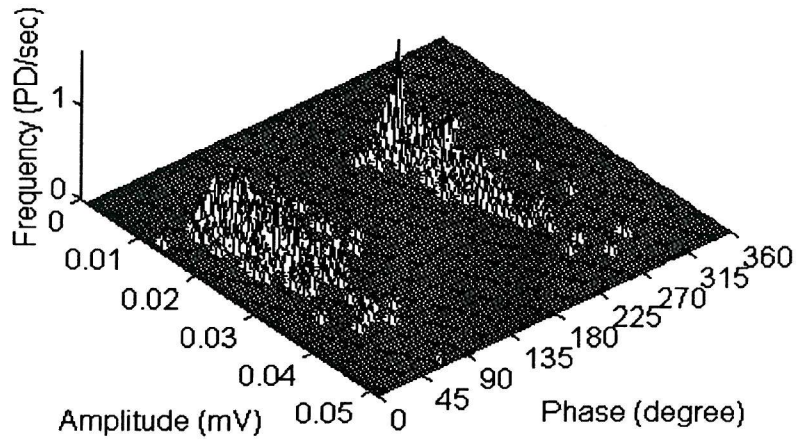

(c) 17 – 25 min.

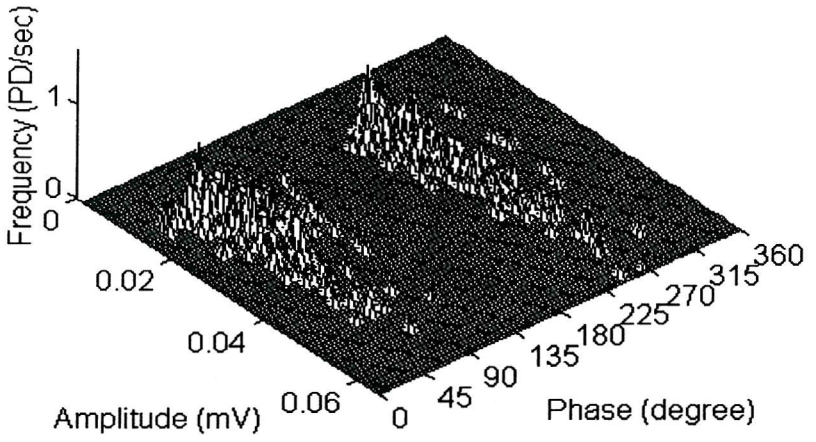

(d) 26 – 33 min.

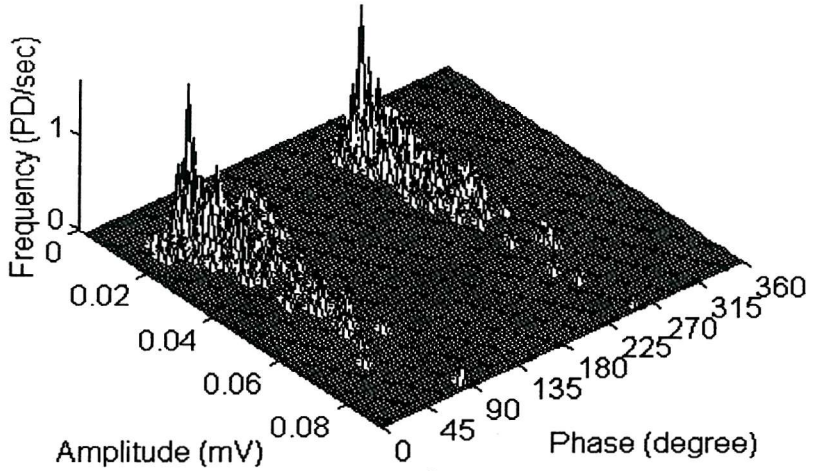

(e) 34 – 42 min.

Figure 4.24 AE signal 3D patterns at different times during tree growth

The statistical operators for the above AE signal patterns were calculated (Table 4.6). Sk(+) and Sk(-) decreases gradually with the increase of test time. Ku(+) and CC are consistent with time, however, MCC is less consistent due to the change on Q and Φ. Ku(-) vary significantly over the test duration.

Table 4.6 Statistical operators for AE signals at different time during tree growth

	Sk(+)	Sk(-)	Ku(+)	Ku(-)	CC	Q	Φ	MCC
0 – 7 min.	0.406	0.421	1.487	-0.15	0.561	1.161	0.65	0.424
8 – 16 min.	0.334	0.388	1.542	1.660	0.727	1.096	0.857	0.683
17 – 25 min.	0.136	0.303	1.568	2.887	0.508	1.023	2.667	1.386
26 – 33 min.	0.052	0.278	1.611	1.838	0.537	0.967	1.091	0.566
34 – 42 min.	-0.049	-0.29	1.639	-0.528	0.644	0.775	1.455	0.725

A second sample has also been tested. In this case, the steel needle tip radius was 5 μm, the distance between electrodes was 3 mm, and the applied voltage 10 kV. Figure 4.25 shows the acoustic emission signal magnitude development with the test time.

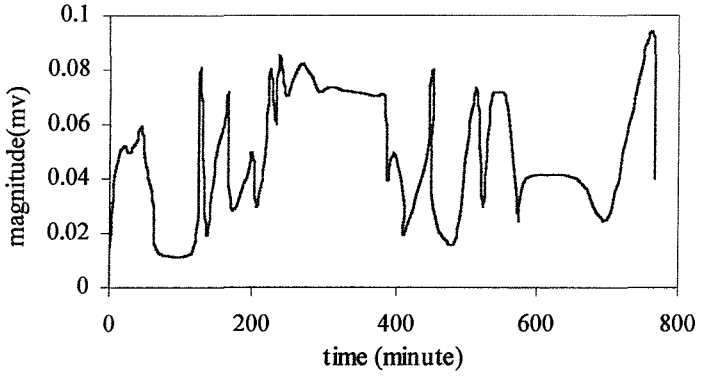

Figure 4.25 AE magnitude against test time (breakdown occurs after 765 minutes)

Figure 4.25 indicates that the acoustic emission signal magnitude fluctuates significantly with the test time. Occasionally, during the process of electrical tree growth, the discharge magnitude is reduced. This can be explained by the following reasons:

- The generated space charge accumulates on the tree channel, thus decreasing the electric field. This will decrease the treeing discharge, and slow down the tree growth rate.
- The discharge can be extinguished due to the increase of gas pressure within the tree channel. As the tree grows, the inner walls of the tree channel decompose and release gases causing an increase in pressure. Discharge activity cannot restart and

electrical tree cannot grow until enough gas has been diffused so that the PD inception voltage is reached again.

Figure 4.26 and 4.27 show two pairs of discharge acoustic and electric signals in one power cycle when the discharge level is low and high respectively. For both figures, the lower one is the discharge apparent quantity obtained using the conventional PD detector. Compared with acoustic signals, pulse-shaped interference exists with the discharge electrical signals.

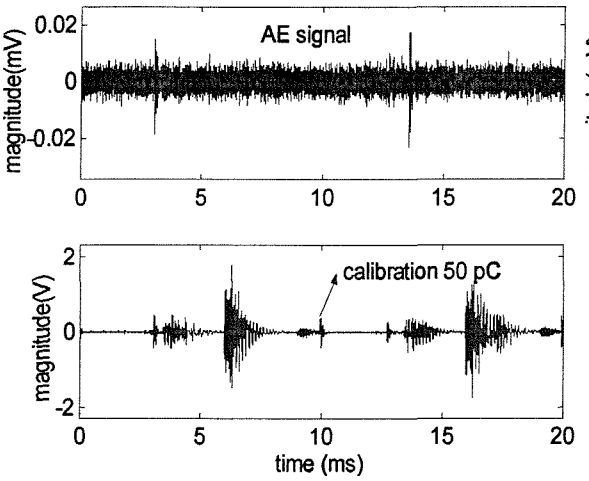

Figure 4.26 Discharge acoustic and electric signals (discharge activity is weak)

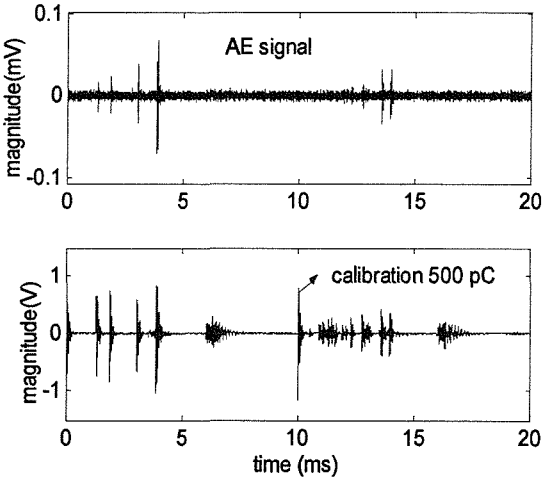

Figure 4.27 Discharge A&E signals (discharge activity is intense)

4.4. Acoustic Emission Measurement of Partial Discharges from an Epoxy Composite Sample

The acoustic emission measurement technique has been applied to detect partial discharges from an epoxy composite sample. There is a small gap of 2.2 mm between the two electrodes within the sample, which will produce partial discharges if the voltage is increased above 22 kV. An AE sensor was placed at two different positions as indicated in Figure 4.28. Conventional electrical detection was applied to provide the PD apparent quantity. The test equipment are as described previously in sections 4.2 and 4.3.

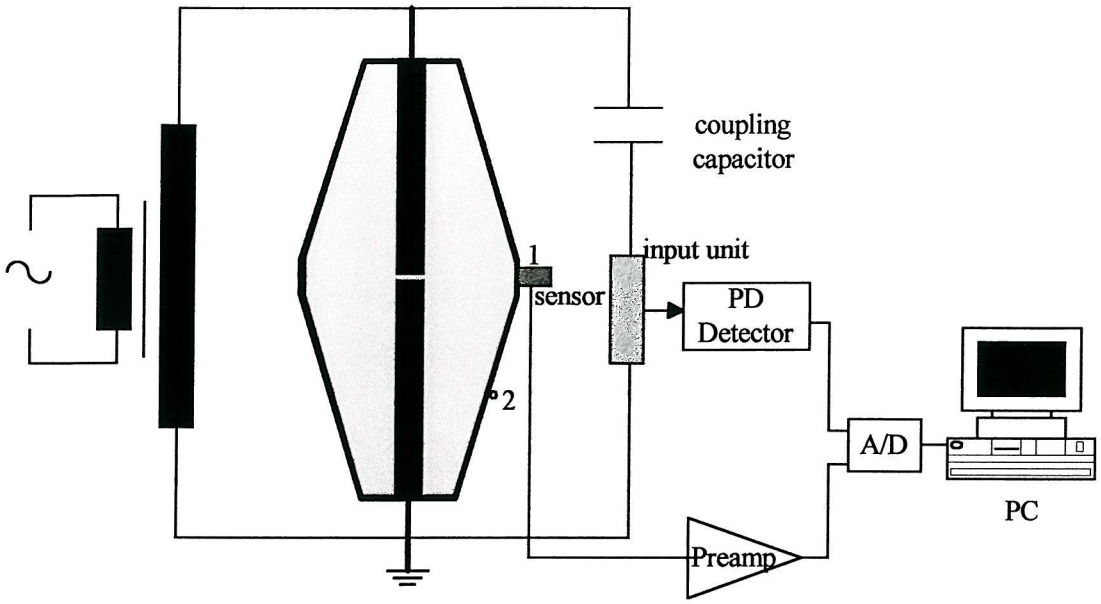

Figure 4.28 Experimental arrangement for detecting PD from an epoxy sample

Figure 4.29 shows the PD acoustic emission and electric signals at position 1. The applied voltage for this experiment is 25 kV. The discharge acoustic emission and electric signals are generally related with each other. Compared with the acoustic emission method, the conventional electrical detection is influenced by electrical interference.

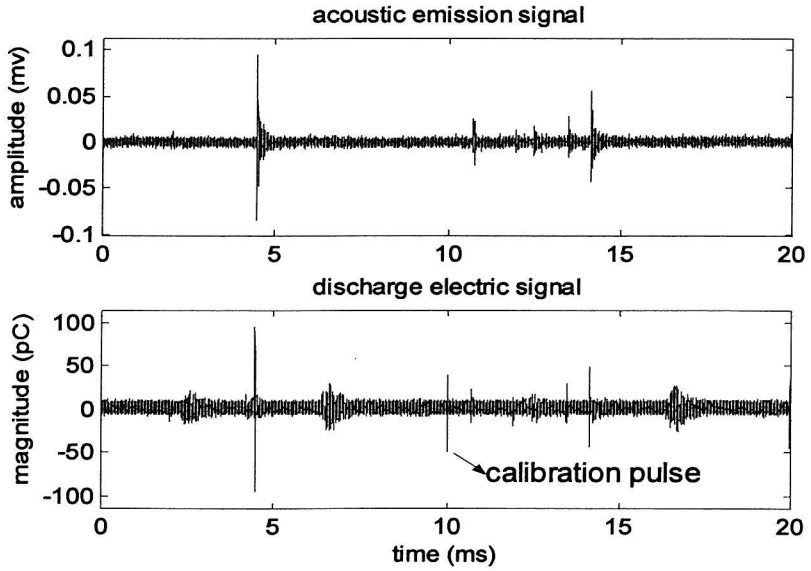

Figure 4.29 Discharge acoustic and electric signals from an epoxy sample

Figure 4.30 shows a pair of related acoustic and electric pulses. The time delay is estimated to be 16 μs, considering the acoustic emission wave travelling speed of 3000 m/s in the epoxy composite [7], the distance from the PD site to the AE sensor is calculated to be 48 mm, which agrees with the practical geometrical dimension.

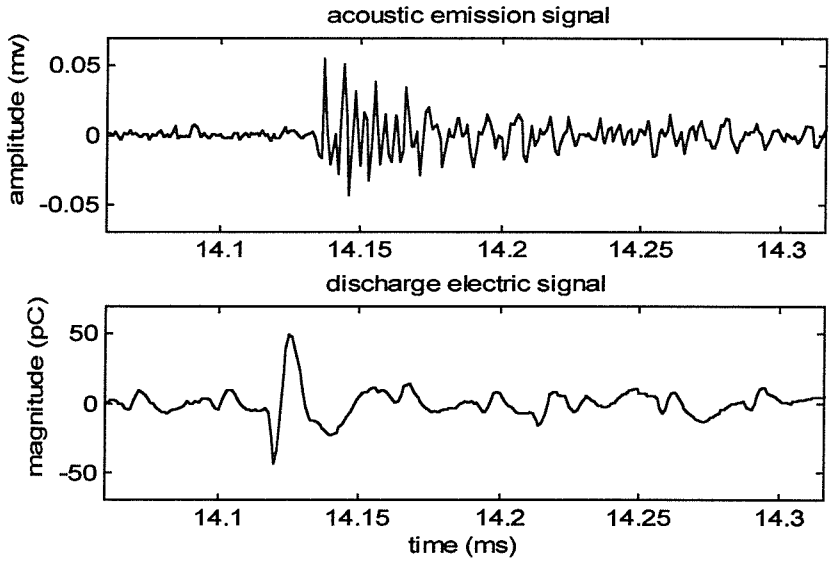

Figure 4.30 A pair of discharge acoustic and electric pulses

The AE sensor was then moved along the sample surface to position 2. The time delay for this case was estimated to be 19 μs, indicating that position 2 is further from the PD site than position 1. Considering the acoustic wave travelling speed in epoxy, the distance between pd site and position 2 is estimated to be 57 mm. Acoustic signal with amplitude of 0.025 mV can be detected for the discharge level of 50 pC. AE signals with amplitude of 0.05 mV can be detected at position 1 for the same discharge level. This is due to the greater attenuation of the AE signal propagation to position 2 than to position 1.

4.5 Summary

The application of the acoustic emission technique for partial discharge detection has been investigated. A planar experimental model was constructed in order to study the acoustic emission signals due to partial discharges within polymeric insulation. The experimental model is modular in construction allowing the void size, location, number and shape, cable material type, mechanical pressure, acoustic interface and working electric stress to be altered.

Conventional partial discharge electrical detection according to IEC-270 was applied to provide the discharge apparent quantity reference and study the relationship between the discharge acoustic emission and electric signals. Discharge acoustic and electric signals were presented in both the time and frequency domain. The latter is obtained by means of Fast Fourier Transform. The discharge acoustic and electric signals relate each other with a time of flight that is the travelling time for the acoustic emission signal from the PD site to the acoustic emission sensor.

Partial discharge is a stochastic process, therefore, discharge signals were analysed using two-dimensional statistical patterns $H_{qmax}(\varphi)$, $H_n(\varphi)$ and $H_{qn}(\varphi)$, as well as the three-dimensional Phase-Charge-Number (φ-q-n) pattern. Several statistical operators, such as Skewness, Kurtosis and Cross-Correlation coefficients, were calculated.

Factors influencing the AE measurement have been investigated. Obtained results indicate that higher electric stress and larger voids produce larger discharge signals with a higher repetition rate. Void(s) at different locations, such as hv-bounded, earth-bounded or internal, may have different statistical characteristics, as observed in their three-dimensional φ-q-n patterns. It was also observed that discharges became self-attenuated against the test time, electrically and acoustically. This can be explained that partial discharge activity causes an increase of gas pressure within the void, which in return leads to the increase of discharge inception voltage, thus reducing the partial discharge activity.

Statistical operators were calculated for different experimental arrangements, and results indicate that they may be significantly influenced by factors such as the electric stress and test time. Consequently it might be difficult to characterise different AE signal patterns using the statistical operator template matching approach.

Acoustic emission signal attenuation through different cable materials and interfaces were investigated. Results indicate that the use of acoustic couplant has a key role for the AE measurement. With acoustic couplant, AE signals attenuate less in polyethylene material than in ethylene propylene rubber.

Relationship between discharge acoustic and electric signals was investigated through theoretical analysis and experimental study. Similar statistical patterns can be obtained, and a proportional relationship between the two might exist. However, due to the complexity of acoustic emission propagation path and attenuation through different

materials and interfaces, it is almost impossible to calibrate the AE signal (in mV) with a discharge apparent quantity (in pC).

Acoustic emission measurement was applied to study the partial discharge behaviour during the electrical tree growth in XLPE cable insulation. The measured acoustic emission signals can indicate the intensity of the partial discharge activity. Different experimental conditions such as pin tip radius, pin-plane spacing and applied voltage, might determine the type of the resultant tree. The gas pressure within the tree channel and the space charge effect might also influence the breakdown progress. Discharge activity may alternate between intense and weak, for this reason, insulation breakdown may not be judged solely by the discharge signal magnitude.

AE measurement was also applied to detect partial discharges produced from an epoxy sample. Results indicate that location of PD site might be determined considering the time of flight and the acoustic wave travelling speed within the material. The investigation provided an insight into the application of acoustic emission techniques to detect partial discharge activity within practical cable joints.

Chapter 5

Acoustic Emission Signal Characterisation Using Artificial Neural Networks (ANN)

5.1 Introduction

The objective of undertaking acoustic emission measurement is to detect the presence of emission sources and to determine characteristics about the source. The main purpose of source characterisation is to evaluate the significance of any PD activity. Pattern recognition techniques can be used to relate measured signal characteristics to possible acoustic emission sources [105].

Artificial neural networks (ANN) can be used for pattern recognition. An artificial neural network is a non-linear and interconnected assembly of simple processing elements. The processing ability of the network is stored in the inter-unit connection strengths or weights, obtained usually by a process of adaptation to or learning from a set of training patterns.

Artificial neural networks can generally be divided into three categories: ANN based on physical models such as the Hopfield neural network and Boltzman neural

network; ANN based on the adaptive signal processing principles such as the multi-layer feed forward neural network using back-propagation (BP) algorithm; ANN based on the self-organised theorem such as the adaptive resonance theory (ART) and the self-organising map (SOM) [133].

It is important to extract features that can represent the information contained in the signal. In addition to the general time domain pulse properties, the acoustic emission signal time series can be transformed into other domains [105]. It should be noted that the transformation carried out to generate new features for source characterisation does not produce new information, alternatively, they represent the existing waveform information in ways that facilitate source characterisation. Moreover, statistical methods can be used to extract data from a group of signals originating from the same source. It would virtually be impossible to obtain the same information from one signal alone.

The ANN pattern recognition consists of the learning or training process and the testing process. During the learning or training state, a set of decision rules is developed. The ANN is supplied with a set of representative signals from each source to be classified. It is considered to be trained when it can use the decision rules to identify an input signal correctly. To test the ANN performance, sample signals not used during the training process are presented to the system that will identify the class to which each unknown signal belongs. Successful identification of input signals is a good indication of a properly trained system.

In most ANN approaches to partial discharge pattern recognition, a multi-layer feed forward network architecture is applied in which training is carried out by means of the back propagation algorithm [134-144]. However, the application of some other network structures such as the Kohonen self-organising map using the learning vector quantization algorithm [135,136,145] has also been investigated.

5.2 Artificial Neural Networks

5.2.1 Back-propagation (BP) neural network

The BP neural network consists of the input layer, at least one hidden layer and the output layer, as shown in Figure 5.1. Each layer is fully connected to the succeeding layer. The main purpose of the hidden layer is to extract features of different PD

sources and pass its knowledge to the output layer or the succeeding hidden layer if there is more than one. The number of processing elements in the hidden layer is usually between the number of elements in the input and the output layer. However, it tends to be larger for more complex problems.

The typical BP processing element (pe) is shown in Figure 5.2, where $X_1^{[k-1]}$, $X_2^{[k-1]}$,..., $X_n^{[k-1]}$ are n outputs from the preceding layer, $W_{i1}^{[k]}$, $W_{i2}^{[k]}$,..., $W_{in}^{[k]}$ are weight connections between the (k-1)-th and k-th layer, $B_i^{[k]}$ is the threshold vector of the k-th layer and $X_i^{[k]}$ is the output of the i-th pe in the k-th layer. The processing element transfers its input according to

$$X_i^{[k]} = f(\sum_{j=1}^{n} W_{ij}^{[k]} X_j^{[k-1]} - B_i^{[k]}) = f(I_i^{[k]}) \tag{5.1}$$

Where f can be hyperbolic tangent function

$$f(x) = \frac{e^x - e^{-x}}{e^x + e^{-x}} \tag{5.2}$$

or a sigmoid function (Figure 5.3):

$$f(x) = \frac{1}{1 + e^{-x}} \tag{5.3}$$

Using labelled training data the back-propagation algorithm determines the error between the desired and the actual computed value at the output layer. Propagating this error back through the network, the element weights are adjusted in order to reduce it to a minimum. The whole procedure is repeated until the root mean square error at the output layer is smaller than a pre-defined convergence criterion. The learning procedure is shown in Figure 5.4. During the classification process the BP ANN produces different outputs that are between zero and one (using a sigmoid function). The class of the input vector is determined by the neuron that has the largest value. In order to increase the reliability of the identification results, additional criteria were defined for this study to ensure that the input pattern was clearly identified:

- The largest output value must be greater than 0.5.
- The next largest value must be less than 0.5.
- The difference between these two values must be greater than 0.3.

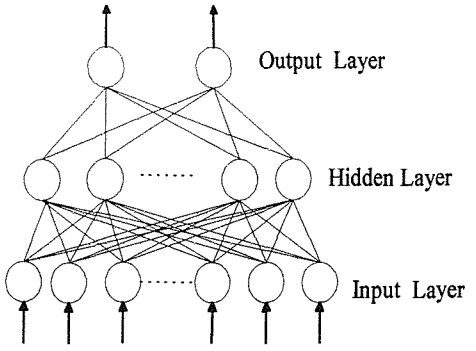

Figure 5.1 BP ANN with three layers

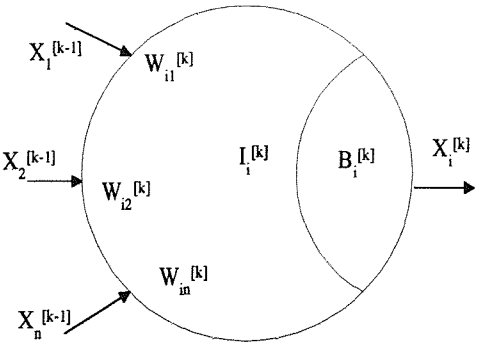

Figure 5.2 Typical BP processing element

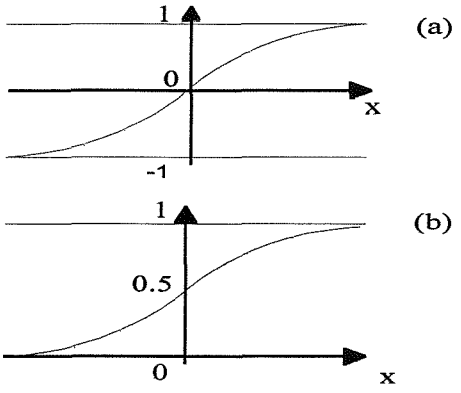

Figure 5.3 Different BP network transfer function
(a) Hyperbolic tangent transfer function
(b) Sigmoid transfer function

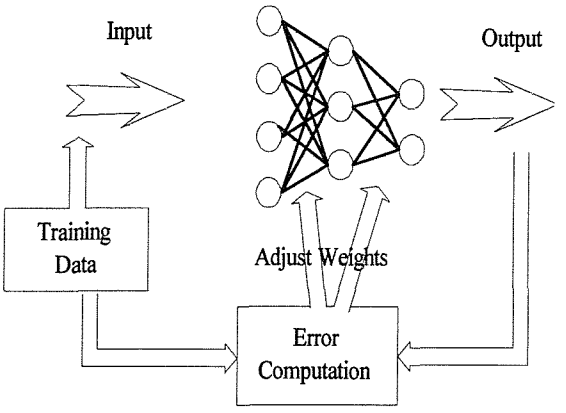

Figure 5.4 BP learning process

5.2.2 Learning vector quantization (LVQ) neural network

The basic structure of the LVQ neural network is shown in Figure 5.5. It also consists of the input, the hidden and the output layers, but the hidden layer or Kohonen layer has an identical number of neurons for each class of output. During the learning process, the Euclidean distance d_j, between the input vector and weights of each neuron at the Kohonen layer is calculated. That is:

$$d_j = \sqrt{\sum_{i=1}^{n} (x_i - w_{ij})^2} \qquad (5.4)$$

Where x_i is the i-th input vector; n is the number of inputs; w_{ij} is the weight from the i-th input to the j-th Kohonen neuron.

The neuron having the minimum distance is selected as the winner. If this neuron is in the class of the learning vector, then the weight of the winning neuron is altered towards the learning vector, decreasing its distance to that class. This increases the probability of the neuron responding more strongly to a similar learning vector in future rounds. If the winning neuron is not in the class of the learning vector then its weight is altered to increase its distance from the learning vector. Having trained the ANN, during the classifying process, the distance of the unknown input vector to each neuron is computed and again the nearest neuron is declared as the winner. The final classification of the input signal is made according to the class associated with the winning neuron.

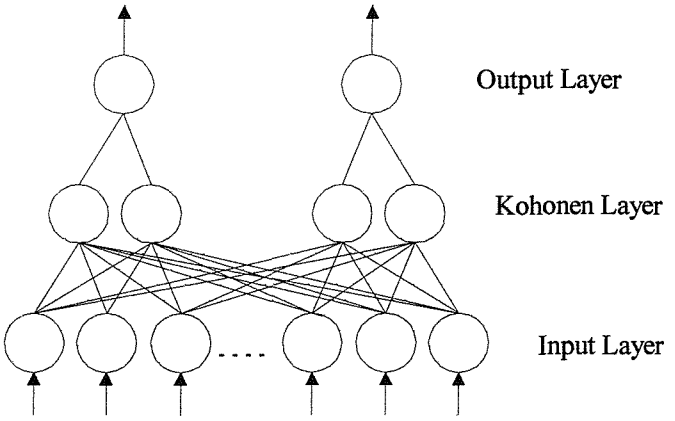

Figure 5.5 Structure of the LVQ neural network

5.3 Features For Pattern Recognition

To apply the above artificial neural networks to partial discharge pattern recognition, the ANN data input is important. The input data should be able to fully represent different patterns in an effective way.

5.3.1 Statistical pattern and operators

A lot of research work has investigated partial discharge pattern recognition using conventional electrical detection. Typically the phase resolved statistical distribution such as the φ-q-n pattern has been applied [134,138,139,145,146]. For this approach the voltage cycle was divided into phase windows representing the phase angle axis and the observation takes place over several voltage cycles. The three-dimensional

distribution φ-q-n represents the relationship between the PD magnitude q and the PD count rate n as a function of the phase angle φ. Many other PD characteristics, such as the maximum pulse magnitude, the average pulse magnitude, the pulse repetition rate for given pulse threshold can be derived from the φ-q-n distribution.

If this approach is adopted, the number of phase and magnitude windows should be significant in order to give reasonable and sufficient resolution. However, in such case a neural network would require very large calculation times in order to learn from φ-q-n patterns. This has been found to be very limiting and consequently the number of phase and magnitude windows are reduced to limit the required size of the ANN [134,138].

Alternatively, statistical operators such as skewness, kurtosis and correlation coefficient, obtained from the phase-resolved distribution using the conventional electrical detection, have been investigated as possible parameters for application to PD pattern recognition. If this approach is adopted, the scale of the input data for pattern recognition is reduced to a few values. In practice, a number of tests for each defect have to be carried out and several observations were made for the same type of PD source to estimate the statistical operators. For each of the statistical operators the mean value was calculated and used for pattern recognition [135].

For conventional electrical detection, electrical interference will influence the φ-q-n distribution and statistical operators. Before any pattern recognition can take place, the interference must be removed from the PD signals. This might be difficult especially when PD test was carried out in the field. For acoustic emission measurements interference is not a major problem due to the nature of this method. However, acoustic waves will attenuate during propagation through different materials and interfaces in a complex way. The statistical operators will vary significantly for different electric stresses, void sizes and test time (Chapter 4). Consequently the use of statistical approaches for PD pattern recognition using acoustic emission measurement data might be very difficult to realise.

5.3.2 Frequency components

The frequency spectra of acoustic emission signals have been used to characterise different partial discharge sources [41,42,105,141-143,147-150]. These studies indicate that the spectrum of an acoustical PD signal may include information about

the defect type, and the shape of the acoustical spectrum will not change significantly with variation in test conditions such as different test voltages.

Figure 5.6 shows the acoustic emission signal and power spectra for one voltage cycle. In this case, partial discharges were generated from two earth electrode-bounded voids, each with diameter of 2 mm and thickness of 0.2 mm. The sampling range of the A/D board is 1 MHz, at 50 Hz there are 20,000 data points for each voltage cycle. The frequency spectrum was obtained by Fourier transform, thus the frequency of interest lies in the first 500 KHz and consists of 10,000 points. If the whole time signal or the relevant frequency spectra for one voltage cycle were used as the ANN input parameter, it would be very time-consuming to train the network.

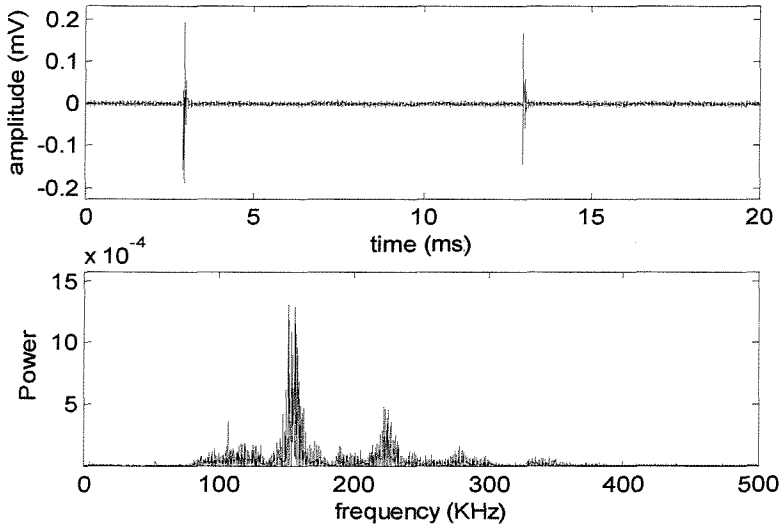

Figure 5.6 Acoustic emission signals and spectra for one voltage cycle

It has been demonstrated that the acoustic emission waveform alone and its relevant frequency spectrum i.e. the application of a Short-Duration Fourier Transform (SDFT) can fully represent the acoustic emission characteristics [98,105,141-143,148,150]. Consequently in this study SDFT of the acoustic emission waveform was used to train artificial neural networks. Figure 5.7 shows an acoustic emission signal and its spectrum obtained from FFT. The original signal was sampled at 1 MHz for 256 points, thus the spectrum of interest consists of 128 points. The frequency spectrum was normalised so that it varies over the same range, i.e. between 0 and 1, to minimise the influence of the absolute magnitude fluctuation on the neural network behaviour. Compared with Figure 5.6, the envelope of the frequency spectrum is not significantly different.

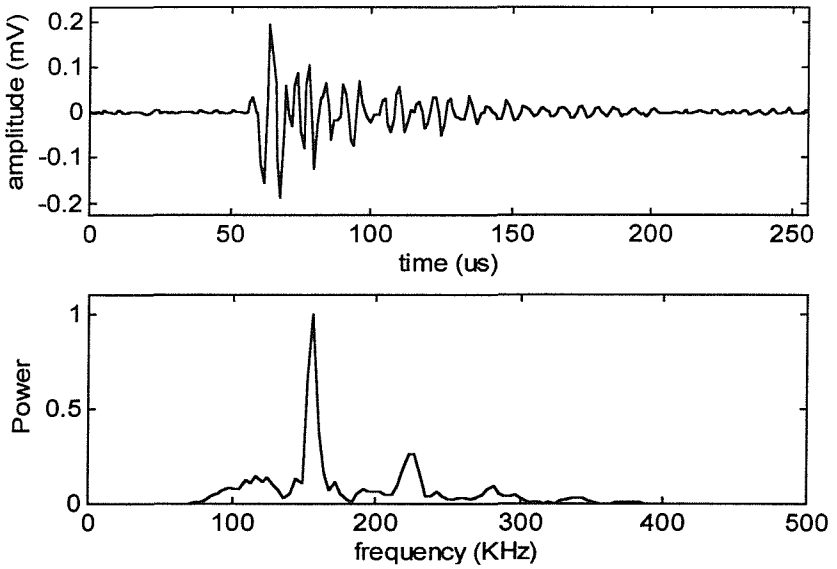

Figure 5.7 Acoustic emission waveform and normalised power spectrum

The influence of the applied voltage on the acoustic frequency spectrum has been investigated. Figure 5.8 shows the SDFT spectrum of an AE signal from an internal void with diameter of 2 mm and thickness of 0.2 mm stressed at 2.5 kv/mm to 5.5 kv/mm. Figure 5.9 shows the acoustic spectrum due to a partial discharge during electrical tree growth. The tungsten needle tip radius was 3μm and the distance between electrodes 3mm. These examples indicate that the acoustic emission frequency spectrum is fairly constant over a range of electric stress.

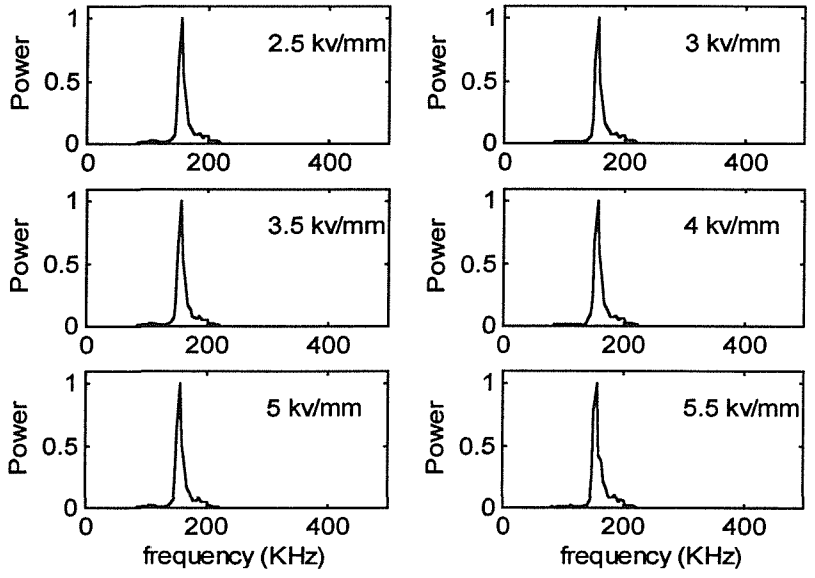

Figure 5.8 Influence of voltage on acoustic spectrum (void)

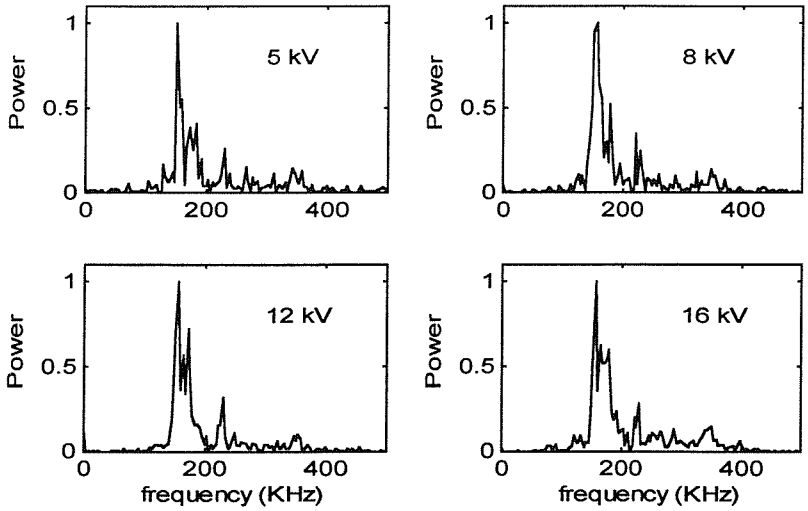

Figure 5.9 Influence of voltage on acoustic spectrum (electrical tree)

5.3.3 Wavelet decomposition coefficients

The first recorded mention of the term "wavelet" was in 1909, in a thesis by Alfred Haar. The concept of wavelet in its present theoretical form, however, was developed at the beginning of the 1980s and has attracted much interest in the field of speech and image processing. It has been applied to the PD detection [151,152], signal de-noising [153,154] and pattern identification [155,156].

To avoid mathematical complexity, only a brief introduction to the wavelet transform is given here, more details can be found in books by Chui [157] and Qin [158]. The continuous wavelet transform is defined as the sum over all time of the signal multiplied by scaled, shifted versions of the wavelet function Ψ:

$$W_f(a,b) = \int_{-\infty}^{+\infty} f(x)\psi_{a,b}(x)dx \tag{5.5}$$

Where the transform function

$$\psi_{a,b}(x) = |a|^{-1/2}\psi(\frac{x-b}{a}) \tag{5.6}$$

is known as the 'mother wavelet'.

For practical application, the discrete dyadic wavelet transform with $a=2^m$ and $b=n2^m$ (m,n are integers) is employed for speed and convenience. Thus the following transform function can be obtained:

$$\psi_{m,n}(x) = 2^{-m/2}\psi(2^{-m}x - n) \tag{5.7}$$

As a result of this processing, an approximation coefficient A and a detail coefficient D are obtained at each level of the decomposition. A reflects a low frequency content of the signal f(x), and D reflects a high frequency content (Figure 5.10). Whilst introducing the above described processing algorithm into subsequent stages following to the A component, a tree structure is obtained (Figure 5.11). From this point of view, the wavelet transform is in fact a changeable band-pass filter. Figure 5.12 shows an acoustic emission waveform decomposed to the fourth level by the wavelet transform. These decomposition coefficients may be used as the neural network training inputs. To minimise the influence of the absolute magnitude fluctuation on the neural network behaviour, all acoustic emission signals were scaled so that they varied over the same range, i.e. between 0 and 1, prior to applying the wavelet transform.

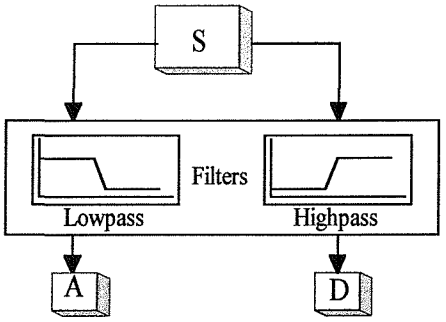

Figure 5.10 Wavelet decomposition at basic level

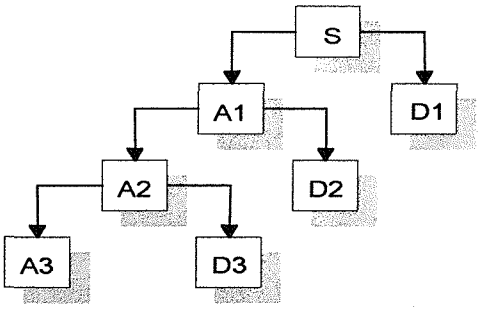

Figure 5.11 Tree structure of the wavelet decomposition process

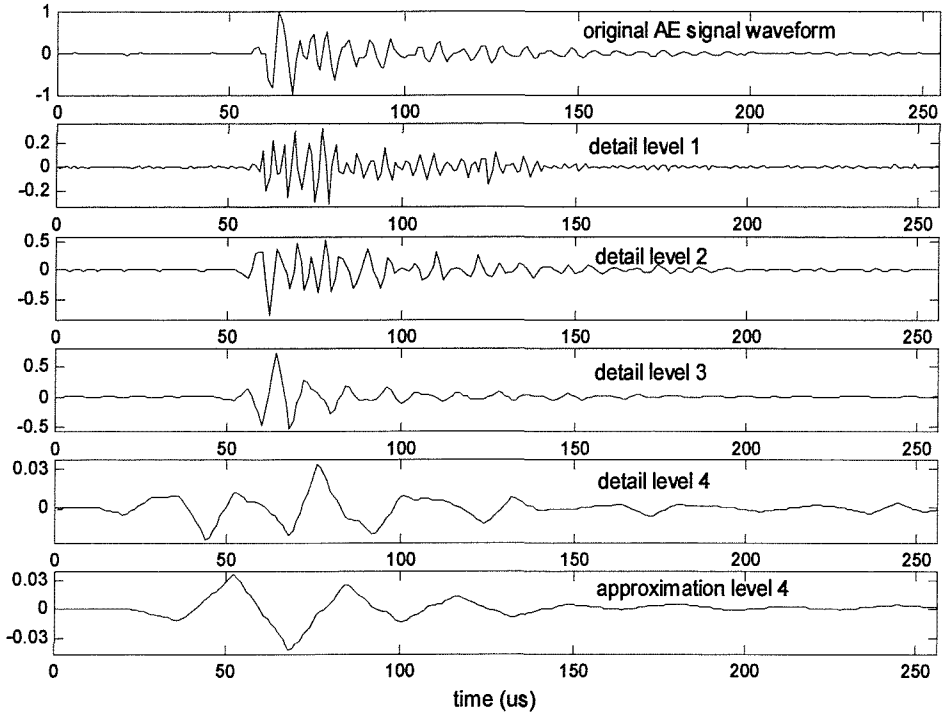

Figure 5.12 Wavelet decomposition of a practical acoustic emission signal

5.4 Applications of Artificial Neural Networks

5.4.1 Identification of different shapes of cavity

Three different shapes of cavity (Figure 5.13) have been used to generate PD activity. The voids were formed by a machined hole in a centre film having a thickness of 0.2mm or 1mm. Experimental arrangement A (flat cavity) consists of a sandwich of seven PE films, each with thickness of 0.2 mm. The centre film contains a hole with diameter of 2 mm. Configuration B (cylindrical cavity) consists of one middle PE film with thickness of 1 mm and two PE films each with thickness of 0.2 mm. The middle film has a hole with diameter of 1 mm. Configuration C (sharp cavity) consists of one middle PE film with thickness of 1 mm and two PE films each with thickness of 0.2 mm. The middle film has a hole with diameter of 0.3 mm. The fourth configuration D does not contain a void and was purely to ascertain that any background noise was not interpreted as PD activity by the artificial neural network.

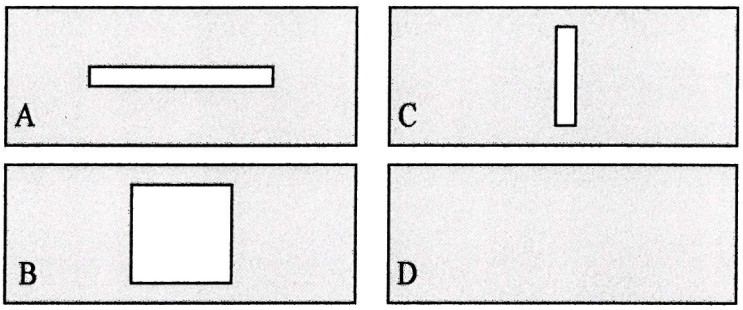

Figure 5.13 Different cavity shapes

Analysis of the frequency spectrum of the measured acoustic signals was undertaken in order to determine if void shape influenced the acoustic emission signal. The acoustic signal was sampled at 1 MHz for 256μs, thus the obtained frequency spectrum consisted of 128 points. Figure 5.14(a)-(d) and Figure 5.15(a)-(d) show the acoustic emission signals and relevant spectra for the four cases respectively. Experiments were carried out at the applied electric stress of 2.5 kV/mm. The frequency spectrum was normalised so that it varies over the same range, i.e. between 0 and 1, to minimise the influence of the absolute magnitude fluctuation on the neural network behaviour. For cavity shape A, the frequency spectrum is concentrated around 150 kHz, which is also the resonant frequency of the acoustic emission sensor. For cavity shape B, the spread

of the spectrum is increased and there are additional peaks at 100 kHz, 225 kHz and 350 kHz. For cavity shape C, there are more frequency peaks above 200 kHz. For noise D, the spectrum is at maximum around 0 Hz, and the frequency components cover the whole frequency range.

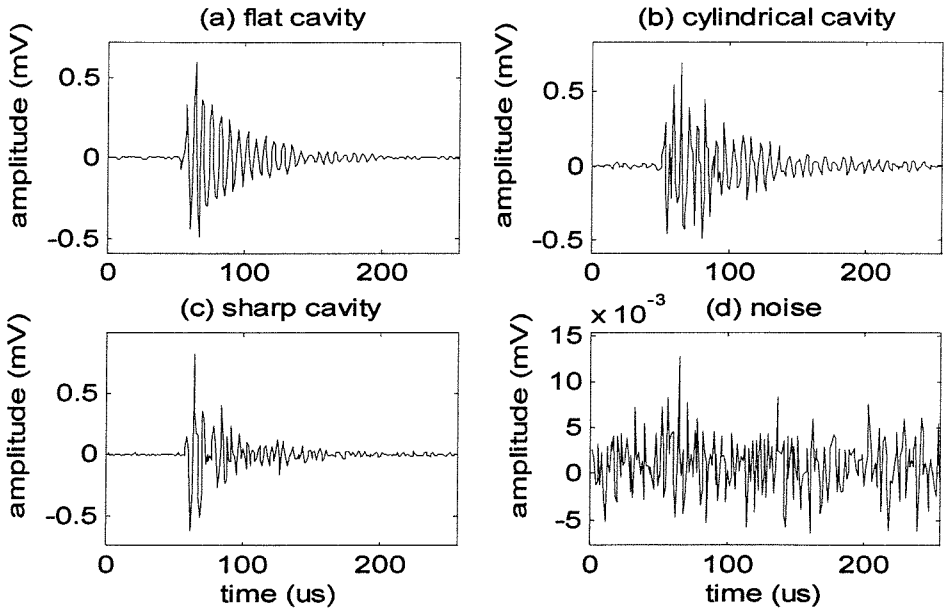

Figure 5.14 Acoustic emission signals for different shapes of cavity and noise

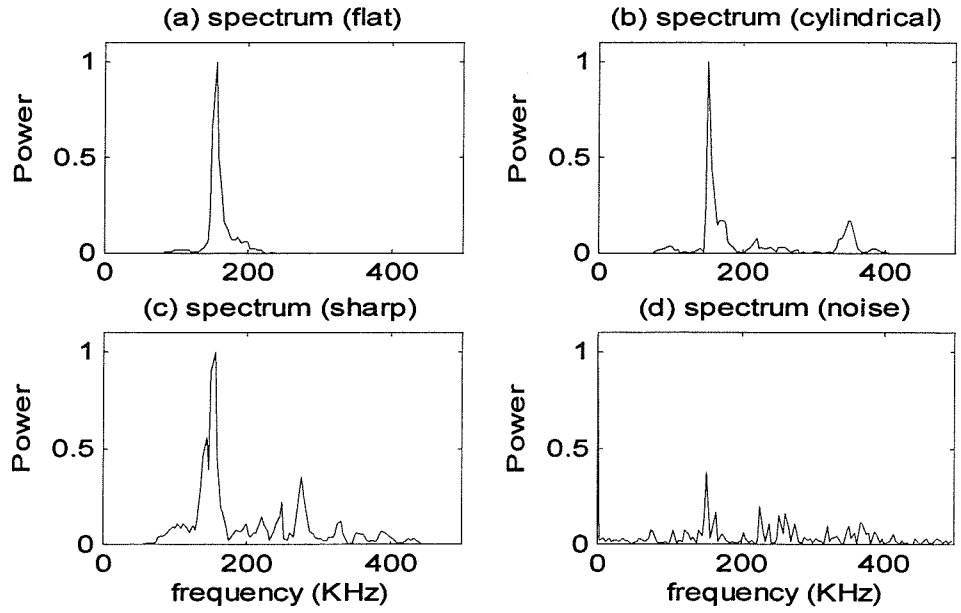

Figure 5.15 Acoustic emission spectra for different shapes of cavity and noise

Figure 5.16 shows the wavelet decomposition for the four acoustic emission signals as shown in Figure 5.14. In this case the acoustic emission signals were normalised before applying the wavelet transform. Using the same 256 data points and wavelet decomposition to the fourth level of detail creates a total of 253 input components for the ANN. The input components consist of 130 data points from the first level of detail, 67 from the second, 36 from the third and 20 from the fourth.

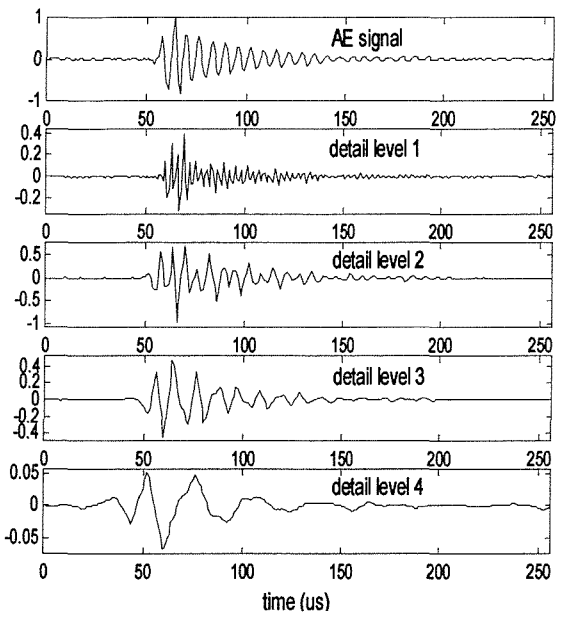

(a) flat cavity

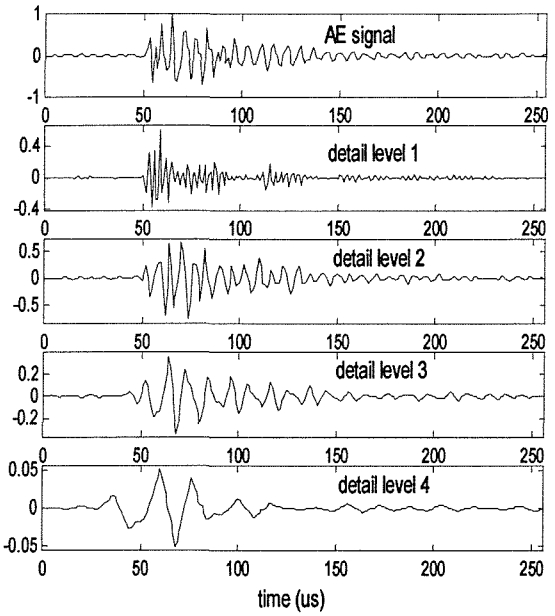

(b) cylindrical cavity

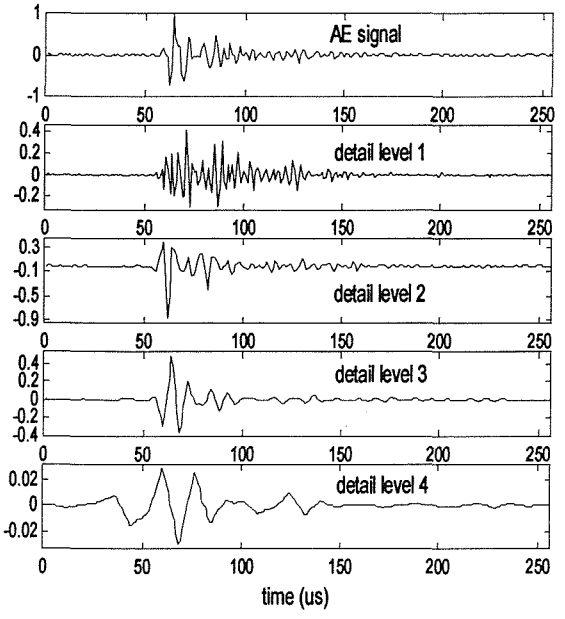

(c) sharp cavity

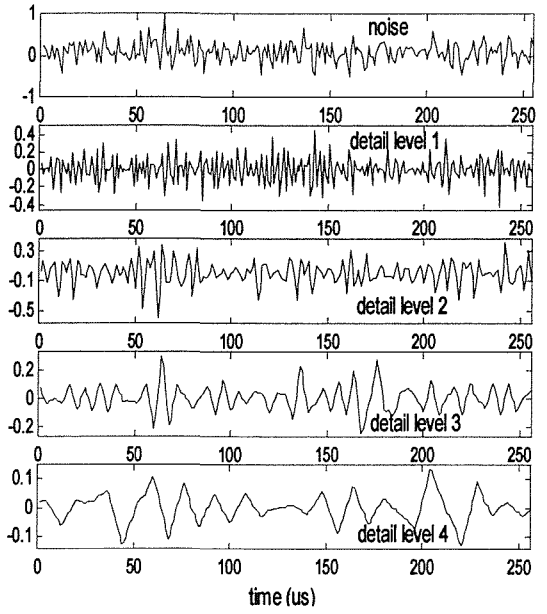

(d) noise

Figure 5.16 Wavelet decomposition for different shapes of cavity and noise

For both ANNs, 10 sets of each of the four different cases were used for training. A further 20 sets of each case were then used to test the ANN. In this case, for the BP ANN, the number of processing elements in the hidden layer was 10 and the convergence criterion was 0.01. There are 4 elements in the output layer, corresponding to the four different arrangements. When SDFT components (128 elements) were used as the ANN input vector, the correct identification rate was 97.5% (Figure 5.17). This indicates that 78 out of 80 sets of test data were correctly recognised. Table 5.1 gives an example of the ANN outputs that correspond to the four patterns.

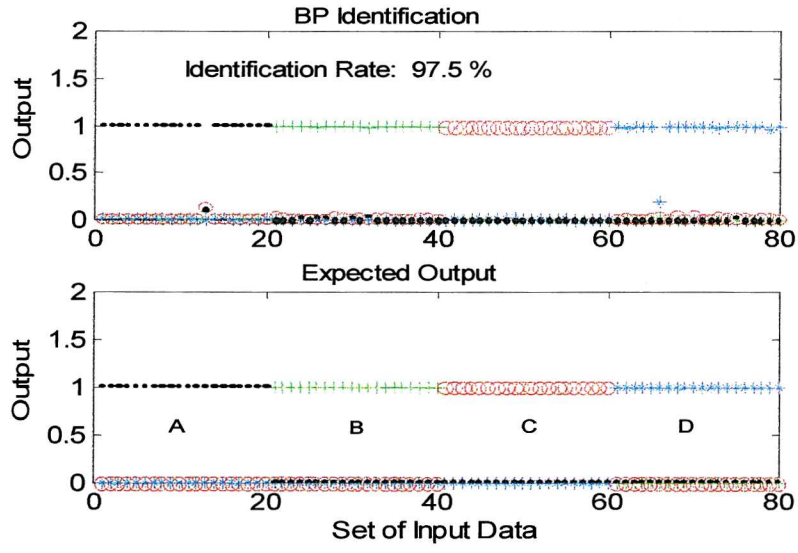

Figure 5.17 BP identification result using SDFT components as input

Table 5.1 BP outputs corresponding to different cavity shapes and noise

	A	B	C	D
Output 1	**0.9900**	0.0080	0.0014	0.0080
Output 2	0.0128	**0.9818**	0.0057	0.0005
Output 3	0.0000	0.0140	**0.9910**	0.0044
Output 4	0.0053	0.0027	0.0087	**0.9693**

If the wavelet decomposition components (253 elements) were used as the BP ANN input vector, the correct identification rate dropped to 91.25% (Figure 5.18). Seven out of 80 were either wrongly recognised or unrecognised (not satisfying the selection criteria described in section 5.2.1). Further analysis of the result indicates that the

reduction of the identification rate is caused by the improper recognition of background noise from the other three cases. The wavelet decomposition of the noise cannot distinguish itself from the wavelet decomposition of three types of AE signals.

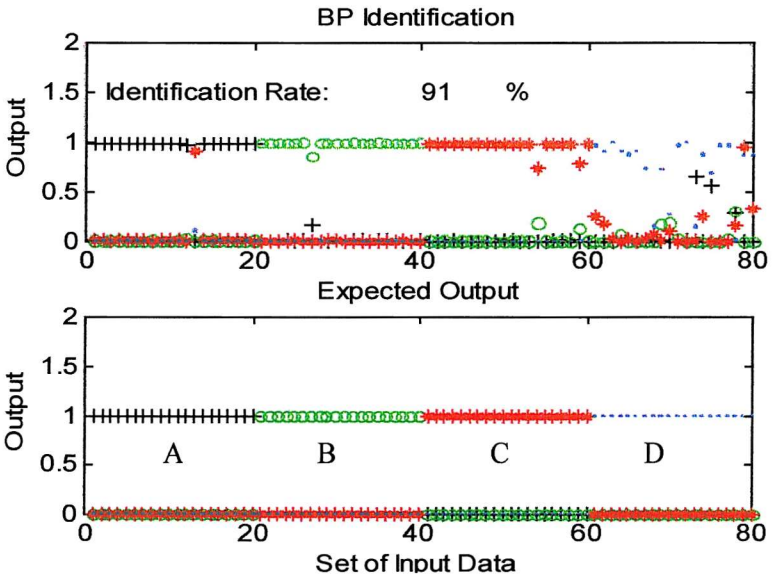

Figure 5.18 BP identification using wavelet decomposition as input

For the LVQ neural network, there were two processing elements for each of the four classes in the Kohonen layer and the number of training cycles was 2000. When the SDFT spectrum (128 elements) were used as the LVQ ANN input vector, the correct identification rate was 100%. If the wavelet decomposition (253 elements) were used as the LVQ ANN input vector, the correct identification rate was 95%. This indicates that 76 out of 80 sets of data were correctly recognised.

The number of elements in the hidden or Kohonen layer influences the overall performance of the ANN. Table 5.2 summarises the obtained identification rates for a range of ANN with different numbers of elements in the hidden or Kohonen layer. Overall, the identification results are good; it is possible to obtain an identification rate of 100%. For both ANNs, using SDFT as the input data obtains a better identification rate than using the wavelet decomposition coefficients. For BP network with SDFT inputs, the best result is 100% when the number of processing elements in the hidden layer is either 6 or 20; For BP network with wavelet inputs, the best result is 92.5% when there are 30 elements in the hidden layer. For the LVQ network with SDFT inputs, the identification rate is 100% for the range of processing elements in the

Kohonen layer; For the LVQ network using wavelet inputs, however, the correct identification result decreases with the increasing size of the Kohonen layer. Generally the LVQ neural network outperforms the BP neural network.

Table 5.2 Influence of number of processing elements in the hidden or Kohonen layer

BP artificial neural network		
Hidden layer processing elements	SDFT input data identification rate	Wavelet decomposition input data identification rate
6	100% (80/80)	85% (68/80)
10	97.5% (78/80)	91.25% (73/80)
20	100% (80/80)	88.75% (71/80)
30	98.75% (79/80)	92.5% (74/80)
40	98.75% (79/80)	87.5% (70/80)
LVQ artificial neural network		
Kohonen layer elements per output	SDFT input data identification rate	Wavelet decomposition input data identification rate
1	100% (80/80)	97.5% (78/80)
2	100% (80/80)	95% (76/80)
3	100% (80/80)	92.5% (74/80)
4	100% (80/80)	86.25% (69/80)
5	100% (80/80)	81.25% (65/80)

For the LVQ neural network the identification rate is also dependent on the number of training cycles used. This has been investigated using 8 processing elements in the Kohonen layer (Table 5.3). When the SDFT data is used as the LVQ inputs, the correct rate remains 100% regardless of the number of training cycles. When Wavelet decomposition is used as input, the number of training cycles slightly influence the identification rate and best result is obtained when 2000 training cycles are used.

Table 5.3 Influence of number of training cycles on the identification of LVQ network

Number of training cycles	SDFT input data identification rate	Wavelet decomposition input data identification rate
1000	100% (80/80)	91.25% (73/80)
2000	100% (80/80)	95% (76/80)
4000	100% (80/80)	92.5% (74/80)
8000	100% (80/80)	90% (72/80)

Table 5.4 shows the influence of the number of training sets of data used on the overall identification rate for both neural networks. For every case a further 20 sets of each output were used to test the ANN. The BP neural network has 10 elements in its hidden layer, whereas the LVQ neural network has two elements per output within the Kohonen layer. When SDFT data is used as the BP network inputs, increasing the number of training sets does not improve performance. When Wavelet decomposition data is used as the BP network inputs, increasing the training sets slightly improves the performance. When SDFT data is used as the LVQ network inputs, the identification rate remains 100% regardless of the number of training sets. When Wavelet decomposition data is used as the LVQ inputs, increasing the training sets slightly improves the overall performance.

Table 5.4 Influence of number of training sets on identification for both ANNs

Number of training sets	BP neural network		LVQ neural network	
	SDFT input	Wavelet input	SDFT input	Wavelet input
5	98.75% (79/80)	83.75% (67/80)	100% (80/80)	76.25% (61/80)
10	97.5% (78/80)	91.25% (73/80)	100% (80/80)	95% (76/80)
15	97.5% (78/80)	92.5% (74/80)	100% (80/80)	97.5% (78/80)
20	98.75% (79/80)	93.75% (75/80)	100% (80/80)	97.5% (78/80)

5.4.2 Identification of different locations of void or voids

Acoustic emission signals due to partial discharges from void or voids at different locations, have been investigated using the planar model. The experimental arrangements were as shown in Figure 5.19. They include one internal void (E), two internal voids (F), one hv-bounded void (G), two hv-bounded voids (H), one earth-

bounded void (I), two earth-bounded voids (J), and no void (K). All arrangements consist of seven PE films, each with thickness of 0.2 mm. The diameter of a void is 2 mm.

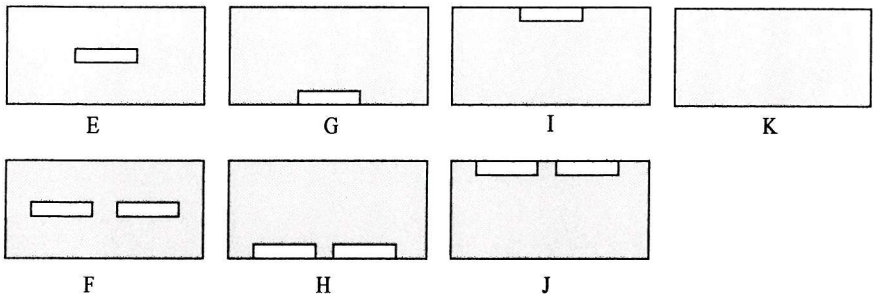

Figure 5.19 Arrangement of different void (s) positions

The short-duration Fourier transform of the measured acoustic signals were investigated. The acoustic signal was sampled at 1 MHz for 256 μs, thus the obtained frequency spectrum consisted of 128 points. Figure 5.20 (e)-(j) show the SDFT for the six cases with void(s). The frequency spectrum was normalised so that it varies over the range 0 to 1.

Apart from the SDFT spectrum analysis, wavelet decomposition was also applied to identify the seven patterns using two artificial neural networks. For both arrangements of ANN, 10 sets of each of the seven different cases were used for training. A further 20 sets of each case were then used to test the ANN. In this case, for the BP network, the number of processing elements in the hidden layer was 10 and the convergence criterion was 0.01. There are seven elements in the output layer, corresponding to the seven different arrangements. For the LVQ network, there were 14 processing elements in the hidden or Kohonen layer (2 for each output pattern) and the number of training cycles was 4000. The input layer of both ANNs has either 128 or 253 elements depending on whether SDFT data or wavelet decomposition data is used as the input vector. The identification results are given in Table 5.5. The results indicate that, for this case, the BP network with SDFT data as the input vector obtains the best identification result (Figure 5.21). The identification rates might be further increased by adjusting the number of processing elements in the hidden or Kohonen layer, the number of training cycles, or the number of training sets, as investigated in 5.4.1.

Table 5.5 Identification results of identifying void(s) positions and noise

	SDFT input data identification rate	Wavelet decomposition input data identification rate
BP network	97.14% (136/140)	87.86% (123/140)
LVQ network	81.43% (114/140)	87.14% (122/140)

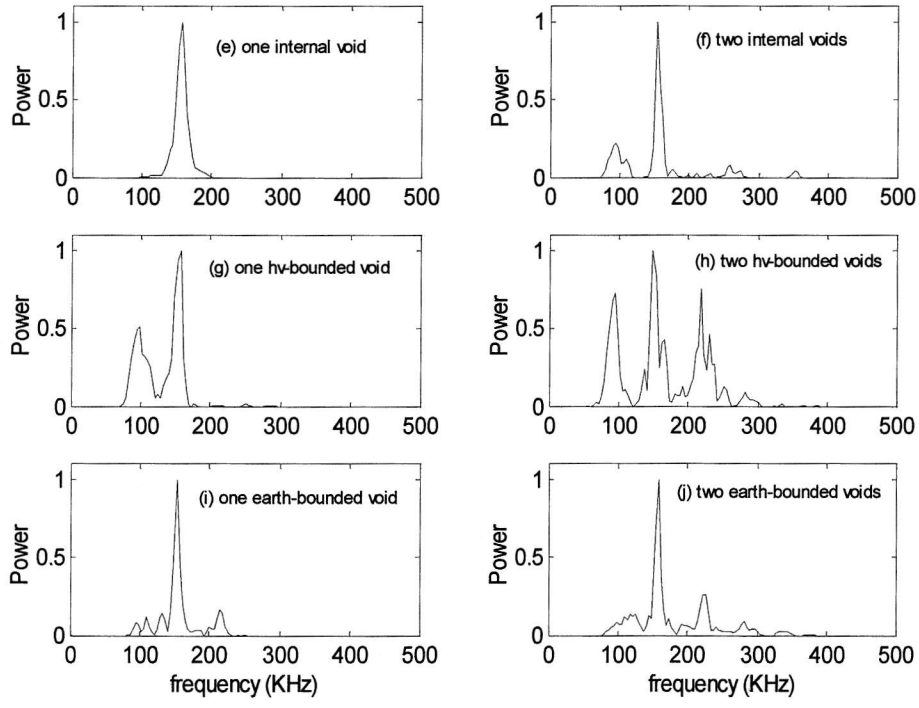

Figure 5.20 SDFT spectrum for different void(s) location(s)

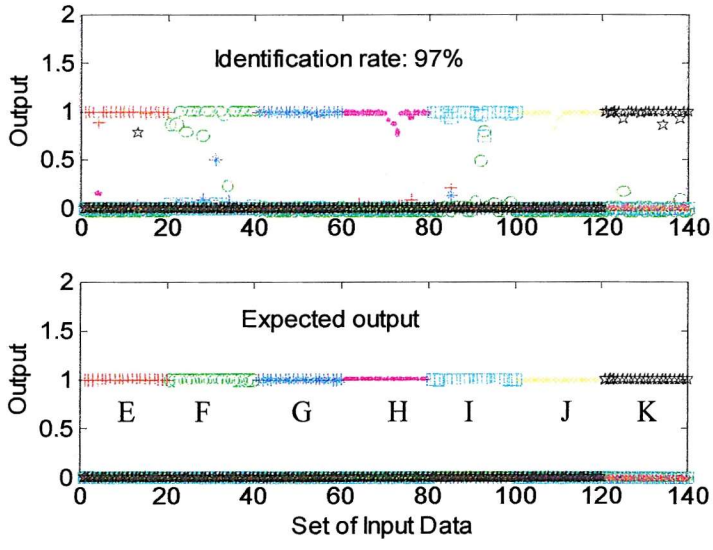

Figure 5.21 BP identification result (SDFT data as input)

5.4.3 Identification of void and electrical tree PD activity

The BP and LVQ neural networks were also used to identify the differences between partial discharges due to void(s) or due to electrical treeing, using the acoustic emission technique. Figure 5.22 shows the experimental model to produce treeing discharges. Figure 5.23 and 5.24 show the short duration Fourier transform and the wavelet decomposition of an acoustic emission signal from a treeing discharge.

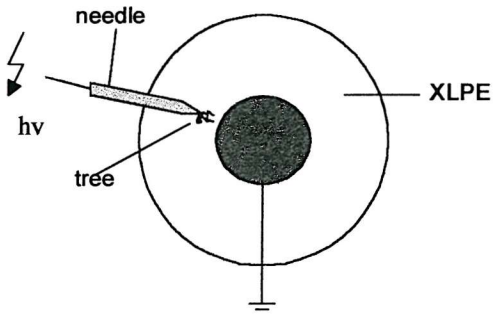

Figure 5.22 Experimental model to generate treeing discharges

Five of the void models covering different void shape and location, i.e. void A, B, C, G, I shown in Figures 5.13 and 5.19, were used to represent typical PD voids. For both arrangements of ANN, two sets of data for each of the five void cases (ten in all), ten sets of discharge data due to electrical treeing and ten sets of background noise were used for training. A further 20 sets of void data (4 for each void model), 20 sets of treeing data and 20 sets of background noise were then used to test the ANN. In this case, for the BP network, the number of processing elements in the hidden layer was 10 and the convergence criterion was 0.01. There are three elements in the output layer, corresponding to the void, treeing and noise respectively. For the LVQ network, there were 6 processing elements in the Kohonen layer (2 for each output pattern) and the number of training cycles was 4000. The input layer of both ANNs has 128 elements if the SDFT spectrum was used as the input vector and 253 elements if the wavelet decomposition data was used as the input vector. The identification results are given in Table 5.6. In this case the best identification rate is 93.33%, indicating that 56 out of 60 testing sets were recognised correctly. The identification rates might be further increased by adjusting such as the number of processing elements in the hidden or Kohonen layer, the number of training cycles, or the number of training sets, as investigated in 5.4.1.

Table 5.6 Identification of void discharge, treeing discharge and noise

	Identification rate SDFT input	Identification rate Wavelet decomposition input
BP network	93.33% (56/60)	76.67% (46/60)
LVQ network	91.67% (55/60)	80% (48/60)

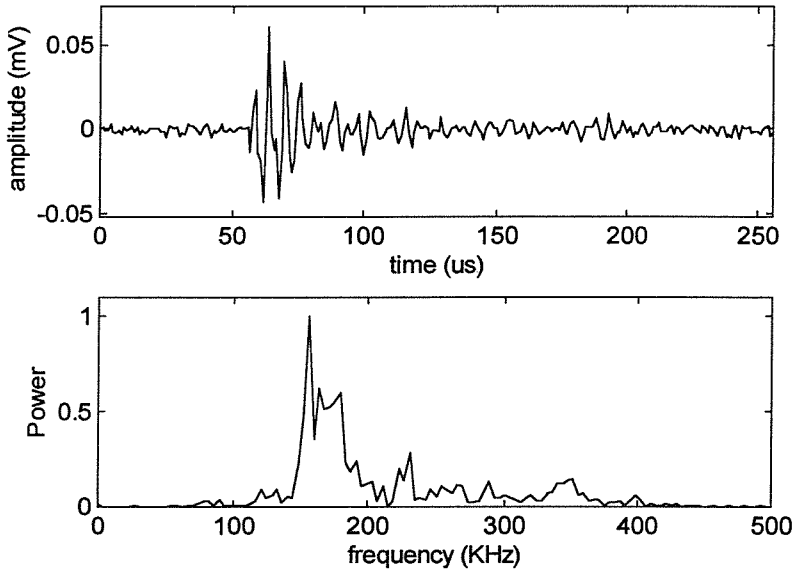

Figure 5.23 Short-duration Fourier transform of an AE signal due to electrical tree

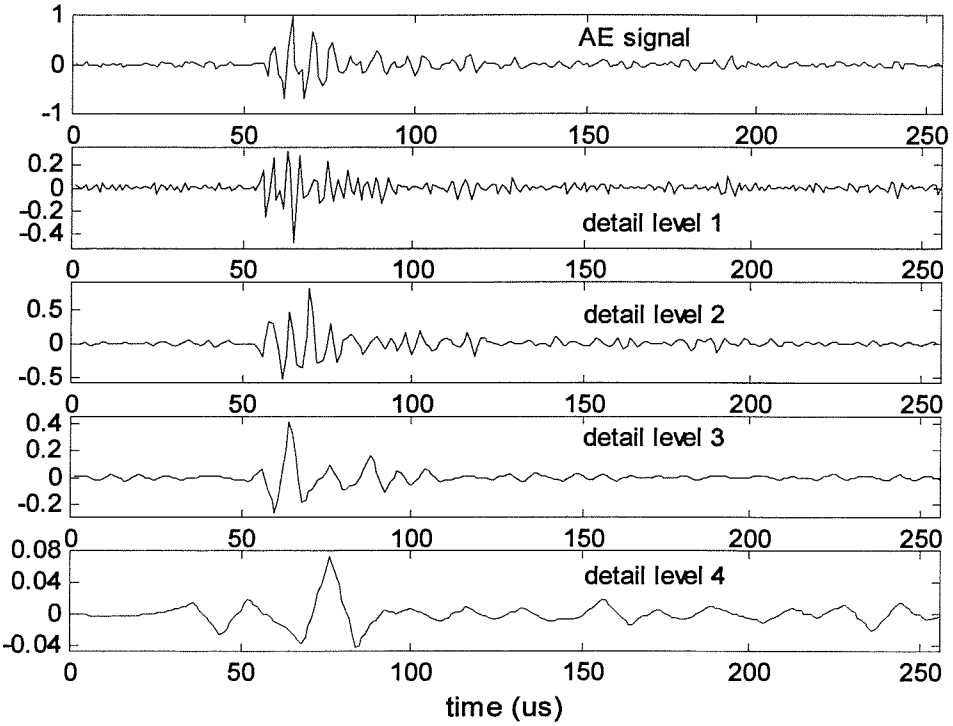

Figure 5.24 Wavelet decomposition of an AE signal due to electrical tree

5.5 Summary

The application of artificial neural networks to partial discharge pattern identification has been investigated. Both the multi-layer feed forward neural network using the back propagation algorithm and the Kohonen self-organising map neural network using the learning vector quantization algorithm were used to recognise PD patterns.

The choice of the input parameter for ANNs is important where pattern identification is concerned. The input parameter should be able to fully represent different patterns in an effective way. The frequency spectrum obtained by short duration Fourier transform (SDFT) of the acoustic emission signal was used as a possible ANN input parameter. One advantage of this approach is that spectrum is less influenced by the applied voltage compared with the use of φ-q-n three dimensional statistical distributions or statistical operators such as skewness and kurtosis. Apart from the Fourier transform, an acoustic emission signal can also be decomposed into a few detailed levels through the use of the wavelet transform. As the ANN input vector, the SDFT data consists of 128 components whereas wavelet decomposition data consists of 253 components (when decomposed into fourth level). Size of input vectors is important as it affects the time required for the ANN to be trained. To increase the reliability of the obtained identification results, additional judging criteria were defined for the BP neural network.

The BP and LVQ neural networks, with SDFT spectrum or Wavelet decomposition coefficients as input vectors, were initially applied to identify between PD acoustic emission signals produced from different cavity shapes. Results indicate that a different shape of cavity produces different frequency spectra and wavelet decomposition components. The obtained results are impressive and 100% correct identification rate can be obtained when using SDFT input data for both ANNs. The identification rate is lower if the wavelet decomposition data is used as the ANN input, as the wavelet components of the noise cannot be clearly distinguished from those of the true PD signal. The performance of ANNs are influenced by the number of processing elements in the hidden or Kohonen layer, the number of training cycles and number of training sets, the effects of these parameters have been investigated.

The two ANNs with SDFT spectrum or Wavelet decomposition as input vectors were then used to identify PD acoustic emission signals produced from different location of single or multiple void(s). During the ANN testing 136 out of 140

testing sets of data (20 for each case) can be correctly identified. Finally both ANNs were used to distinguish signal patterns due to void, electrical tree or noise. Different shapes and locations of voids were used to represent the void pattern. The obtained results are also good and 56 out of 60 sets of testing data can be correctly identified.

The required time for the ANN training tends to be longer for a more complicated network structure, for example ANN with more input vectors, more processing elements in the hidden layer, and a great number of output patterns. The increase in the number of training sets of data and training cycles also increases the training time. For all the cases investigated in this chapter, the maximum required time for training is less than two minutes using a Pentium II 233 MHz computer. It takes much less time for the neural networks to classify than to be trained.

The performance of both neural networks, using the SDFT components or the wavelet decomposition coefficients, for classifying different partial discharge experimental conditions is very encouraging. However, for practical conditions, partial discharge patterns are much more complicated than the experimental model data and several discharge sources may co-exist. It seems that the only way to build a comprehensive and effective PD pattern identification system for a cable system is to collect as much information as possible, not only from experimental models but also from practical cable systems containing known defects. Results obtained indicate that it might be possible to build a PD on-line detection and identification system by applying acoustic emission techniques with artificial neural networks.

Chapter 6

PD Detection Using A Capacitive Coupler

6.1 Introduction

This chapter describes the development of a capacitive coupler approach to partial discharge detection. The design of the capacitive coupler is described. A network model has been established to simulate the coupler and to investigate the influence of the coupler stray capacitance and resistance. The influence of coupler dimension, sensor materials and patch types on the capacitive coupler performance have also been investigated.

Capacitive couplers were applied to detect partial discharges from a cable section having water terminations. The location of the PD site was studied using two couplers and evaluating the time of flight.

An alternative PD test method for cable/joint system is detailed. This method reduces the demand on power supply of the test system but requires a gap within the cable semicon screen. The influence of such an insulation gap on the capacitive coupler signal attenuation has been investigated. The effect of a gap was modelled using the equivalent circuit. The frequency response of a capacitive coupler placed after an insulation gap was also studied (section 6.4). A cross correlation algorithm

was implemented to automatically estimate the time of flight between different coupler output signals. Finally the calibration of the capacitive coupler signal to a discharge quantity in pico-coulombs has been investigated.

6.2 The Capacitive Coupler

6.2.1 Fundamental design

A capacitive coupler was incorporated into a 66 kV XLPE-insulated cable, as shown in Figure 6.1. 100 mm (D) of cable metal sheath was removed, and tin tape with diameter of 40 mm (D2) was wrapped around the cable outer semicon layer. D1 is the distance between the tape and the cable sheath. This design does not effect the insulation system because the high-potential electrode of the coupler is attached on top of the semicon screen that serves as the power frequency ground, leaving the internal field distribution of the cable unaffected. The high frequency ground, however, is defined by the metal sheath of the power cable, due to the limited conductivity of the semiconducting polyethylene.

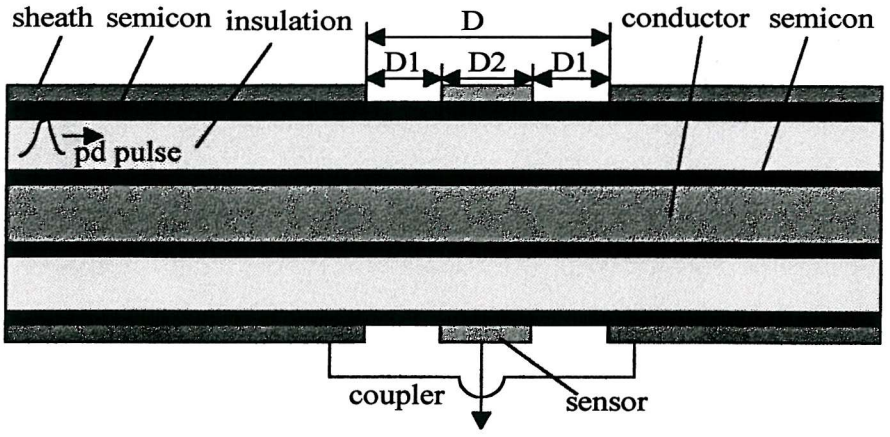

Figure 6.1 Schematic diagram of the capacitive coupler

6.2.2 A network model for the capacitive coupler

To better understand the principle of the capacitive coupler and to investigate the influence of the stray capacitance and the impedance between the coupler sensor and the cable sheath, a simple network model for a cable capacitive coupler has been developed (Figure 6.2). In this case V1 is a HP® 8082A pulse generator generating a

step wave with transition time of less than 1ns; T1 simulates a 1m long 66 kV XLPE cable section with a characteristic impedance of Z_0; T2 simulates a 1.6m long cable section with a characteristic impedance of Z_0; C1 is the distributed capacitance of the coupler between the metal tape and the cable core; L1 is the distributed coupler inductance; C2 is the coupler stray capacitance; R3 is the impedance between the coupler sensor and the cable sheath, which depends on the resistance of the semicon layer; R2 is the detection impedance, which is the input impedance of the measuring instrument. In this case, a Tektronix digital oscilloscope with input impedance of 50 Ω was used as the measuring instrument. R1 is the matching impedance with a value of Z_0, to minimise any reflections at the cable end.

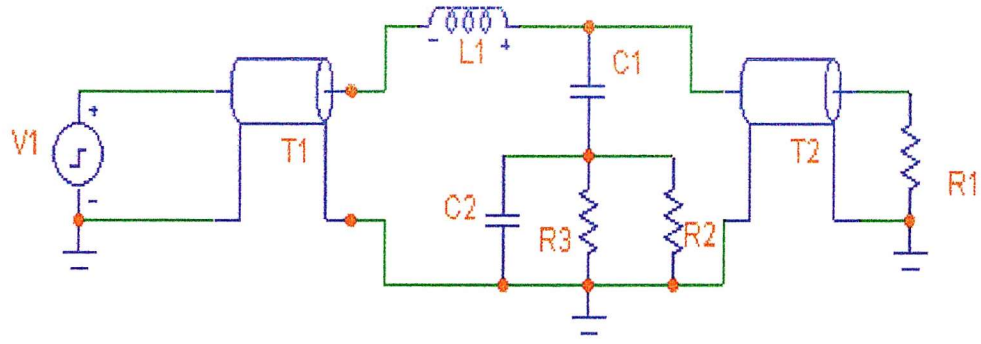

Figure 6.2 A network model for the capacitive coupler

Capacitance per meter of cable C_0, inductance per meter of cable L_0, and the cable characteristic impedance Z_0 can be calculated using the following equations:

$$C_0 = \frac{2\pi\varepsilon_0\varepsilon_r}{\ln(D_i / D_c)} \tag{6.1}$$

$$L_0 = \frac{\mu_0}{2\pi}\ln(D_i / D_c) \tag{6.2}$$

$$Z_0 = \sqrt{L_0 / C_0} \tag{6.3}$$

Where D_i is the diameter of the insulation (excluding the thickness of the cable outer semicon screen); D_c is the diameter of the conductor (including the thickness of the inner semicon screen); ε_0 is the dielectric constant in vacuum, which is 8.85 pF/m; ε_r is the relative dielectric constant of the insulation material; μ_0 is the permeability in vacuum, which is $4\pi\times10^{-7}$ H/m.

For the cable, D_i is 660 mm, D_c is 300 mm, and ε_r is 2.3 for XLPE. Consequently the capacitance per meter of cable C_0 is calculated to be 162 pF/m, the inductance per meter of cable L_0 is 0.158 μH/m and the cable characteristic impedance Z_0 is 31 Ω.

Using the model the influence of the impedance R3 and the coupler stray capacitance C2 have been investigated. Obtained results are shown in Figure 6.3. Figure 6.3(a) indicates that the magnitude of the coupler output increases with the increase of the impedance between the coupler sensor and the cable sheath. However, the influence is not significant if R3 is greater than 2 kΩ. Figure 6.3(b) indicates that the magnitude of the coupler decreases and the falling time of the waveform increases with the increase of the coupler stray capacitance.

6.2.3. Practical performance of the capacitive coupler

The influence of coupler dimension on output signal magnitude has been investigated, using a step wave from a pulse generator with rise time of 1 ns and magnitude of 2 V. The coupler output was directly connected to a Tektronix digital scope with a 50 Ω matching impedance.

Figure 6.4 shows the relationship between the coupler output magnitude and the length of the coupler sensor (D2), when the distance between the coupler sensor (tin tape) and the cable sheath D1 has a constant value of 30 mm. The result indicates that the coupler output magnitude increases with the increase of the sensor length. This can be verified by the simulation model (Figure 6.2). C1 increases and its relevant impedance decreases with the increase of the sensor length. Consequently the coupler output magnitude increases.

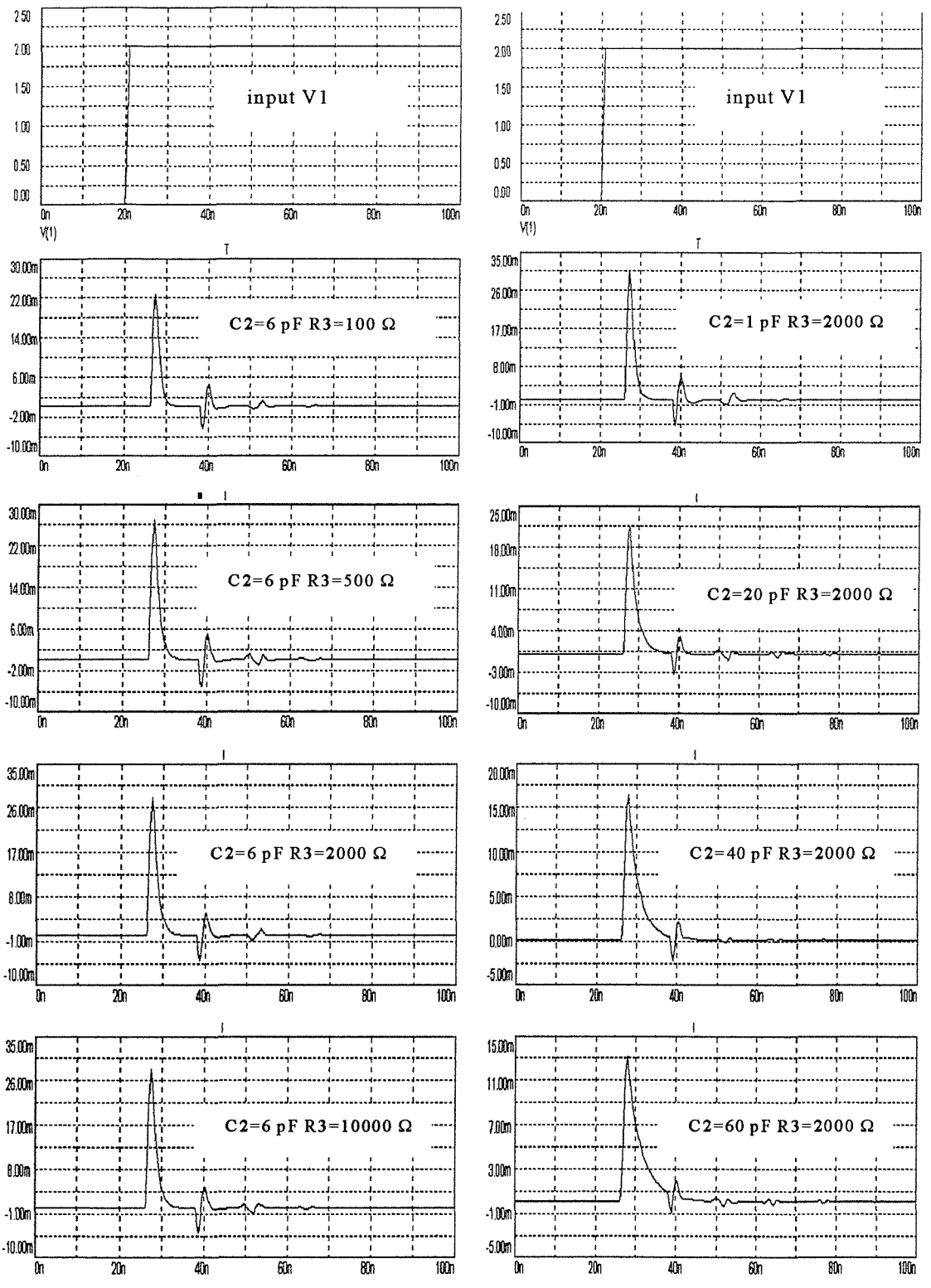

(a) Influence of impedance R3 (b) Influence of stray capacitance C2

Figure 6.3 Influence of the coupler stray capacitance and impedance

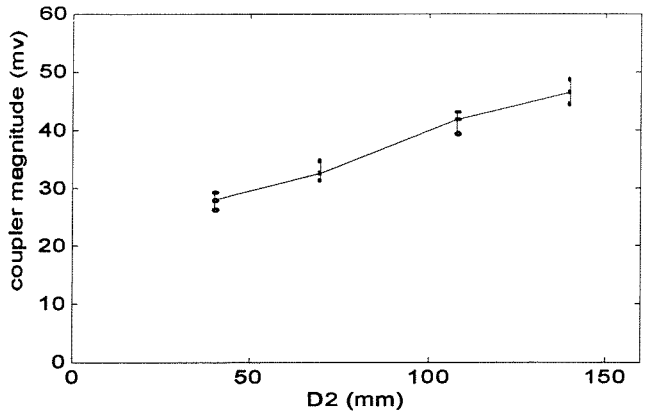

Figure 6.4 Coupler magnitude against coupler dimension D2 (D1 is constant)

Figure 6.5 shows the relationship between the coupler output magnitude and the length of sensor D2, if the length of the whole sheath break (D) is constant. When D2 is increased, the coupler output magnitude should increase. However, on the other hand, the decrease of D1 causes a decrease in the stray impedance and an increase of the stray capacitance. This in turn decreases the coupler output magnitude according to the simulation model. The accumulative effect causes a decrease in the coupler output magnitude.

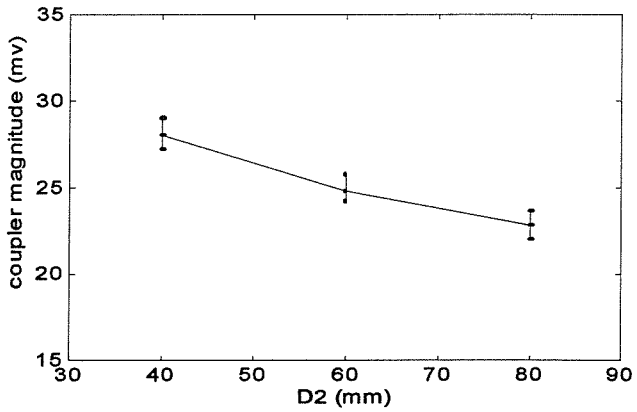

Figure 6.5 Coupler magnitude against coupler dimension D2 (D is constant)

The coupler output magnitude and waveform are very similar for the two different sensor materials (tin and aluminium) that were tested, as shown in Figure 6.6. The output magnitude for the aluminium sensor is only slightly higher (28.4 mV) than the tin sensor (28.1 mV).

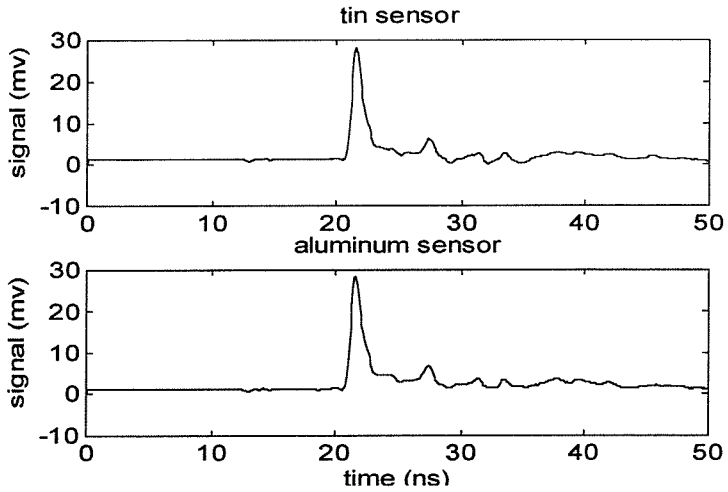

Figure 6.6 Coupler waveform for different sensor materials

Figure 6.7 shows the coupler outputs when the coupler sensor covers whole, half or a quarter of the exposed cable outer semicon periphery respectively. Results indicate that a patch type of coupler sensor can still provide a reasonably good result.

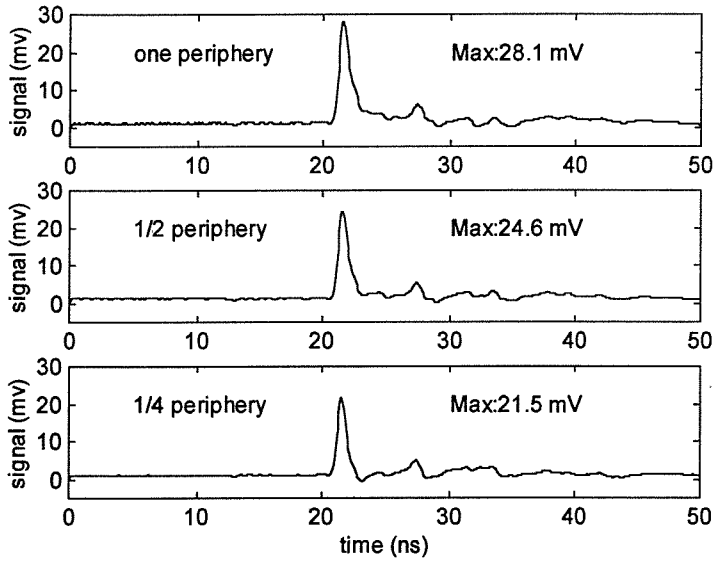

Figure 6.7 Coupler outputs vs. different sensor parameters

The frequency spectrum of the capacitive coupler was also investigated, as shown in Figure 6.8. The frequency spectrum was obtained using the Fast Fourier Transform (FFT). The frequency components extend throughout the whole frequency range of 500 MHz.

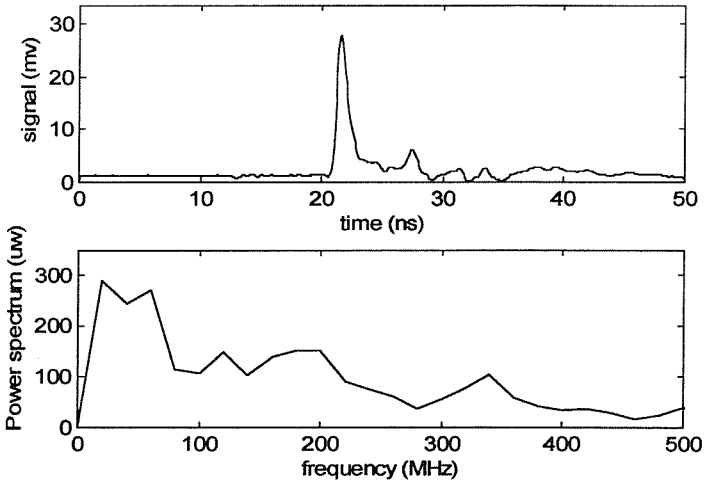

Figure 6.8 Coupler signal and spectrum

6.3 Application of Capacitive Coupler to PD Detection within a Cable Section

Capacitive couplers were applied to partial discharge detection for an 11 kV XLPE cable loop having water terminations. It should be noted that the water terminations were manufactured many years ago and according to the supplier were not partial discharge free. The experimental set-up is shown in Figure 6.9.

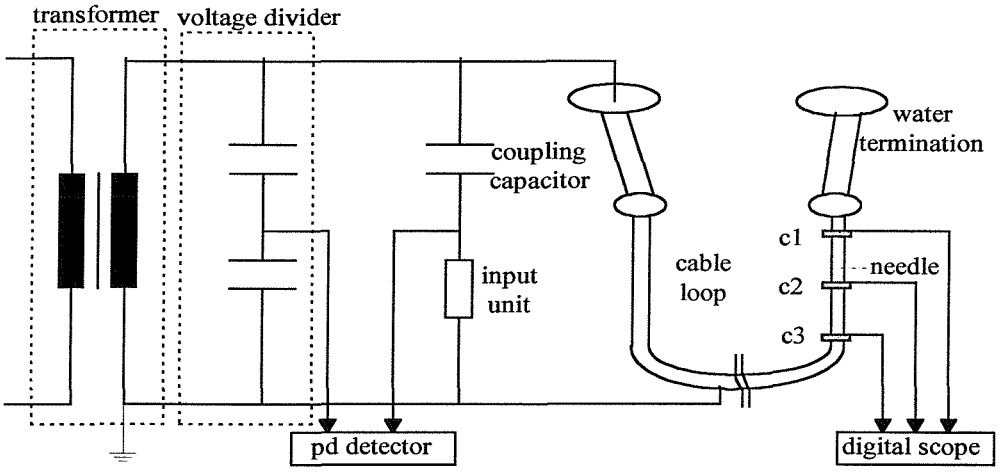

Figure 6.9 Arrangement of PD detection for a cable loop

The cable loop was approximately 15 m long. Coupler 1 is 0.3 m from the bottom of the water termination. The distances between coupler 1 and 2, coupler 2 and 3 are both 1.2 m. To construct the coupler, a 100 mm length of cable metal sheath was removed and tin tape 40 mm wide was wrapped around the whole periphery of the cable semicon screen.

At first, the PD pulse travelling speed along the cable was investigated. A step wave with a peak value around 2V and a rising time of 1ns was directly injected into coupler 1. The outputs from coupler 2 and 3 are shown in Figure 6.10. The time of flight between coupler 2 and 3 is 7.1ns. Therefore, the travelling speed of the injected pulse in the cable is calculated to be 0.17 m/ns.

A PD conventional test was performed using IEC 270 detection. Partial discharge occurred when the voltage was increased to 17 kV, with a discharge level of around 5 pC. Figure 6.11 shows the coupler 1 and coupler 2 output signals. Coupler 1 leads coupler 2 with a time of flight 7.1 ns which corresponds with the distance between coupler 1 and 2. It was believed that the partial discharges came from within the water termination.

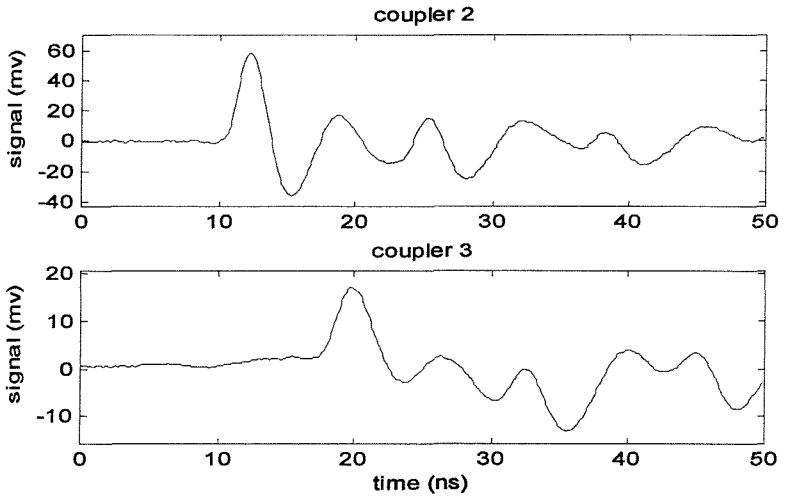

Figure 6.10 Time of flights of two couplers

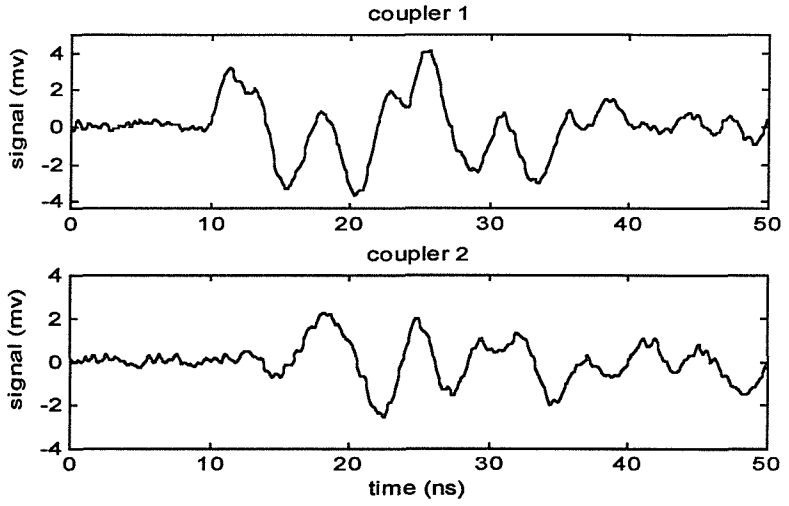

Figure 6.11 Coupler outputs due to a PD within the water termination

In order to produce PDs from the cable section rather than from the water termination, a sharp needle was punched into the cable insulation between coupler 1 and 2 (0.3 m to coupler 2 and 0.9 m to coupler 1). The needle was then pulled out and silicon grease was injected into the hole. The void that was left at the hole head acted as the PD source. In this case the PD inception voltage was 10 kV and the discharge level was

less than 3 pC. Figure 6.12 shows the coupler signals relating to this partial discharge. The discharge pulse arrives at coupler 2 first, coupler 1 second, and coupler 3 last. This indicates that the PD site is somewhere between coupler 1 and 2. By considering both the distance between coupler 1 and 2, and the time of flight between the two couplers, the PD site can be accurately located. Figure 6.13 shows the coupler frequency spectrum. The frequency components range to 400 MHz.

To study the influence of the metal sheath (wrapped foil in this case), which acts as the high frequency earth, on the coupler output magnitude, the foil between coupler 1 and the needle site was removed for 0.8 m. The coupler 1 output magnitude is attenuated by about 40% (from 5.1 mV to 3.1 mV).

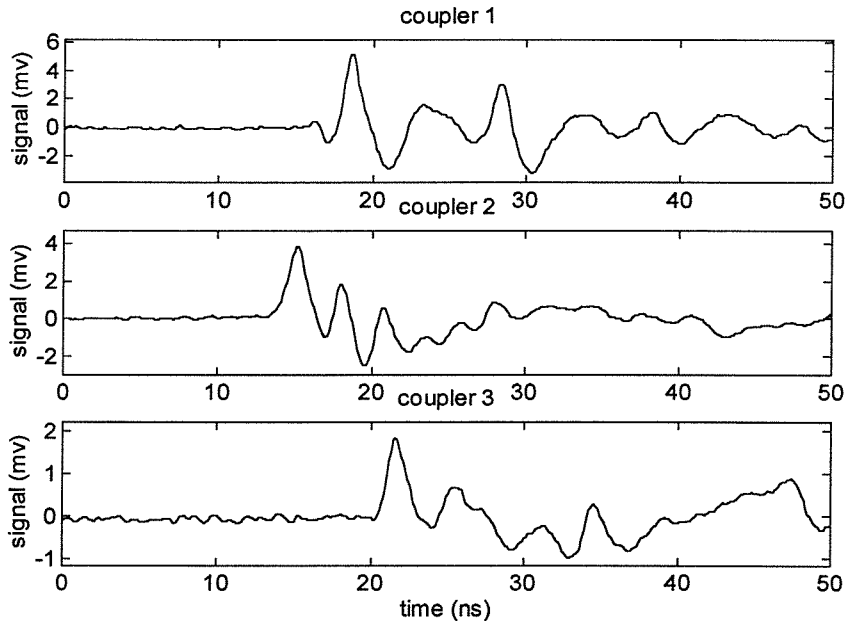

Figure 6.12 Coupler outputs for a discharge at cable section

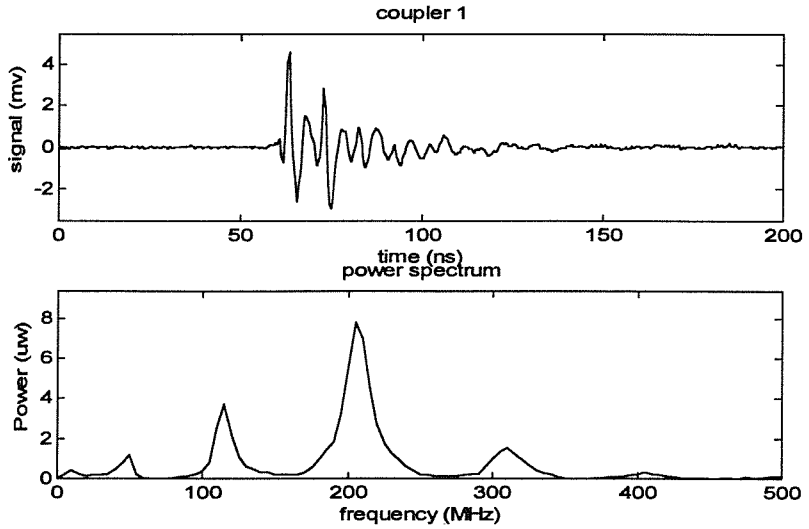

Figure 6.13 Coupler frequency spectrum for a discharge within cable section

Finally the coupler response to external corona discharge was investigated. A sharp metal wire was connected to the top of the water termination (hv) and pointed toward the earth. When the voltage was increased to about 6 kV, discharges with magnitudes of 50 pC occurred around the negative peak of the power cycle, when the voltage was further increased, more discharges occurred but the magnitudes were unchanged. This is the typical characteristic for corona discharge produced from a hv electrode. Figure 6.14 shows the relevant coupler output signal and frequency spectrum. Frequency components are within 100 MHz, which is lower compared with the discharge spectrum at the cable section. Figure 6.15 shows the coupler output waveforms. The waveform starting edge is less obvious compared to Figure 6.12. Figure 6.16 shows the coupler output signals for one power cycle. The coupler signals are distorted by a significant power frequency component. This can be explained by the coupler simulation model. The ac voltage is very low in frequency compared with the discharge spectrum, however, the magnitude is so high that it can still be reflected from the coupler output. A high-pass filter is thus necessary to remove the low frequency ac components. An amplifier is also required to amplify the low coupler output signals.

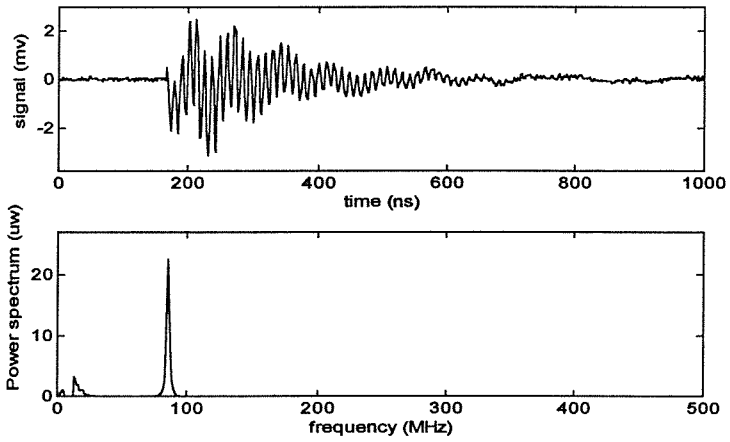

Figure 6.14 Coupler frequency spectrum for a corona discharge

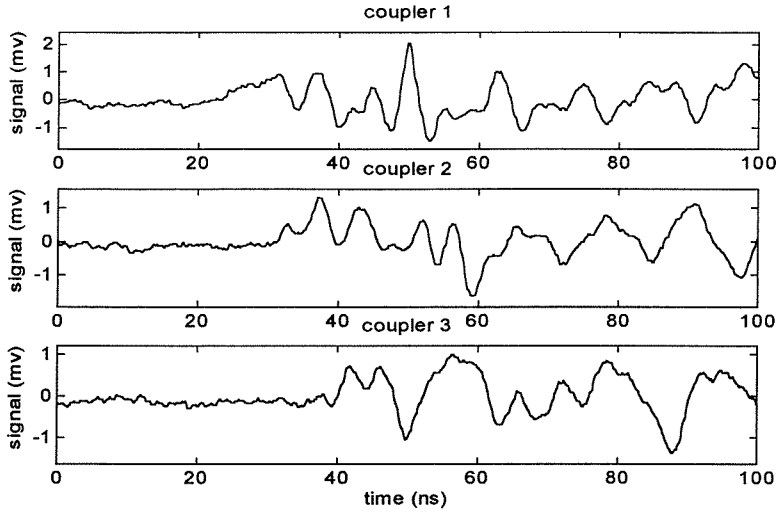

Figure 6.15 Coupler output waveforms for a corona discharge

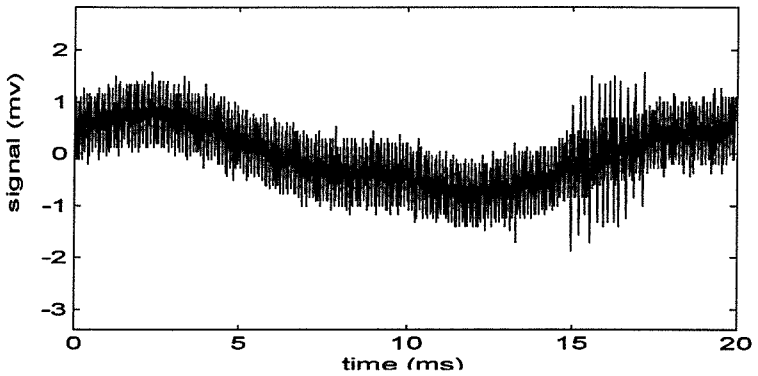

Figure 6.16 Coupler outputs due to corona discharge for one voltage cycle

6.4 Investigation into the Feasibility of an Insulation Gap

Long lengths of cable will have a large capacitance, therefore, in order to test the cable the hv supply for a conventional PD test would require a large power rating. However in some cases, only cable joints or small cable sections need to be tested for PD activity. Based on the above consideration, the hv supply can be connected to the outer metal sheath of the cable section or cable joint, and the cable inner conductor grounded. It is necessary to ensure that the metal sheath in contact with the hv electrode is isolated from rest of the cable sheath to minimise power requirements, and to prevent application of a high voltage to the rest of cable. Consequently both the cable metal sheath and the outer semiconducting layer have to be removed over a certain distance. This creates an insulating gap in the cable outer semiconducting screen between the detector and the likely source of PD activity where high voltage

was applied. An investigation into whether a capacitive coupler can still detect discharge pulses with the existence of such an insulation gap is therefore necessary.

6.4.1 Signal attenuation

The experimental arrangement to investigate this is shown in Figure 6.17. The input pulse from the pulse generator had a rise time of 1ns. R_a and R_b are the input matching impedance to ensure that the maximum of the input pulse is injected into the 66 kV XLPE cable and minimal reflection occurs, and to ensure that the pulse voltage into the cable is the same as observed on channel 1 of the oscilloscope. The Tektronix digital oscilloscope has a sampling rate of 5 GS/s and bandwidth of 1 GHz. R_c is a matching impedance to ensure that minimal reflection occurs at the cable end. Knowing that the impedance of the pulse generator and the oscilloscope are both 50 Ω, R_a, R_b and R_c can be estimated using the following equations:

$$50 = \frac{(R_a + Z_0)(R_b + 50)}{(R_a + Z_0) + (R_b + 50)} \tag{6.4}$$

$$\frac{Z_0}{R_a + Z_0} = \frac{50}{R_b + 50} \tag{6.5}$$

$$R_c = Z_0 \tag{6.6}$$

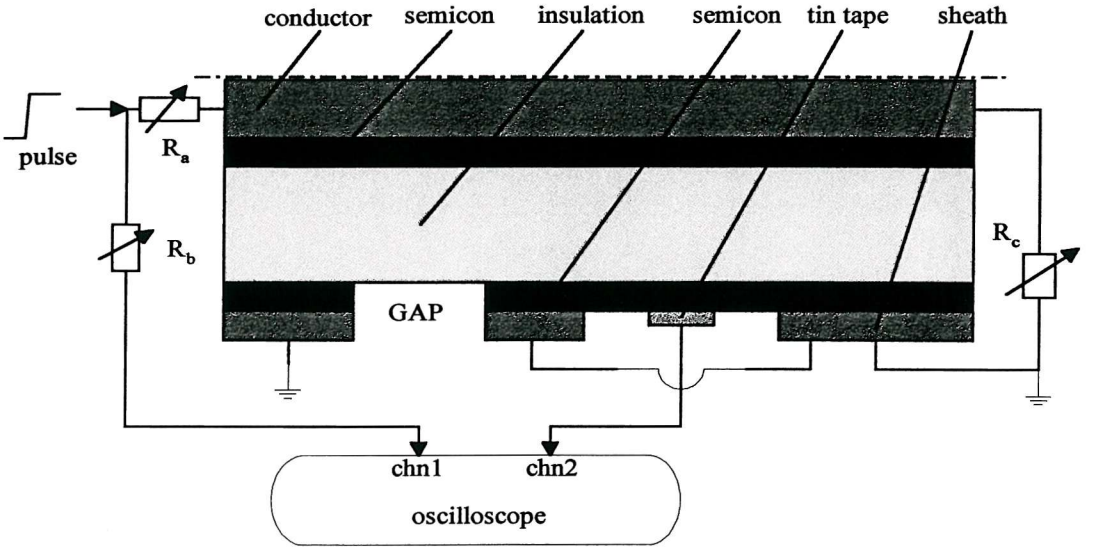

Figure 6.17 Arrangement to investigate the signal attenuation due to gap

A gap, created by removal of the cable outer semicon screen and the metal sheath, was introduced incrementally from 12 mm to 300 mm. Figure 6.18 shows the input pulse, the coupler output without gap, the coupler output with 12 mm gap, and the coupler output with 300 mm gap respectively. Figure 6.19 shows the coupler outputs for different gap lengths. The relationship between the first peak magnitude of the coupler output and the gap dimensions is shown in Figure 6.20. These figures indicate that the coupler output is affected more by the existence of a gap than by the gap dimension. Any generated PD pulses will have to travel through the stray capacitance that exists due to the gap. Consequently the PD pulse propagation characteristics are changed. On the other hand, as shown in Figures 6.18-6.20, the effect of the gap stray capacitance is fairly constant.

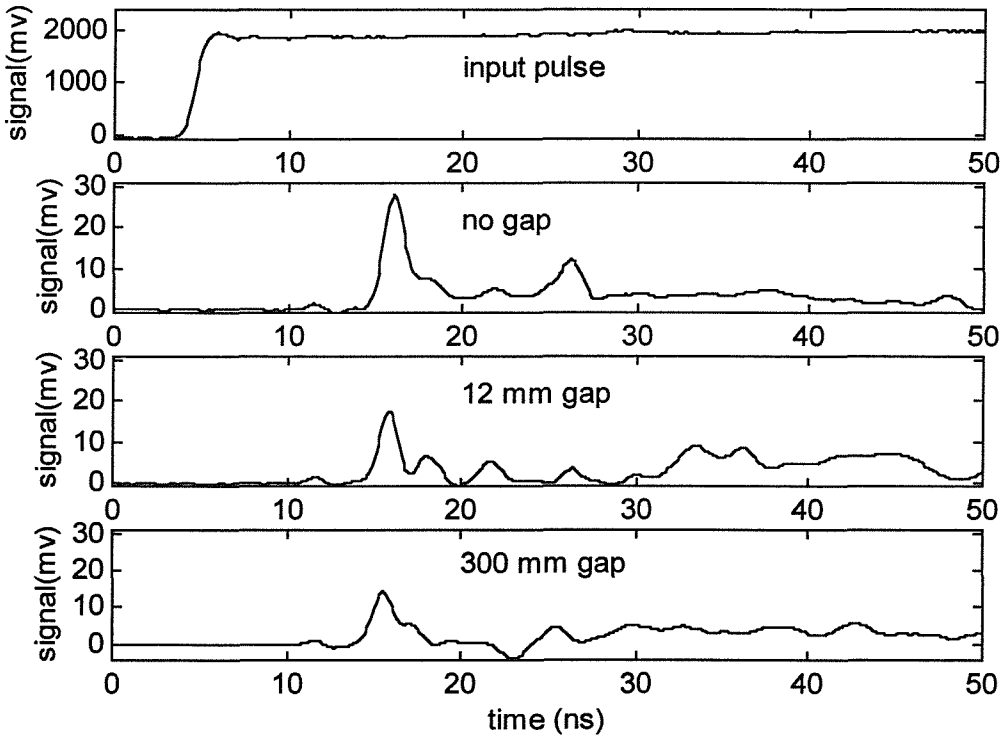

Figure 6.18 Coupler output with and without gap

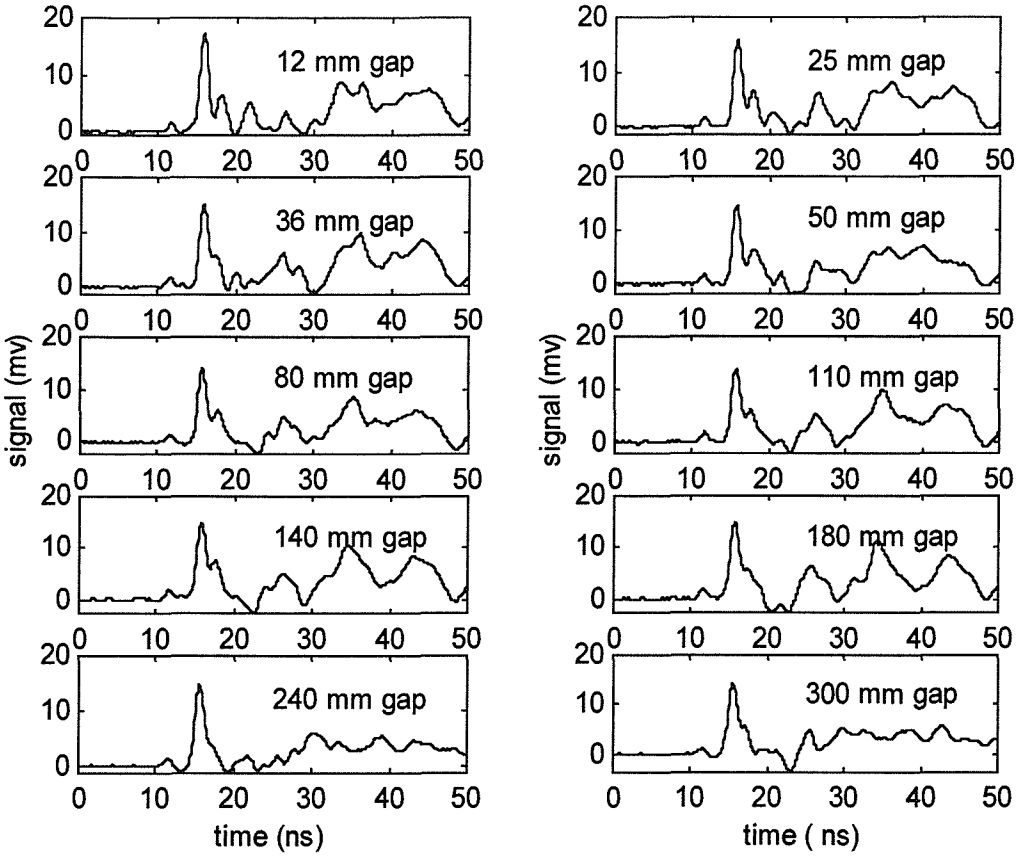

Figure 6.19 Coupler output with different gap dimensions

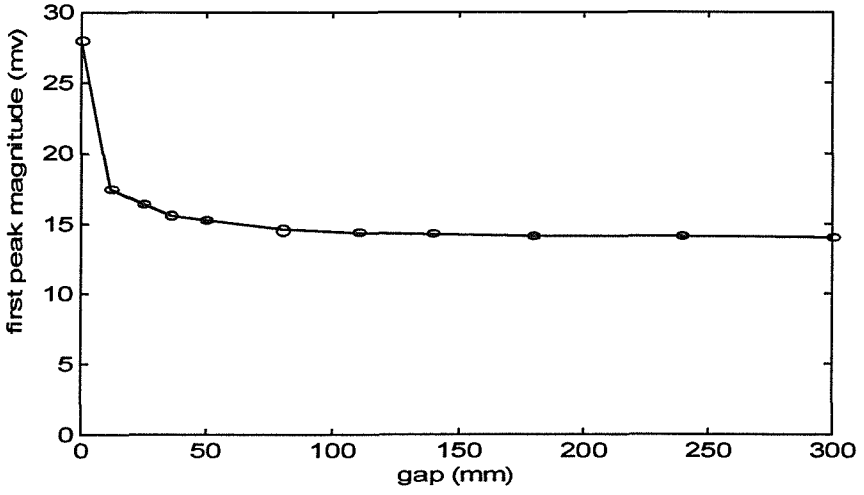

Figure 6.20 Coupler output magnitude against gap dimension

6.4.2 A simple model for insulation gap and capacitive coupler

A simple model was also established to model the effect of the insulation gap (Figure 6.21). L2 and C3 are used to simulate the inductance and capacitance respectively for

the cable section with insulation gap. L2 and C3 can be calculated using Equations (6.1) and (6.2). C4 is used to simulate the stray capacitance of the insulation gap. Other parameters are all as defined in Figure 6.2. In this case, C2 of 6 pF and R3 of 2000 Ω were used to approximate the coupler stray capacitance and the impedance between the coupler sensor and the cable sheath respectively.

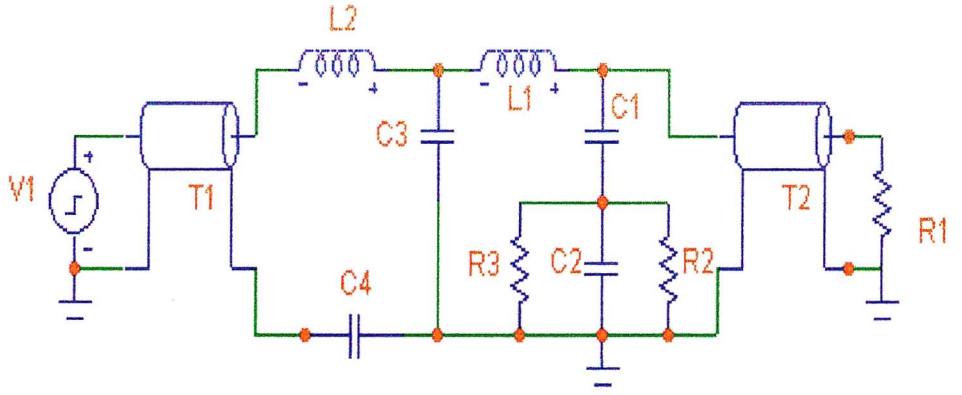

Figure 6.21 Simulation model for the gap and coupler

The influence of stray capacitance C4, due to the existence of a gap in the semicon screen, was investigated (Figure 6.22). The magnitude of the coupler output increases with the increase of gap stray capacitance. However, the influence of stray capacitance is small when it is higher than 300 pF. The maximal coupler output with the insulation gap is about 60% of what obtained when there is no existence of gap. This agrees with the obtained experimental results.

The experimental result (with a 300-mm gap) is shown in Figure 6.23 (a). Simulation results with different gap stray capacitances have been cross-correlated with the experimental result. The obtained maximal cross correlation coefficients are shown in Figure 6.24, which indicates that the gap stray capacitance is probably within the range from 50 pF to 150 pF, and most probably around 80 pF.

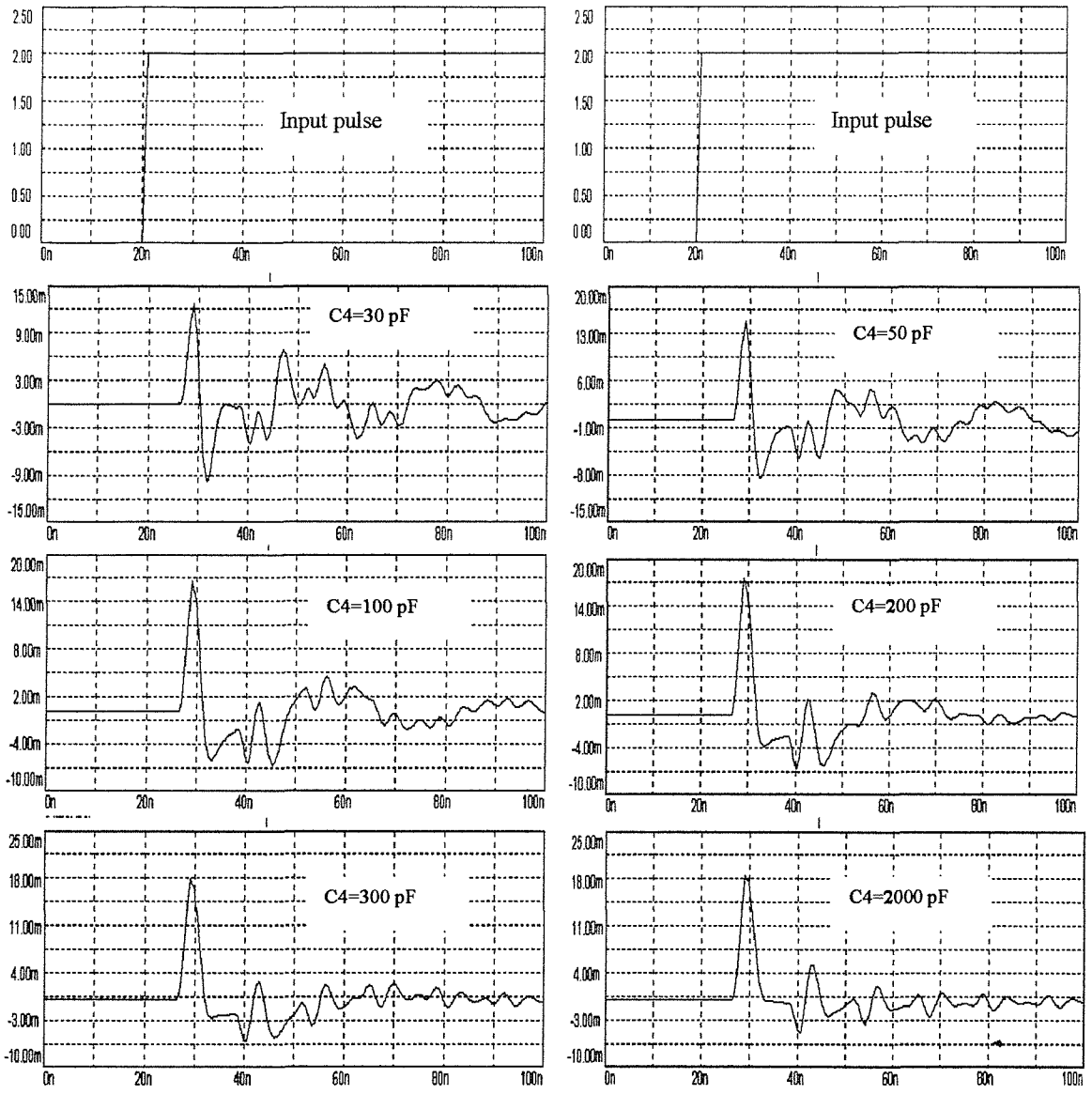

Figure 6.22 Influence of the gap stray capacitance

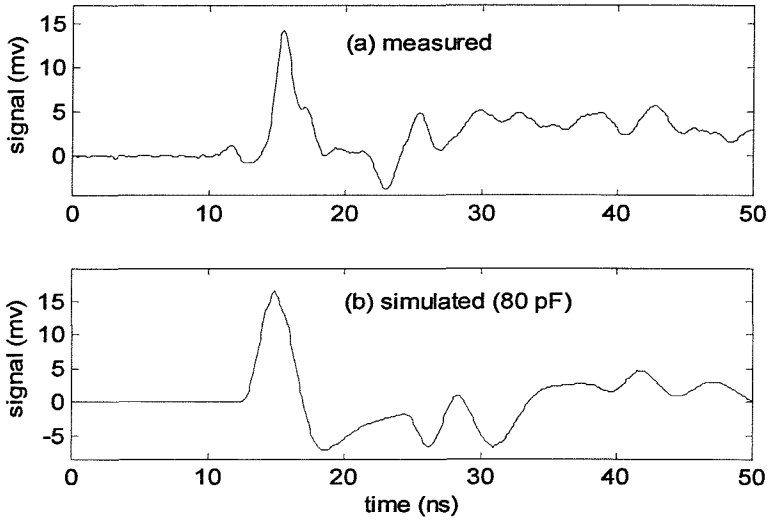

Figure 6.23 Measured and simulated results for a 300mm gap

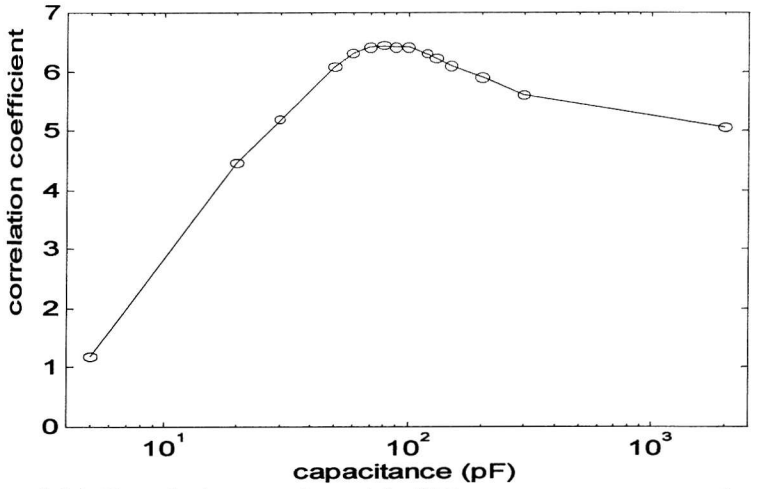

Figure 6.24 Correlation results with different gap stray capacitance

6.4.3 Frequency response

The frequency response of the capacitive coupler was determined for a range of inputs using the experimental arrangement shown in Figure 6.25. There was a 300mm isolation gap between the coupler and the signal source. Two different positions of the coupler were investigated.

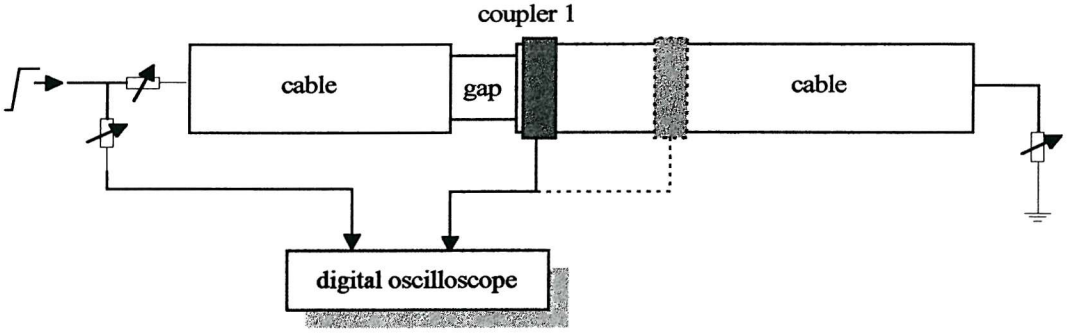

Figure 6.25 Arrangement to study the coupler frequency response (with gap)

Figure 6.26 and 6.27 show the coupler outputs when placed near to the gap for an input pulse with magnitude of 2 v, pulse width of 35 ns, rise and fall time 1ns and rise and fall time 3ns respectively. When the rise and fall time of the input pulse was increased, the upper frequency range of the coupler output signal reduced and the coupler output magnitude decreased.

The coupler was moved 600 mm away from the gap and the experiment was repeated. Figure 6.28 shows the coupler output for a pulse with magnitude of 2 v, pulse width of 35 ns, rise and fall time of 1 ns. Higher frequency components were

attenuated by the increase of distance between the signal source and capacitive coupler.

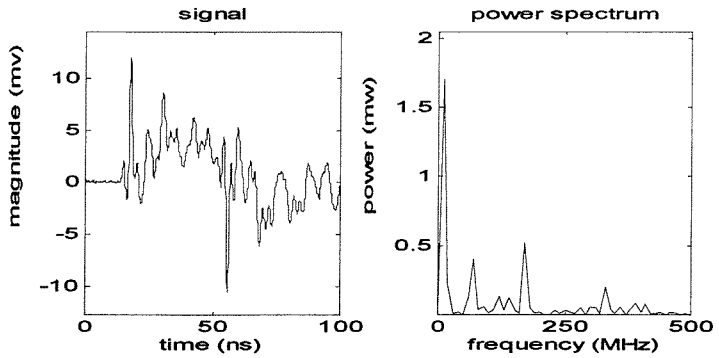

Figure 6.26 Coupler close to gap and input pulse with rise time of 1 ns

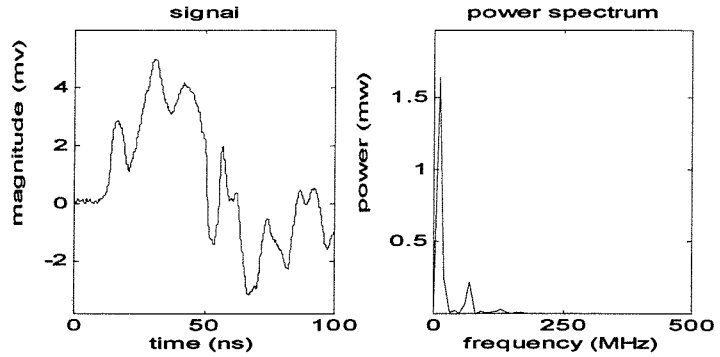

Figure 6.27 Coupler close to gap and input pulse with rise time of 3 ns

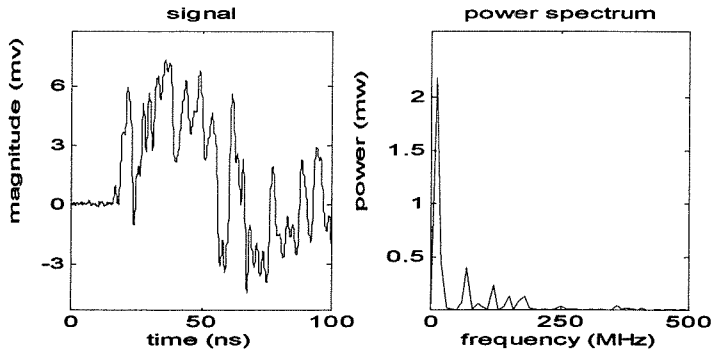

Figure 6.28 Coupler 600 mm away from the gap and input pulse rise time of 1 ns

6.4.4 Time of flight study through cross-correlation analysis

The source of partial discharges might be located by applying two couplers and studying the time of flight. The cross-correlation function can be useful in determining the time of flight. Two implementation methods of cross-correlation, i.e. the time-based algorithm and the FFT-based algorithm, were investigated. The experimental arrangement is as shown in Figure 6.25.

6.4.4.1 Time-based cross-correlation implementation [159]

The cross-correlation algorithm can be implemented using the following approach. Considering two outputs x and y such that

$$\begin{aligned} x_n &= (x_0, x_1, \ldots x_{N-1}) \qquad n = 0, 1, \ldots N-1 \\ y_n &= (y_0, y_1, \ldots y_{N-1}, 0, \ldots 0) \qquad n = 0, 1, \ldots 2N-1 \end{aligned} \tag{6.7}$$

$$rxy(m) = \sum_{n=0}^{n=N-1} x(n) \bullet y(n+m) \qquad m = 0, 1, \ldots N-1 \tag{6.8}$$

$$\begin{aligned} x_n &= (x_0, x_1, \ldots x_{N-1}, 0, \ldots 0) \qquad n = 0, 1, \ldots, 2N-1 \\ y_n &= (y_0, y_1, \ldots y_{N-1}) \qquad n = 0, 1, \ldots, N-1 \end{aligned} \tag{6.9}$$

$$ryx(m) = \sum_{n=0}^{n=N-1} y(n) \bullet x(n+m) \qquad m = 0, 1, \ldots N-1 \tag{6.10}$$

It is advisable to smooth the signal fluctuations by averaging over several non-overlapping data sets, i.e.

$$rxy(m) = \frac{1}{k} \sum_{i=1}^{k} rxy(m,i) \tag{6.11}$$

$$ryx(m) = \frac{1}{k} \sum_{i=1}^{k} ryx(m,i) \tag{6.12}$$

Where rxy is the cross-correlation function for signals x and y, indicating that signal x leads signal y; ryx is the cross-correlation function indicating signal y leads signal x.

6.4.4.2 FFT-based cross-correlation implementation [160]

By zero padding $\{x_n\}$ can be split into two sequences given by

$$\begin{aligned} \{\alpha_n\} &= (x_0, x_1, \ldots x_{N-1}, 0, \ldots 0) \qquad n = 0, 1, \ldots (2N-1) \\ \{\beta_n\} &= (0, \ldots 0, x_N, \ldots x_{2N-1}) \qquad n = 0, 1, \ldots (2N-1) \end{aligned} \tag{6.13}$$

$$X_m^{+} = FFT(\alpha_n) \qquad m = 0, \ldots (2N-1) \tag{6.14}$$

$$X_m^{-} = FFT(\beta_n) \qquad m = 0, \ldots (2N-1) \tag{6.15}$$

together with

$$Y_m = FFT(y_n) \qquad m = 0, \ldots (2N-1) \tag{6.16}$$

Using the transformed sequences and their complex conjugates, the following products can be formed:

$$\psi_{xy}(m) = \frac{1}{N}\text{conj}(X_m^{+}) * Y_m \tag{6.17}$$

$$\psi_{yx}(m) = \frac{1}{N}X_m^{-} * \text{conj}(Y_m) \tag{6.18}$$

which are the cross-spectrum estimates. The cross correlation function can be found by applying the inverse transformation. It is also advisable to smooth the spectral fluctuations by averaging over estimates obtained from several non-overlapping data sets, i.e.

$$\psi_{xy}(m) = \frac{1}{k}\sum_{i=1}^{k}\psi_{xy}(m,i) \tag{6.19}$$

$$\psi_{yx}(m) = \frac{1}{k}\sum_{i=1}^{k}\psi_{yx}(m,i) \tag{6.20}$$

Using these averaged estimates we can determine correlation between the two signals from

$$R_{xy}(k) = \text{FFT}^{-1}(\psi_{xy}(m)) \qquad k = 0, 1, \ldots (2N-1) \tag{6.21}$$

$$R_{yx}(k) = \text{FFT}^{-1}(\psi_{yx}(m)) \qquad k = 0, 1, \ldots (2N-1) \tag{6.22}$$

Where R_{xy} is the cross-correlation function for signals x and y, indicating signal x leads signal y, R_{yx} is the cross-correlation function indicating signal y leads signal x.

Figure 6.29 and 6.30 show the coupler 1 and coupler 2 output waveform without and with the 300-mm gap respectively. Figure 6.31 and 6.32 show the time-based and FFT-based cross-correlation implementation for two coupler outputs, without and with gap respectively. In this study, the cross correlation efficient was normalised between 0 and 1. The time location that corresponds with the maximal cross correlation coefficient is the relevant time of flight for two signals. If the maximal value is situated within the positive time range, then it indicates that coupler 1 signal leads coupler 2 signal. On the other hand, if the maximal value is within the negative time range then it indicates that coupler 1 lags behind the coupler 2 signal. Results indicate that both algorithms can be used to determine the time of flight between two coupler signals. When a gap exists, the cross correlation result is less obvious, but the relative time of flight can still be determined.

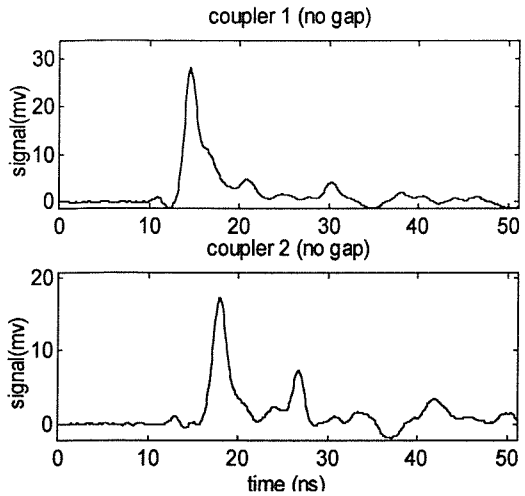

Figure 6.29 Coupler outputs (no gap)

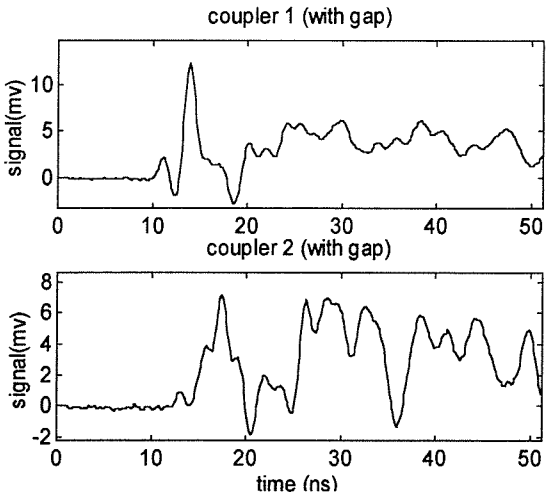

Figure 6.30 Coupler outputs (with gap)

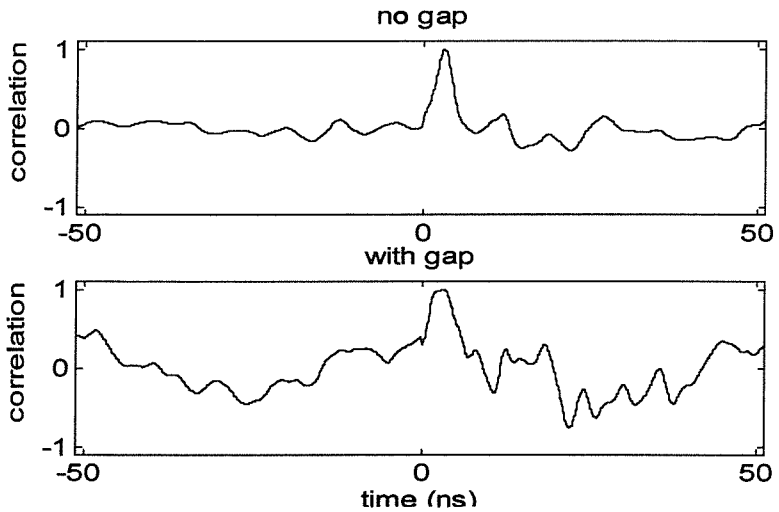

Figure 6.31 Time-based cross correlation for two coupler signals

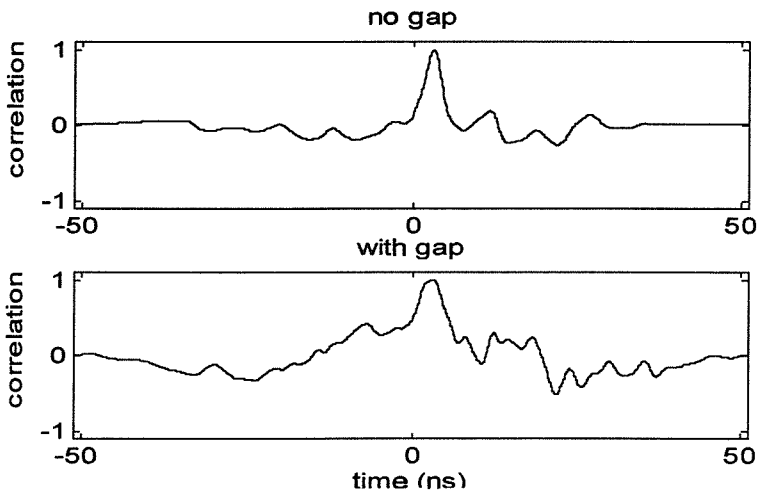

Figure 6.32 FFT-based cross correlation for two coupler signals

6.4.5 Calibration of capacitive coupler with insulation gap

Two calibration methods have been investigated in order to calibrate the detected coupler signal across the insulation gap with the discharge apparent quantity.

- Using pulse generator (8082A,Hewlett Packard®). To calibrate the discharge quantity injected into the cable, a small sandwich experimental model was connected in series with the cable section (Figure 6.33). The model consists of three layers of low-density polyethylene (LDPE) films each with thickness of 0.2 mm. The relevant capacitance of the model can be approximately calculated using the following equation:

$$C_m = \varepsilon_0 \varepsilon_r \frac{\pi r^2}{d} \tag{6.23}$$

Where ε_0 is the dielectric constant in vacuum (8.85 pF/m); ε_r is the relative dielectric constant for LDPE (2.3); r is the radius of the electrodes on the top and bottom film (9 mm); d is the distance between electrodes (0.6 mm). The capacitance of the model is calculated to be about 8.5 pF.

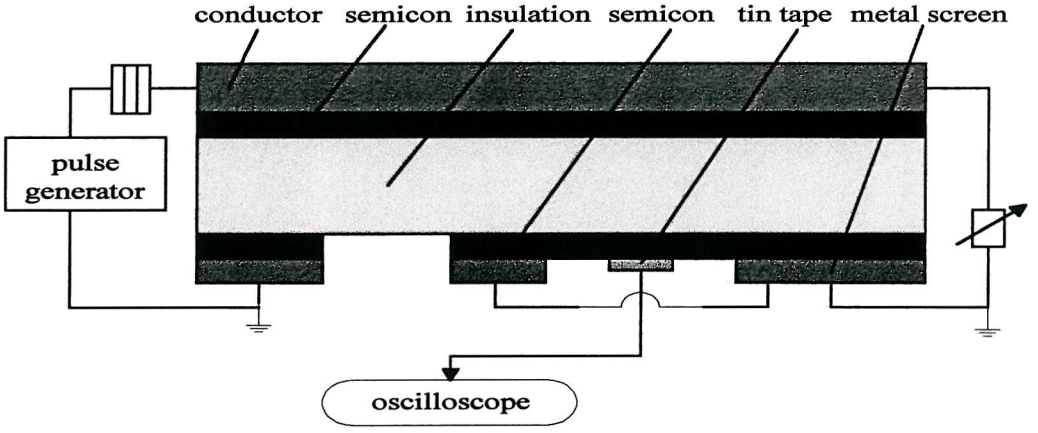

Figure 6.33 Calibration of coupler following a gap with pulse generator

The equivalent circuit can be given by Figure 6.34.

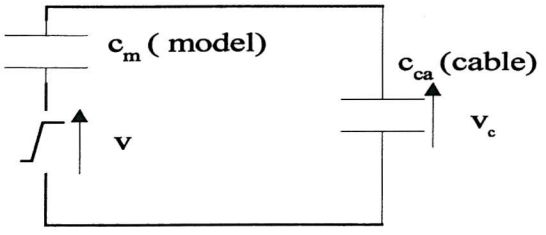

Figure 6.34 Calibration equivalent circuit using a pulse generator

From the circuit, the discharge quantity into the cable section can be calculated as:

$$q = c_{ca} \times v_c = c_{ca} \times v \times \frac{c_m}{c_m + c_{ca}} = v \times \frac{c_m}{1 + c_m / c_{ca}} \qquad (6.24)$$

Given that the capacitance of the cable is much greater than the capacitance of the PD model ($C_{ca} >> C_m$), thus the discharge into the cable is approximately equal to the pulse generator output magnitude multiplied by the capacitance of the model. Figure 6.35 shows the coupler signals and spectra for the pulse generator output magnitude of 1 v, 2 v and 5 v respectively, the rise time of the step wave is 1 ns. The results indicate that the coupler output magnitude is proportional to the pulse generator output magnitude and the frequency characteristic is fairly consistent.

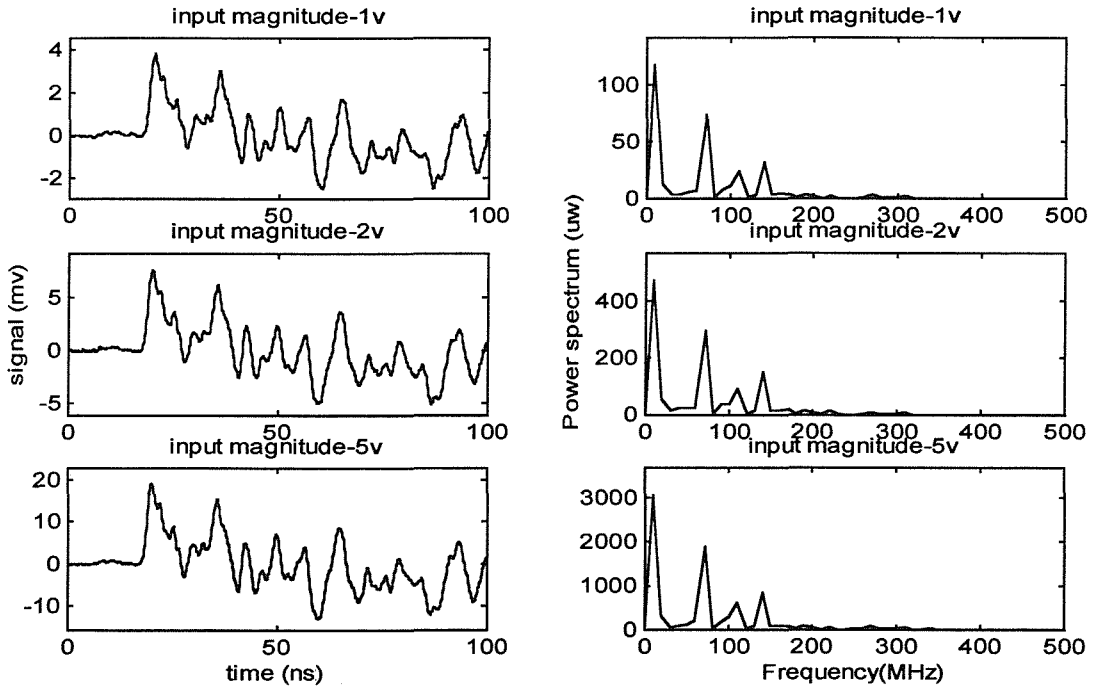

Figure 6.35 Coupler outputs with different pulse generator magnitudes

- Using standard PD calibrator (Type 753vs-1, Robinson®). The experimental arrangement is shown in Figure 6.36. The PD calibrator provides a discharge quantity in Pico-coulomb, it should be connected directly to the cable conductor core, as in the conventional electrical detection calibration. Figure 6.37 shows the coupler signals and spectra for PD calibrator output of 500 pC and 50 pC respectively.

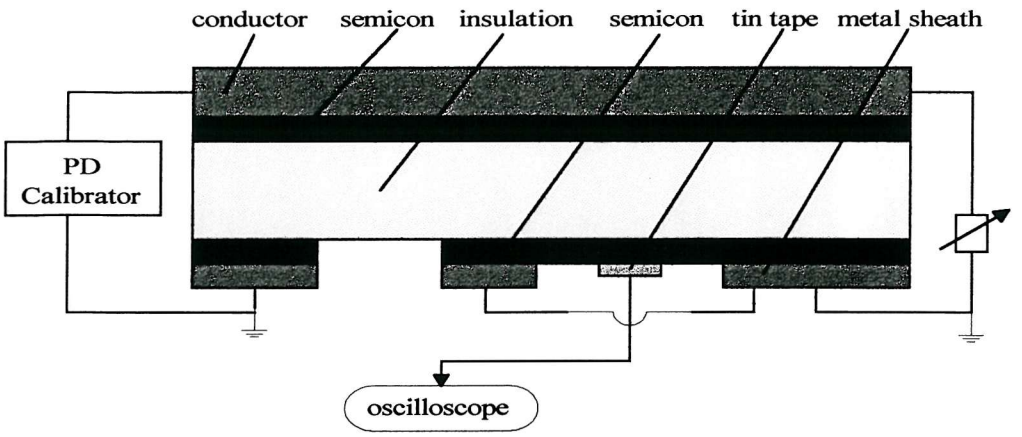

Figure 6.36 Calibration of coupler following a gap with standard PD calibrator

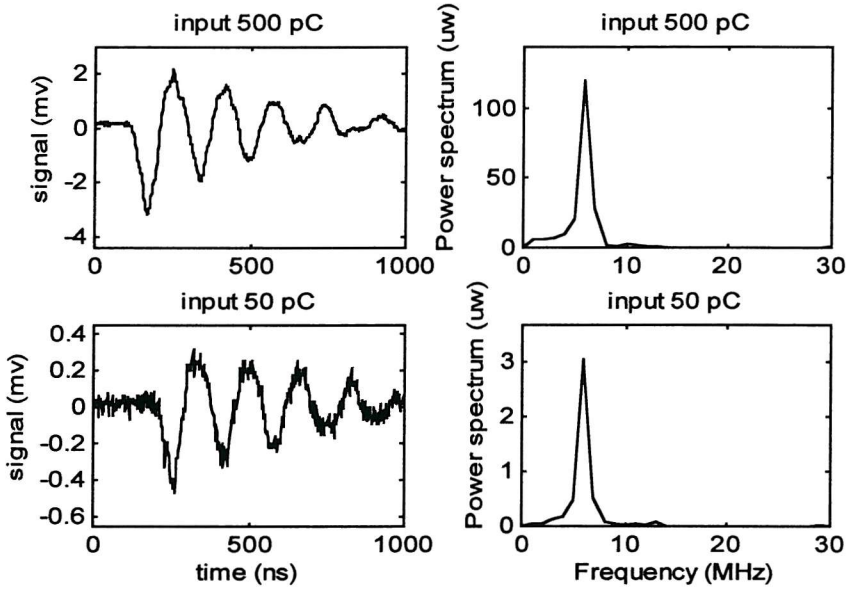

Figure 6.37 Coupler outputs with different calibrator magnitudes

Table 6.1 shows the calibration results using the above two approaches. The calibration sensitivity for the pulse generator method is much higher than that of the PD calibrator approach, and is constant for different input magnitudes.

Table 6.1 Calibration results

Calibration methods	Injected discharge magnitude	Coupler output Amplitude	Calibration Sensitivity
Standard calibrator	50 pC	0.47 mV	0.0094 (mV/pC)
	500 pC	3.28 mV	0.0066 (mV/pC)
Pulse generator	8.5 pC	3.8 mV	0.447 (mV/pC)
	17.0 pC	7.6 mV	0.447 (mV/pC)
	42.5 pC	19.0 mV	0.447 (mV/pC)

A void with diameter of 1 mm was drilled in the middle film of the sandwich PD model. High voltage was then applied to produce partial discharges. The test arrangement is shown in Figure 6.38. The coupler output signal and spectrum for an applied voltage of 2.9 kV is shown in Figure 6.39. Most of the coupler frequency components are between 50 and 350 MHz. This discharge spectrum is comparable with the coupler spectrum when pulse generator is used as the calibration source, while the maximal coupler frequency range for calibration pulse from the PD calibrator calibration pulse is only within 10 MHz. Calibration with the pulse generator approach is therefore the more feasible approach. For Figure 6.39, the maximal coupler signal magnitude is about 11.2 mV. Conventional detection according to IEC 270 was also applied to the PD model and the discharge apparent quantity at the same applied voltage was found to be around 30 pC, which corresponds to 13.4 mV according to Table 6.1.

It should be noted that in practice it might be very difficult, if not impossible, to obtain a strict calibration relationship regarding mV/pC. However, it would still be very helpful if the coupler output can provide information about the approximate discharge level that produces the coupler signal.

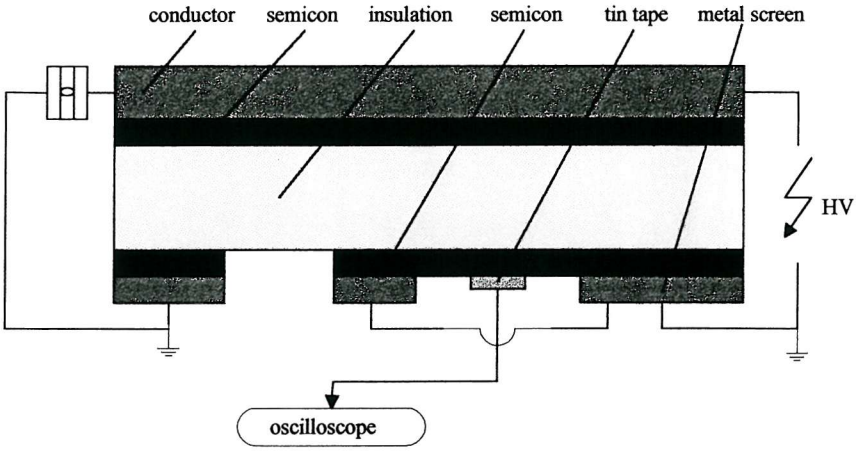

Figure 6.38 PD detection using coupler with existence of insulation gap

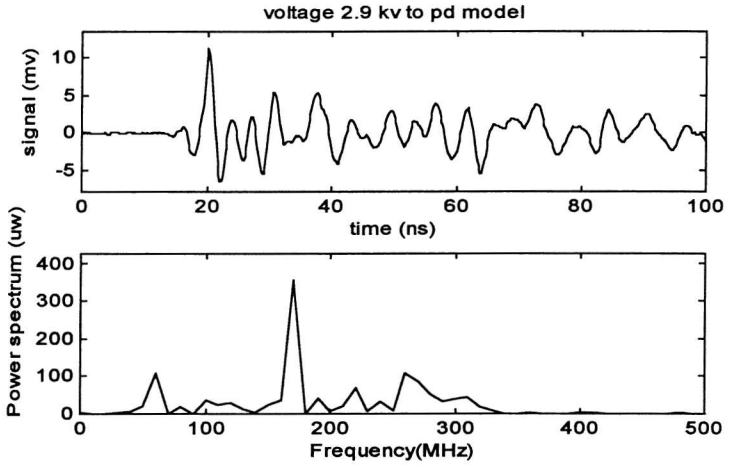

Figure 6.39 Coupler signal and spectrum due to practical discharge

6.5 Summary

The capacitive coupler technique and the influence of insulation gap (removing the cable semicon screen) have been investigated. The capacitive coupler does not affect the insulation system because the high potential electrode of the coupler is attached on top of the cable semicon screen which serves as the power frequency ground. The physical dimensions of the coupler affect the coupler output. Different coupler sensor materials such as tin and aluminium, however, do not have much effect on coupler performance. The capacitive coupler may be constructed as a patch rather than covering the whole periphery of the cable semicon, and reasonable performance is still possible. The spectrum response of the coupler indicates that it has a useful frequency range up to 500 MHz. Discharge signals attenuate more at higher frequencies, on the other hand, interference may be less significant at higher frequencies. Generally the

capacitive coupler can perform well within the very high frequency range from 30 MHz to 300 MHz.

Capacitive couplers have been applied to the detection of partial discharges from a cable section with water terminations. The test results indicate that the PD site at the cable section can be accurately located if two capacitive couplers are used. The capacitive coupler is rather sensitive and a discharge of 3 pC can be clearly detected by a coupler 1.5 m away. The coupler output magnitude attenuates by a maximum of 40% if the metal sheath between the coupler and the PD site is removed. Therefore, the cable should be properly screened in order to obtain a high sensitivity. The attenuation of a discharge during its propagation causes the loss of high frequency components and results in a less obvious starting edge of the output waveform, thus producing less discernible time of flight traces. Discharges attenuate more in the water termination than in the cable. To remove the ac background noise due to the applied power frequency voltage from the coupler output and to obtain higher detection sensitivity, it is helpful to apply a high-pass filter and amplifier in connection with the capacitive coupler output. A certain length of the cable metal sheath has to be removed in order to implement the capacitive coupler, which is a disadvantage if partial discharge on-line monitoring is considered.

An alternative PD test method for long cable systems has been outlined. This method reduces the demand on the power supply from the test system, but requires the existence of insulation gap by removing both the cable metal sheath and the semicon screen. The existence of such an insulating gap causes attenuation of the coupler signal. The peak amplitude of the detected pulse is reduced by about 50% after a 300 mm gap. However, the coupler can still detect signals in such a case. A network simulation model was used to investigate the performance of the capacitive coupler with an insulation gap, and simulation results agree with practical experiments. Through cross correlation analysis, the stray capacitance for a 300-mm insulation gap may be roughly determined. Cross correlation analysis can also be used to determine the time of flight traces from different coupler signals. Both time-based algorithm and FFT-based algorithms can be used to implement the cross correlation analysis. The calibration of a capacitive coupler following the insulation gap was investigated using the pulse generator approach and the standard PD calibrator approach. The pulse generator approach obtains much higher calibration sensitivity than the PD standard

calibrator approach. The practical PD test result on a sandwich experimental model agrees with the calibration result using the pulse generator approach.

Chapter 7

Practical Application of Various PD Detection Methods to Cable Systems

7.1 Introduction

This chapter investigates the application of various on-line methods of PD detection within cable systems. The capacitive coupler, the acoustic emission sensor and the radio frequency current transducer (RFCT), have been applied to detect partial discharges within a 132 kV cable joint. For the capacitive coupler detection, two different calibration methods were investigated, and the calibration results were compared with practical PD test results. Location of PD site was studied by time of flight from different couplers. The capacitive coupler response to internal partial discharges within the cable joint was compared with externally generated noise.

Acoustic emission sensors were applied to detect partial discharges within the cable joint. The acoustic wave attenuation characteristics of the cable joint were investigated. PD location by means of acoustic approach and time of flight analysis was studied.

RFCTs were used to detect the discharge current flowing through the cable sheath. A wavelet transform was applied to improve the signal to noise ratio when the detection sensitivity is low.

The capacitive coupler was also implemented for PD detection within a 90 kV XLPE cable section having water terminations. In this case the calibration of the capacitive coupler was further investigated, as well as PD location by means of time of flight.

Finally the possible application of the screen interruption method (section 3.3.2.1) was investigated for the cable section arrangement. The frequency response and time of flight traces were studied. A comparison was made between this approach and the capacitive coupler technique.

7.2 PD Test for a 132 kV Cable / Joint System

7.2.1 Test arrangement

Capacitive couplers, acoustic emission sensors, radio frequency current transducers, and conventional electrical detection according to IEC-270, were used for PD detection from a 132 kV cable system. The test arrangement is shown in Figures 7.1 and 7.2. Two cable sections were connected by a prefabricated cable joint. The main insulation material of the cable joint is ethylene propylene rubber (EPR), whereas the cable insulation is cross-linked polyethylene (XLPE). Cable ends were connected to oil-filled cable terminations. The maximum voltage output for the high voltage transformer is 300 kV. The coupling capacitor has a capacitance of 1000 pF. The input unit for the PD detector has a capacitance tuning range of 400-6000 pF. The partial discharge detector used is a Robinson® model 5 type 700. The acoustic emission sensor used in the experiment R15D has a resonant frequency of 150 KHz. Signals from the AE sensor were amplified using the AE preamplifier 1220A which has a frequency range of 20-1200 KHz and a selectable amplification gain of 40/60 dB. A power supply unit, which can be operated by mains or by battery, provides the 28 V dc supply voltage for the AE preamplifier. A wide band amplifier with frequency range of 0.01-500 MHz and amplification gain of 24 dB was used to amplify the coupler signals. The surge protector (sgp) has a maximum operating frequency of 1000 MHz and a response time less than 10 ns. The surge protector was used to protect the measuring system from any possible over-voltage during the partial discharge test. The Tektronix® digital oscilloscope has a sampling rate of 5 GS/s and bandwidth of 1 GHz. Apart from the acoustic emission sensors and the capacitive couplers, two ferrite-core

radio frequency current transducers with frequency response of 2.5 KHz -150 MHz or 10 KHz – 200 MHz were also applied. A Pentium® II 233 MHz computer was used to further process the measured discharge signals. The signal processing and analysis software were developed using MatLab®.

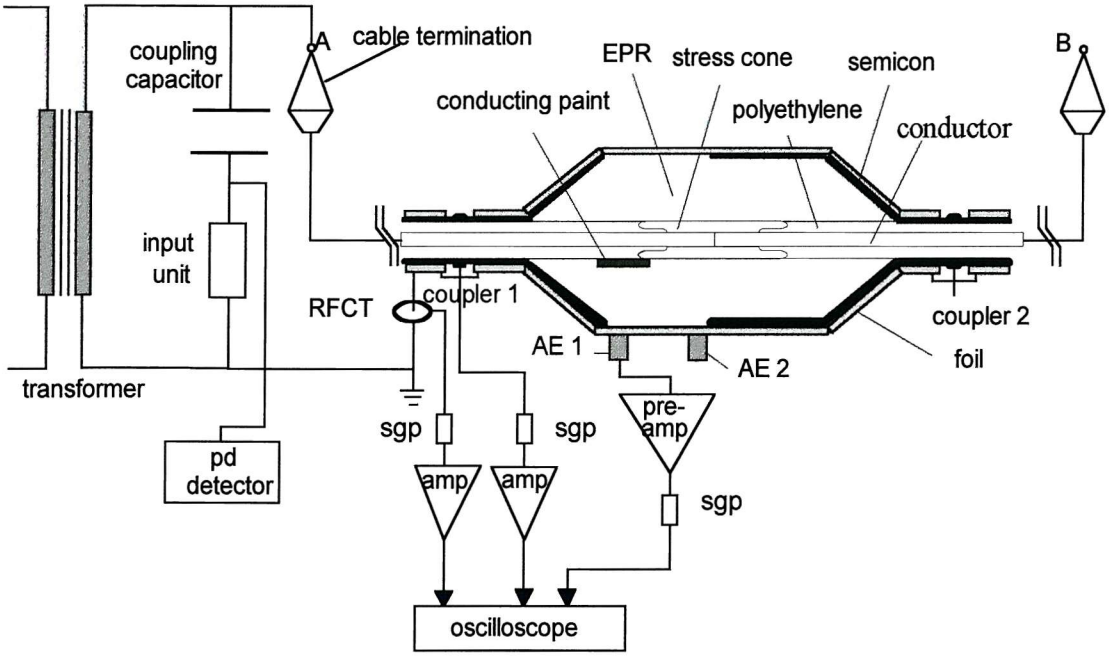

Figure 7.1 Schematic diagram for the 132 kV cable/joint PD test arrangement

Figure 7.2 Photo for the 132 kV cable/joint PD test arrangement

Initially various disturbances were detected for different applied voltages. Observation of the Robinson® PD detector oscilloscope revealed that disturbances were due to either poor electrical contact, floating discharges or corona discharges from the test system and surrounding objects within the laboratory. Figure 7.3 shows typical disturbance histograms. With reference to Figure 7.3, corona discharges (7.3a) occur around the positive or the negative peak of the applied voltage. The discharge

repetition rate is increased but the magnitude remains constant with any increase in the applied voltage. Floating discharges (7.3b) are equally spaced with the same magnitude, independent of the applied voltage. Discharges due to bad contact (7.3c) are irregular and are distributed around the zero-voltage points. The phase range of discharge increases with any increase in the applied voltage.

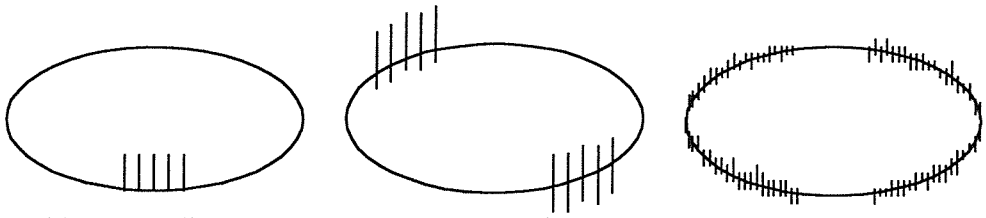

(a) corona discharge (b) floating discharge (c) bad contact

Figure 7.3 Typical elliptical histograms of disturbances

After removing the disturbances systematically, the whole system was found to be discharge free for applied voltages up to 150 kV. The joint was then dismantled and conducting paint in the shape of a 'v' was installed on top of the cable XLPE between the cable joint stress cone (conductor) and the cable joint outer semi-conducting layer. This acts as a PD source within the cable joint.

Figure 7.4 shows the arrangement of capacitive coupler, acoustic emission sensor and RFCT. The AE sensor is placed on the cable joint to detect the acoustic wave produced by partial discharges. The RFCT surrounds a conductor that connects the cable sheath to the system earth, to detect the discharge current flowing through it. Capacitive couplers are installed at the cable section close to the cable joint. 100mm long cable metal sheath was removed. A tin tape with diameter of 40 mm was wrapped around the exposed cable outer semicon screen. In this case the tin tape acts as the coupler sensor. To reduce the influence of electromagnetic interference, the capacitive coupler was screened with copper. To avoid the connection between the coupler sensor that acts as the high potential electrode for high frequency signals and the cable sheath, insulation tape was wrapped around the coupler sensor and the semicon between the coupler sensor and the cable sheath.

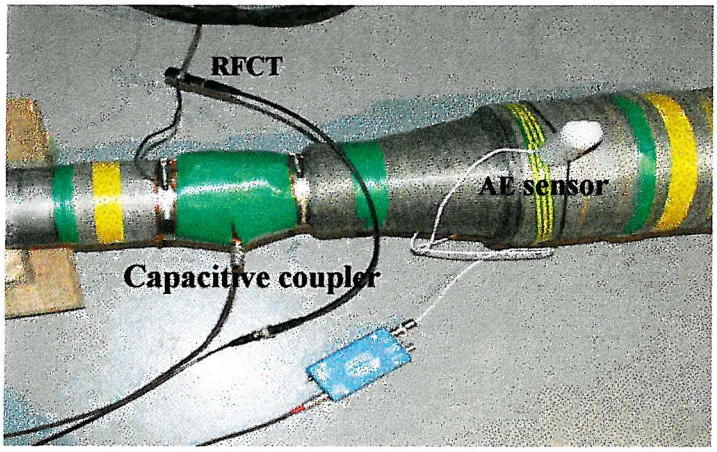

Figure 7.4 Arrangement of capaictive coupler, AE sensor and RFCT

7.2.2 Capacitive coupler measurements

7.2.2.1 Calibration

Calibration can be achieved by injecting calibration pulses and associating the measured amplitude from the detector output with the injected charge. This may lead to calibration results, which not only depend on the charge of the injected pulse, but also on its wave shape, and consequently the spectrum of the pulse which reaches the detector and the frequency range chosen for the detector to detect the signal. For a bandwidth of 10 to 350 MHz, a pulse with 1ns rise time is needed to ensure proportionality between output voltage and injected charge [76]. There are different calibration methods for non-conventional PD measurement systems.

7.2.2.1.1 Calibration from the cable termination

Step waves from a pulse generator, in series with a capacitance of 6 pF, was injected into the cable termination between the HV conductor and the ground. The step wave always had a rise time of 1ns but different amplitudes were applied. The injected charge can be approximately taken as the step wave amplitude multiplied by the capacitance. Figure 7.5 shows the relationship between the coupler 1 (the length of the coupler metal tape being 40 mm) output amplitude and the injected charge. A nearly linear relationship exists, and the calibration result is about 0.7 mV/ pC.

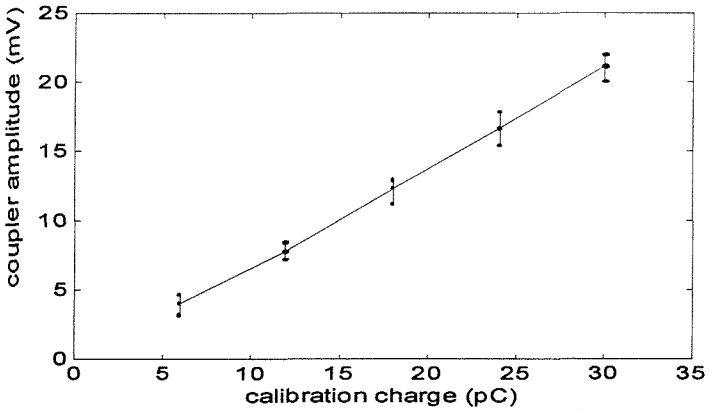

Figure 7.5 Coupler calibration from the cable termination

Attenuation in the cable system may reduce calibration signals and change their waveform before they reach the coupler, which will consequently introduce calibration errors. Another disadvantage is that the nature of this calibration method makes it unsuitable for on-line calibration of in service cable systems.

7.2.2.1.2. Calibration using a similar cable joint

If an extra cable joint, similar to the one measured, is available, it would be possible to cut the cable close to the joint and inject a calibration voltage pulse in series with a known capacitance directly into the cable core. The calibration pulse can then be measured by a coupler installed on the other side of the cable joint. In this way the attenuation or distortion of calibration pulse would be less significant compared with calibration using the cable termination. Obviously this method is still not suitable for capacitive coupler on-line calibration.

7.2.2.1.3 Calibration using one coupler to inject a pulse and another to receive it

If two capacitive couplers are installed either side of the cable joint, one can be used to inject a calibration pulse while the signal is detected using the second coupler. Considering the simulation model for capacitive coupler, the principle of this calibration method is as shown in Figure 7.6. C is the cable distributed capacitance covered by the coupler sensor, C_s and R_s are the stray capacitance and stray resistance between the coupler sensor and the cable sheath. C can be calculated (Equation 6.1). For this experiment, the capacitance per metre of the 132 kV cable was calculated to be 270.6 pF/m.

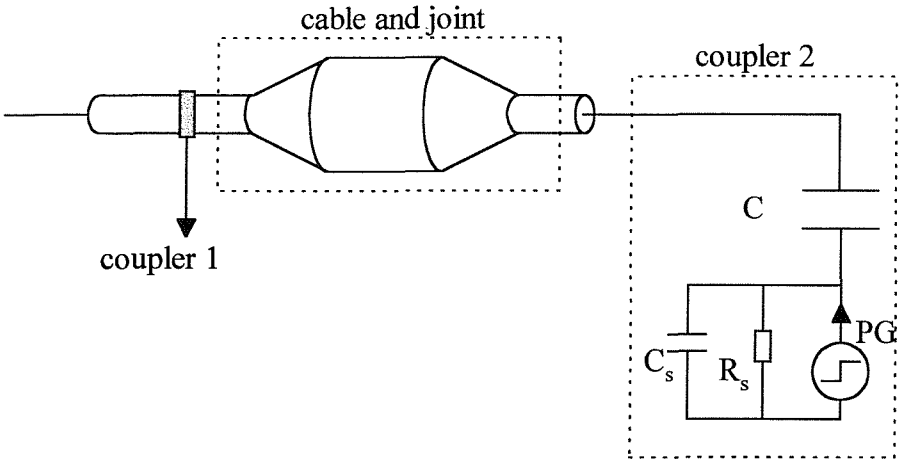

Figure 7.6 Principle of calibration through another coupler

If the influence of the stray capacitance C_s and stray resistance R_s is ignored, the injected charge can be estimated as the pulse generator output magnitude multiplied with the capacitance C. For this study, a step wave from the pulse generator with a magnitude of 5V and rise time of 1ns, was injected into coupler 2, for a range of coupler 2 sensor lengths which is equivalent to different cable capacitances. Figure 7.7 shows that a generally proportional relationship exists between the output magnitude of coupler 1 and the sensor length of coupler 2.

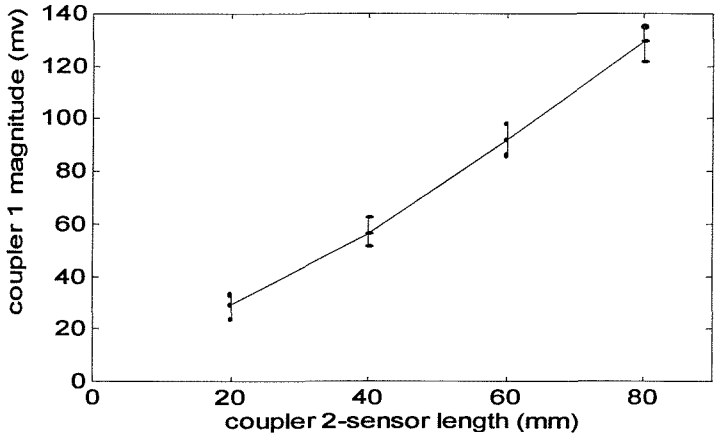

Figure 7.7 Influence of coupler sensor dimension on calibration

Step waves from the pulse generator, with a 1ns rise time but with different amplitudes, were then injected into coupler 2. In this case, the length of the coupler sensor was 40 mm equivalent to a cable capacitance C of 10.8 pF. Figure 7.8 shows the relationship between the output amplitudes of coupler 1 and the approximate injected charges. A nearly linear relationship exists, and the calibration result is about 0.97 mV/ pC.

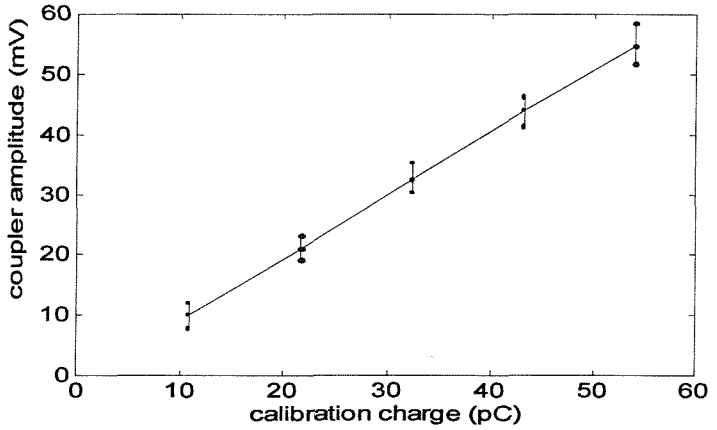

Figure 7.8 Calibration results using another coupler

Figure 7.9 shows the coupler 1 output waveform due to a step wave with rise time of 1ns and magnitude of 5V injected into coupler 2. There are reflected pulses in the coupler output. Investigation indicates that these reflections occur at the two cable terminations.

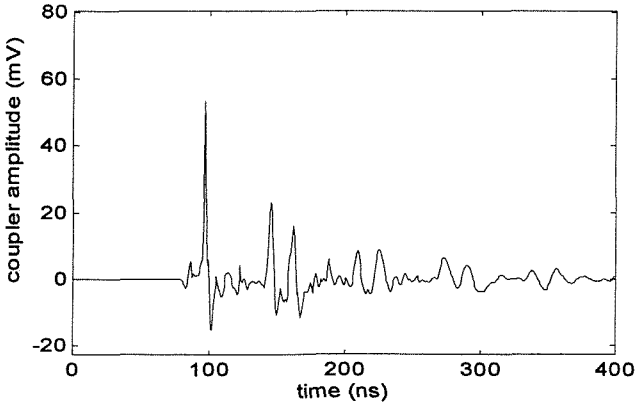

Figure 7.9 Coupler response to a calibration pulse from another coupler

In principle this method can only provide an approximate calibration result, as the calibration signal is injected into a coupler rather than the cable core. However, it might provide the only acceptable solution to capacitive coupler on-line calibration.

7.2.2.2 Internal discharge detection

A high voltage was applied to the joint in order to generate partial discharges from the conducting paint. The PD inception voltage was found to be 34 kV. Figure 7.10 shows coupler 1-output signal and the relevant discharge quantity obtained by conventional electrical detection. Discharges with magnitude of 5 pC can be detected by the capacitive coupler. Generally a proportional relationship exists between the capacitive coupler output and the discharge quantity, which is about 1.6 mV/pC. Considering the calibration result of 0.7 mV/pC from the cable termination and 1 mV/pC from injection via a second coupler, calibration errors exist for either of the proposed calibration methods although calibration from another coupler obtains a closer result.

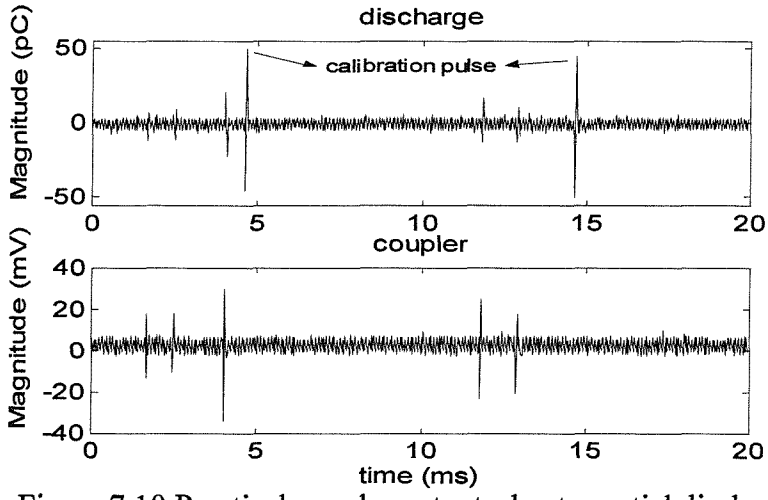

Figure 7.10 Practical coupler outputs due to partial discharges

The discharge pulse travelling speed within the cable section/joint was determined using the method introduced in chapter 6.3. A step wave was injected into cable termination A (Figure 7.1), and the time delay between coupler 1 and 2 is measured to be 6.7 ns. Given that the distance between the couplers is 1.05 m, the discharge pulse travelling speed for this cable/joint arrangement was thus estimated to be 0.157 m/ns. Figure 7.11 shows the output of the two couplers seeing the same discharge pulse. Coupler 1 leads coupler 2 with a time flight of 3.4 ns. This information gives an accurate estimate of the PD site location.

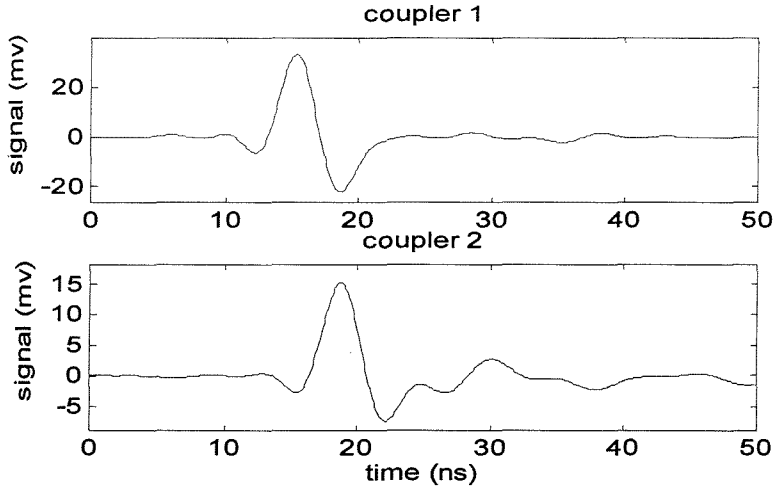

Figure 7.11 Time of flight for couplers installed at the cable joint system

Figure 7.12 shows the coupler 1 output waveform and frequency spectrum. Frequency components are within the frequency range up to 300 MHz. There are some reflections within the coupler waveform. The discharge pulse from the PD site travelled along the cable in opposite directions. The one travelling to the left was detected by the coupler (pulse 1). The same pulse continued to travel to the left and was reflected by cable termination A. The reflected pulse then travelled to the right and was detected again by the coupler (pulse 2). The original discharge pulse travelling to the right from the PD site was reflected by cable termination B, the reflected pulse travelled back to the left and later was detected by the coupler (pulse 3). Analysis of time of flights indicates that they agree with individual travelling distances, considering the known discharge pulse travelling speed along the cable system. The reflected pulses would continue to travel along the cable and were further reflected by cable terminations. However, due to the propagation attenuation and reflection, further reflections were not clearly visible.

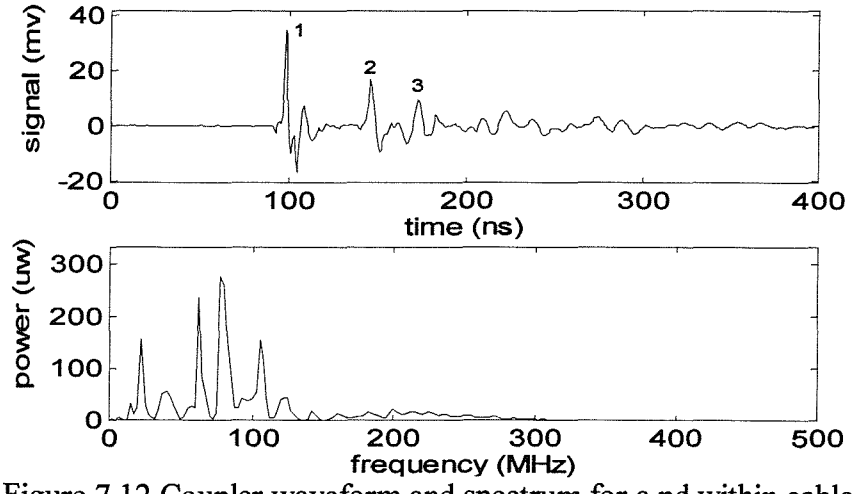

Figure 7.12 Coupler waveform and spectrum for a pd within cable joint

7.2.2.3 Corona discharge detection

Corona discharges were generated in order to study the capacitive coupler response to them. A sharp metal conductor was placed at cable termination A and pointed toward the earth. In this case, the corona inception voltage was 21 kV and the discharge level was 150 pC. Figure 7.13 shows the coupler 1-output magnitude within one voltage cycle, and is typical of the corona discharge characteristics. Figure 7.14 shows a single corona discharge waveform and its relevant power spectrum. Compared with Figure 7.12, the coupler output due to corona discharge has a longer time duration and contains lower frequency components. Figure 7.15 shows the time based signals for two coupler outputs due to corona discharge. Comparing the two traces reveals that the source of corona discharge is from the left side of coupler 1 rather than between the two couplers.

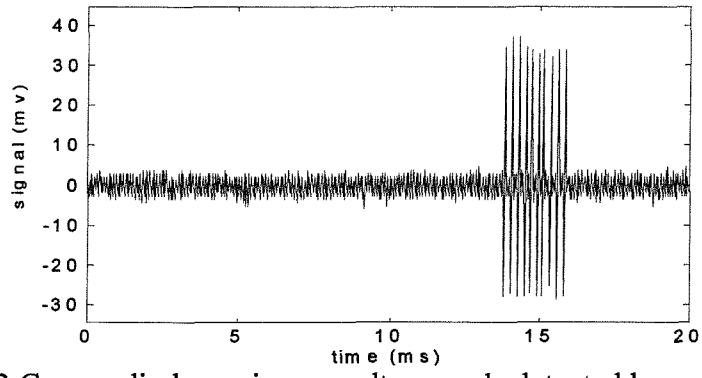

Figure 7.13 Corona discharge in one voltage cycle detected by capacitive coupler

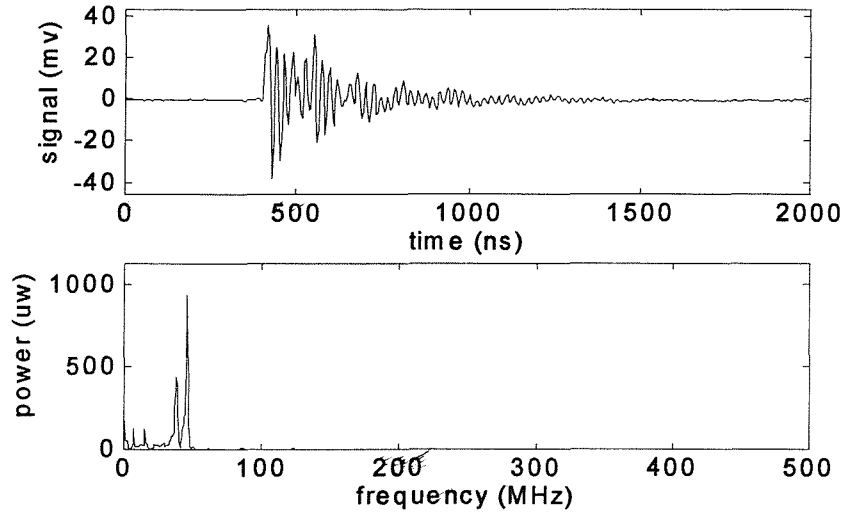

Figure 7.14 Capacitive coupler response to corona discharges

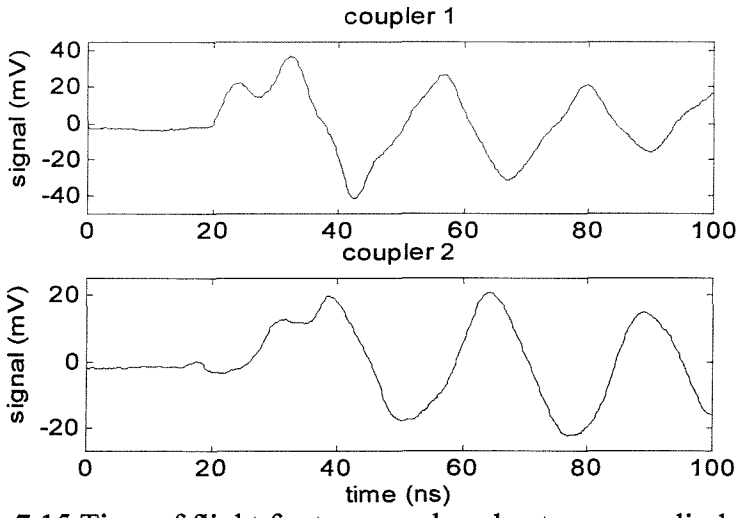

Figure 7.15 Time of flight for two couplers due to corona discharge

The obtained results indicate that the discharge pulse shape, its relevant frequency spectrum, and time of flight may be helpful in distinguishing between PD pulses from within the cable joint and external noise, providing two capacitive couplers are placed either side of the cable joint under test.

7.2.3 Acoustic emission detection

Acoustic emission sensors were applied to detect partial discharge activity within the cable joint. Investigation indicates that the AE sensor is immune to external electrical interference (Figure 7.3). Figure 7.16 shows the discharge acoustic and electric signals obtained immediately after the PD source was installed within the cable joint, at an applied voltage of 36 kV. The electric signals were obtained by conventional electrical detection. Partial discharge produces both acoustic and electric signals, and they relate each other with a time of flight which is the time required for the acoustic emission signal to travel from the PD site to the AE sensor. It should be noted that the PD source (v-shape conducting paint) may be altered by the partial discharge activity, due to the high temperature produced by discharge and local carbonisation of the insulation material. Figure 7.17 shows another set of discharge acoustic emission and electric signals, at the same voltage but after several weeks of testing. Compared to the initial case, the discharge level has decreased but the discharge repetition rate has increased. This indicates that the source of PD activity has altered as a result of the test regime.

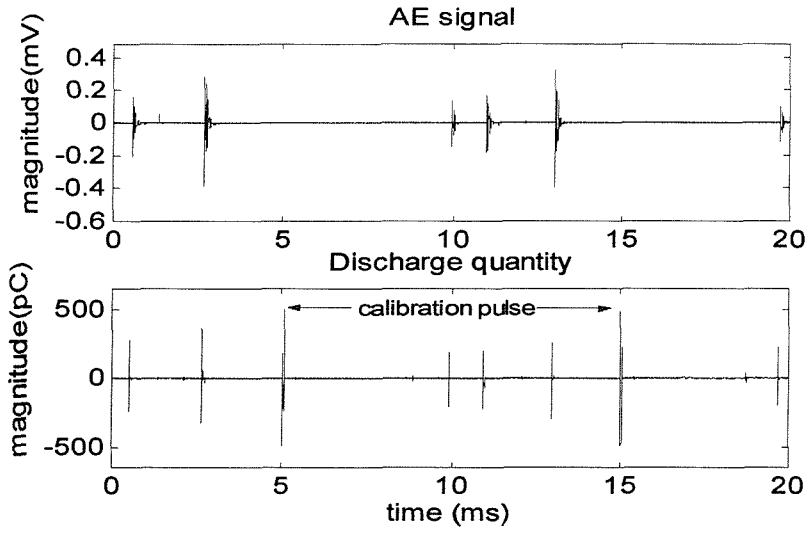

Figure 7.16 Discharge acoustic & electric signals (initially)

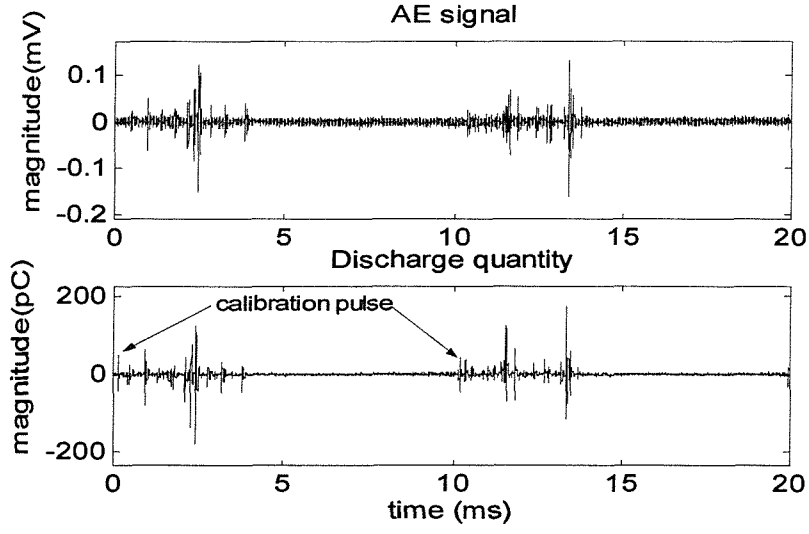

Figure 7.17 Discharge acoustic & electric signals (after several weeks)

A second AE sensor was then placed 85 mm away from AE sensor 1 and the discharge site, as shown in Figure 7.1. When the discharge level was 15 pC, AE sensor 1 can detect the acoustic emission signals but AE sensor 2 cannot (Figure 7.18). When the test voltage was increased and discharge level of 150 pC was obtained, both sensors can detect the acoustic signals, but the sensitivity is different (Figure 7.19). The results indicate that the AE signal attenuation is significant within the cable joint, which will consequently limit the PD acoustic emission detection sensitivity. However, in situations where electric noise is severe such as in the field, acoustic emission methods

may be more effective at detecting partial discharge activity rather than electrical couplers.

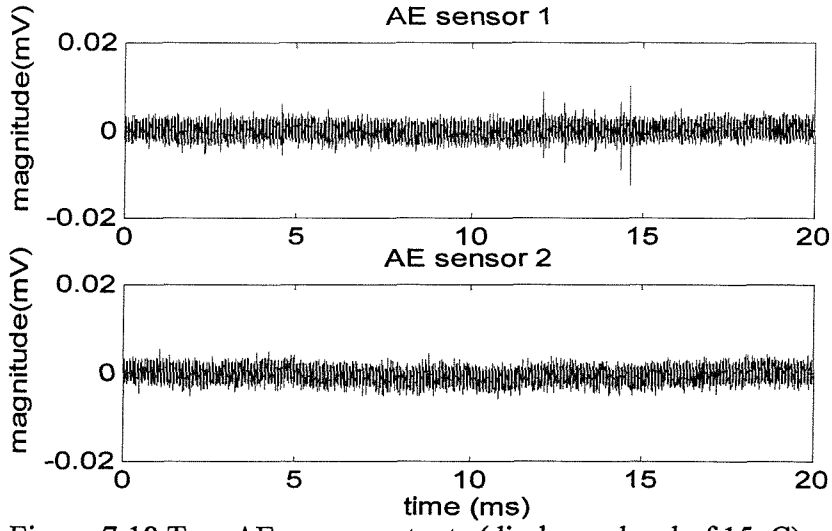

Figure 7.18 Two AE sensor outputs (discharge level of 15pC)

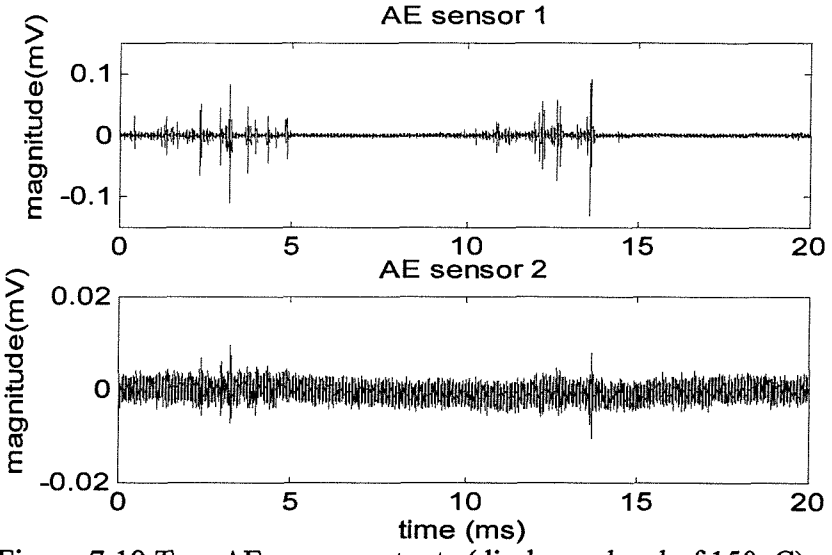

Figure 7.19 Two AE sensor outputs (discharge level of 150pC)

The distance from the PD site to the acoustic emission sensor can be calculated as the multiplication of the acoustic emission propagation time and velocity. Figure 7.20 shows the discharge electric pulse and two corresponding acoustic emission sensor output signals. In this case, the discharge electric pulse is obtained by the IEC 270 conventional detection. The time of flight is 45 μs between AE sensor 1 and the discharge pulse and 93 μs between AE sensor 2 and the discharge pulse. They agree with the practical geometric distance of 68 mm and 146 mm respectively from two AE sensors to the PD site, given that the acoustic emission wave propagation velocity is 1546 m/s in ethylene propylene rubber [7].

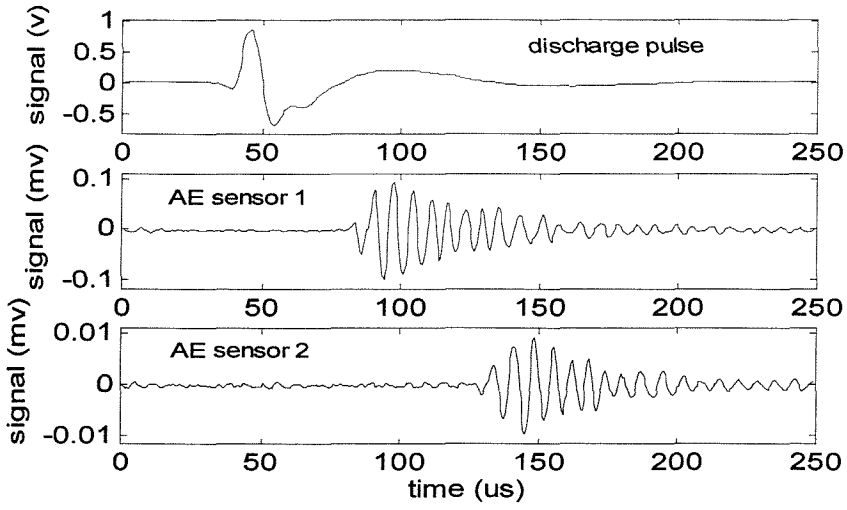

Figure 7.20 Time of flight measurements using AE sensors

For PD location using acoustic emission measurements, AE sensors have been applied to PD location in power transformers. Transformers have a relatively regular geometry and may be approximated as a rectangular object. Consequently the location in the three-dimensional space can be investigated. Three or more AE sensors can be installed at different positions, three-dimensional distances from the PD site to different sensors with known co-ordinates are related with the multiplication of the acoustic wave velocity and time of flight. Thus a series of equations can be obtained, which can be solved using a least squares algorithm and an iteration method [7,161]. Theoretically a similar location method can be applied to a cable joint. However, compared to a power transformer, the cable joint has less regular geometric shape and much smaller dimensions. Different insulation materials such as EPR and XLPE, semiconducting screen layers and conductors, will influence the acoustic wave propagation path and velocity. Therefore, in practice a convenient and feasible location method might be applying two AE sensors and moving them along the cable joint surface till the same time of flight is obtained for both sensors. This indicates that the PD site is in the middle of the two sensors.

Combination of PD electrical and acoustic emission detection can also be used for discriminating between partial discharges and noise. For partial discharges, the electric pulse leads the acoustic pulse with a time of flight, which corresponds to the propagation time of the acoustic wave from the PD site to the sensor (Figure 7.20). For any noise, one of three cases may apply: an electric pulse with no related acoustic

pulse; an acoustic pulse with no related electric pulse; or no time flight between the electric and acoustic pulses. Apart from the conventional electrical detection, the discharge electric pulse can also be obtained by non-conventional electrical sensor such as inductive current transducer.

7.2.4 RFCT approach

Intially only a RoCoil® ferrite core radio frequency current transducer (model 991/005) with small aperture (5mm) was available. It has a frequency range 2.5 KHz to 150 MHz. Figure 7.21 shows the detected signal. The RFCT output was amplified by the available wide band amplifier with frequency range up to 500 MHz and amplification gain of 24 dB. The discharge quantity was obtained by the conventional electrical detection. In this case the signal to noise ratio (SNR) is found to be low, resulting in low detection sensitivity. Only discharges above 90 pC were detectable.

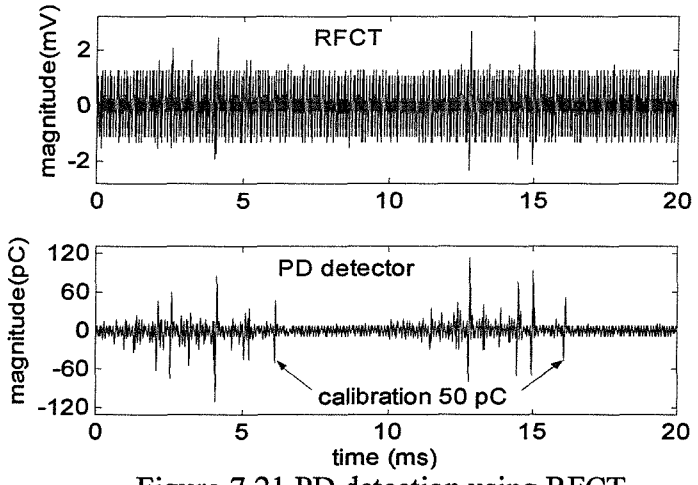

Figure 7.21 PD detection using RFCT

Figure 7.21 indicate that the measured RFCT signals are significantly influenced by the presence of electrical noise. The SNR can be improved using appropriate filtering techniques.

Many existing discharge signal de-noising methods are based on the Fast Fourier transform (FFT), where analysis of partial discharges is obtained using frequency information. The spectra of noise can be seen as sharp lines with peak values at respective frequencies, which can be minimised by applying a suitable threshold. An inverse transform is then applied to obtain filtered time-based data. However, a discharge pulse may cover a wide range of frequencies. Therefore, when

noise is reduced, some components of PD signal itself may be lost through conventional filtering. Moreover, the FFT algorithm is based on a deterministic data set. De-noising methods developed using the FFT are therefore limited in processing PD signals that are stochastic in nature.

Due to the limitation of the conventional de-noising methods using Fourier transforms, the wavelet transform is becoming popular for PD signal de-noising. Discharge signals and random noise have different behaviour under the wavelet transform. In section 5.3.3, wavelet transform was applied to decompose the acoustic emission signals. For filtering the signal is decomposed into a series of approximation and detail coefficients at various scales. Thresholding of wavelet coefficients is then conducted by retaining the wavelet coefficients corresponding to discharge events and discarding all noise coefficients. Finally PD signals are reconstructed using the modified approximation and detail coefficients. For wavelet de-noising, the selection of the wavelet basis function (wavelet family) and the selection of thresholding method are important. There are various wavelet families, such as Haar, Daubechies, Biorthogonal, Coiflets, Symlets, Morlet, Mexican Hat, and Meyer wavelet. Usually two thresholding methods are used: "soft"and "hard"[162].

In this case, Daubechies db2 wavelet (2 denotes a wavelet order) and soft thresholding method were found to be able to obtain the best result. Figure 7.22 shows the RFCT signals after de-noising and the relevant discharge quantity obtained by conventional PD detection. The SNR has been improved, and discharges of 30 pC can now be recognised.

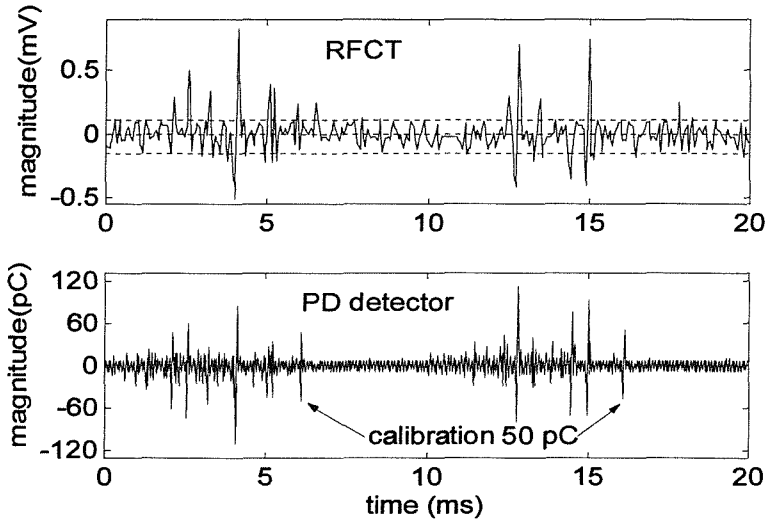

Figure 7.22 Wavelet de-noising of RFCT signals

An EMCO® ferrite core RFCT (model 93686-5) was also applied. It has a frequency range 10 KHz to 200 MHz, and an aperture of 67 mm. The RFCT is a split type, therefore it can be applied without interrupting the circuit. Figure 7.23 shows the detected PD signals. The RFCT output was amplified using the wide band amplifier. The discharge quantity was obtained by conventional electrical detection. The detection sensitivity for this RFCT is about 20 pC, which is much higher than the result obtained using the Rocoil® small aperture ferrite RFCT.

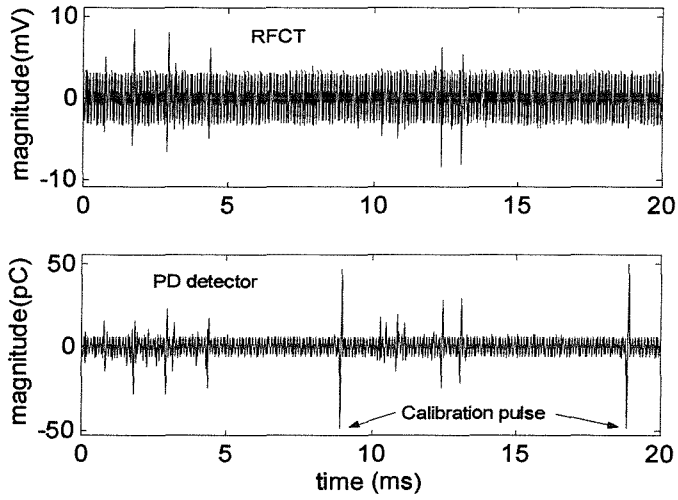

Figure 7.23 PD detection using EMCO RFCT

Figure 7.24 shows a RFCT detected discharge waveform and its relevant power spectrum. The frequency components extended to 100 MHz but were dominant below 40 MHz.

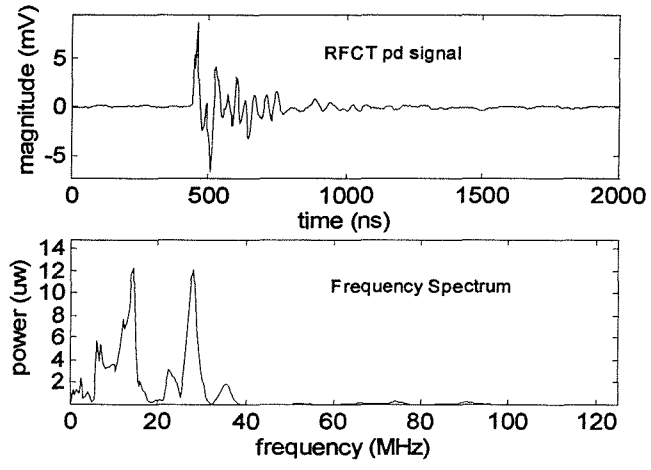

Figure 7.24 RFCT PD signal and frequency spectrum

The RFCT was also used to detect corona discharge. A sharp point was placed at the high voltage coupling capacitor and pointed toward the earth. In this case, the corona inception voltage was 15 kV and the discharge level was 35 pC. Figure 7.25 shows the RFCT detected signals and the discharge quantity obtained by the conventional electrical detection, which indicates the typical characteristics of corona discharge.

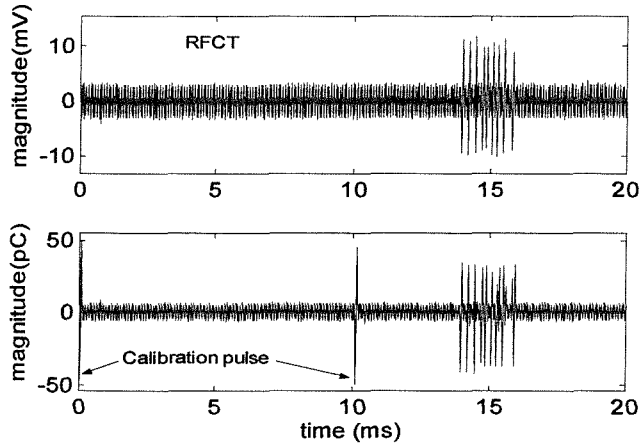

Figure 7.25 Corona discharge in one voltage cycle detected by RFCT

7.3 PD Test for a Cable Section with Water Terminations

7.3.1 Test arrangement

The capacitive coupler, the screen interruption method (section 3.3.2.1), and conventional electrical detection were also used for PD detection within a 90 kV XLPE cable section having de-ionised water terminations. The test arrangement is shown in Figures 7.26 and 7.27. The test transformer, high voltage coupling capacitor, partial discharge detector, input unit, surge protector, amplifier and digital oscilloscope are the same as used for the cable joint PD test (section 7.2.1). In this case the detection sensor was either a capacitive coupler or a screen interruption sensor.

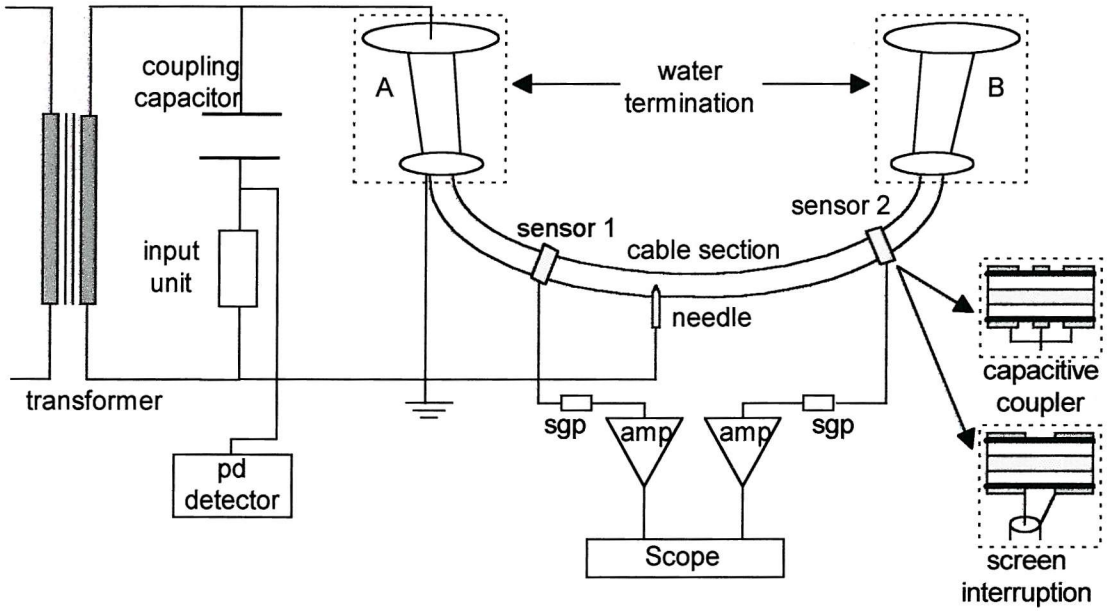

Figure 7.26 PD test arrangement for cable section with water terminations

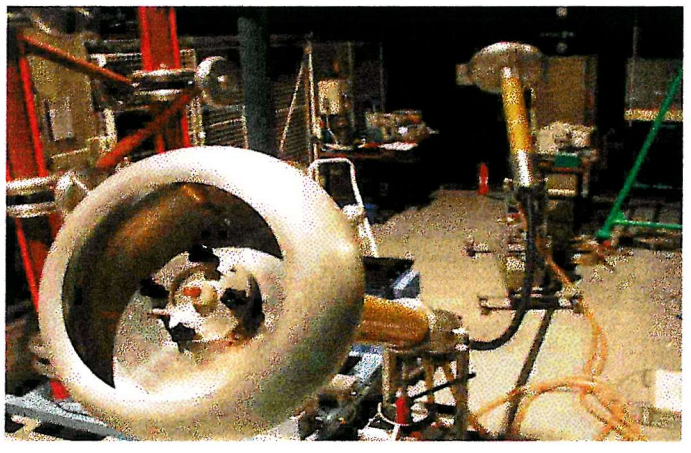

Figure 7.27 Photo of the PD test arrangement for cable section

The cable section (excluding the water terminations) is about 3m long. Sensor 1 is 0.8m away from the bottom of water termination A, and sensor 2 is 0.4 m away from the bottom of water termination B. The distance between the two sensors is 1.8 m.

In order to produce partial discharges from the cable section, a sharp tungsten needle was inserted into the cable insulation between the two sensors (0.6 m to sensor 1 and 1.2 m to sensor 2), approximately 3mm away from the inner conductor semicon screen. The tungsten needle has a 1mm-diameter shank leading to 3 μm pin-tip radius.

7.3.2 Capacitive coupler measurements

To make a capacitive coupler, 100mm long cable sheath was removed and a tin tape with diameter of 40 mm was wrapped around the exposed cable outer semicon screen.

Capacitive coupler calibration was attempted using a step wave from a pulse generator, in series with a capacitance of 6 pF, injected into the cable core at water termination A. The step wave had a rise time of 1ns and magnitude of 5v. The equivalent injected charge is therefore estimated to be 30 pC. Coupler 1 output magnitude was about 160 mV, indicating a calibration result of 5.3 mV/pC. This calibration result is different from the cable joint, indicating that each cable system would need to be calibrated individually.

The step wave from the pulse generator, with rise time of 1ns and magnitude of 5v, was then injected into coupler 2. According to Equation (6.1), the capacitance per meter of the 90 kV XLPE cable is calculated to be 153 pF/m. Consequently the capacitance is about 6pF and the equivalent injected charge is about 30pC. The relevant coupler 1 output magnitude was about 195 mV, indicating a calibration result of approximately 6.5 mV/pC for the cable system under PD test.

When the applied voltage was increased to 3 kV, some discharges occurred from the needle tip. Figure 7.28 shows the conventional PD detector output and the coupler 1 output respectively. The coupler gives an output magnitude of 18 mV, which corresponds to 2.8 pC if calibration across coupler is applied. The discharge pulses that relate to the two coupler pulses were mixed up with the background noise that is about 3 pC.

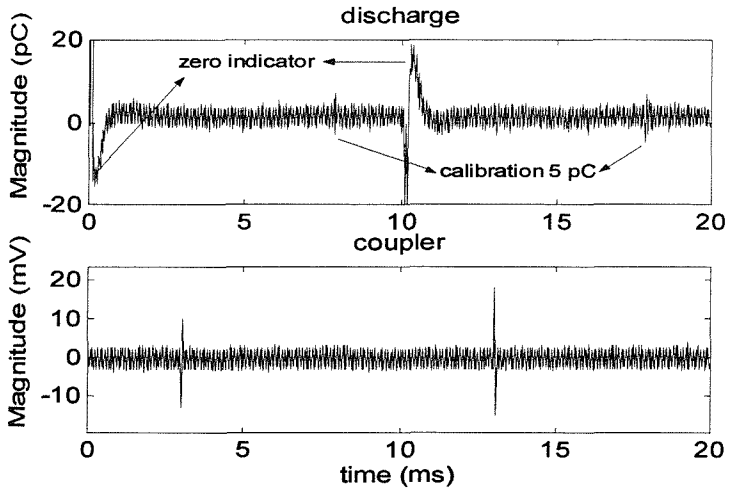

Figure 7.28 Detection of PD from cable section using capacitive couplers

A pulse from the pulse generator, with a rise time of 1ns and width of 2ns, was injected into water termination A, and the time of flight between coupler 1 and 2 was found to be 10.2ns. Considering the distance between coupler 1 and 2, the discharge travelling speed for the cable was estimated to be 0.176 m/ns.

Figure 7.29 shows the coupler 1 and 2 outputs, due to a partial discharge from the needle. Coupler 1 leads coupler 2 with a time of flight of 3.4ns. This corresponds with a distance of 0.6 m, which is the distance difference from the PD site to the two couplers.

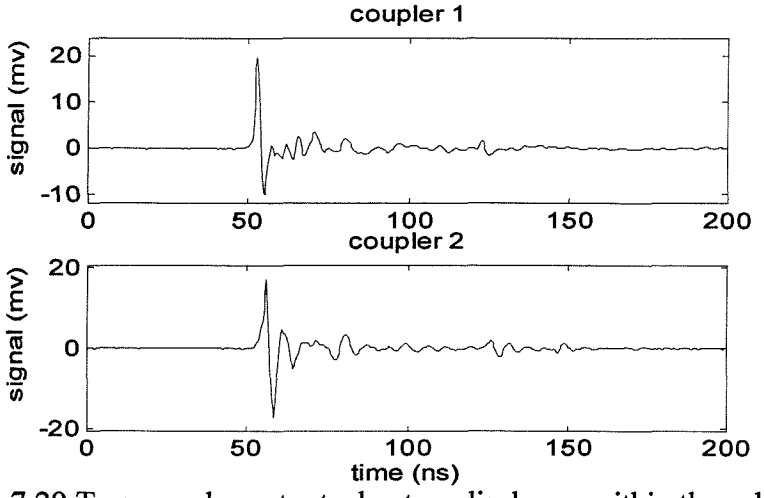

Figure 7.29 Two coupler outputs due to a discharge within the cable section

7.3.3 Screen interruption method

The PD screen interruption detection, as introduced in section 3.3.2.1, was also tried in this case. Different lengths of cable sheath from 25 mm to 200 mm was removed, and

a coaxial measuring cable was connected over the interruption in the cable metal sheath (Figure 7.26).

The influence of length of the screen interruption on the signal measurement was investigated. A step wave from the pulse generator with magnitude of 1v and rise time of 1 ns, in series with a capacitance of 6 pF, was injected into water termination A. The relationship between the measurement and the sheath interruption length is shown in Figure 7.30. The results indicate that the output magnitude generally increases with the length of sheath interruption, but the rate of increase is less significant once the interruption is over 65 mm.

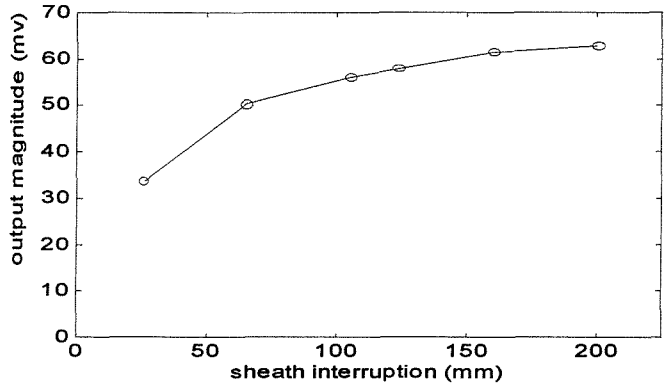

Figure 7.30 Influence of sheath interruption dimension on signal measurement

Figure 7.31 shows the two screen interruption outputs due to a discharge from the needle tip. Interruption 1 leads interruption 2 with a time flight of 3.4 ns. This agrees with the coupler measurement and indicates that this method may also be used to locate PD site.

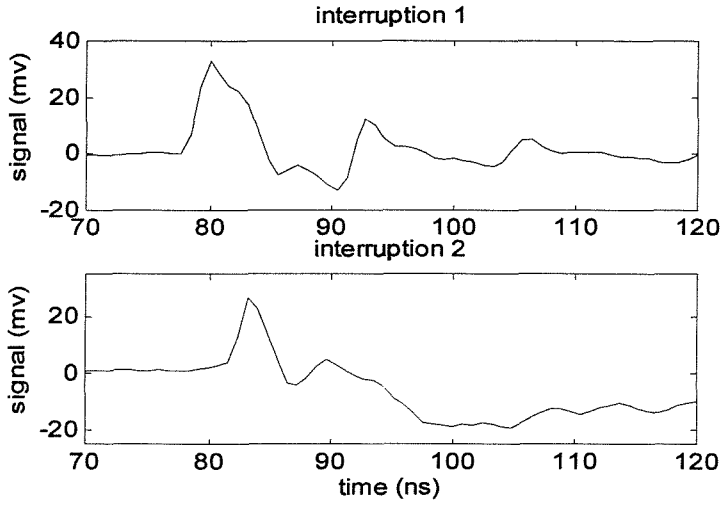

Figure 7.31 Investigation of time of flight using interruption detection

Figure 7.32 shows the signal and frequency spectrum for the interruption method and the capacitive coupler method respectively. The screen interruption method also works in the very high frequency range, but its bandwidth is less than the capacitive coupler approach.

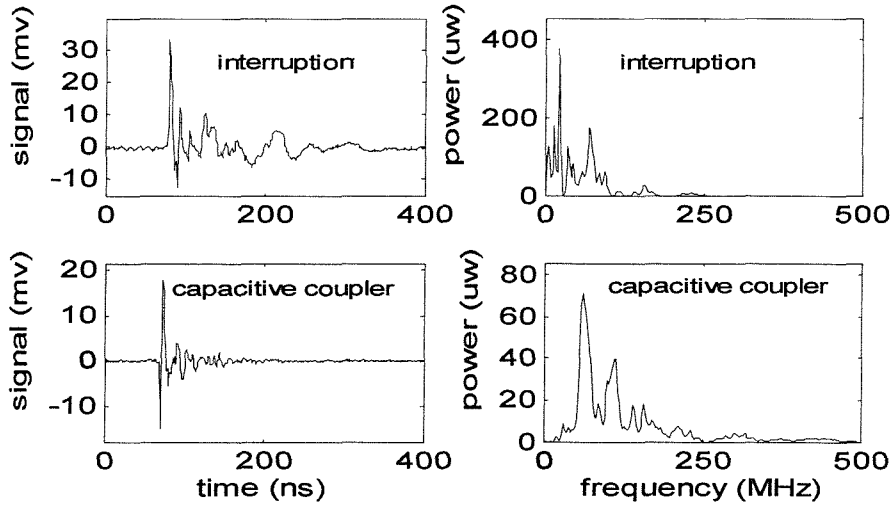

Figure 7.32 Signal and spectrum for interruption and coupler methods

Figure 7.33 shows the detected signals for one voltage cycle for the screen interruption and the capacitive coupler method respectively. For both approaches, 100m long cable metal sheath was removed. The interruption approach gives higher output signal magnitude. However, the background noise level is also much higher. The overall SNR for the interruption method is lower than the capacitive coupler method.

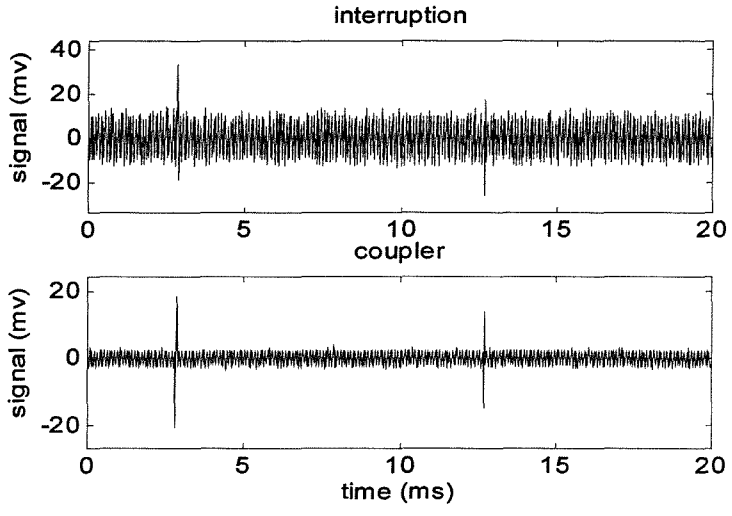

Figure 7.33 Comparison of interruption and coupler results for one power cycle

It should also be noted that the screen interruption method might limit the short circuit current handling ability. For on-line measurements, one has either to short the measurement impedance by an inductor which can handle the short circuit current or over voltage protection needs to be placed in parallel with the impedance. Moreover, the open structure of the screen interruption method means that it is easily influenced by external electromagnetic noise.

7.4 Summary

An investigation into different PD detection methods for cable systems has been undertaken. Capacitive couplers, acoustic emission sensors and radio frequency current transducers were applied to detect partial discharges from a 132 kV cable/joint system. Calibration for a capacitive coupler was realised by injecting a very high frequency calibration pulse into either the cable termination or into another capacitive coupler. For calibration using the cable termination, attenuation in the cable termination and cable itself effect calibration signals and change their waveform before they reach the coupler, which introduces calibration errors. Calibration using two capacitive couplers may provide the only practical solution to on-line calibration. The equivalent model for this calibration method has been established. The calibration result is generally proportional to the injected charge.

Location of a PD site can be realised by analysis of time of flight from two or more capacitive couplers. Capacitive couplers were also used to detect external corona discharges. The results indicate that the coupler output pulse shape, relevant frequency spectrum, and time of flight traces may be used to distinguish between internal discharges from the cable joint and external sources of noise.

Acoustic emission sensors were used to detect partial discharges from within the cable joint. Investigation indicates that AE sensor is immune to the electrical interference. Partial discharges produce both electric pulses and acoustic emission waves, and they are related to each other by a small time delay that is the required time for the acoustic emission wave to travel from the PD site to the sensor. Acoustic wave attenuation within the cable joint has been studied, and the obtained results indicate that signal attenuation is significant. The acoustic wave attenuation will limit the detection sensitivity, and also makes it very difficult to quantify the detected AE signal with a discharge quantity in Pico-coulomb. However, in situations where noise is

severe, the acoustic emission method may provide higher detection sensitivity than electrical methods of conventional detection or non-conventional coupling.

Acoustic location of a PD site was investigated by the analysis of time of flight between the discharge electric pulse, and different AE sensor output waveforms. The location of a PD site may be determined by calculating the three-dimensional distances from the PD site to different sensors, which is calculated as the multiplication of the acoustic wave velocity and time of flight. Acoustic wave propagation paths and velocities are influenced by different cable insulation materials such as EPR, XLPE, and semiconducting PE. Considering the cable joint geometry, in practice it would be convenient to apply two AE sensors and move them along the cable joint surface, to estimate the PD site.

Intially a Rocoil® ferrite core RFCT with small aperture was used to detect the discharge current flowing through it. Obtained results indicate that the detection sensitivity is low, only discharges above 90 pC were detectable. A wavelet transform was applied to process the obtained signals. Signals were decomposed into the approximation and detail components, then the decomposed components were modified by a thresholding operation, and finally the time-based signals were reconstructed from the modified components. Through the use of wavelet de-noising the SNR was improved such that discharges of 30 pC could be observed. An EMCO® split ferrite RFCT with large aperture was also applied to detect the discharge current. Obtained results indicated that in this case the detection sensitivity increased to 20 pC without the need for additional signal processing.

Capacitive couplers were used to detect PD activity within a 90 kV XLPE cable section with water terminations. Calibration of the coupler yielded a different sensitivity compared to values obtained from the 132 kV cable joint, indicating that different cable systems need to be calibrated individually.

Finally the screen interruption method was investigated. Frequency spectrum analysis revealed that this method also works in the very high frequency range up to about 250 MHz. PD location by time of flight can also be achieved using the screen interruption method. Compared with capacitive coupling, it gives a higher output signal magnitude, but the background noise is significant, resulting in lower overall SNR. The open structure of the screen interruption method means that it is easily influenced by external electromagnetic noise. Furthermore, the screen interruption limits the short current handling ability. For both the screen interruption and capacitive

coupler methods, a short length of cable metal sheath has to be removed, which is a disadvantage for on-line monitoring applications.

Chapter 8

Conclusions and Further Work

8.1 Conclusions

The application of the acoustic emission and capacitive coupling techniques to partial discharge detection for cable insulation system has been investigated.

Acoustic emission measurement of partial discharges was initially investigated using a planar experimental model. Signal processing of measurement data was carried out in both the time and frequency domains. As partial discharge is a stochastic process, the statistical characteristics of PD AE signals were also analysed. This was realised by the use of two-dimensional phase-related histograms ($H_{qmax}(\varphi)$, $H_n(\varphi)$ and $H_{qn}(\varphi)$), the three-dimensional φ-q-n pattern, and statistical operators including skewness, kurtosis and the correlation coefficients. It was found that the AE signal magnitude and repetition rate both increase with increased electric stress and void size. On the other hand, the void discharge activity gradually attenuated with increased test time. The electric stress, void size and test time all affected the statistical operators. The acoustic emission attenuation at the acoustic interface, e.g. between the AE sensor and the cable insulation, was found to be more significant than attenuation within cable insulation. Therefore, application of an acoustic couplant was necessary. Acoustic emission signals are attenuated more in ethylene propylene rubber than in polyethylene. The relationship between the discharge acoustic and electric signal was investigated both by theoretical analysis and by experimental measurement. The

discharge electric signals were obtained by conventional PD electrical detection according to IEC 270. Under experimental conditions, similar statistical characteristics could be obtained for both the discharge acoustic and electric signal. However, it should be noted that it is very difficult to quantify the apparent charge (pC) from acoustic emission measurement.

Acoustic emission measurements were used to investigate partial discharge behaviour during electrical tree growth within XLPE insulation. Different experimental conditions such as pin tip radius, pin-plane spacing and applied voltage, determine the type of tree, such as bush-type or branch-type. The gas pressure within the tree channel and the space charge effect also influence the breakdown process. Investigation indicates that insulation breakdown could not be predicted solely from discharge magnitude. AE measurements were also used to detect and locate partial discharges produced from within epoxy samples. These experimental investigations provided an insight into PD acoustic emission detection for practical cable systems.

Two artificial neural networks, the feed forward neural network using back propagation and the self organising map neural network using learning vector quantization, were implemented to characterise different acoustic emission sources. Frequency spectra obtained by the short duration Fourier transform (SDFT) and wavelet decomposition components were used as ANN input data. Generally the identification performance of both artificial neural networks using SDFT spectrum or wavelet decomposition were good, and 100% identification rate could be obtained when different void shapes and noise were characterised. When ANNs were applied to identify AE signals produced from six patterns of void(s) with different locations and noise, a 97% correct rate was obtained. 93% correct rate was obtained when ANNs were applied to identify between void discharge, treeing discharge and noise. The performance of the artificial neural networks was improved by careful selection of the number of processing elements in the hidden layer, the number of training cycles and the number of training sets.

PD detection by means of the capacitive coupler technique has been investigated. The capacitive coupler does not affect the insulation system because the high potential electrode of the coupler is attached on top of the cable semicon screen that serves as the power frequency ground. The influence of coupler dimension, sensor material and contact area were investigated. The capacitive coupler performs well in the very high frequency range. Capacitive couplers were applied to detect partial

discharges on a cable section. The PD site can be accurately located by studying the time of flight between two capacitive couplers. The attenuation of a discharge during its propagation caused the loss of higher frequency components and resulted in a less obvious starting edge of the output waveform. To remove the power frequency background due to the applied voltage from the capacitive coupler output, a high pass filter and amplifier can be used.

An alternative PD test method for long cable systems using the capacitive coupler technique has been investigated. This method reduces the power supply demands of the testing system but requires an insulation gap, by removing both the cable ground sheath and the semicon screen, to be implemented at either end of the test section. Obtained results indicate that the peak amplitude of the detected signal is reduced by 50% after a 300 mm gap, but PD activity is still detectable. A simulation model was developed to investigate the performance of capacitive coupler with an insulation gap, and simulation results agree with practical experiments. A fast pulse generator was used to calibrate a capacitive coupler following an insulation gap, and the practical PD test results are in agreement with the calibration results.

Potential PD on-line detection methods for cable joints, including the acoustic emission technique, the capacitive coupler technique and the radio frequency current transducer technique, have been investigated. An artificial defect was created within a cable joint. Location of the PD site was realised by studying the time of flight from different capacitive couplers. The investigation indicated that the coupler output pulse shape, relevant frequency spectrum, and time of flight traces can be used to distinguish internal discharge activity from external noise. On-line calibration of the capacitive coupler was realised by injecting a very high frequency calibration pulse into one coupler and measuring the signal at another coupler. Acoustic location of the PD site was investigated by evaluating time of flight between the discharge electric pulse, and different acoustic emission sensor outputs. Acoustic emission sensors did not respond to electrical noise, however, the acoustic emission attenuation within the cable joint was significant. Attenuation reduced the detection sensitivity, and made it difficult to quantify the detected AE signal with a discharge quantity in pico-coulomb. However, in field situations where electrical noise may be severe, the acoustic emission method might provide higher detection sensitivity than other electrical methods (conventional detection or non-conventional coupling). Ferrite core RFCTs were applied to detect the discharge current. A detection sensitivity of 20 pC can be obtained using a RFCT.

Investigation indicates that the signal/noise ratio can be improved by means of wavelet denoising. A screen interruption method, which works in the very high frequency range up to about 250 MHz, has also been investigated. Location of a PD site can also be realised by time of flight analysis. Investigation indicated that the overall detection sensitivity for this method is lower than the capacitive coupler. The screen interruption also limits the short circuit current handling ability.

8.2 Further Work

Further research is required in the following areas:

- Partial discharge pattern identification

Voids of different shape, size, location and number could be created within a practical cable joint. In such cases the acoustic emission signal statistical characteristics, frequency spectrum, relationship between the discharge electric and acoustic signals, could be further investigated. The developed pattern identification technique (chapter 5) could then be applied and verified for a practical cable/joint system. It would also be helpful to further investigate the electrical ageing process due to electrical tree growth within practical cable/ joint system.

PD pattern identification using the capacitive coupler technique could be further investigated by means of artificial neural networks. The feasibility of using the capacitive coupler frequency spectrum as an ANN input vector should be investigated.

- PD on-line monitoring

The acoustic emission, capacitive coupler and inductive current transducer techniques could be applied to PD on-line detection and location for practical cable system. Environmental noise under field conditions could be significant, rejection of noise would therefore be vital to successfully implement on-line monitoring. It would be helpful to improve the design and manufacture of the capacitive coupler, to increase its electromagnetic noise rejection capability. Various signal processing methods, such as time averaging, cross correlation analysis, frequency filtering, adaptive digital filtering, wavelet denoising, could be further investigated. Application of fibre optics to signal transmission should be investigated. This could provide protection for the measurement system, as well as reducing the influence of noise. The application of

acoustic emission, capacitive coupler and inductive current transducer techniques to PD detection and location could also be extended to cable terminations.

Appendix A

Developed Software

The flow chart of the developed software is shown in Figure A.1. Figure A.2 shows examples of the software user interface. The software includes the following MatLab® programs:

Initialization Part:

pddetect.m---------- Initialization

pd.m ---------- Software Menu&Submenu

Acoustic Part:

aloaddat.m ----------Load acoustic signal part 1

aload.m ----------Load acoustic signal part 2

abfilter.m ----------Acoustic signal before filter

aafilter.m ----------Acoustic signal filter part 1

aawlet.m ----------Acoustic signal filter part 2

acalib.m ----------Acoustic signal calibration part1

acalibd.m ----------Acoustic signal calibration part 2

asfig.m ---------- Acoustic signal statistics figure

asval.m ---------- Acoustic signal statistics value

ascomput.m ---------- Acoustic signal statistics computation

caliball.m ---------- Calibrate all acoustic signals

wavelet.m ---------- Wavelet decomposition

frequency.m---------- Frequency spectrum

freqfilt.m ----------Frequency filter

Electric Part:

eloaddat.m ---------- Load electric signal part 1

eload.m ---------- Load electric signal part 2

elenoise.m ---------- Electric noise

ebfilter ---------- Electric signal before filter

efilter.m ---------- Electric signal filter part 1

eawlet.m ---------- Electric signal filter part 2

ecalib.m ---------- Electric signal calibration part 1

ecalibd.m ---------- Electric signal calibration part 2

esfig.m ---------- Electric signal statistics figure

esval.m ---------- Electric signal statistics value

escomput.m ---------- Electric signal statistics computation

ecaliball.m ---------- Calibrate all electric signals

Acoustic&Electric Part:

aefig.m ---------- Acoustic &Electric figures

aerelat.m ---------- Acoustic & Electric amplitude comparison

Neural Network Part:

nnload ---------- NN dialogue

nnloadf ---------- Load NN data

annbpff.m ---------- BP NN using SDFT

annbpdff.m ---------- BP NN training using SDFT

annbptff.m ---------- BP NN testing using SDFT

annbpwv.m ---------- BP NN using Wavelet

annbpdwv.m ---------- BP NN training using Wavelet

annbptwv.m ---------- BP NN testing using Wavelet

annlvqff.m ---------- LVQ NN using SDFT

annlvqdff.m ---------- LVQ NN training using FFT

annlvqtff.m ---------- LVQ NN testing using FFT

annlvqwv.m ---------- LVQ NN using Wavelet

annlvqdwv.m---------- LVQ NN training using Wavelet

annlvqtwv.m---------- LVQ NN testing using Wavelet

Electric coupler part:

eccorrt.m	----------	Time-based correlation
eccorrf.m	----------	FFT based correlation
ecfft.m	----------	Frequency response
ecgap.m	----------	Amplitude attenuation with gap
ecgapsig.m	----------	Coupler output with different gap
eccal.m	----------	Coupler calibration
ectest.m	----------	Practical test signal processing

Other part:

running.m	----------	Software interface
quitask.m	----------	Software interface

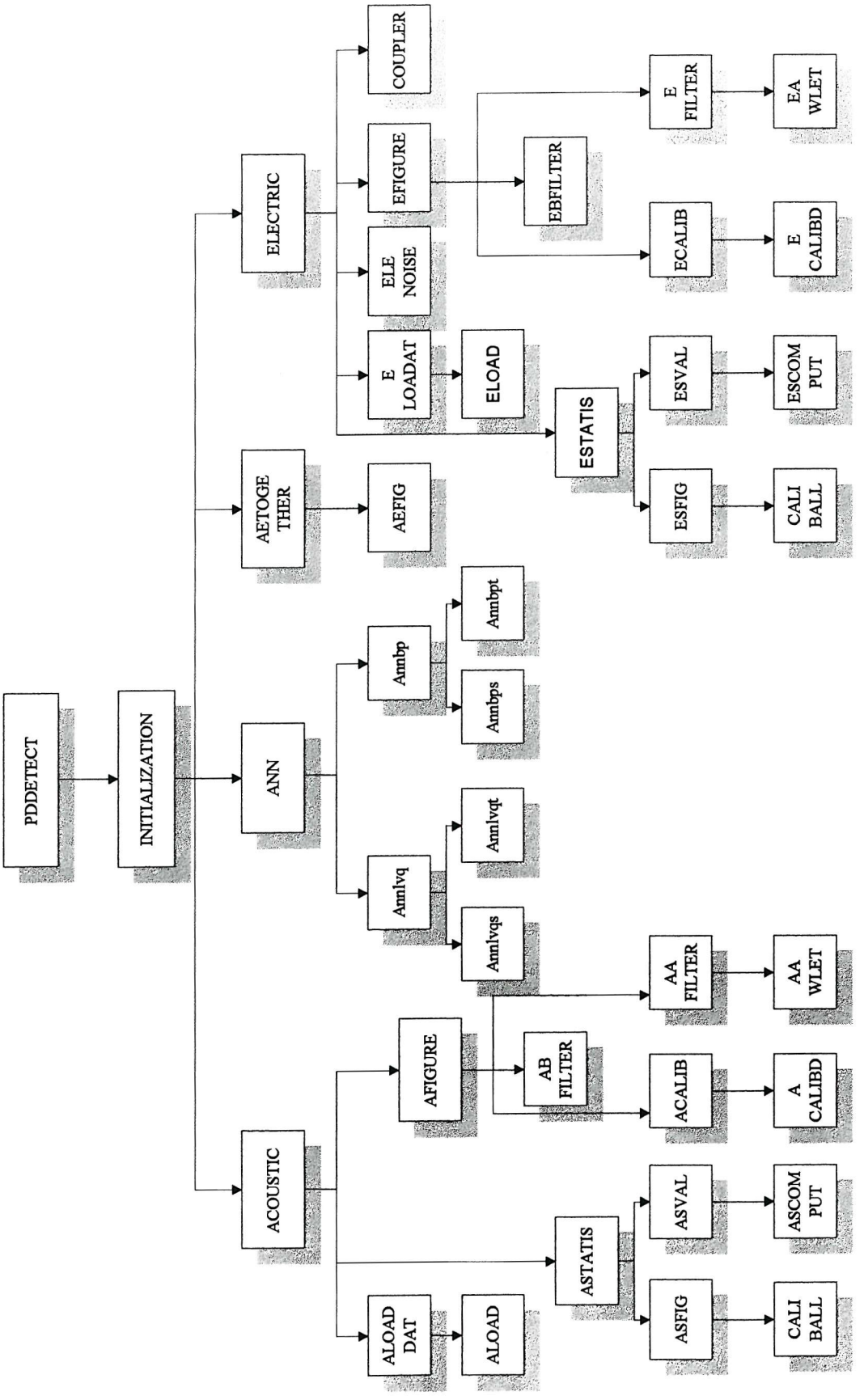

Figure A.1 The software flow chart

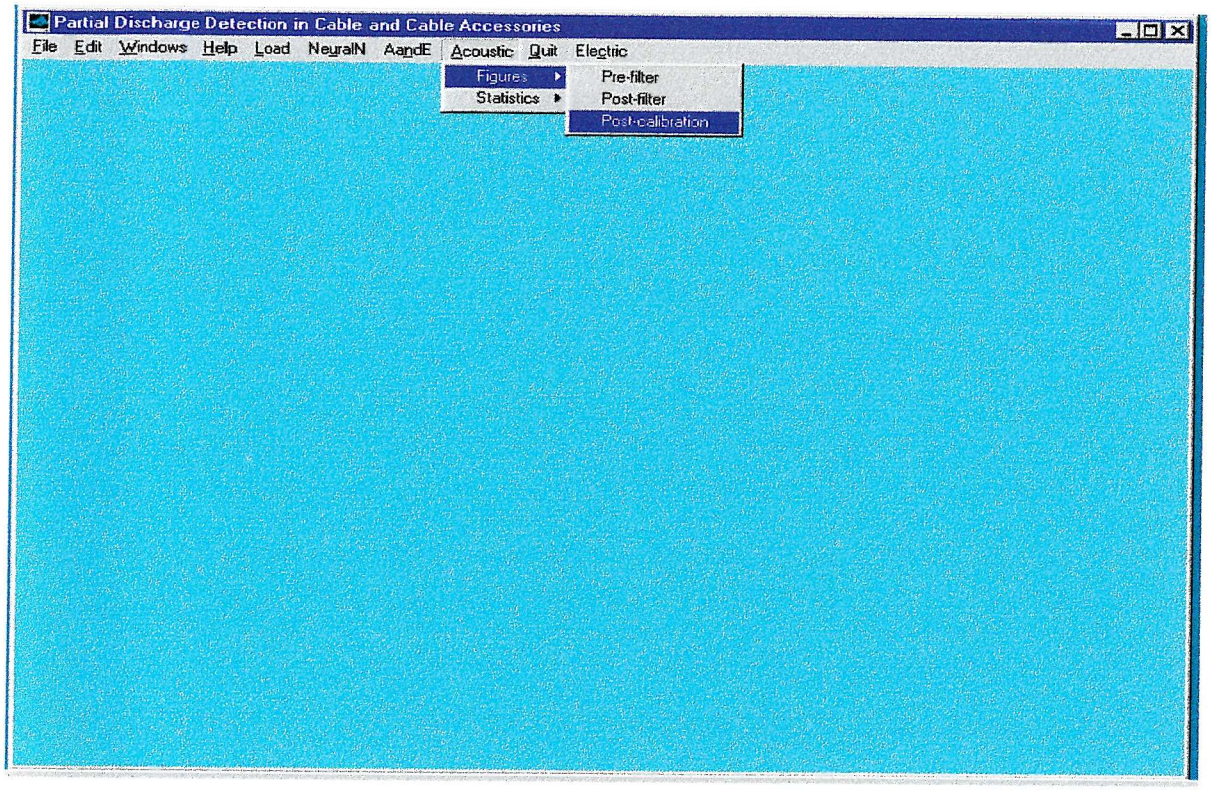
Partial Discharge Detection in Cable and Cable Accessories
File Edit Windows Help Load NeuralN AandE Acoustic Quit Electric
Figures
Statistics
Pre-filter
Post-filter
Post-calibration

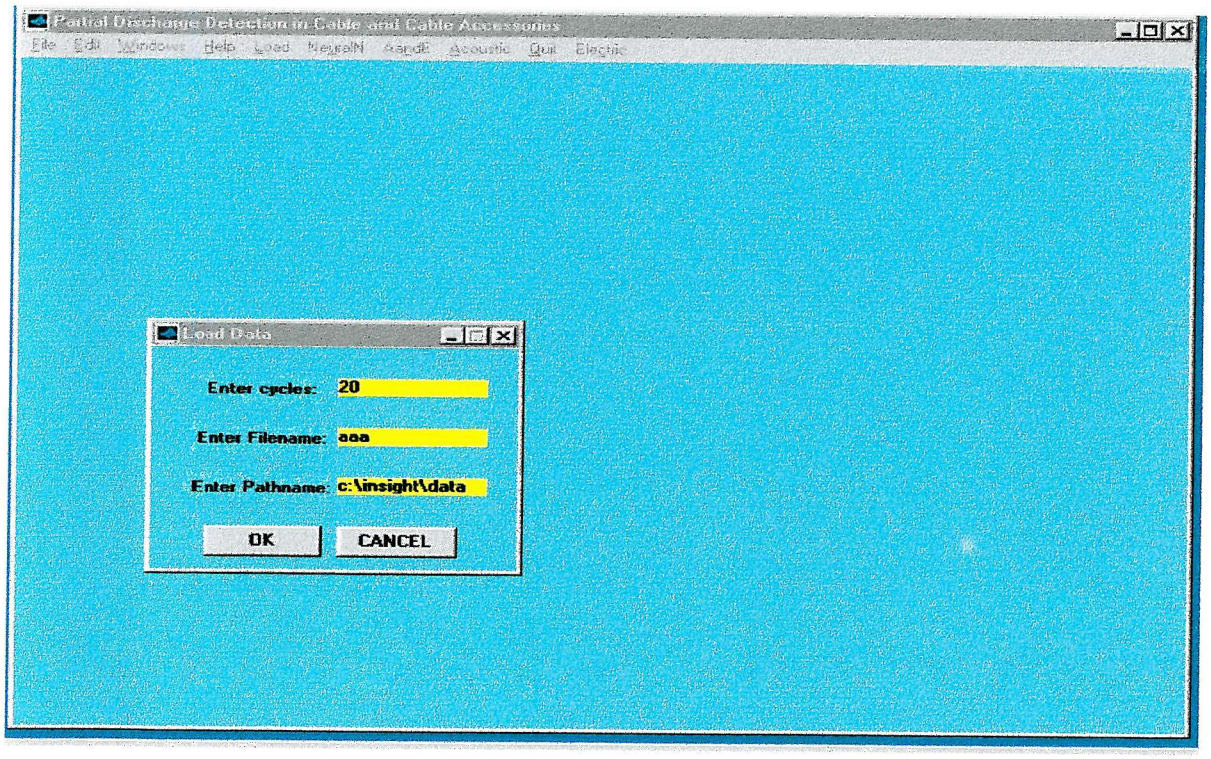
Partial Discharge Detection in Cable and Cable Accessories
Load Data
Enter cycles: 20
Enter Filename: aaa
Enter Pathname: c:\insight\data
OK
CANCEL

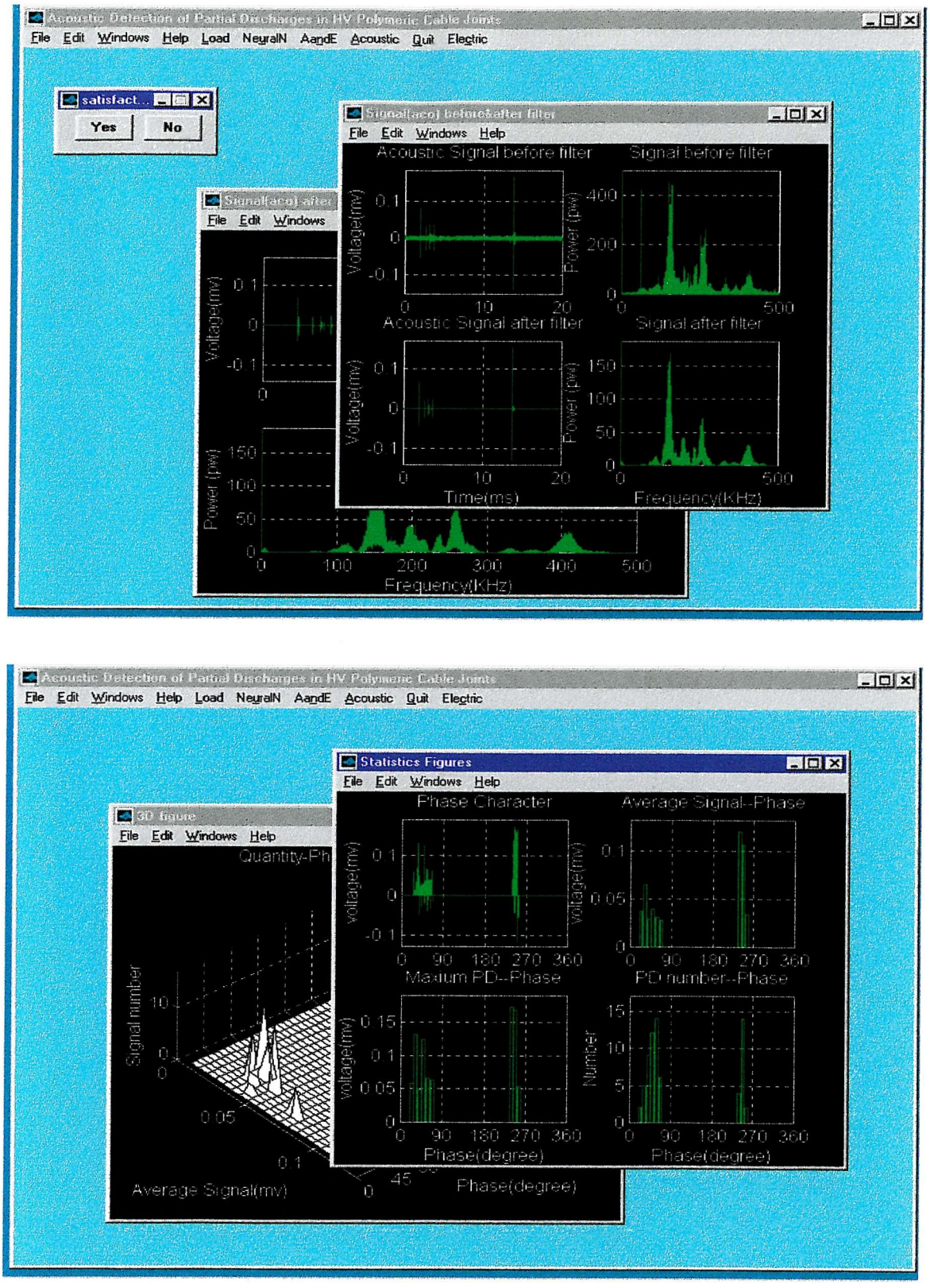

Figure A.2 Examples of the software user interface

A Selection of Software Programs

```
%-------------------------------------------------%
% Written by Yuan Tian. 1998. Version 1.0    %
%-------------------------------------------------%
```

```
% PDDETEN.M                    % initialization

function[]=pddeten();

global ACOU ELEC ECAL EFIL ACAL AALL AFIL sigt N frs NNF NNT NNJ ANN;
ACOU=0; ELEC=0; ECAL=0; EFIL=0; ACAL=0; AALL=0; AFIL=0; NNF=100; NNT=0; NNJ=0;
ANN=0; ANNBP=0; ANNLVQ=0; ANNSM=0;

pd;                          % call the user interface program
```

```
% PD.M                        % creating user interface

function PD(command,parameter1)

if nargin == 0
        command = 'new';
end

if isstr(command)
        if strcmp(lower(command),'initialize') | strcmp(lower(command),'new')
                command = 0;
        elseif strcmp(lower(command),lower('h_uim_quit'))
                command = 1;
        elseif strcmp(lower(command),lower('h_uim_quitquit'))
                command = 2;
        elseif strcmp(lower(command),lower('h_uim_aco'))
                command = 3;
        elseif strcmp(lower(command),lower('h_uim_acosta'))
                command = 4;
        elseif strcmp(lower(command),lower('h_uim_acostav'))
                command = 5;
        elseif strcmp(lower(command),lower('h_uim_acostaf'))
                command = 6;
        elseif strcmp(lower(command),lower('h_uim_acofig'))
                command = 7;
        elseif strcmp(lower(command),lower('h_uim_acosigaf'))
                command = 8;
        elseif strcmp(lower(command),lower('h_uim_acosigaa'))
                command = 9;
        elseif strcmp(lower(command),lower('h_uim_acosigbf'))
                command = 10;
        elseif strcmp(lower(command),lower('h_uim_ae'))
                command = 11;
        elseif strcmp(lower(command),lower('h_uim_aefig'))
                command = 12;
        elseif strcmp(lower(command),lower('h_uim_ele'))
                command = 13;
        elseif strcmp(lower(command),lower('h_uim_elesig'))
                command = 14;
        elseif strcmp(lower(command),lower('h_uim_elesigaf'))
                command = 15;
        elseif strcmp(lower(command),lower('h_uim_elefigac'))
                command = 16;
        elseif strcmp(lower(command),lower('h_uim_elesigbf'))
                command = 17;
        elseif strcmp(lower(command),lower('h_uim_elenoise'))
                command = 18;
        elseif strcmp(lower(command),lower('h_uim_nn'))
                command = 19;
        elseif strcmp(lower(command),lower('h_uim_sm'))
                command = 20;
        elseif strcmp(lower(command),lower('h_uim_2'))
                command = 21;
        elseif strcmp(lower(command),lower('h_uim_lvq'))
```

```
                command = 22;
        elseif strcmp(lower(command),lower('h_uim_1'))
                command = 23;
        elseif strcmp(lower(command),lower('h_uim_load'))
                command = 24;
        elseif strcmp(lower(command),lower('h_uim_loadele'))
                command = 25;
        elseif strcmp(lower(command),lower('h_uim_loadaco'))
                command = 26;
        end
end

if command ~= 0
        h_fig_list = findobj(get(0,'children'),'flat',...
                'tag','PD');
                if length(h_fig_list) > 1
                        h_fig_list = gcf;
                elseif length(h_fig_list) == 0
                        error('There are no figures with Tag = PD.');
                end
        handle_list = get(h_fig_list,'userdata');
        if length(handle_list) > 0
                h_uim_quit = handle_list(1); h_uim_quitquit = handle_list(2);
                h_uim_aco = handle_list(3); h_uim_acosta = handle_list(4);
                h_uim_acostav = handle_list(5); h_uim_acostaf = handle_list(6);
                h_uim_acofig = handle_list(7); h_uim_acosigaf = handle_list(8);
                h_uim_acosigaa = handle_list(9); _uim_acosigbf = handle_list(10);
                h_uim_ae = handle_list(11); h_uim_aefig = handle_list(12);
                h_uim_ele = handle_list(13); h_uim_elesig = handle_list(14);
                h_uim_elesigaf = handle_list(15);
    h_uim_elefigac = handle_list(16);
                h_uim_elesigbf = handle_list(17);
                h_uim_elenoise = handle_list(18);
                h_uim_nn = handle_list(19); h_uim_sm = handle_list(20);
                h_uim_2 = handle_list(21); h_uim_lvq = handle_list(22);
                h_uim_1 = handle_list(23);
                h_uim_load = handle_list(24);
                h_uim_loadele = handle_list(25);
                h_uim_loadaco = handle_list(26);
        end
end

if command == 0

  fig = figure('position',[ 10 15 785 545 ],...
        'NumberTitle','off',...
        'Name','Acoustic Detection of Partial Discharges in HV Polymeric Cable Joints',...
        'Color',[0.5,0.75,0.75],...
                'resize','on','tag','PD',...
          'visible','off');
        % Uicontrol Object Creation
        % Menu Object Creation
        h_uim_quit = uimenu(...
                'CallBack','PD("h_uim_quit");',...
                'Accelerator','Q',...
                'Position',[ 6 ],...
                'Label','&Quit',...
                'Tag','h_uim_quit',...
                'UserData','');
                drawnow;
        h_uim_quitquit = uimenu(h_uim_quit, ...
                'CallBack','quitask',...
                'Position',[ 1 ],...
                'Label','Exit from PD',...
                'Tag','h_uim_quitquit',...
                'UserData','');
                drawnow;
        h_uim_aco = uimenu(...
                'CallBack','PD("h_uim_aco");',...
                'Accelerator','A',...
                'Position',[ 5 ],...
                'Label','&Acoustic',...
                'Tag','h_uim_aco',...
                'UserData','');
                drawnow;
        h_uim_acosta = uimenu(h_uim_aco, ...
```

```
            'CallBack','PD("h_uim_acosta");',...
            'Position',[ 2 ],...
            'Label','Statistics',...
            'Tag','h_uim_acosta',...
            'UserData','');
            drawnow;
h_uim_acostav = uimenu(h_uim_acosta, ...
            'CallBack','asval',...
            'Position',[ 2 ],...
            'Label','Value',...
            'Tag','h_uim_acostav',...
            'UserData','');
            drawnow;
h_uim_acostaf = uimenu(h_uim_acosta, ...
            'CallBack','asfig',...
            'Position',[ 1 ],...
            'Label','Figure',...
            'Tag','h_uim_acostaf',...
            'UserData','');
            drawnow;
h_uim_acofig = uimenu(h_uim_aco, ...
            'CallBack','PD("h_uim_acofig");',...
            'Position',[ 1 ],...
            'Label','Figures',...
            'Tag','h_uim_acofig',...
            'UserData','');
            drawnow;
h_uim_acosigaf = uimenu(h_uim_acofig, ...
            'CallBack','aafilter',...
            'Position',[ 3 ],...
            'Label','Post-filter',...
            'Tag','h_uim_acosigaf',...
            'UserData','');
            drawnow;
h_uim_acosigaa = uimenu(h_uim_acofig, ...
            'CallBack','acalib',...
            'Position',[ 2 ],...
            'Label','Post-calibration',...
            'Tag','h_uim_acosigaa',...
            'UserData','');
            drawnow;
h_uim_acosigbf = uimenu(h_uim_acofig, ...
            'CallBack','abfilter',...
            'Position',[ 1 ],...
            'Label','Pre-filter',...
            'Tag','h_uim_acosigbf',...
            'UserData','');
            drawnow;
h_uim_ae = uimenu(...
            'CallBack','PD("h_uim_ae");',...
            'Accelerator','n',...
            'Position',[ 4 ],...
            'Label','Aa&ndE',...
            'Tag','h_uim_ae',...
            'UserData','');
            drawnow;
h_uim_aefig = uimenu(h_uim_ae, ...
            'CallBack','aefig',...
            'Position',[ 1 ],...
            'Label','Figures',...
            'Tag','h_uim_aefig',...
            'UserData','');
            drawnow;
h_uim_ele = uimenu(...
            'CallBack','PD("h_uim_ele");',...
            'Accelerator','c',...
            'Position',[ 3 ],...
            'Label','Ele&ctric',...
            'Tag','h_uim_ele',...
            'UserData','');
            drawnow;
h_uim_elesig = uimenu(h_uim_ele, ...
            'CallBack','PD("h_uim_elesig");',...
            'Position',[ 2 ],...
            'Label','Signal',...
            'Tag','h_uim_elesig',...
```

```
            'UserData','');
            drawnow;
h_uim_elesigaf = uimenu(h_uim_elesig, ...
            'CallBack','efilter',...
            'Position',[ 3 ],...
            'Label','Post-filter',...
            'Tag','h_uim_elesigaf',...
            'UserData','');
            drawnow;
h_uim_elefigac = uimenu(h_uim_elesig, ...
            'CallBack','ecalib',...
            'Position',[ 2 ],...
            'Label','Post-calibration',...
            'Tag','h_uim_elefigac',...
            'UserData','');
            drawnow;
h_uim_elesigbf = uimenu(h_uim_elesig, ...
            'CallBack','ebfilter',...
            'Position',[ 1 ],...
            'Label','Pre-filter',...
            'Tag','h_uim_elesigbf',...
            'UserData','');
            drawnow;
h_uim_elenoise = uimenu(h_uim_ele, ...
            'CallBack','elenoise',...
            'Position',[ 1 ],...
            'Label','Noise',...
            'Tag','h_uim_elenoise',...
            'UserData','');
            drawnow;
h_uim_nn = uimenu(...
            'CallBack','PD("h_uim_nn");',...
            'Accelerator','u',...
            'Position',[ 2 ],...
            'Label','Ne&uralN',...
            'Tag','h_uim_nn',...
            'UserData','');
            drawnow;
h_uim_sm = uimenu(h_uim_nn, ...
            'CallBack','annsmff',...
            'Position',[ 4 ],...
            'Label','SorgMap',...
            'Tag','h_uim_sm',...
            'UserData','');
            drawnow;
h_uim_2 = uimenu(h_uim_nn, ...
            'CallBack','annbpff',...
            'Position',[ 3 ],...
            'Label','BP',...
            'Tag','h_uim_2',...
            'UserData','');
            drawnow;
h_uim_lvq = uimenu(h_uim_nn, ...
            'CallBack','annvqff',...
            'Position',[ 2 ],...
            'Label','LVQ',...
            'Tag','h_uim_lvq',...
            'UserData','');
            drawnow;
h_uim_1 = uimenu(h_uim_nn, ...
            'CallBack','nnload',...
            'Position',[ 1 ],...
            'Label','Load_dat',...
            'Tag','h_uim_1',...
            'UserData','');
            drawnow;
h_uim_load = uimenu(...
            'CallBack','PD("h_uim_load");',...
            'Accelerator','L',...
            'Position',[ 1 ],...
            'Label','&Load',...
            'Tag','h_uim_load',...
            'UserData','');
            drawnow;
h_uim_loadele = uimenu(h_uim_load, ...
            'CallBack','eloadf',...
```

```
                'Position',[ 2 ],...
                'Label','Electric',...
                'Tag','h_uim_loadele',...
                'UserData','');
                drawnow;
        h_uim_loadaco = uimenu(h_uim_load, ...
                'CallBack','aloaddat',...
                'Position',[ 1 ],...
                'Label','Acoustic',...
                'Tag','h_uim_loadaco',...
                'UserData','');
                drawnow;

        %  Axes and Text Object Creation
        handle_list = [ ...
                 h_uim_quit h_uim_quitquit h_uim_aco ...
                h_uim_acosta h_uim_acostav h_uim_acostaf h_uim_acofig ...
                h_uim_acosigaf h_uim_acosigaa h_uim_acosigbf h_uim_ae ...
                h_uim_aefig h_uim_ele h_uim_elesig h_uim_elesigaf ...
                h_uim_elefigac h_uim_elesigbf h_uim_elenoise h_uim_nn ...
                h_uim_sm h_uim_2 h_uim_lvq h_uim_1 ...
                h_uim_load h_uim_loadele h_uim_loadaco ...
                        ];
        set(gcf,'userdata',handle_list);
        drawnow;pause(.1);
        set(gcf,'visible','on');
end
```

% ALOAD.M % load acoustic data

```
function[]=aloadnew();

  global sig Ncycle ACOU fig_alo alo_path alo_file alo_ncycle;
  pathload=get(alo_path,'String');
  pathload=[pathload,'\'];
  file=get(alo_file,'String');
  %if ~exist(file), break, end
  Ncycle=get(alo_ncycle,'String');
  Ncycle=str2num(Ncycle);

  k=1;
  sig=zeros(20000,Ncycle);
  while k<=Ncycle
  if k<10
       filek=[file,'00',int2str(k),'.fil'];
  elseif k<100
      filek=[file,'0',int2str(k),'.fil'];
  elseif k<1000
      filek=[file,int2str(k),'.fil'];
  else
      filek=[file,int2str(k),'.fil'];
  end
      fid=fopen([pathload,filek]);
      fpstat=fseek(fid,150,'bof');
      sig(:,k)=fscanf(fid,'%f',20000);
      status=fclose(fid);
      k=k+1;
   end
close(fig_alo);
ACOU=1;
aloinq=figure('NumberTitle','off',...
            'Name','Acoustic data Loaded!',...
            'MenuBar','none',...
            'Color',[0.75,0.75,0.75],...
            'Resize','off',...
            'Position',[90 145 205 145]);
alosuc=uicontrol(gcf,...
             'Style','text',...
             'String','Load Completed!',...
             'BackgroundColor',[1,1,0],...
             'Position',[35 80 130 25]);
alosucok=uicontrol(gcf,...
             'Style','push',...
             'String','OK',...
```

```
            'Position',[55 30 70 25],...
            'CallBack','close(gcf);');
```

```
% AAWLET.M                    % filter acoustic signal using wavelet
function[]=aawlet();
global figaaw1 figaaw2;
global sigt sig Ncycle N siglet AFIL frs;
global aa_filnamee aa_fillevele aa_filter siga;

   wname=get(aa_filnamee,'String');
   flv=get(aa_fillevele,'String');
   flv=str2num(flv);
   %wname=input('Input the Filter Method=>','s');
   %flv=input('Input the Filter Level=>');
         %lev=10;
         %siglet=wden(sig,'heursure','s','one',lev,'sym8');
         %siglet=wden(sig,'sqtwolog','s','one',lev,'sym8');
         %[C,l]=wavedec(sig,lev,'sym8');
         %siglet=wden(C,l,'minimaxi','s','sln',lev,'sym8');
         %siglet=wden(sig,'heursure','s','one',lev,'sym8');
         %[thr,sorh,keepapp]=ddencmp('den','wv',sig(1,:));
         %siglet=wdencmp('gbl',sig,'db3',12,thr,sorh,keepapp);
         %siglet=wdencmp('gbl',sig,'coif3',12,thr,sorh,keepapp);
         %siglet=wdencmp('gbl',sig,'sym5',7,thr,sorh,keepapp);
         %siglet(1,:)=wdencmp('gbl',sig(1,:),wname,flv,thr,sorh,keepapp);
  close(aa_filter);

  siglet=zeros(20000,Ncycle);
   for i=1:Ncycle
       [thr,sorh,keepapp]=ddencmp('den','wv',sige(:,i));
      siglet(:,i)=wdencmp('gbl',sig(:,i),wname,flv,thr,sorh,keepapp);
   end
       figaaw1=figure('NumberTitle','off',...
        'Name','Signal(aco) after filter',...
        'Position',[165 25 425 355]);

subplot(2,1,1); plot(sigt,siglet(:,1),'g');
ymax=max(siglet(:,1)); ymin=min(siglet(:,1));
grid on;
title('Acoustic Signal after filter');
xlabel('Time(ms)'); ylabel('Voltage(mv)');
if ymax>ymin
 axis([0 20 ymin*1.1 ymax*1.1]);
end
y=fft(siglet(:,1)); pwr=y.*conj(y)/20000;
pwrlet=pwr(1:N/2)*1e6; clear y;
subplot(2,1,2); plot(frs,pwrlet,'g');
grid on;
xlabel('Frequency(KHz)');ylabel('Power (pw)');
ymax=max(pwrlet(2:N/2));axis([0 500 0 ymax*1.1]);
zoom;
%  choice=menu('Satisfactory with the filter?','Yes','No,Filter Again');
% end
nextscreen=ginput(1);
AFIL=1;
```

```
% CALIBALL.M                   % acoustic signal calibration

function[]=caliball();
global Ncycle ssss thre thre1 sig siglet Qmaxwin Qave Num TNum AALL
global PHWIN2 PHWIN21 PHVAL PHWIN NPERWIN QWIN Qdiv Qmax;

QWIN=50;
PHWIN=200;
NPERWIN=20000/PHWIN;
PHWIN2=PHWIN/2;
PHWIN21=PHWIN2+1;
PHVAL=360/PHWIN;

ssss=zeros(1,20000);Q=zeros(1,PHWIN);Num=zeros(1,PHWIN);
Qave=zeros(1,PHWIN);Qmaxwin=zeros(1,PHWIN);Qmax=max(max(abs(sig)));
Qdiv=Qmax/QWIN;TNum=zeros(PHWIN,QWIN);
```

```
for inum=1:Ncycle
            i=1;
            imax=1;
            maxtemp=thre;
  while i<20000
            if abs(sig(i,inum))>=abs(maxtemp)
              ssss(imax)=0;
       maxtemp=sig(i,inum);
              imax=i;
       ssss(imax)=sig(i,inum);
              i=i+1;
    elseif max(abs(sig(i:(i+thre1),inum)))<thre &
    abs(sig(imax,inum))>=thre
   %  elseif max(abs(sig(i:(i+thre1),inum)))<thre
      phasenum=floor(imax/NPERWIN)+1;
      Q(phasenum)=Q(phasenum)+abs(maxtemp);
      Num(phasenum)=Num(phasenum)+1;
     if abs(maxtemp)==Qmax
       Ndiv=QWIN;
       TNum(phasenum,Ndiv)=TNum(phasenum,Ndiv)+1;
     else
       Ndiv=floor(abs(maxtemp)/Qdiv)+1;
       TNum(phasenum,Ndiv)=TNum(phasenum,Ndiv)+1;
     end
     if abs(maxtemp)>Qmaxwin(phasenum)
       Qmaxwin(phasenum)=abs(maxtemp);
     end
           i=i+thre1;
      imax=i+thre1-4;
      maxtemp=thre;
    elseif max(abs(sig(i:(i+thre1),inum)))<thre & abs(sig(imax,inum))<thre
      i=i+thre1;
      imax=i+thre1-4;
      maxtemp=thre;
    else
      i=i+1;
    end

      if i>(20000-thre1)
        if max(abs(sig(i:20000,inum)))>thre
         maxpulse=max(sig(i:20000,inum));
         minpulse=min(sig(i:20000,inum));
        if abs(maxpulse)>abs(minpulse)
          pulseamp=maxpulse;
          imax1=find(~(sig(i:20000,inum)-maxpulse));
          imax2=i+min(imax1)-1;
          ssss(imax2)=pulseamp;
        else
          pulseamp=minpulse;
          imax1=find(~(sig(i:20000,inum)-minpulse));
          imax2=i+min(imax1)-1;
          ssss(imax2)=pulseamp;
        end
        if imax2==20000
          phasenum=PHWIN;
        else
          phasenum=floor(imax2/NPERWIN)+1;
        end
        Q(phasenum)=Q(phasenum)+abs(pulseamp);
        Num(phasenum)=Num(phasenum)+1;
        if abs(pulseamp)==Qmax
          Ndiv=QWIN;
          TNum(phasenum,Ndiv)=TNum(phasenum,Ndiv)+1;
        else
          Ndiv=floor(abs(pulseamp)/Qdiv)+1;
          TNum(phasenum,Ndiv)=TNum(phasenum,Ndiv)+1;
        end
        if abs(pulseamp)>Qmaxwin(phasenum)
          Qmaxwin(phasenum)=abs(pulseamp);
        end
      end
     i=20000;
    end
  end
end
```

```
for k=1:PHWIN;
  if Num(k)==0
    Qave(k)=0;
  else
    Qave(k)=Q(k)./Num(k);
  end
end

AALL=1;
```

% ASCOMPUT.M % compute acoustic statistical operators

```
function[]=ascomput();
global Qave Num cc mcc P Q skp skn kup kun sk ku
global NPERWIN PHWIN PHVAL PHWIN2 PHWIN21;

% 1. Calculate cc,mcc

Qtotalp=sum(Qave(1:PHWIN2));
Qtotaln=sum(Qave(PHWIN21:PHWIN));
Ntotalp=sum(Num(1:PHWIN2));
Ntotaln=sum(Num(PHWIN21:PHWIN));
Q=(Qtotaln/Ntotaln)/(Qtotalp/Ntotalp);
m=1;
while Num(m)==0
 m=m+1;
end
Phasep=m; n=PHWIN21;
while Num(n)==0
 n=n+1;
end
Phasen=n-PHWIN2;
P=Phasen/Phasep;
ccu1=sum(Qave(1:PHWIN2).*Qave(PHWIN21:PHWIN));
ccu2=sum(Qave(1:PHWIN2))*sum(Qave(PHWIN21:PHWIN))/PHWIN2;
ccl1=sum(Qave(1:PHWIN2)*Qave(1:PHWIN2)')-(sum(Qave(1:PHWIN2)))^2/PHWIN2;
ccl2=sum(Qave(PHWIN21:PHWIN)*Qave(PHWIN21:PHWIN)')-(sum(Qave(PHWIN21:PHWIN)))^2/PHWIN2;
cc=(ccu1-ccu2)/(sqrt(ccl1*ccl2));
mcc=Q*cc;

% 2. Calculate sk in Positive and negative cycle

x=PHVAL:PHVAL:180;
o1qp=0; o1qn=0; o1np=0; o1nn=0; o2qp=0; o2qn=0; o2np=0; o2nn=0;
sk1p=0; sk1n=0; ku1n=0; ku1p=0; sk2p=0; sk2n=0; ku2n=0; ku2p=0;
o1q=0; o1n=0; o2q=0; o2n=0;     sk1=0; ku1=0; sk2=0; ku2=0;

if sum(Qave(1:PHWIN2))==0 & sum(Qave(PHWIN21:PHWIN))==0
  skp='All Q in positive cycle are zero';
  skn='All Q in negative cycle are zero';
elseif sum(Qave(1:PHWIN2))==0
  skp='All Q in positive cycle are zero';
  mqn=sum(x.*Qave(PHWIN21:PHWIN))/sum(Qave(PHWIN21:PHWIN));
 for n=1:PHWIN2,
  o1qn=o1qn+(x(n)-mqn)^2*Qave(PHWIN2+n);
  o2qn=o2qn+Qave(PHWIN2+n);
  sk1n=sk1n+(x(n)-mqn)^3*Qave(PHWIN2+n);
  sk2n=sk2n+Qave(PHWIN2+n);
 end
  oqn=sqrt(o1qn/o2qn);
  skn=sk1n/(oqn^3*sk2n);
elseif sum(Qave(PHWIN21:PHWIN))==0
  skn='All Q in negative cycle are zero';
  mqp=sum(x.*Qave(1:PHWIN2))/sum(Qave(1:PHWIN2));
 for n=1:PHWIN2,
  o1qp=o1qp+(x(n)-mqp)^2*Qave(n);
  o2qp=o2qp+Qave(n);
  sk1p=sk1p+(x(n)-mqp)^3*Qave(n);
  sk2p=sk2p+Qave(n);
 end
  oqp=sqrt(o1qp/o2qp);
  skp=sk1p/(oqp^3*sk2p);
else
  mqn=sum(x.*Qave(PHWIN21:PHWIN))/sum(Qave(PHWIN21:PHWIN));
```

```
    mqp=sum(x.*Qave(1:PHWIN2))/sum(Qave(1:PHWIN2));
   for n=1:PHWIN2,
    o1qn=o1qn+(x(n)-mqn)^2*Qave(PHWIN2+n);
    o2qn=o2qn+Qave(PHWIN2+n);
    sk1n=sk1n+(x(n)-mqn)^3*Qave(PHWIN2+n);
    sk2n=sk2n+Qave(PHWIN2+n);
    o1qp=o1qp+(x(n)-mqp)^2*Qave(n);
    o2qp=o2qp+Qave(n);
    sk1p=sk1p+(x(n)-mqp)^3*Qave(n);
    sk2p=sk2p+Qave(n);
   end
    oqn=sqrt(o1qn/o2qn);
    skn=sk1n/(oqn^3*sk2n);
    oqp=sqrt(o1qp/o2qp);
    skp=sk1p/(oqp^3*sk2p);
end

% 3. Calculate Ku in positive and negative cycle

if sum(Num(1:PHWIN2))==0 & sum(Num(PHWIN21:PHWIN))==0
   kup='All Q in positive cycle are zero';
   kun='All Q in negative cycle are zero';
elseif sum(Num(1:PHWIN2))==0
   kup='All Q in positive cycle are zero';
   mnn=sum(x.*Num(PHWIN21:PHWIN))/sum(Num(PHWIN21:PHWIN));
    for n=1:PHWIN2,
     o1nn=o1nn+(x(n)-mnn)^2*Num(PHWIN2+n);
     o2nn=o2nn+Num(PHWIN2+n);
     ku1n=ku1n+(x(n)-mnn)^4*Num(PHWIN2+n);
     ku2n=ku2n+Num(PHWIN2+n);
    end
   onn=sqrt(o1nn/o2nn);
   kun=ku1n/(onn^4*ku2n)-3;
elseif sum(Num(PHWIN21:PHWIN))==0
   kun='All Q in negative cycle are zero';
   mnp=sum(x.*Num(1:PHWIN2))/sum(Num(1:PHWIN2));
    for n=1:PHWIN2,
     o1np=o1np+(x(n)-mnp)^2*Num(n);
     o2np=o2np+Num(n);
     ku1p=ku1p+(x(n)-mnp)^4*Num(n);
     ku2p=ku2p+Num(n);
    end
   onp=sqrt(o1np/o2np);
   kup=ku1p/(onp^4*ku2p)-3;
else
   mnn=sum(x.*Num(PHWIN21:PHWIN))/sum(Num(PHWIN21:PHWIN));
   mnp=sum(x.*Num(1:PHWIN2))/sum(Num(1:PHWIN2));
    for n=1:PHWIN2,
     o1nn=o1nn+(x(n)-mnn)^2*Num(PHWIN2+n);
     o2nn=o2nn+Num(PHWIN2+n);
     ku1n=ku1n+(x(n)-mnn)^4*Num(PHWIN2+n);
     ku2n=ku2n+Num(PHWIN2+n);
     o1np=o1np+(x(n)-mnp)^2*Num(n);
     o2np=o2np+Num(n);
     ku1p=ku1p+(x(n)-mnp)^4*Num(n);
     ku2p=ku2p+Num(n);
    end
   onn=sqrt(o1nn/o2nn);
   kun=ku1n/(onn^4*ku2n)-3;
   onp=sqrt(o1np/o2np);
   kup=ku1p/(onp^4*ku2p)-3;
end

% 4.Caulculate Sk and Ku in whole cycle

x=PHVAL:PHVAL:360;

if sum(Qave)==0
  ku='All Q in whole cycle are zero';
  sk='All Q in whole cycle are zero';
else
  mq=sum(x.*Qave)/sum(Qave);
  mn=sum(x.*Num)/sum(Num);
 for n=1:PHWIN
   o1q=o1q+(x(n)-mq)^2*Qave(n);
   o1n=o1n+(x(n)-mn)^2*Num(n);
```

```
    o2q=o2q+Qave(n);
    o2n=o2n+Num(n);
    sk1=sk1+(x(n)-mq)^3*Qave(n);
    ku1=ku1+(x(n)-mn)^4*Num(n);
    sk2=sk2+Qave(n);
    ku2=ku2+Num(n);
  end
   oq=sqrt(o1q/o2q);
   on=sqrt(o1n/o2n);
   sk=sk1/(oq^3*sk2);
   ku=ku1/(on^4*ku2)-3;
end
```

% ASFIG.M % acoustic 2D&3D figures

```
function[figsta1]=asfig();

global  QWIN PHWIN NPERWIN PHVAL PHWIN2 Qmax thre;
global ACOU ssss Qave Qdiv Qmaxwin Num TNum ACAL AFIL;

running;
caliball;

figsta1=figure('NumberTitle','off',...                    % 2D figure
        'Name','Statistics Figures',...
        'Position',[145 25 445 365]);

t=linspace(PHVAL,360,PHWIN);
subplot(3,1,3); bar(t-PHVAL/2,Qave,'g');
%fill(t-PHVAL,Qave,'g');
xticks=0:90:360; set(gca,'XTick',xticks);
grid on; title('Average amplitude-phase window');
xlabel('Phase(degree)'); ylabel('voltage(mv)');
Qavemax=max(Qave); axis([0 360 0 Qavemax*1.1]);

subplot(3,1,1);bar(t-PHVAL/2,Qmaxwin,'g');
%fill(t-PHVAL,Qmaxwin,'g');
xticks=0:90:360; set(gca,'XTick',xticks);
grid on; title('Maximal amplitude-phase window');
ylabel('voltage(mv)'); Qmaxmax=max(Qmaxwin);
axis([0 360 0 Qmaxmax*1.1]);

subplot(3,1,2); bar(t-PHVAL/2,Num,'g');
%fill(t-PHVAL,Num,'g');
xticks=0:90:360;set(gca,'XTick',xticks);
grid on;title('Cumulative numbers-phase window');
ylabel('Number');Nummax=max(Num);axis([0 360 0 Nummax+10]);
zoom;

nextscreen=ginput(1);
figsta2=figure('NumberTitle','off',...                    % 3D figure
        'Name','3D figure',...
        'Position',[165 35 445 365]);
hold on;
view(50,60);
surf((1:QWIN)*Qdiv,(1:PHWIN)*PHVAL,TNum(1:PHWIN,1:QWIN));
colormap([1 1 1]);
%set(gca,'XTickLabels',XTick_Labels);
%axis('auto');%surf(Qave,t-0.9,TNum);%shading flat;%view(3);
yticks=0:45:360;
set(gca,'YTick',yticks);
ylabel('Phase(degree)');
xlabel('Signal amplitude(mv)');
zlabel('Signal number');
TNummax=max(max(TNum));
axis([0 Qmax 0 360 0 TNummax+10]);
grid on;
title('3D Characterisation');
%print -dgif8 3d.gif;
hold off;
close(figrun);
end
```

```
% FREQFILT.M                    % filter in frequency

% Filter using IIR, FIR or Windows(Hamming...)  %

disp(['Click on left frequency']);
lp=ginput(1);
disp(['Click on right frequency']);
rp=ginput(1);
fhz0=[0 0.9*lp(1) lp(1) rp(1) 1.1*rp(1) 500];
m0=[0 0 1 1 0 0];
f0=fhz0/500;
wn=[lp(1) rp(1)]/500;

[b,a]=yulewalk(8,fhz0,m0);
[b,a]=butter(8,wn);
bFIR=remez(20,f0,m0); aFIR=[1,zeros(1,20)];
B = FIR1(N,Wn,'high',chebwin(N+1,R)) uses a Chebyshev window.
bFIR=fir1(30,wn);
aFIR=[1,zeros(1,20)];

fhz1=linspace(1,500,50);
om1=2*pi*fhz1;
z=exp(sqrt(-1)*om1/1000);
mFIR=abs(polyval(bFIR,z));
mIIR=abs(polyval(b,z)./polyval(a,z));

figure(3);
signew=filter(bFIR,aFIR,sig);
x=0.001:0.001:20;
subplot(2,1,1); %plot(x,signew);
grid on; %xlabel('Time(ms)'); %ylabel('Voltage');
axis([0 20 -2 2]); %hold on;
N=20000; b=1:N/2; frs=(b-1)/20;
y=fft(signew);
pwr=y.*conj(y)/20000; pwrnew=pwr(1:N/2);
subplot(2,1,2); plot(frs,pwrnew,'g');
grid on; title('Frequency Domain');
xlabel('Frequency(KHz)'); ylabel('Power');
ymax=max(pwrnew); axis([0 500 0 ymax]);


%WAVELET.M                      % wavelet decomposition

load d:\insight\a1r004.fil;

%sigg=a1r004(1:20000)*3;
maxsigg=max(sigg);
minsigg=min(sigg);
    if abs(maxsigg)>abs(minsigg)
      loc=find(sigg-maxsigg>=0);
      sig=sigg(loc-63:loc+192)/maxsigg;
%       sig=sigg(loc-63:loc+192);
    else
      loc=find(abs(sigg)-abs(minsigg)>=0);
      sig=-sigg(loc-63:loc+192)/abs(minsigg);
%       sig=-sigg(loc-63:loc+192);
    end

    N=256;
    % Decompose and Recontruct
    w='db3';
[c,l]=wavedec(sig,4,w);
%% USING APPCOEF AND DETCOEF, Extract Approximation and Detail Coefficients
ca4=appcoef(c,l,'db3',4);
cd4=detcoef(c,l,4);
cd3=detcoef(c,l,3);
cd2=detcoef(c,l,2);
cd1=detcoef(c,l,1);
ttca4=1:(length(ca4));
ttcd4=1:(length(cd4));
ttcd3=1:(length(cd3));
ttcd2=1:(length(cd2));
ttcd1=1:(length(cd1));

w='db3';
```

```
[c,l]=wavedec(sig,4,w);
for i=1:4,
  d(:,i)=wrcoef('d',c,l,w,i);
end
tts=1:N;

figure;
subplot(511);plot(tts,sig,'k');
set(gca,'fontname',['arial']);
set(gca,'fontsize',[10]);
axis([0 N-1 -1 1]);
%text(150,0.5,'AE signal ','fontname',['arial'],'fontsize',[12]);
subplot(512);plot(tts,d(:,1),'k');
set(gca,'fontname',['arial']);
set(gca,'fontsize',[10]);
%yticks=-0.4:0.4:0.6;
%set(gca,'YTick',yticks);
axis([0 N min(d(:,1))*1.1 max(d(:,1))*1.1]);
%text(150,0.2,'detail level 1','fontname',['arial'],'fontsize',[12]);
subplot(513);plot(tts,d(:,2),'k');
set(gca,'fontname',['arial']);
set(gca,'fontsize',[10]);
%yticks=-0.9:0.4:0.5;
%set(gca,'YTick',yticks);
axis([0 N min(d(:,2))*1.1 max(d(:,2))*1.1]);
%text(150,0.3,'detail level 2','fontname',['arial'],'fontsize',[12]);
subplot(514);plot(tts,d(:,3),'k');
set(gca,'fontname',['arial']);
set(gca,'fontsize',[10]);
axis([0 N min(d(:,3))*1.1 max(d(:,3))*1.1]);
%text(150,0.2,'detail level 3','fontname',['arial'],'fontsize',[12]);
subplot(515);plot(tts,d(:,4),'k');
set(gca,'fontname',['arial']);
set(gca,'fontsize',[10]);
yticks=-0.04:0.04:0.08;
set(gca,'YTick',yticks);
axis([0 N min(d(:,4))*1.1 max(d(:,4))*1.1]);
%text(150,0.06,'detail level 4','fontname',['arial'],'fontsize',[12]);
xlabel('time (us)','fontname',['arial'],'fontsize',[11]);
zoom;
```

%SPECTRUM.M % short duration fourier transform

```
load d:\insight\ter01.fil;

sigg=ter01(1:20000);
maxsigg=max(sigg);
minsigg=min(sigg);
    if abs(maxsigg)>abs(minsigg)
      loc=find(sigg-maxsigg>=0);
 %      siggg=sigg(loc-63:loc+192)/maxsigg;
      sig1=sigg(loc-63:loc+192);
    else
      loc=find(abs(sigg)-abs(minsigg)>=0);
 %      siggg=-sigg(loc-63:loc+192)/abs(minsigg);
      sig1=-sigg(loc-63:loc+192);
    end

N=256;b=1:N/2;frs=(b-1)*500*2/N; ts=1:N;
y=fft(sig1); pwr1=y.*conj(y)/N; pwr1=pwr1(1:N/2);
clear y; pwr1=pwr1/max(pwr1);

figure;
subplot(2,1,1);
plot(ts,sig1,'k');
%title(file);
set(gca,'fontname',['arial']);
set(gca,'fontsize',[12]);
ylabel('amplitude (mV)');
xlabel('time (us)');
axis([0 N 1.2*min(sig1) 1.2*max(sig1)]);
subplot(2,1,2);
plot(frs,pwr1,'k');
set(gca,'fontname',['arial']);
```

```
set(gca,'fontsize',[12]);
ylabel('Power');
xlabel('frequency (KHz)');
axis([0 500 0 1.1]);
zoom;
```

%ANNBPFF.M % AE signal characterisation with BP network

```
function[]=annbpff();

global aesignal testpd tarbp testbp;
global ELEC ACOU TOTALN Ncycle eNcycle HAVEPD NNF sig8;

SN=20;
TYPE=3;
TOTALN=TYPE*SN;

if ELEC==0 & ACOU==0
fig_error=figure('NumberTitle','off',...
            'Name','ERROR!',...
            'MenuBar','none',...
            'Color',[0.5,0.75,0.75],...
            'Resize','off',...
            'Position',[150 270 185 115]);
 error_disp=uicontrol(gcf,...
             'Style','text',...
             'String','Load Data First !!',...
              'ForegroundColor',[1 1 0],...
             'BackgroundColor',[0.5,0.75,0.75],...
             'Position',[25 50 130 45]);
 error_close=uicontrol(gcf,...
             'Style','push',...
             'String','Close',...
             'Position',[55 20 80 25],...
             'CallBack','close(gcf)');
else

annbpdff;
annbptff;

figbptr=figure('NumberTitle','off',...
        'Name','ANN( BP ) Training',...
        'MenuBar','none',...
        'Position',[105 35 495 385]);
hold on;
[r,q]=size(aesignal);
s1=6;
[w1,b1,w2,b2]=initff(aesignal,s1,'logsig',tarbp,'logsig');
w1=w1*0.01;
b1=b1*0.01;
w2=w2*0.01;
b2=b2*0.01;
df=20; me=2000; eg=0.01; mc=0.95;
%tp=[df me eg NaN NaN NaN mc];
tp=[df me eg];
% df: Frequency of Progress displays;
% me: Maxium number of epochs to train;
% eg: Sum-Squared Error goal;
% lr: Learning rate;
% ep: Actual number of epoches trained;
% tr: training record(row of errows);
% w: weight coefficients;
% b: biase coefficients;
% SSE: Sum Squared Error practical value;
T=tarbp;
[w1,b1,w2,b2,ep,tr]=trainbpx(w1,b1,'logsig',w2,b2,'logsig',aesignal,T,tp);
network=[];
simupd=simuff(testpd,w1,b1,'logsig',w2,b2,'logsig');
correct=0;
for i=1:TOTALN,
  simupd2(:,i)=sort(simupd(:,i));
  simumax1=simupd2(TYPE,i);
  simumax2=simupd2((TYPE-1),i);
  if simumax1>0.5 & simumax2<0.5 & (simumax1-simumax2)>0.3,
```

```
    AAn=compet(simupd(:,i));
    correct=correct+1-sum(sum(abs(AAn-testbp(:,i))))/2;
  end
end
idenrate=correct/TOTALN*100

figannbp=figure('NumberTitle','off',...
        'Name','ANN( BP ) Identification Result',...
        'Position',[105 35 495 385]);
datanum=1:TOTALN;
subplot(211);
plot(datanum,simupd(1,:),'r+',datanum,simupd(2,:),'bo',datanum,simupd(3,:),'g*');
set(gca,'fontname',['arial']);
set(gca,'fontsize',[12]);
ylabel('Output');
yticks=0:0.5:2;
set(gca,'YTick',yticks);
%title('BP Identification ');
axis([0 TOTALN 0 2]);
set(gca,'fontname',['arial']);
set(gca,'fontsize',[12]);
%text(4,1.5,'Identification Rate:','Color',[0 0 0],'fontname',['arial'],'fontsize',[12]);
%text(20,1.5,int2str(idenrate),'Color',[0 0 0],'fontname',['arial'],'fontsize',[12]);
%text(30,1.5,'%','Color',[0 0 0],'fontname',['arial'],'fontsize',[12]);
subplot(212);
plot(datanum,testbp(1,:),'r+',datanum,testbp(2,:),'bo',datanum,testbp(3,:),'g*');
set(gca,'fontname',['arial']);
set(gca,'fontsize',[12]);
xlabel('Set of Input Data');
ylabel('Output');
%title('Expected Output');
axis([0 TOTALN 0 2]);
zoom;
end
```

% ANNLVQWV.m % AE signal characterisation with LVQ network

```
%function[]=annlvqwv();

global aesignal testpd tarlvq testlvq;
global ELEC ACOU TOTALN Ncycle eNcycle epathload;

TYPE=3;
SN=20;
TOTALN=TYPE*SN;

annlvqdwv;
annlvqtwv;

figlvq=figure('NumberTitle','off',...
        'Name','      ANN( LVQ ) Training',...
        'MenuBar','none',...
        'Position',[105 35 495 385]);
[r,q]=size(aesignal);

s1=TYPE*3;
%T=ind2vec(tarlvq);
[w1,w2]=initlvq(aesignal,s1,tarlvq);
df=20; me=4000; lr=0.05;
%tp=[df me eg NaN NaN NaN mc];
tp=[df me lr];
%P=aesignal;
[w1,w2]=trainlvq(w1,w2,aesignal,tarlvq,tp);

network=[];
simupd=simulvq(testpd,w1,w2);
simupd=full(simupd);
%Tsimupd=vec2ind(simupd);
error=sum(sum(abs(simupd-testlvq)))/2;
errorlvq=ceil((TOTALN-error)/TOTALN*100);
idenrate=(TOTALN-error)/TOTALN*100

figannlvq=figure('NumberTitle','off',...
        'Name','ANN( LVQ ) Identification Result',...
```

```
        'Position',[105 35 495 195]);
datanum=1:TOTALN;

subplot(211);
plot(datanum,simupd(1,:),'r+',datanum,simupd(2,:),'bo',datanum,simupd(3,:),'g*');
set(gca,'fontname',['arial']);
set(gca,'fontsize',[12]);
yiabel('Output');
%title('LVQ Identification');
axis([0 TOTALN 0 2]);
subplot(212);
plot(datanum,testlvq(1,:),'r+',datanum,testlvq(2,:),'bo',
   datanum,testlvq(3,:),'g*');
set(gca,'fontname',['arial']);
set(gca,'fontsize',[12]);
xlabel('Set of Input Data');
ylabel('Output');
%title('Expected Identification Result');
axis([0 TOTALN 0 2]);
zoom;
```

% ECCORRT.M % time-based correlation

```
load c:\tek11\tek00021.dat;load c:\tek11\tek00023.dat;
NN=500;
for i=1:NN,
 data1(i)=tek00021(i+3); data2(i)=tek00023(i+3);
end
tek1=zeros(1,512); tek2=zeros(1,512);
for i=1:NN,
  tek1(i+12)=data1(i); tek2(i+12)=data2(i);
end
N=512;
teka=zeros(10,N); tekb=zeros(10,N);
%teka=[tek1 tek3 tek5 tek7 tek9 tek11 tek13 tek15 tek17 tek19];
%tekb=[tek2 tek4 tek6 tek8 tek10 tek12 tek14 tek16 tek18 tek20];

n=length(teka); ndata=fix(n/N);
for i=1:ndata,
  x(i,:)=teka((i*N-(N-1)):N*i);
  y(i,:)=tekb((i*N-(N-1)):N*i);
end
clear teka; clear tekb;

for i=1:ndata,
  xm=mean(x(i,:)); xm=ones(size(x(i,:)))*xm;  x(i,:)=x(i,:)-xm;
  ym=mean(y(i,:)); ym=ones(size(y(i,:)))*ym;  y(i,:)=y(i,:)-ym;
end

Z=zeros(ndata,N/2);I=ones(ndata,N/2);
pad01=[Z,I]; pad10=[I,Z];
xb=x.*pad01; xa=x.*pad10;

Z=zeros(ndata,N);
txa=[x,Z];
tya=[y,Z];
trxy1=zeros(ndata,N);
tryx1=zeros(ndata,N);

for i=1:ndata,
 for m=1:N,
  for n=1:N,
    trxy1(i,m)=trxy1(i,m)+txa(i,n)*tya(i,n+m);
    tryx1(i,m)=tryx1(i,m)+tya(i,n)*txa(i,n+m);
  end
 end
end

trxy1=sum(trxy1)*(1/ndata)*(1/N); trxy=trxy1/max(trxy1);
tryx1=sum(tryx1)*(1/ndata)*(1/N); tryx=tryx1/max(trxy1);
```

```
% ECCORRF.M                % FFT-based correlation

load c:\tek11\tek00021.dat;load c:\tek11\tek00023.dat;

NN=500;
for i=1:NN,
  data1(i)=tek00021(i+3);  data2(i)=tek00023(i+3);
end
tek1=zeros(1,512); tek2=zeros(1,512);
for i=1:500,
  tek1(i+12)=data1(i); tek2(i+12)=data2(i);
end

ndata=4;
mdata=512/ndata;
for i=1:ndata,
  x(i,:)=tek1((i*mdata-(mdata-1)):mdata*i);
  y(i,:)=tek2((i*mdata-(mdata-1)):mdata*i);
end

for i=1:ndata,
  xm=mean(x(i,:)); xm=ones(size(x(i,:)))*xm;   x(i,:)=x(i,:)-xm;
  ym=mean(y(i,:)); ym=ones(size(y(i,:)))*ym;   y(i,:)=y(i,:)-ym;
end

Z=zeros(ndata,mdata/2);I=ones(ndata,mdata/2);
pad01=[Z,I]; pad10=[I,Z];
xb=x.*pad01; xa=x.*pad10;

for i=1:ndata,
  XP(i,:)=fft(xa(i,:));
  XN(i,:)=fft(xb(i,:));
  Y(i,:)=fft(y(i,:));
end

if ndata==1,
  for i=1:ndata,
  phixy=(conj(XP(i,:)).*Y(i,:))/(mdata/2);
  phiyx=(XN(i,:).*conj(Y(i,:)))/(mdata/2);
end
else
for i=1:ndata,
  phixy(i,:)=(conj(XP(i,:)).*Y(i,:))/(mdata/2);
  phiyx(i,:)=(XN(i,:).*conj(Y(i,:)))/(mdata/2);
end
end

if ndata==1,
  Rxy=ifft(phixy);Rxy=real(Rxy);
  Ryx=ifft(phiyx);Ryx=real(Ryx);
else
  phixy=sum(phixy)*(1/ndata);phiyx=sum(phiyx)*(1/ndata);
  Rxy=ifft(phixy);Rxy=real(Rxy);
  Ryx=ifft(phiyx);Ryx=real(Ryx);
End

fid1 = fopen('rxynogap.txt','w');
fprintf(fid1,'%8.4f\n',Rxy);
fclose(fid1);

t2=(0:1:(mdata-1))*0.1;

figure;
subplot(1,2,1);
plot(t2,Rxy,'k');title('without gap (FFT)');
ymin3=min(Rxy);ymax3=max(Rxy);
axis([0 mdata*0.1 ymin3*1.2 ymax3*1.2]);
xlabel('time (ns)');
ylabel('correlation coeffcient');
subplot(1,2,2);
plot(t2,Rxyxy,'k');title('with gap (FFT)')
ymin3=min(Rxyxy);ymax3=max(Rxyxy);
axis([0 mdata*0.1 ymin3*1.2 ymax3*1.2]);
xlabel('time (ns)');
ylabel('correlation coeffcient');
```

```
zoom;
```

% AERELAT.M % A&E amplitude comparison

```
load d:\insight\na.fil;
load d:\insight\ne.fil;

x=na(1:20000);
y=ne(1:20000);

p=polyfit(x,y,2);          % curve fitting
z=0:0.1*max(x):max(x);
f=p(1).*z.*z+p(2).*z+p(3);

figure;
plot(x,y,'ok',z,f,'-k');
axis([0 max(y) 0 max(f)]);
set(gca,'fontname',['arial']);
set(gca,'fontsize',[12]);
xlabel('acoustic magnitude ( mv)');
ylabel('electric magnitude ( pC)');
zoom;
%z=(0.1:0.1:4.2)*25;
%f=polyval(p,x);
```

% QUITASK.M % Dialogue to confirm exit

```
figquit=figure('NumberTitle','off',...
        'Name','Quit from Partial Discharge?',...
        'MenuBar','none',...
        'Color',[0.5,0.75,0.75],...
        'Resize','off',...
        'Position',[90 245 205 120]);
quit_inq=uicontrol(gcf,...
        'Style','text',...
        'String','REALLY WANT TO QUIT?',...
        'ForegroundColor',[1 0 0],...
        'BackgroundColor',[0.5,0.75,0.75],...
        'Position',[25 70 160 25]);
quit_yes=uicontrol(gcf,...
        'Style','push',...
        'String','YES',...
        'Position',[25 20 70 25],...
        'CallBack',['close(gcf);',...
                'close(1);']);
quit_no=uicontrol(gcf,...
        'Style','push',...
        'String','NO',...
        'Position',[115 20 70 25],...
        'CallBack','close(gcf)');
clear quit_inq; clear quit_yes; clear quit_no;
```

Appendix B

Investigation of the Partial Discharge Detection Instrument (PDDI)

The PDDI is manufactured by the Ontario Hydro Company in Canada. It is designed for PD detection in cables. It is supposed to have several advantages over conventional system such as RF noise rejection through selectable filters at the input and high-gain and broad bandwidth amplifiers for maximum sensitivity. The signal input is filtered, amplified, digitised and then sent to computer through RS232 port (Figure B.1).

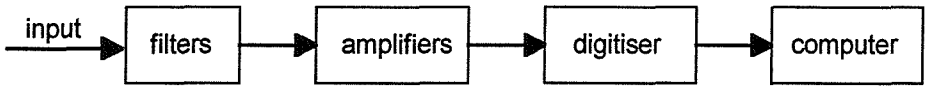

Figure B.1 Basic flowchart of the PDDI system

High voltage was applied to the 132 kV cable/joint in order to generate PD activity (Figure 7.1). The capacitive coupler output was connected to the surge protector, then amplified using the 0.01-500 MHz wide-band amplifier, and finally input into the PDDI. The software standard settings were selected to obtain the maximal signal/noise ratio. Figure B.2 shows the PDDI '3d scattered plot' at a trigger level above the background noise. Conventional PD detection indicates that the detection sensitivity is 10-15 pC, which is lower than the sensitivity (3 pC) using the capacitive coupler and

the oscilloscope. The cause of lower sensitivity was due to the PDDI system internal noise.

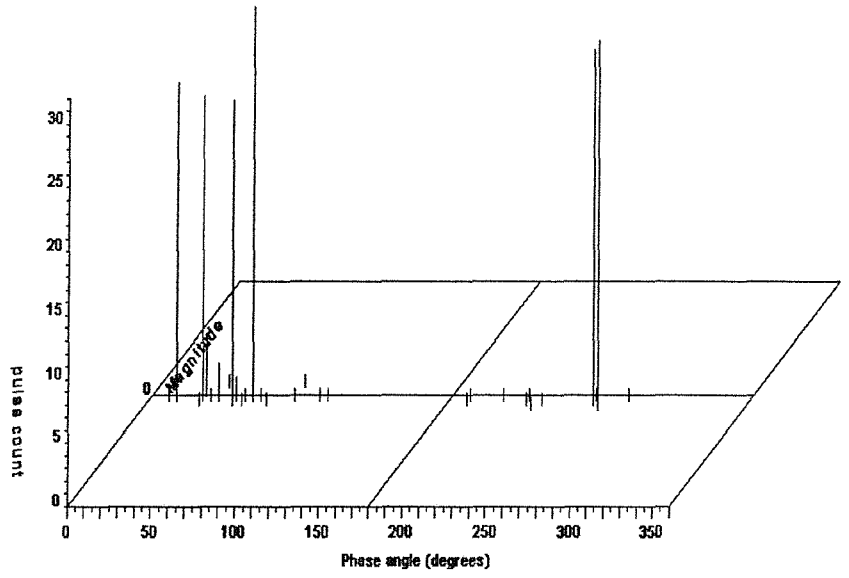

Figure B.2 PDDI '3d-scattered plot' of discharge within cable joint

Corona discharge was produced by placing a sharp conductor at the system earth. When the voltage was increased to 5 kV, discharges of 30 pC occurred. Figure B.3 shows the relevant '3D scattered plot', which indicates the typical corona discharge.

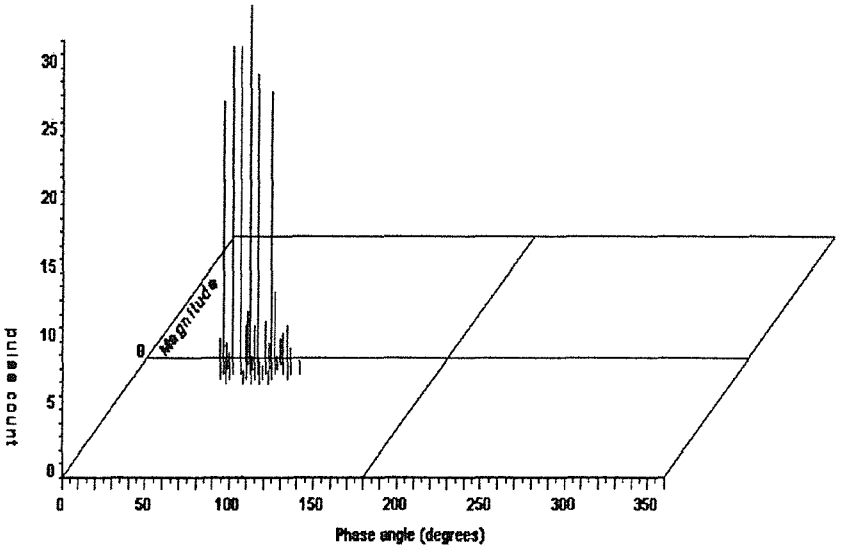

Figure B.3 PDDI '3d-scattered plot' of corona discharge

Appendix C

List of Publications

(1) Y Tian, P L Lewin, A E Davies and Z Richardson, "Acoustic Emission Detection of Partial Discharges in Polymeric Insulation", *Proceedings of 11th ISH*, London, August 1999

(2) Y Tian, P L Lewin, A E Davies and Z Richardson, "PD Pattern Identification using Acoustic Emission Measurement and Neural Networks", *Proceedings of 11th ISH*, London, August 1999

(3) Y Tian, P L Lewin, A E Davies and G Hathaway, "Acoustic Emission Techniques for Partial Discharge Detection within Cable Insulation", *Proceedings of 8th DMMA*, Edinburgh, September 2000

(4) Y Tian, P L Lewin, A E Davies, G Hathaway and S Swingler, "Acoustic Emission Measurement of Partial Discharge during Electrical Tree Growth in XLPE Cable Insulation", submitted to *7th International Conference on Solid Dielectrics*, Kema, Netherlands, June 2001

(5) "Partial Discharge Detection and Identification within High Voltage Polymeric Dielectrics Using Acoustic Emission Measurements", to be submitted to *IEEE Transactions on Dielectrics and Electrical Insulation*

(6) "Partial Discharge Detection in Cable System using VHF Capacitive Coupler", to be submitted to *IEEE Transactions on Dielectrics and Electrical Insulation*

(7) "Practical Application of Various PD Detection Methods to Cable/Joint System", to be submitted to *IEE Science, Measurement and Technology*

REFERENCES:

[1] "Partial Discharge Measurements", *IEC Publication 270*, 1981

[2] J. S. Townsend, "Electrons in Gases", *Hutchinson Ltd.*, 1948

[3] H. Raether, "Electron Avalanches and Breakdown in Gases", *Butterworths Press*, London, 1964

[4] J. M. Meek and J. D. Craggs, "Electrical Breakdown of Gases", *John Wiley & Sons Ltd*, 1978

[5] W. P. Baker, "Electrical Insulation Measurements", *George Newnes Ltd*, London, 1965

[6] D. Zhu and Z. Yan, "High Voltage Insulation", *Tsinghua University Press*, China, 1990

[7] C. Qiu and N. Wang, "Techniques for Measuring Partial Discharges in Electrical Apparatus", *Mechanical Industry Press*, China, 1994

[8] F. H. Kreuger, "Industrial High Voltage", *Delft University Press*, 1992

[9] F. M. Penning, "Electrical Discharges in Gases", *Cleaver-Hume Press Ltd.*, 1965

[10] F. H. Kreuger, "Discharge Detection in High Voltage Equipment", *Temple Press Books Ltd*, London, 1964

[11] R. W. Sillars, "Electrical insulating materials and their application", *Peter Peregrinus Ltd.*, 1973

[12] D. M. Robinson, "Dielectric Phenomena in High Voltage Cables", *Chapman & Hall Ltd.*, 1936

[13] S. Boggs and J. Densley, "Fundamentals of Partial Discharge in the Context of Field Cable Testing", *IEEE Electrical Insulation Magazine*, Vol. 16, No. 5, pp. 13-18, September/October 2000

[14] "Evaluation of Field Diagnostic Techniques for Transmission Cable Accessories", *Report No. TR-112676*, EPRI, California, and NEETRAC – A centre of Georgia Institute of Technology, Georgia, 1999

[15] Z. Shi, "Application of Electromagnetic Wave", *Higher Education Press*, China, 1990

[16] I. J. Kemp, "Developments in Partial Discharge Plant-Monitoring Technology", *International Conference on Partial Discharge*, pp. 52-55, September 1993, University of Kent in Canterbury, UK

[17] G. C. Stone, "The Use of Partial Discharge Measurement to Assess the Condition of Rotating Machine Insulation", *DEIS*, Vol. 12, No. 4, pp. 23-27, July/August, 1996

[18] Q. Su, "A New Partial Discharge Detector for On-line Insulation Condition Monitoring of Generators", *Proc. 10th ISH*, Montreal, August 19997

[19] J. P. Zondervan, E. Gulski, J. J. Smit, "Fundamental Aspects of PD Patterns of On-line Measurements on Turbogenerators", *IEEE Transactions on Dielectric and Electrical Insulation*, Vol. 7, No. 1, pp. 59-70, February, 2000

[20] K. Itoh, Y. Kaneda, S. Kitamura, K. Kimura, K. Hayashi, H. Tokura, "Partial Discharge Detection in High Voltage Rotating Machines", *International Conference on Partial discharge*, pp. 111-112, September 1993, University of Kent in Canterbury, UK

[21] G. Wu and D.H. Park, "On-line Monitoring Instrument of Fault Discharge in Large Generators", *11th International Symposium on High Voltage Engineering*, pp. 340-343, Vol. 5, London, August 1999

[22] H. B. Cummings, J. R. Boyle, B. W. Arp, "Continuous online monitoring of free-standing, oil-filled current transformers to predict imminent failure", *IEEE Trans. Power Delivery*, 1988

[23] C. Boisseau, "Instrument Transformers On Line Monitoring by Means of Partial Discharge Measurement", *Proc. 7th ISH*, Vol. 7, pp. 123-126, 1991

[24] R. Lortie, J. Aubin, G. H. Vaillancourt and Q. Su, "Partial Discharge Detection on Power Transformers using a Multi-terminal Measurement Method", *Proc. 10th ISH (Montreal)*, August 1997

[25] C. Wang et al, "On-line Partial Discharge Monitoring System for Power Transformer", *Proc. 10th ISH (Montreal),* August 1997

[26] J. Bolhuis, E. Gulski, J. Smit, T. Grun and M. Turner, "Comparison of Conventional and VHF Partial Discharge Detection Methods for Power Transformers", *11th International Symposium on High Voltage Engineering*, Vol. 5, pp. 49-52, London, August 1999

[27] J. S. Pearson et al, "Partial Discharge Diagnostics for Gas Insulated Substations", *IEEE Trans. EI*, Vol. 2, No. 5, pp. 893-905, 1995

[28] M. Judd, B. F. Hampton and W. Brown, "UHF Partial Discharge Monitoring for 132 kV GIS", *Proc. 10th ISH*, Montreal, August 1997

[29] M. D. Judd, O. Farish and B. F. Hampton, "Excitation of UHF signals by partial discharges in GIS", *IEEE Trans. DEI*, Vol. 3, No. 2, pp. 213-228, 1996

[30] R. Kurrer and K Feser, "Attenuation measurements of UHF partial discharge signals in GIS", Proc. *10th ISH (Montreal),* Vol. 2, pp. 161-164, 1997

[31] M. Hikita, T. Horiuchi, Z. H. Tian, H. Suzuki, "Study on Mechanisms and Propagation Characteristics of Partial Discharges in SF_6 GIS", *Proc. 11th ISH (London)*, Vol. 5, pp. 66-69, 1999

[32] J. A. Cosgrave et al, "An Optical Fibre-based Acoustic Sensor for Detecting Electrical Discharges in SF_6 Puffer Circuit Breakers", *Proc. 7th DMMA conference*, pp. 307-312, September, 1996

[33] M. Runde, B. Skyberg and M. Ohlen, "Vibration Analysis for Periodic Diagnostic Testing of Circuit-Breakers", *Proc. 11th ISH (London),* Vol. 1, pp. 98-101, 1999

[34] H. K. Hoidalen et al, "Continuous Monitoring of Circuit-Breakers using Vibration Analysis", *Proc. 11th ISH (London),* Vol. 1, pp. 102-106, 1999

[35] B.T. Phung, R.E. James, T.R. Blackburn and Q. Su, "Partial discharge ultrasonic wave propagation in steel transformer tanks", *Proc. 7th ISH (Dresden)*, pp. 131-134, August 1991

[36] T. Bengtsson, H. Kols and B. Jonsson, "Transformer PD Diagnosis using Acoustic Emission Technique", *Proc. 10th ISH, Montreal,* Canada, August, 1997

[37] E. Howells and E. T. Norton, "Detection of Partial Discharges in Transformers using Acoustic Emission Techniques", *IEEE Trans. On PAS.* Vol. PAS-97, No. 5, pp. 1538-1549, 1998

[38] S. Rengarajan, A. Bhoomariah, K. K. Kishore, "Acoustic Partial Discharge Measurements for Transformer Insulation-an Experimental Validation", *Proc. 11th ISH (London),* Vol. 5, pp. 288-291, 1999

[39] B. H. E. Wahlstrom et al, "Acoustic Detection, Localisation and Identification of Anomalies in GIS", *Proc. 6th ISH*, 23.07, New Orleans, USA, August 1989

[40] L. E. Lundgaard, M. Runde and B. Skyberg, "Acoustic Diagnosis of Gas Insulated Substations: A Theoretical and Experimental Basis", *IEEE Trans. Power Delivery*, Vol. 5, No. 4, pp. 1751-1759, November 1990

[41] A. Bargigia, W. Koltunowicz and A. Pigini, "Detection of Partial Discharges in Gas Insulated Substations", *IEEE Trans. Power Delivery*, Vol. 7, No. 3, pp. 1239-1249, July 1992

[42] R. Bozzo, F. Guastavino, "PD Detection and Localisation by means of Acoustic Measurements on Hydogenerator Stator Bars", *IEEE Trans. EI*, Vol. 2, pp. 660-665, 1995

[43] L. Ghirelli et al, "Acoustical Method for Partial Discharge Detection in High Power Capacitors", *Proc. International Conf. Partial Discharge*, pp. 92-93, 1993

[44] B. Cox, "Partial Discharge Detection in GIS by an Optical Technique", *Proceeding of International Symposium on GIS*, pp. 341-349, Toronto, 1985

[45] L. Maria, E. Colombo and W. Koltunowicz, "Comparison among PD Detection Methods for GIS On-site Testing", *Proc. 11th ISH (London),* Vol. 5, pp. 90-93, 1999

[46] F. Y. Chu, "SF_6 Decomposition in Gas-Insulated Equipment", *IEEE Trans. EI*, Vol. EI-21, No. 5, pp. 693-725, October 1986

[47] O. Celi et al, "Study of Diagnostic Methods for the Identification of Defects in side GIS", *Proc. 6th ISH*, No 32.04, New Orleans, 1989

[48] J. Unsworth and F. Mitchell, *IEEE Trans. EI*, EI-25, No. 4, p. 737, 1990

[49] C. Xue, "Monitoring Paper Insulation Ageing by Measuring Furfural Contens in Transformer Oil", *Proc. 7th ISH*, 74.06, pp. 139-142, August 1991

[50] M. Duval, "Dissolved Gas Analysis: It Can Save Your Transformer", *IEEE Elect. Insul. Mag.*, Vol. 5, No. 6, pp. 22-27, November/December 1989

[51] Technical Operation Manual of Discharge Detector (model 5 type 700), *Robinson Instruments Company*

[52] "Partial Discharge Detector TE 571 - True Digital Partial Discharge Analysing System", *Tettex Instruments Division*, Haefely Trench AG, Switzerland

[53] "LDIC Digital Partial Discharge Detector", *LEMKE Diagnostics GmbH*, Germany

[54] T. Okamoto and T. Tanaka, "Novel PD measurement Computer Aided System", *IEEE Trans. EI-21*, pp. 1015-1019, 1986

[55] T. Tanaka, "PD Pulse Distribution Pattern Analysis", *International Conference on Partial Discharge*, pp. 31-34, September 1993

[56] E. Gulski and F. H. Kreuger, "Computer-aided Recognition of Discharge Sources", *IEEE Trans. EI*, No. 21, pp. 82-92, 1992

[57] F. H. Kreuger, E. Gulski and A. Krivda, "Classification of Partial Discharges", *IEEE Trans. EI*, Vol. 28, No. 6, pp. 917-931, 1993

[58] E. Gulski, "Computer-aided Measurement of Partial Discharges in HV Equipment", *IEEE Trans. EI*, Vol. 28, No. 6, pp. 969-982, 1993

[59] R. E. James, B. T. Phung, "Development of Computer-based Measurement and their Application to PD Pattern Analysis", *IEEE Trans. EI*, No. 2, pp. 838-853, 1995

[60] A. Contin, G. C. Montanari and C. Ferraro, "PD Source Recognition by Weibull Processing of Pulse Height Distributions", IEEE Trans. EI, Vol. 7, No. 1, pp. 48-58, 2000

[61] E Pultrum, M Van Riet, "HF partial discharge detection of HV extruded cable accessories", *JICABLE*, pp. 662-665, 1995

[62] E Ildstad, H Faremo, O Lillevik, D Linhjell, "Detection and Location of Partial Discharges Sources in XLPE Cables", *10th International Symposium on HV Engineering* , Montreal, Canada, August 1997

[63] G. Katsuta, A. Toya, T. Endoh, Y.Sekii and C. Ikeda, "Development of a Method of Partial Discharge Detection in Extra-HV Cross-Linked Polyethylene Insulated Cable Lines", *IEEE Trans. Power Delivery*, Vol. 7, No. 3, pp. 1068-1079, 1992

[64] N. H. Ahmed and N. N. Srinivas, "On-Line Partial Discharge Detection in Cables", *IEEE Transactions on Dielectrics and Electrical Insulation*, Vol.5, No. 2, pp. 181-188, April, 1998

[65] H Bidhendi and Q Su, "Partial Discharge Location for Cables with Helical Earth Screens", *10th International Symposium on HV Engineering, Montreal,* Canada, August 1997

[66] P. Wouters, E. Hetzel and E. Steennis, "New on-line PD measurement technique for polymer insulated cables and accessories", *Proc. 8th ISH*, 63.08, 1993

[67] M Mashikian, R Bansal and R B Northrop, "Location and Characterisation of Partial Discharge Sites in Shielded Power Cables", *IEEE Transaction on Power Delievery*, Vol. 5, No.2, pp. 833-839, April 1990

[68] R. J. Jackson, A. Wilson, and D.B. Giesner, "Partial discharges in power cable Joints: their propagation along a crossbonded circuit and methods for their detection", *IEE Proc.* Vol. 127, Pt. C, No. 6, pp. 420-429, November 1980

[69] B. T. Phung, Z. Liu, T. R. Blackburn and R. E. James, "On-line Partial Discharge Measurement on High Voltage Power Cables", *Proc. 11th ISH* (London), Vol. 4, pp. 328-332, August 1999

[70] Y. Yasuda et al, "Application of FWT (Fast Wavelet Transform) for Auto-Detection System of Partial Discharge in Power Cables", *Proc. of 11th ISH* (London), Vol. 5, pp. 301-304, August 1999

[71] H. N. Bidhendi and Q. Su, "A New Partial Discharge Location Technique for Power Cables Based on the Extension of the Characteristic Impedance", *10th International Symposium on High Voltage Engineering*, Montreal, Canada, August, 1997

[72] Th. Heizmann, Th. Aschwanden, H. Hahn, M. Laurent and L. Ritter, "On-Site Partial Discharge Measurements on Premoulded Cross-Bonding Joints of 170 kV XLPE and EPR Cables", *IEEE Transactions on Power Delievery*, Vol. 13, No. 2, pp. 330-335, April, 1998

[73] B. M. Oliver, "Directional Electromagnetic Couplers", *Proc. of the IRE*, 42 (1954), pp. 1686-1692

[74] H. G. Sedding, S. R. Campbell, G. C. Stone and G. S. Klempner, "A New Sensor for Detecting Partial Discharges in Operating Turbine Generators", *IEEE Trans. On Energy Conversion*, Vol. 6, No. 4, pp. 700-706, December 1991

[75] D Pommerenke, T Strehl and W Kalkner, "Directional Coupler Sensor for Partial Discharge Recognition on High Voltage Cable Systems", *10th International Symposium on HV Engineering,* Montreal, Canada, August 1997

[76] D. Pommerenke, T. Strehl, R. Heinrich, W. Kalkner, F. Schmidt, W. Weiβenberg, "Discrimination between Internal PD and Other Pulses Using Directional Coupling Sensors on HV Cable Systems", *IEEE Transactions on Dielectrics and Electrical Insulation*, pp. 814-824, Vol. 6, No. 6, December 1999

[77] E. Lemke, T. Strehl and D. Ruβwurm, "New Development in the Field of PD Detection and Location in Power Cables under On-site Condition", *Proc. 11th ISH*, Vol. 5, pp. 106-111, London, August 1999

[78] P. Craatz, R. Plath, R. Heinrich and W. Kalkner, "Sensitive On-site PD Measurement and Location using Directional Coupler Sensors in 110 kV Prefabricated Joints", *Proc. 11th ISH*, Vol. 5, pp. 317-321, London, August 1999

[79] Y. Kagawa and S. Yamazaki, "Acoustic Emission Associated with Tree Growth in Polymeric Materials", *IEEE Trans. EI.*, Vol. 67-17, No. 4, August 1982

[80] R. T. Harrold, "Acoustical Technology Applications in Electrical Insulation and Dielectrics", *IEEE Trans. EI,* Vol. EI-20, No. 1, pp. 3-19, February 1985

[81] N. Pomeroy, "Partial Discharge Detection Within HV Polymeric Cable Joints using Acoustic Emission Techniques", *Technical report*, University of Southampton, 1995

[82] W. Swindlehurst, "A series on acoustic emission – Acoustic emission introduction", *Non-destructive Testing*, pp. 152-158, June 1973

[83] CIGRE WG 21-05, "Partial discharge detection by means of acoustic detection", 1993

[84] D Zhu, A McGrail, S Swingler, D Auckland, B Varlow, "Partial Discharge Detection in Cable Termination Using Acoustic Emission Techniques and Adaptive Signal Processing", *IEEE International Symposium on Electrical Insulation (Pittsburgh),* pp. 74-76, June 1994

[85] M Ekberg, A Gustafsson, M Leijon, T Bengtsson, T Eriksson, C Tornkvist, K Johansson and L Ming, "Recent Results in HV Measurement Techniques", *IEEE Transactions on Dielectrics and Electrical Insulation*, Vol. 2, No. 5, pp. 906-913, 1995

[86] D. W. Auckland, A. J. McGrail, C. D. Smith, B. R. Varlow, J. Zhao and D. Zhu, "The Application of Ultrasound to the Inspection of Insulation", IEEE 5th *International Conference on Conduction and Breakdown in Solid Dielectrics*, pp. 590-594, 1995

[87] M. Leijon, L. Ming, T. Bengtson, O. Kristofersson, "PD detection in cable terminations using acoustic technique", CIGRE symp. Diagnostic and Maintenance Techniques, paper 140-06, Berlin, 1993

[88] L. E. Lundgaard and W. Hansen, "Acoustic Method for Quality Control and In-Service Periodic Monitoring of Medium Voltage Cable Terminations", *Conference Record of the IEEE International Symposium on Electrical Insulation (Virginia)*, pp. 130-133, June 1998

[89] Y Tian, P L Lewin, A E Davies and G Hathaway, "Acoustic Emission Techniques for Partial Discharge Detection within Cable Insulation", *8th International Conference on Dielectric Materials, Measurements and Applications*, Edinburgh, UK, 2000

[90] N. Singh, O. Morel and S. Singh, "the Condition Assessment through Dissolved-Gas Analysis of 138 kV extruded Cable Terminations", *Detroit Edison® Report for EPRI and NEETRAC centre of Georgia Institute of Technology*, USA, TR-112676, pp. 9.16-9.20, 1999

[91] M. S. Mashikian, R. Bansal and R. B. Northrop, "Location and Characterization of Partial Discharge Sites in Shielded Power Cables", *IEEE Trans. Power Delievery*, Vol. 5, No. 2, pp. 833-839, 1990

[92] M. Mashikian, G. Valdes, V. Gonzalez and C. Katz, "Partial discharge location as a cable operating tool", Jicable'95, pp. 649-654, 1995

[93] Z. Du, P. K. Willett and M. S. Mashikian, "Performance Limits of PD Location Based on Time-domain Reflectometry", *IEEE Trans. EI*, Vol. 4, No. 2, pp. 182-188, April 1997

[94] F. H. Kreuger et al, "Partial Discharge Part XVIII: Errors in the Location of Partial Discharges in High Voltage Solid Dielectric Cables", *IEEE Electrical Insulation Magazine*, Vol. 9, No. 6, pp. 15-23, November/December 1993

[95] M. S. Mashikian, F. Palmieri, R. Bansal and R. B. Northrop, "Location of Partial Discharges in Shield Cables in the Presence of High Noise", *IEEE Trans. EI*, Vol. 27, No. 1, pp. 37-43, February 1992

[96] H. Borsi, "Digital Location of Partial Discharges in HV Cables", *IEEE Trans. EI*, Vol. 27, No. 1, pp. 28-36, February 1992

[97] "Guide for Partial Discharge Measurements", *British Standard*, 1985

[98] A. A. Pollock, "Practical Guide to Acoustic Emission Testing", *Physical Acoustics Corporation,* New Jersey, USA, 1988

[99] H. Suzuki and T. Endoh, "Pattern Recognition of Partial Discharges in XLPE Cables Using a Neural Network", *IEEE Trans. EI,* Vol. 27, No. 3, pp. 543-549, June 1992

[100] G. Katsuta, A. Toya, T. Endoh, Y. Sekii and C.lkeda, "Development of a Method of Partial Discharges Detection in Extra-HV Cross-Linked Polyethylene Insulated Cable Lines", *IEEE Trans. On Power Delivery*, Vol. 7, No. 3, pp. 1068-1079, 1992

[101] H. Borsi, E. Gockenbach, D. Wenzel, "Separation of Partial Discharges from Pulse Shaped Noise Signals with the help of Neural Networks", *Proc. of International Conference on Partial Discharge*, pp. 47-48, September 1993

[102] T. Brosche, W. Hiller, E. Fauser and W. Pfeiffer, "Novel Characterisation of PD Signals by Real-time Measurement of Pulse Parameters", *IEEE Trans. EI.* Vol. 6, No. 1, pp. 51-59, Feb 1999

[103] B. A. Fruth and D. W. Gross, "Tools and Sensors for Flexible On-line Diagnosis of High Voltage Insulation Systems", *Proc. IEEE Int. Symp. on Electric Power Engineering*, pp. 68-73, Stockholm, Sweden, June 1995

[104] P. Grunewald and J. R. Weidner, "On-line PD Analysis in Power Plants – A Successful Tool For Early Fault Detection", *Proc. of International Conference on Partial Discharge*, pp. 86-87, September 1993

[105] R. K. Miller and P. Mcintire, "Nondestructive Testing Handbook", Published by *American Society for Nondestructive Testing*, 1988

[106] T. Okamoto and T. Tanaka, "Novel PD Measurement Computer Aided System", *IEEE Trans. EI*, Vol. 21, pp. 1015-1019, December 1986

[107] M. Kahle, E. Neudert and J. Maaβ, "PD – Source Characterization by Computer Aided Analysis", *7th Internaitonal Symposium on High Voltage Engineering* (Dresden, Germany), pp. 113-116, August 1991

[108] E. Gulski and F. H. Kreuger, "Computer-aided recognition of Discharge Sources", *IEEE Trans. EI,* Vol. 27, No. 1, pp. 82-92, February 1992

[109] T. Tanaka, "PD Pulse Distribution Pattern Analysis", *Proc. of International Conference on Partial Discharge*, pp. 31-34, September 1993

[110] E. Gulski, "Computer-aided Measurement of Partial Discharges in HV Equipment", *IEEE Trans. EI*, Vol. 28, No. 6, pp. 969-982, December 1993

[111] F. H. Kreuger, E. Gulski and A. Krivda, "Classification of Partial Discharges", *IEEE Trans. EI,* Vol. 28, No. 6, pp. 917-931, December 1993

[112] R. E. James and B. T. Phung, "Development of Computer-based Measurements and their Application to PD Pattern Analysis", *IEEE Trans. EI*, Vol. 2, No. 5, pp. 838-854, October 1995

[113] T Hucker and H G Kranz, "A New Approach in PD Diagnosis and PD Pattern Recognition", *Proc. of International Conference on Partial Discharge*, pp. 74-75, September 1993

[114] R. Candela, G. Mirelli and R. Schifani, "PD Recognition by Means of Statistical and Fractal Parameters and a Neural Network", *IEEE Trans. EI,* Vol. 7, No. 1, pp. 87-94, February 2000

[115] J. P. Zondervan, E. Gulski and J. J. Smit, "Fundamental Aspects of PD Patterns of On-line Measurements on Turbogenerators", *IEEE Trans. EI*, Vol. 7, No. 1, pp. 59-70, February 2000

[116] A. Krivda, E. Gulski, L. Satish and W. S. Zaengl, "The Use of Fractal Features for Recognition of 3-D Discharge Patterns", *IEEE Trans. EI*, Vol. 2, No. 5, pp. 889-892, October 1995

[117] G. C. Stone, "The Use of Partial Discharge Measurement to Assess the Condition of Rotating Machine Insulation", *DEIS,* Vol. 12, No. 4, pp. 23-27, July/August, 1996

[118] J. S. Pearson et al, "Partial Discharge Diagnostics for Gas Insulated Substations", *IEEE Trans. EI*, Vol. 2, No. 5, pp. 893-905, 1995

[119] B. Hampton, "UHF Diagnosis for Gas Insulated Substations", *Proc. of 11th ISH* (London), Vol. 5, pp. 6-16, August 1999

[120] J. P. Bolhuis et al, "Comparison of Conventional and VHF Partial Discharge Detection Methods for Power Transformers", *Proc. of 11th ISH* (London), Vol. 5, pp. 49-52, August 1999

[121] Y. Liu and C. Qiu, "Electrical Insulation Measurement Technique", *Xi'an Jiaotong University Press*, August 1991

[122] R.M. Eichhorn, "Treeing in Solid Extruded Electrical Insulation", *IEEE Trans. EI*, Vol. 12, No. 1, 1977

[123] Suwarno et al, "Partial Discharge Patterns of Electrical Treeing in Polyethylene", *Proceedings of the 4th International Conference on Properties and Applications of Dielectric Materials*, pp. 379-382, Brisbane Australia, July 1994

[124] T. Kalicki et al, "Partial Discharge Pulse Characteristics of Electrical Trees in XLPE Cable Insulation", *IEEE 5th International Conference on Conduction and Breakdown in Solid Dielectrics*, pp. 528-532, 1995

[125] H. N. Nagamani et al, "Electrical Tree Growth in XLPE Material under AC and Impulse Voltages", *7th International Conference on Dielectric Materials Measurement & Applications*, pp. 259-262, 1996

[126] S. H. Kim et al, "A Composite System for Simultaneous Detection of Electrical Charge and Acoustic Emission Pulse of Partial Discharges", *Proceedings of the 5th International Conference on Properties and Applications of Dielectric Materials*, Seoul, Korea, pp. 817-819, May 1997

[127] A. S. Malinovski et al, "Simulation of Partial Discharges and Electrical Tree Growth in Solid Insulation under AC Voltage", *IEEE International Conference on Conduction and Breakdown in Solid Dielectrics*, pp. 305-308, Vasteras, Sweden, June 1998

[128] L. A. Dissada and J. C. Fothergill, "Electrical Degradation and Breakdown in Polymers", *IEE Materials and Devices series*, 1992

[129] D. W. Auckland and B. R. Varlow, "Electrical treeing in solid polymeric insulation", *Engineering Science and Education Journal*, pp. 11-16, February 1995

[130] G. Wu et al, "The Experimental Study on Tree Growth in XLPE using 3D PD Patterns", *IEEE 6th International Conference on Properties & Applications of Dielectric Materials*, Xi'an, China, June 2000

[131] J. V. Champion, S. J. Dodd and J. M. Alison, "The correlation between the partial discharge behaviour and the spatial and temporal development of electrical trees grown in an epoxy resin", *J. Phys, D: Appl. Phys.*, pp. 2689-2695, Vol. 29, 1996

[132] I. W. Simmonds, "Investigation into the Electrical Tree Growth and Breakdown Characteristics in High Voltage XLPE Cable Insulation", *Final year project report*, University of Southampton, May 1999

[133] X. Yang and J. Zheng, "Artificial Neural Networks", *Higher Education Press*, China, September 1992

[134] N. Hozumi, T. Okamoto and T. Imajo, "Discrimination of Partial Discharge Patterns Using a Neural Network", *IEEE Trans. EI*, Vol. 27, No. 3, pp. 550-556, June 1992

[135] A. Krivda and E. Gulski, "Neural Networks as a tool for Recognition of Partial Discharges", *Proc. of International Conference on Partial Discharge*, pp. 84-85, September 1993

[136] E. Gulski and A. Krivda, "Neural Networks as a Tool for Recognition of Partial Discharges", *IEEE Trans. EI*, Vol. 28, No. 6, pp. 984-1001, December 1993

[137] H. G. Kranz, "Diagnosis of Partial Discharge Signals using Neural Networks and Minimum Distance Classification", *IEEE Trans. EI*, Vol. 28, No. 6, pp. 1016-1024, December 1993

[138] T. Okamoto and T. Tanaka, "Partial Discharge Pattern Identification for three kinds of model electrodes with a Neural Network", *IEE Proceedings-Science and Measurement*, pp. 75-84, Vol. 142, No. 1, 1995

[139] K. Tan et al, "Recognition of Partial Discharge based on Artificial Neural Network", *Proc. 10th ISH (Montreal)*, August 1997

[140] T. Medjeldi et al, "Identification of Partial Discharges Sources using a combination of Linear Prediction and Neural networks", *IEEE International Conference on Conduction and Breakdown in Solid Dielectrics*, pp. 165-167, Vasteras, Sweden, June 1998

[141] D. Zhu et al, "Partial Discharge Detection in Cable Termination Using Acoustic Emission Techniques and Adaptive Signal Processing", *Conference Record of IEEE International Symposium on Electrical Insulation*, Pittsburgh, USA, June 1994

[142] D. W. Auckland, A. J. McGrail, C. D. Smith, B. R. Varlow, J. Zhao and D. Zhu, "Application of ultrasound to the inspection of insulation", *IEE Proc.-Sci. Meas. Technol.* Vol. 143, No. 3, pp. 177-181, May 1996

[143] B. R. Varlow, D. W. Auckland, C. D. Smith and J. Zhao, "Acoustic emission analysis of high voltage insulation", *IEE Proc.-Sci. Meas. Technol.* Vol. 146, No. 5, pp. 260-263, September 1999

[144] T. R. Blackburn, B. T. Phung and R. E. James, "Neural Network application in PD Pattern Analysis", *Proc. of International Conference on Partial Discharge*, pp. 82-83, September 1993

[145] A. A. Mazroua, R. Bartnikas and M. Salama, "Discrimination between Partial Discharge Pulse Shapes using different Neural Network Paradigms", *IEEE Trans. DEI*, Vol. 1, No. 6, pp. 1119-1131, 1994

[146] B. Fruth, L. Niemeyer, "The importance of Statistical Characteristics of Partial Discharge Data", *IEEE Trans. EI*, Vol. 27, pp. 60-69, 1992

[147] T Hucker and H G Kranz, "A New Approach in PD Diagnosis and PD Pattern Recognition", *Proc. of International Conference on Partial Discharge*, pp. 74-75, September 1993

[148] M. Mukai et al, "Degradation Diagnosis of The Solid Insulation Using Sound Waves Emitted by Partial Discharges", *Proc. of 4th International Conference on Properties and Applications of Dielectric Materials*, pp. 614-617, Brisbane, Australia, July 1994

[149] M Leijon, L Ming and T. Bengtsson, "PD-Source Identification in Solids", *Conference Record of IEEE International Symposium on Electrical Insulation*, pp. 415-418, Baltimore USA, June 1992

[150] R. K. Elsley and L. J. Graham, "Pattern Recognition Techniques Applied to Sorting Acoustic Emission Signals", *IEEE Ultrasonics Symposium Proceedings*, pp. 147-150, 1976

[151] S Xu, Z Zhu and C Chen, "Application of Signal-adapted Wavelet to the Detection of PD", *IEEE 6th International Conference on Properties & Applications of Dielectric Materials*, Xi'an, China, June 2000

[152] X. Han, Y. Qiu and R. Feng, "Application of wavelet analysis to PD detection in GIS", *High Voltage Apparatus*, No. 4, 1996

[153] M. Florkowski, "Wavelet Denoising of Partial Discharge Images", *IEEE 6th International Conference on Properties & Applications of Dielectric Materials*, Xi'an, China, June 2000

[154] X. Ma, C. Zhou and I. J. Kemp, "Investigation into the use of wavelet theory for partial discharge pulse extraction in electrically noisy environments", pp.

123-126, *8th International Conference on DMMA*, September 2000, Edinburgh, U.K.

[155] Y. Yasuda et al, "Application of FWT (Fast Wavelet Transform) for Auto-Detection System of Partial Discharges in Power Cables", *Proc. of 11th ISH*, Vol. 5, pp. 301-304, London, UK, August 1999

[156] H. Li, D. Xiao and Y. Chen, "Wavelet ANN Based Transformer Fault Diagnosis Using Gas-in-oil Analysis", *IEEE 6th International Conference on Properties & Applications of Dielectric Materials*, Xi'an, China, June 2000

[157] C. K. Chui, "An Introduction to Wavelets", Academic Press, USA, 1992

[158] Q. Qin and Z. Yang, "Wavelet Analysis", *University of Electronic Technology Press*, China, 1994

[159] K. Zong and G. Hu, "Digital Signal Processing", *Tsinghua University Press*, China, 1988

[160] P L Lewin, "Development of an efficient correlation algorithm", *Technical Report*, University of Southampton, 1995

[161] Y. Lu, X. Tan and X. Hu, "PD detection and localisation by acoustic measurements in an oil-filled transformer", *IEE Proc.-Sci. Meas. Technol.*, Vol. 147, No. 2, pp. 81-85, March 2000

[162] M. Misiti et al, "Matlab Wavelet Toolbox User's Guide", *Mathworks Inc.* , 1996

[163] D. F. Mix, "Random Signal Processing", *Prentice Hall International Inc.*, 1985

[164] C. Feng, "Electromagnetics", *Higher Education Press,* China, 1983

[165] G. Qiu, "Electric Circuit", *Higher Education Press*, China, 1989

[166] R. V. Williams, "Acoustic Emission", *Adam Hilger Ltd.*, U.K., 1980

[167] X. Liang, Z. Guan and C. Chen, "High Voltage Engineering", Tsinghua University Press, China, 1995